Detection of Atmospheric Muon Neutrinos with the AMANDA Neutrino Telescope

Diplomarbeit

Humboldt–Universität zu Berlin
Mathematisch–Naturwissenschaftliche Fakultät I
Institut für Physik

eingereicht von

Markus Gaug
geb. am 06.05.1973 in Wels

Berlin, Oktober 2000

Maar wat wij bedoelen is dit: jullie zijn dan wel sterfelijk, maar het feit dat dat ene, minimale brein over de eeuwigheid na kan denken, of over het verleden, en dat jullie daardoor, met de beperkte ruimte en de beperkte tijd die jullie gegeven is, juist zo onmetelijk veel ruimte en tijd kunnen innemen, dat is het raadsel. Stuk voor stuk koloniseren jullie, als jullie dat tenminste willen, tijdperken en werelddelen. Jullie zijn de enige wezens in het hele universum die dat kunnen, en dat uitsluitend door te denken. De eeuwigheid, God, de geschiedenis, het zijn allemaal jullie uitvindingen, het is zoveel dat jullie er zelf in verdwaald zijn. Alles is tegelijkertijd echt en een illusie, daar valt ook moeilijk mee te leven[1].

[1] *Cees Noteboom, in Allerzielen*

Contents

1 Introduction **1**

2 Cosmic Rays **2**
2.1 Astro-Particle Physics . . . 3
2.2 Astronomy with Neutrinos . . . 5
2.3 Atmospheric Neutrinos . . . 9

3 The AMANDA Detector **11**
3.1 History . . . 11
3.2 The Detection Medium . . . 11
3.3 Performance and Calibration . . . 15
3.3.1 The Data Acquisition System (1997) . . . 15
3.3.2 Calibration . . . 15

4 Simulation **17**
4.1 Atmospheric Muon Background Monte Carlo . . . 17
4.2 Atmospheric Neutrino Signal Monte Carlo . . . 17
4.2.1 Mass Production 1998 . . . 17
4.2.2 Mass Production 2000 . . . 19

5 Reconstruction and Filtering **21**
5.1 Preprocessing . . . 21
5.2 The Line Fit and Level 1 Filter . . . 22
5.3 The Maximum Likelihood Fits and Level 2 Processing . . . 24
5.4 Tensor of Inertia, Shower and Energy Fits . . . 27
5.4.1 Filtering on the "Center-of-Gravity" (c.o.g.)-Background . . . 30
5.5 The Dipole Fit, Multi-PE-Fits and Bayesian Approach . . . 34
5.6 Conclusions . . . 37

6 Cut Evaluation **39**
6.1 Cut Parameters . . . 40
6.1.1 L_{up} and L_{down} . . . 41
6.1.2 Differences between Reconstructed Directions . . . 41
6.1.3 The Smoothness Parameters . . . 42
6.2 Products of Direct Hits with Lengths of Direct Hits . . . 44
6.3 The CUTEVAL Method . . . 46
6.4 The Functional $F[S(\vec{x}^{cut}), B(\vec{x}^{cut})]$ . . . 47
6.4.1 Signal vs. Background Distributions . . . 48
6.4.2 Cut Extrapolation . . . 51
6.4.3 Signal vs. (Background+Signal) Distributions . . . 53

7 Computing $F^{max}[S(\vec{x}^{cut}), B(\vec{x}^{cut})]$ 58
7.1 The Downhill-Simplex Algorithm with Simulated Annealing 58
7.2 Adjusting Parameters 58

8 Results - Analysis A 62
8.1 Pre-Study 63
8.2 2-Dimensional Optimization 65
8.3 3- and 4-Dimensional Optimization 65
8.4 Final Optimization and Extrapolation 67
8.5 Results 70
8.6 Conclusions 71

9 Results - Analysis B 75
9.1 Changes with Respect to Analysis A 75
9.2 The Correct Normalization α 76
9.3 The Minimum Set of Independent Cut Parameters 80
9.4 Selection of Final Cut Parameters 86
9.5 Extrapolation of Cuts 86
9.6 Results of Analysis B 88
9.7 Conclusion 95

10 Summary and Outlook 101

11 References 105

A Definitions Used to Work with Step-Wise Defined Functions I

B Maximum Conditions for S vs. B Distributions II
B.1 Derivation of the Maximum Condition for $F[\vec{x}^{cut}] = \alpha S(\vec{x})/(B(\vec{x}))^{\beta}$ II

C Maximum Conditions for S vs. $(S+B)$ Distributions II
C.1 The Maximum Condition for $F[\vec{x}^{cut}] = \alpha S(\vec{x})/(S(\vec{x}) + B(\vec{x}))^{\gamma}$ II
C.2 The Maximum Condition for $F[\vec{x}^{cut}] = \alpha S(\vec{x}) - (S(\vec{x}) + B(\vec{x}))$ II
C.3 The Maximum Condition for $F[\vec{x}^{cut}] = \frac{\alpha S(\vec{x})}{((S+B)(\vec{x}) - \alpha S(\vec{x}))^{\gamma}}$ II
C.4 The Maximum Condition for $F[\vec{x}^{cut}] = \frac{\alpha S(\vec{x})}{\lvert(S+B)(\vec{x}) - \alpha S(\vec{x})\rvert^{\gamma}}$ III

D The Downhill-Simplex Algorithm IV

E Relation between T_0, K, α and Number of Dimensions n V

F Results from the Grid Search in 5 Cut Parameter Dimensions VII

G Stability Cross-Check for Analysis A X

H CUTEVAL Results for Analysis B **XII**
H.1 The Optimization Mode *atm* ν $\%BG\ MC$ (00) XII
H.2 The Optimization Mode *atm* ν $\%BG\ MC$ (98) XXI
H.3 The Optimization Mode *atm* ν $\%experiment$ XXVII
H.4 The Optimization Mode *exp* (*inv.cuts*)$\%experiment$ XXXVI

1 Introduction

In the past ten years, two disciplines in modern particle physics have startled the world with discoveries: On the one hand, neutrino detectors like the Super-Kamiokande Large Water Cherenkov Detector [1, 2, 3] and others [4, 5, 6, 7] have found evidence for neutrino oscillations. On the other hand, high-energy astro particle physics has made much progress with the discoveries of point sources in the UHE gamma-ray sky [8, 9] by air-shower Cherenkov-telescopes and detection of primary particles with kinetic energies above 10^{20} eV[1] by cosmic ray experiments [10]. Neutrino oscillations go beyond the borders of the Standard Model of Elementary Particle Physics which does not provide masses for the neutrino [11]; extragalactic gamma ray point sources, on the other hand, bring us an important step closer to one of the most intriguing riddles of cosmology: the origin of high energy cosmic rays.

Underwater/-ice neutrino telescopes like AMANDA combine both fields of research. Because of their large detection areas, they can push forward their sensitivity to neutrino energies where the extraterrestrial flux could exceed the one of atmospheric neutrinos. By this, a completely new research discipline is born: high-energy neutrino astronomy. Theoretical models predict a huge potential for discoveries [12]. Neutrinos could be the only high-energy messengers from very far-distant objects like Active Galactic Nuclei or Gamma Ray Bursts which reach the Earth and point back to their production sites.

But as the neutrino itself is under investigation, neutrino telescopes will also yield new insight into the nature of this fugitive and highly unexplored elementary particle. For instance, atmospheric neutrino fluxes in the TeV range have not been *measured* yet and since the discovery of neutrino oscillations by Super-Kamiokande, the hunt for entries in the MNS-matrix[2] [13] describing the neutrino mixing is opened. Underwater/-ice neutrino telescopes can play a role in filling the matrix (see e.g. [14, 15]). A possible magnetic moments or decay of the neutrino could be investigated via high-energy neutrino point sources at great distance.

Much effort had been spent on finding a way to construct an underwater/-ice neutrino telescope [16, 18, 12]. It took several decades before this technology has become sufficiently reliable [19]. At present, AMANDA, the Antarctic Muon and Neutrino Detection Array is the largest of its kind. The most difficult stage of the analysis seems to be accomplished: the rejection of the large amount of atmospheric muons background while keeping a reasonably high signal efficiency. In order to achieve this, simulation, reconstruction and finally filtering of data, had to be developed.

This work mostly concentrates on the last task: finding an appropriate way of selecting a pure neutrino signal sample at the last stage of filtering. For this purpose, data from the AMANDA-B10 detector, in operation during the austral winter of 1997, was analyzed. In addition, topics of physical interest, as neutrino oscillations, will be discussed.

[1] This corresponds to the kinetic energy of a tennis ball flying at 200 km/h concentrated in one single particle !

[2] This is the equivalent of the CKM-matrix in the quark sector

2 Cosmic Rays

Ever since the Austrian physicist Viktor Hess discovered in 1912 that ionizing radiation constantly hits the Earth's atmosphere, the newly discovered "cosmic rays" have been puzzling the physical community. Questions like:

- Where do they come from? What are the sources?
- What do they consist of? What is their composition?
- How (or how far) do they propagate in space?

have still not found fully satisfying answers. With the aid of cosmic rays, researchers found also:

- New particles like the positron, the pions, the muon, the kaon and the lambda
- A structured activity of the Sun
- A fine structure of the earth's magnetic field [20]
- Evidence for neutrino oscillations
- High-energy gamma-rays from the most luminous astrophysical objects in the universe

The latter refer to Active Galactic Nuclei (AGNs), galaxies which are believed to contain a central black hole of the size of about 10^8 masses of the Sun [22], and to Gamma Ray Bursts (GRBs), probably far distant objects which emit enormous amounts of gamma rays on a short time scale [23]. Figure 2.2a shows the measured cosmic ray energy spectrum. One can see that the energy range extends over more than 13 orders of magnitude with fluxes reaching from 1 particle/cm^{2}s at energies of 100 MeV to less than 0.01 particles/km^{2}century for the highest observed energies. Fluxes follow a strict power law $\frac{dN}{dE} \sim \mathrm{E}^{-\gamma}$, first with $\gamma \approx 2.7$ and later with $\gamma \approx 3.1$ There is structure visible, namely a "knee" at $\approx$ 4-5 PeV and an "ankle" at $\approx$ 3 EeV.

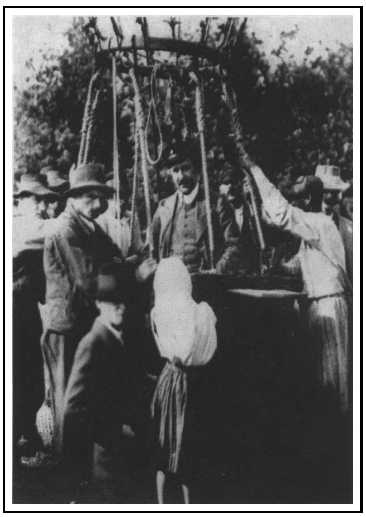

Figure 2.1: Viktor Hess in his research balloon, with which he discovered the cosmic radiation. Picture taken from ref. [21]

Every time, when power law spectra occur, non-thermal processes are likely to be the reason. When particle densities are low, interactions between them are rare and cannot provide thermal equilibrium. Fermi-acceleration, where particles are reflected stochastically back and forth, e.g. on moving shock waves, can push particles to very high energies and produce a power law spectrum. Assume, a particle receives an increase of energy proportional to its energy every time when it crosses the shock wave: $\Delta E = \xi E$. After n crossings and an injection energy E_0, E_n becomes $E_0(1+\xi)^n$. The number of crossings needed to reach energy E_n can then be calculated: $\mathrm{n} = \ln(\frac{E}{E_0})/\ln(1+\xi)$. If we add a probability of escape, P_{esc}, per shock wave

crossing, the probability of remaining in the acceleration region multiplies to $(1 - P_{esc})^n$. Now the proportion of particles accelerated to energies greater than E can be calculated:

$$N(\geq E) \propto \sum_{m=n}^{\infty} (1 - P_{esc})^m = \frac{(1 - P_{esc})^n}{P_{esc}}$$
$$N(\geq E) \propto \frac{1}{P_{esc}} (\frac{E}{E_0})^{-\gamma}$$

with $\gamma = ln(\frac{1}{1-P_{esc}})/ln(1 + \xi)$ [51].

Therefore, most models assume ultra-relativistic plasma waves and strong magnetic fields which enclose charged particles in a manner that multiple back and forth scattering through the shock wave is possible.

Cosmic rays below the "knee" seem to be dominated by protons (79% of the primary nucleons). 70% of the rest consists of helium. Less than 1% of the spectrum consists of electrons, the relative abundance decreasing with energy [26]. Only about 0.1 % is made up of gamma rays. At higher energies the content of heavier nuclei seems to increase [27]. While the origin of the low-energy part with $E < 1$ GeV can be traced back to the Sun, the high-energy part of the spectrum gives reason for wide speculation and a large variety of models. The spectrum below the knee could be due to particle acceleration in Supernova-remnants [28]. The spectrum above the knee is believed to be due to Active Galactic Nuclei [22, 29, 30] or Gamma Ray Bursts [31].

2.1 Astro-Particle Physics

Several attempts have been made to achieve a higher experimental sensitivity in the very high energy region. Used and planned techniques include balloon flights, air Cherenkov telescopes, solar power facilities as light collectors, underground muon detectors, underwater/-ice neutrino detectors, particle detection or observation of the earth's atmosphere by satellites, air shower arrays with particle detectors and atmospheric fluorescence experiments [32]. These experiments are specialized on direct or indirect identification and detection of various particles: nuclei as main contribution to trigger the air showers, photons and neutrinos[1].

Each of these particle species carries its characteristic deficiency: While nuclei below E $\approx 10^{18}$ eV loose all directional information because of deflection in the galactic and inter-galactic magnetic fields, gamma rays get absorbed by the diffuse infra-red, microwave and radio backgrounds above E $\approx$ 100 TeV. Although gamma ray astronomy has made incredible progress with satellite experiments like the Compton Gamma Ray Observatory (CGRO)[34] and Air Shower Cherenkov Telescopes like Whipple [8] and Hegra [9], their range of view is limited. Figure 2.2b shows at which energies photons - emitted at a certain distance from the Earth - get absorbed in the intergalactic space. One can see that in the PeV-region, gamma rays cannot travel further than the radius of our Galaxy (0.01 Mpc). Neutrinos constitute the only probe to observe the inner structure of very distant high-energy cosmic-ray production candidates.

[1] I have omitted here gravitational wave experiments [33].

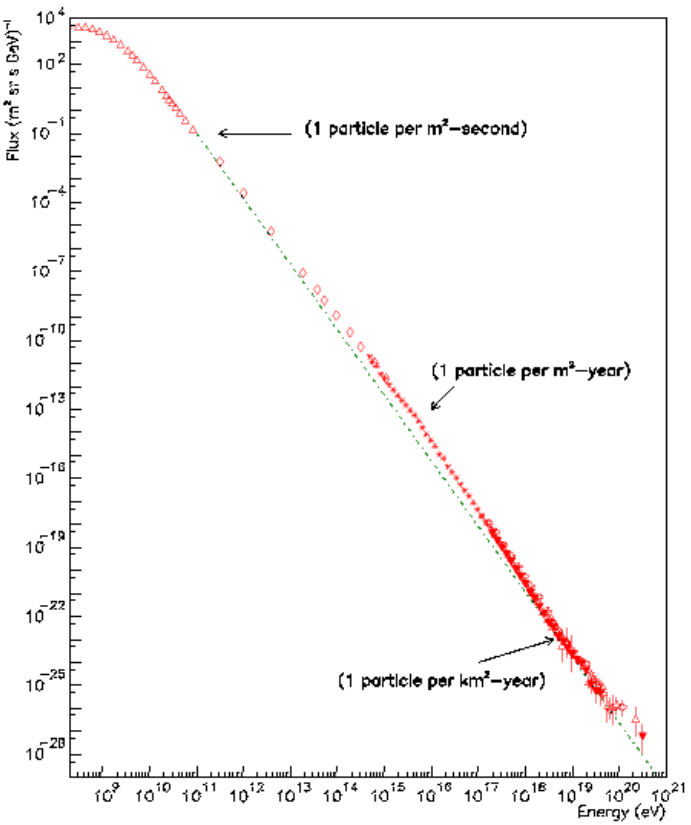

(a) Energy spectrum of cosmic rays. Figure taken from [25].

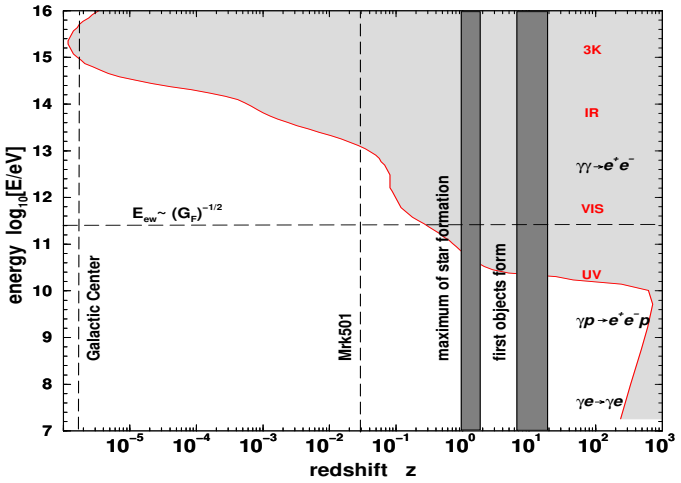

(b) Gamma ray horizon. Shown is the distance from earth in units of red-shift z on the x-axis. The y-axis gives the energy of photons at production. Grey areas correspond to zones where photons get absorbed by cosmic background radiation, the diffuse infrared-background or starlight. At very large distances (far beyond our present experimental capacities to explore), a "natural" limit is set by the opaqueness of the universe before $p^+ - e^-$ recombination to Hydrogen. Figure taken from [12].

Figure 2.2:

2.2 Astronomy with Neutrinos

Neutrinos are a strange kind of matter: As they interact only via the weak force, they are not susceptive to wide range forces, apart from negligible gravitational attraction. Because of the very small interaction range of the weak force, they can travel through most of the universe or large regions of matter without being absorbed at all but extremely high energies. Thus they are ideal probes for in-situ diagnoses of high-energy processes inside opaque objects like the interior of the Sun (measured by the solar neutrino experiments), the core of Supernova explosions (detected 1987 by the experiments Kamiokande II [36] and IMB [37]) or even more cataclysmic events like Gamma Ray Bursts [18] and Active Galactic Nuclei [22]. They are unaffected by scattering processes and magnetic fields.

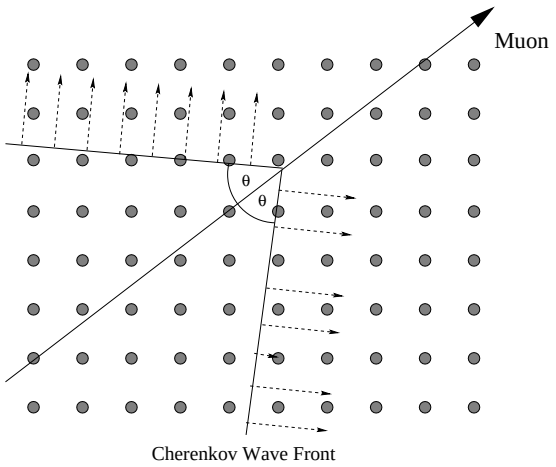

Figure 2.3: A relativistic muon emits Cherenkov light and travels through an array of photo-multipliers. Figure taken from [35].

For neutrino detection, on the other hand, the small cross-sections are a disadvantage, in the sense that large target volumes are needed to register neutrino-induced events. Especially in order to detect the small fluxes of extra-galactic sources, even the largest existing neutrino detectors fail. One has to rely on natural targets found in abundance on Earth.

One possible way to be followed, is to install a detector deep underground and filter out only upwards moving tracks, was first suggested by Markov and Zheleznykh in 1960 [38]. The DUMAND project developed thereupon the underwater/-ice Cherenkov technique [39]. An array of high-sensitive photo-multiplier tubes gets installed in the ocean, deep lakes or the ice. The water above the detector can be used as a shield against cosmic ray induced muons.

When a muon neutrino hits a nucleus, a muon can be produced in the reaction

$$\nu_\mu + N \xrightarrow{W} \mu + anything \tag{2.1}$$

It travels through the detection medium in about the same direction as the neutrino.

Figure 2.4a shows the inclusive cross-sections for $\nu_\mu N$ reactions[2], rising over more than six orders of magnitude for energies ranging from 10-10^{12} GeV. This effect can somehow compensate smaller fluxes at higher energies.

[2]I neglect here cross-sections for $\nu_\mu - e^-$ scattering because they are generally two orders of magnitude smaller. There is, however, one interesting phenomenon for *muon* detection in underwater/-ice detectors: At the Glashow resonance (6.3 PeV), cross-sections for the reaction $\overline{\nu}_e e^- \to W^- \to \overline{\nu}_\mu \mu$ become 40 times larger than the charged-current *muon neutrino* reaction. Unfortunately, the mean free path for such an anti-electron neutrino is only about 70 kmwe, so one could detect a muon only looking at the horizon where background separation is difficult. Of course, showers via the reaction $\overline{\nu}_e e^- \to W^- \to hadrons$ are then much easier to detect [41].

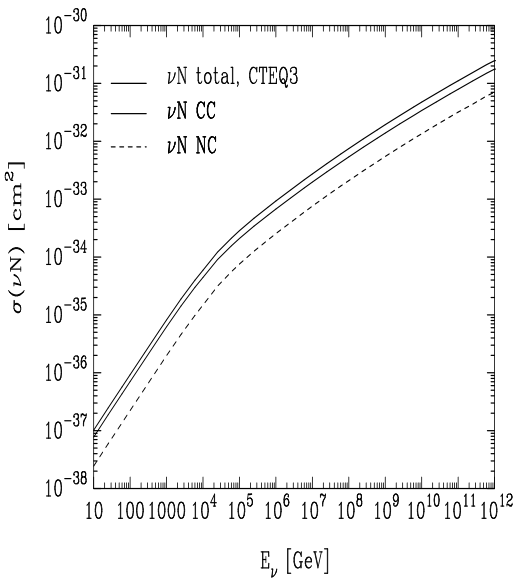

(a) Cross section for νN interactions at high energies: dotted line, $\sigma(\nu N \to \nu + anything)$; thin line, $\sigma(\nu N \to \mu^- + anything)$; thick line, total (charged-current plus neutral current) cross section. (Figure taken from ref. [40])

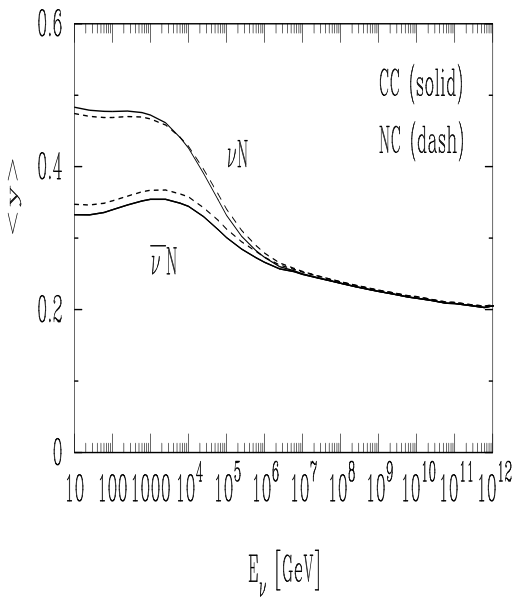

(b) Mean relative energy transfer from muon neutrinos which is not available for the muon (for neutrino interactions with nuclei). Taking (1-$< y >$), the mean relative energy transfer to the muon can be obtained. y stands for $\frac{E_\nu - E_\mu}{E_\nu}$. Figure taken from [40].

Figure 2.4:

Figure 2.4b shows that with energies above 10 GeV, on average more than 1/2 and for energies above 10 TeV, more than 2/3 of the neutrino energy is passed onto the muon. It has then sufficient energy to pass a long way through the array and emit Cherenkov radiation. The photo-multipliers register arrival times and amplitudes of the incoming light. With appropriate reconstruction techniques (described in chapter 5), one can then trace back the muon-track. Taking only upward moving tracks is the equivalent to an unambiguous neutrino signature using the earth as a shield against cosmic-ray induced muons.

Energy loss in water or ice can be approximated as [42]

$$-\frac{dE_\mu}{dx} \approx a + b \cdot E_\mu \tag{2.2}$$

where a ≈ 0.0025 GeV g^{-1}cm^2 represents continuous ionization loss and b $\approx 3.6{\cdot}10^{-6}$g^{-1}cm^2 marks stochastic energy losses due to bremsstrahlung, pair production, delta-electrons and nuclear interactions[3]. For an initial muon energy of about 700 GeV, the two terms are of

[3]Both parameters vary slightly with energy: a(10 GeV) $\approx$ 0.00217 GeVg^{-1}cm^2, a(10 TeV) $\approx$ 0.00293 GeVg^{-1}cm^2, b(10 GeV) $\approx 1.9{\cdot}10^{-6}$g^{-1}cm^2, b(10 TeV) $\approx 4.3{\cdot}10^{-6}$g^{-1}cm^2. In fact, the parameter b has not yet been measured experimentally above energies of $\approx$ 1 TeV in water [43, 42].

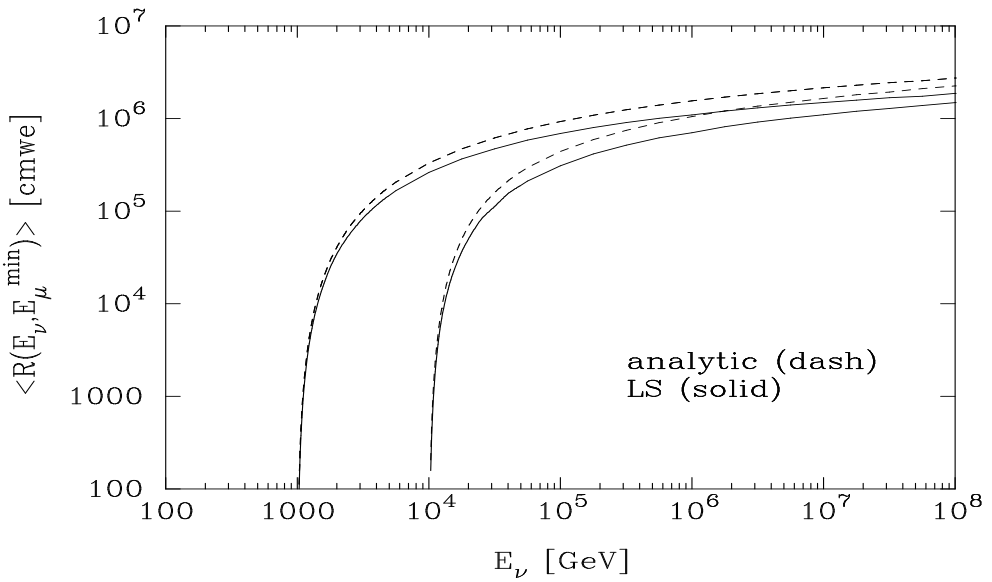

Figure 2.5: Mean ranges of muons produced in charged-current interactions of neutrinos with energy E_ν. Solid lines show a numerical calculation including energy dependent parameters a and b [43] and dashed lines an analytic approximation. The two curves correspond to hypothetical detector energy thresholds of 1 and 10 TeV, respectively. Figure taken from [40].

equal size and above 1 TeV, catastrophic energy losses clearly dominate. In the approximation of constant coefficients a and b and if one assumes a (hypothetical) experiment capable of accepting all muons above a distinct threshold energy E_μ^{min}, but none below, one can integrate equation 2.2 analytically and get an average range of the muon seen by the detector [40]:

$$R(E_\mu, E_\mu^{min}) = \frac{1}{b} ln \frac{a + bE_\mu}{a + bE_\mu^{min}} \tag{2.3}$$

$$< R(E_\nu, E_\mu^{min}) > = \frac{1}{\sigma_{CC}(E_\nu)} \int_0^{\frac{E_\nu - E_\mu^{min}}{E_\nu}} dy R(E_\nu(1-y), E_\mu^{min}) \frac{d\sigma_{CC}(E_\nu, y)}{dy} \tag{2.4}$$

The mean range for a muon of 50 GeV is about 130 mwe, whereas a 10 TeV muon usually travels about 7 kmwe (assuming a threshold energy of 20 GeV). Equation 2.4 gives a mean muon range as function of the initial neutrino energy E_ν and is plotted in figure 2.5. Note that mean muon ranges do not give a complete picture of the reality because muon range distributions are very asymmetric with large tails to small values due to catastrophic energy loss [43].

The mean scattering angle between neutrino and muon also improves with energy [12]:

$$< \theta_{\nu\mu} > \approx \frac{0.7^\circ}{(E_\nu / TeV)^{0.7}} \tag{2.5}$$

One can therefore trace back the direction of the neutrino with less than 1° above a neutrino energy of about 600 GeV, provided the angular resolution of the muon track

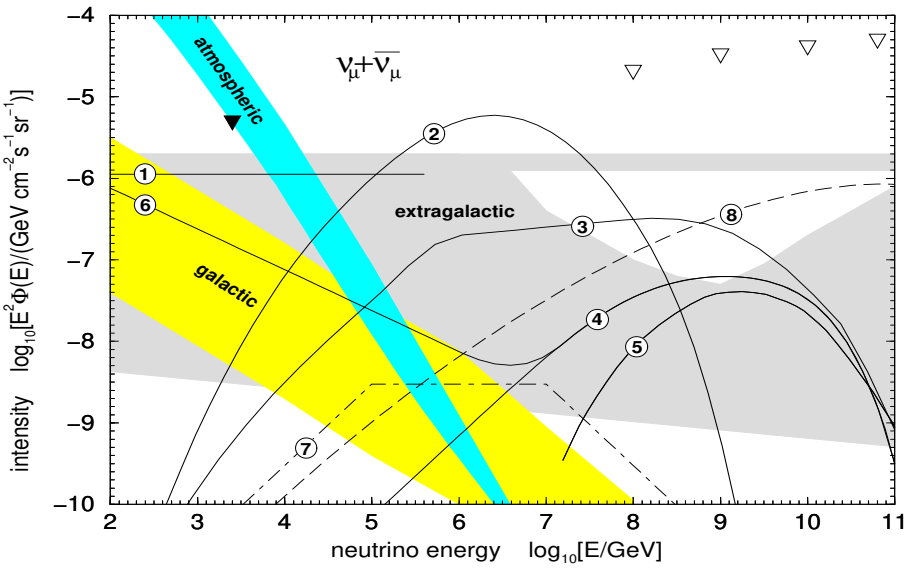

Figure 2.6: Summary of expected $\nu_\mu+\overline{\nu}_\mu$ intensities. Numbered lines: 1-4,6) AGN models [22, 44, 30, 45], 5) neutrinos from interaction of UHE protons with cosmic microwave background [46] 7) GRB model [31] 8) neutrinos from topological defects [47] Shaded regions: theoretical limits on diffuse fluxes from [12]. Bold triangle: limit on any excess above the atmospheric background from the Fréjus experiment [48] Blank triangle: limits on upward events from the Fly's Eye fluorescence detector [49]. Figure taken from [12])

reconstruction is not worse. The increase of cross-sections and muon ranges with neutrino energy (although only logarithmically above $\approx$ 3 TeV) make the case for this detection technique appealing. Assuming a differential neutrino flux $dN/dE_\nu \sim E_\nu^\alpha$, the detection capability goes like $dN_{det}/dE_\nu \sim E_\nu^\alpha \cdot E_\nu(cross-sections) \cdot E_\nu(muonranges) \approx E_\nu^{\alpha+2}$ (unlike other experiments observing high-energy gamma rays or primary nucleons). Figure 2.7 shows this behavior.

There is one drawback: Most detectors have high energy thresholds of some tens of GeV. It appears desirable to lower the threshold for the investigation of neutrino oscillations. On the other hand, for the same amount of invested budget, one pays with angular resolution and detection volume. Additionally, backgrounds are much larger at lower energies. Underwater/-ice neutrino telescopes are therefore optimized to neutrino energies $>$ 1 TeV.

An indistinguishable background to astrophysical neutrinos are neutrinos produced in the Earth's atmosphere by cosmic rays. Astrophysical neutrinos are believed to have much harder spectra (probably going with E^{-2}). Therefore, threshold energies must exist, above which the flux of those neutrinos will exceed that of the atmospheric ones. Figure 2.6 shows some predicted neutrino fluxes of different models. The threshold energies vary therein from some TeV to PeV neutrino energy. Figure 2.7 gives expected event rates for a given E^{-2} energy spectrum.

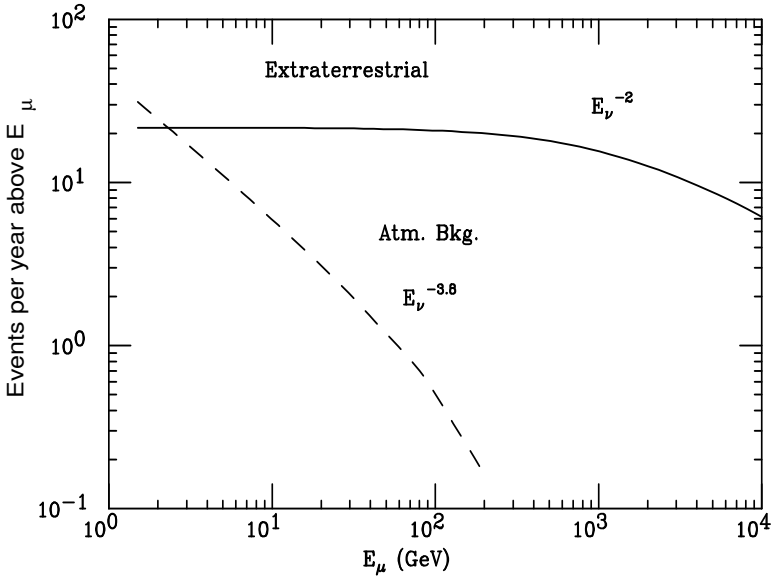

Figure 2.7: Muon spectrum at an underground detector for a hypothetical E^{-2} neutrino spectrum. (The normalization of this spectrum has arbitrarily been chosen to 20 events produced by a hypothetic source.) Due to higher cross-sections and muon ranges, the event rate decreases only slightly with energy. Shown is also the background of atmospheric neutrinos which falls strongly with energy. Figure taken from [12])

2.3 Atmospheric Neutrinos

When cosmic rays hit the Earth's atmosphere, atmospheric neutrinos are produced mainly through decay of pions and kaons.

$$\begin{aligned} N + N &\rightarrow \pi^\pm/K^\pm + X \\ &\rightarrow \mu^\pm + {}^{(}\overline{\nu}{}^{)}_\mu \\ &\rightarrow e^\pm + {}^{(}\overline{\nu}{}^{)}_\mu + {}^{(}\overline{\nu}{}^{)}_e \end{aligned} \tag{2.6}$$

The absolute fluxes are difficult to predict because the pion (and kaon) can either decay (and produce neutrinos) or be absorbed by the atmosphere before reaching the surface of the earth. The standard atmosphere can be thought of as an absorber of 1013 g/cm^2 vertical column density. This corresponds to $\approx$ 12 and $\approx$ 24 interaction lengths for a 100 GeV and a 1 EeV proton, respectively. So, primary cosmic rays will almost always produce a shower starting in the very upper region of the atmosphere. The resulting pions and kaons will decay with characteristic decay lengths of $L = \frac{E}{m} \cdot c \cdot \tau$ or interact themselves with the atmosphere. One can now approximate the density of the atmosphere as decreasing exponentially with a typical scale height of $h_0 \approx 8.4$ km. Setting the characteristic decay length equal to the scale height yields a characteristic energy ϵ which reflects the competition between decay and interaction. This quantity is $\epsilon_{\pi^\pm} \approx 115$ GeV for pions and $\epsilon_{K^\pm} \approx 850$ GeV for kaons[4] [12]. Muons above ~ 2.5 GeV

[4]The next mesons in question for neutrino production, the D-mesons has already $\epsilon_{D^\pm} \approx 40$ PeV. They

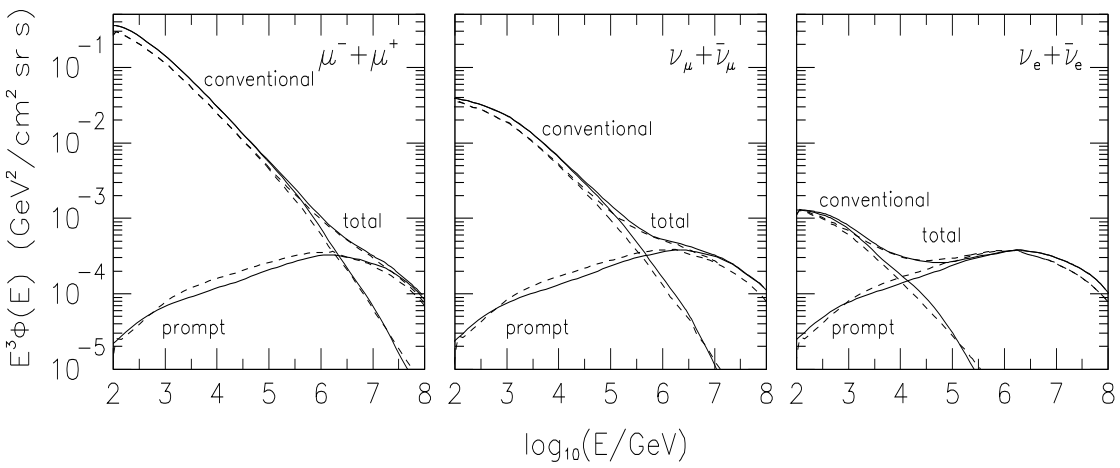

Figure 2.8: E^3 weighted fluxes of atmospheric muons, muon neutrinos and electron neutrinos. Shown are particles from pion and kaon decays (conventional) and from D-meson decay (prompt). Figure taken from [50].

usually reach the Earth before decaying because their decay length becomes larger than their typical production height ($\sim$ 15 km) [51]. The kinematics of pion and muon decay is such that about an equal amount of energy is passed onto the three neutrinos arising [51]. Therefore, the following relation of fluxes holds for a given energy range below 2.5 GeV:

$$\frac{\nu_e + \overline{\nu}_e}{\nu_\mu + \overline{\nu}_\mu} \approx \frac{1}{2} \tag{2.7}$$

Above 2.5 GeV, this ratio quickly decreases with energy because only (muon) neutrinos from pion decay remain. Electron neutrinos are created in much smaller numbers by kaon decay via the semileptonic decay chain $\mathrm{K}_L \rightarrow \pi^{\pm}\mathrm{e}^{\mp}\overline{\nu}_e(\nu_e)$. Figure 2.8 shows predicted fluxes for ν_μ and ν_e neutrinos. Again, a power law can be observed for energies below $\sim$ 1 PeV, albeit with a spectral index increased from 2.7 to 3.7 as compared to the original cosmic ray spectral index [12].

become important at high energies $>$ 100 TeV and produce so-called "prompt neutrinos"

3 The AMANDA Detector

3.1 History

The idea to build large underwater neutrino detectors came from the DUMAND group in the 1970's [39, 52]. Several Workshops were held and possible detector designs discussed [16, 17]. Because of extreme conditions in deep water, photo-multipliers and electronics have to be housed in glass pressure vessels. Such a unit is then called an "Optical Module" (OM) and is connected to the surface via cables.

Unfortunately, the prototype experiment itself, DUMAND, was decomissioned in 1996. The first prove of feasibility was achieved by the BAIKAL experiment in the lake Baikal in Russia [53]. This detector consists meanwhile of 192 OMs. Because of water luminescence, OMs are arranged in pairs and trigger only on double coincidences.

In the 1980s, a group of US-American scientists came up with the idea to use deep polar ice instead of water as the detection medium [54]. Problems such as bio-luminescence and -fouling (light emission from living organisms and sedimentation of OMs by bacteria [55]), deployment from ships, detector stability, online position monitoring and many others could be overcome that way. Besides, good infrastructure is available, e.g. at the *Amundsen-Scott South Pole Station.*

Figure 3.9 gives a sketch of the current AMANDA detector. A first part comprising four strings with 80 OMs was deployed in the austral summer of 1993/94 at depths between 810 and 1000 m, now referred to as AMANDA-A. The optical properties of the ice however, turned out to be still dominated by residual air bubbles [56]. These were responsible for an unacceptably small effective scattering length varying from 50 cm to 1 m with depth [57]. An acceptable muon track reconstruction was impossible. Efforts thus went into the construction of a deeper detector encouraged by sample cores taken at the Vostok station and by glaciologists' estimates. In a 1995/96 campaign, four new strings were deployed with OMs ranging from 1520 to 2000 m of depth. Effective scattering lengths greater than $\sim$ 20 m allowed for muon track reconstruction. With this detector, called AMANDA-B4, first neutrino events have been separated from background [102].

AMANDA-B4 was upgraded in the polar season 1996/97 with 6 additional strings which form a cylinder around the previous deployed strings. The 10-string detector contains 302 OMs and is referred to as AMANDA-B10. Data of it constitutes the focus of this work.

Meanwhile, new detector extensions have been deployed: 3 strings ranging from 1150m to 2350m in the following season 1997/98 and 6 additional ones 99/00. By this, the whole detector AMANDA-II has been completed and is taking data.

Besides the functioning detectors AMANDA and BAIKAL, three new underwater detectors are planned in the Mediterranean: ANTARES will be deployed off shore near the French city of Toulon [14]. Installation of NESTOR is currently tested near Greece [59]. Another km^3 detector project called NEMO has found a deep sea site near Sicily and plans to deploy a test station [60].

3.2 The Detection Medium

The different sites each have their own advantages [114, 61]. One class of the crucial quality parameters are the optical properties of the detection medium because reconstruction of

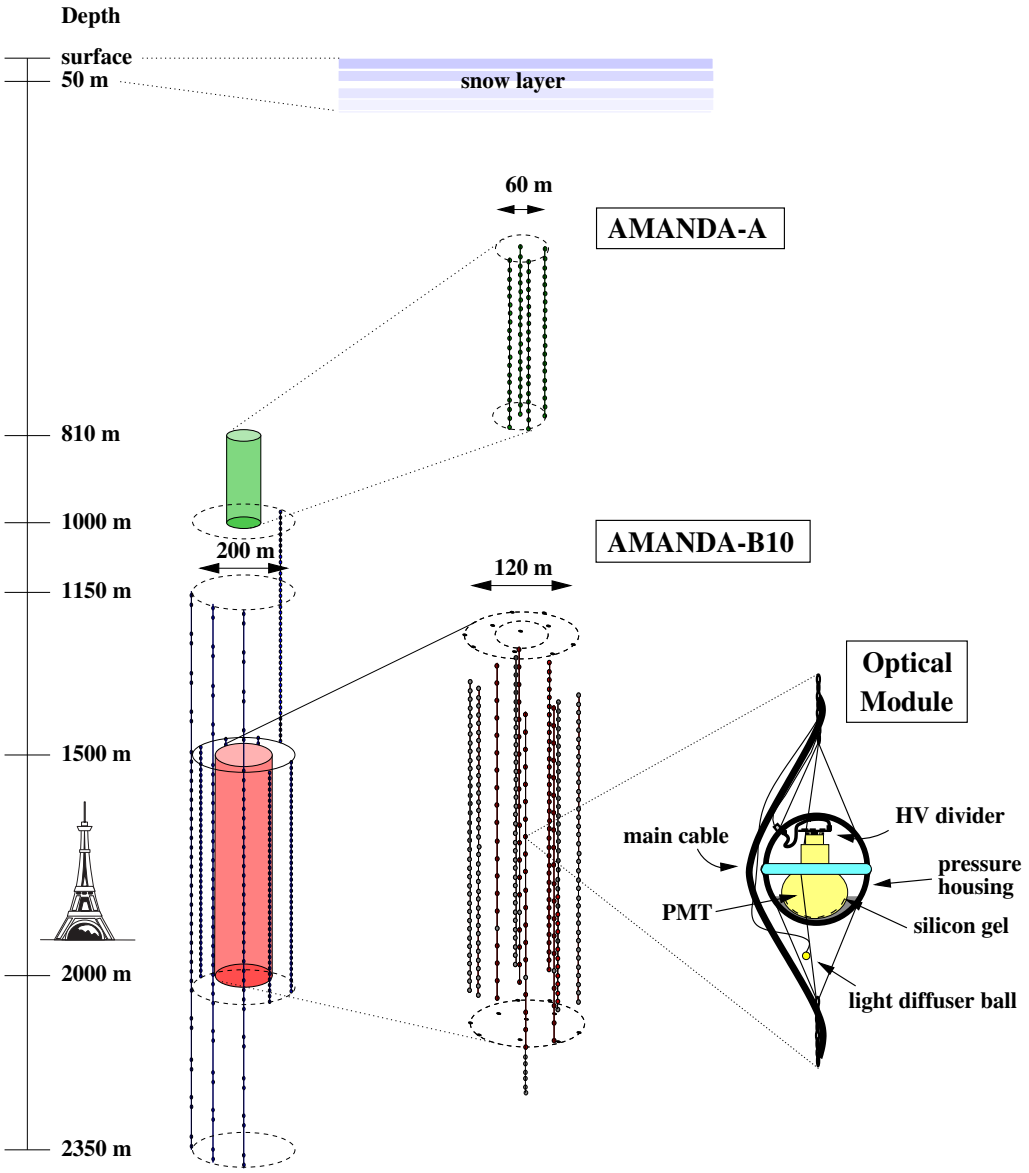

Figure 3.9: A sketch of the present status of the AMANDA array: A shallow detector called AMANDA-A consisting of 80 optical modules on four strings and a deeper one called AMANDA-B. In the middle of the AMANDA-B array, the prototype detector AMANDA-B10 is situated from 1520m to 2000m depth. It consists of 302 optical modules on 10 strings. Four of these containing 86 optical modules are found in the middle and referred to as AMANDA-B4. The rest of 216 modules is located on 6 strings forming a cylinder around the inner part. Additionally, 9 strings with 374 optical modules ranging from 1150 to 2350 m depth have been deployed which on their turn form a cylinder around the AMANDA-B10 detector. The whole 19 strings detector is called AMANDA-II. One of the later strings is located at shallower depth.

the muon tracks relies on propagation of the emitted Cherenkov light (see more details in chapter 4).

Cherenkov radiation is emitted in the case of electrically charged particles propagating through medium with a velocity higher than that of light ($v = \frac{c}{n}$). In water/ice, the refraction index n is 1.33 [62]. The spectrum of Cherenkov radiation extends over a typical wavelength interval of about 310 - 500 nm for water. The number of photons produced in that interval can be approximated by [63, 64]

$$\frac{d^2N}{d\lambda dx} = \frac{2\pi\alpha z^2}{\lambda^2}(1 - \frac{1}{\beta^2 n^2(\lambda)}) \tag{3.8}$$

This corresponds to about 200 photons/cm. α stands here for the fine structure constant ($\sim$1/137), z counts the charge of the particle and β is v_p/c which is very close to 1 for muons in the GeV regime. The emission angle of Cherenkov radiation is

$$cos(\theta_c) = \frac{1}{n\beta} \tag{3.9}$$

For the case of relativistic muons with energies above a few GeV, the emission angle can be treated as constant.

Medium	Ice	Ocean		Lake
Site	AMANDA	ANTARES	NESTOR	BAIKAL
Absorption Length (m)	90-120	55-65	50-60	20
Scattering Length (m)	3-5	>24	55	18
$< \cos(\theta) >$	0.86 (?)	0.88	0.88	0.95
Eff. Scatt. Length (m)	20-40	>200	460	380
Eff. Atten. Length (m)	$\sim$ 25	40-60	45-65	15

Table 3.1: Optical Parameters at $\sim$460 nm for different underwater/-ice detector sites. Values obtained from [61, 65, 12, 59, 66, 57]

The emitted Cherenkov light is affected by absorption and scattering during its propagation through the ice. Table 3.1 gives a short overview of the most important optical parameters at the different detector sites. The absorption length of photons is very large for highly pure deep polar ice but is a limiting factor for the detection efficiency in water. On the contrary, scattering because of residual ice contamination like dust plays a dominant role for under-ice telescopes. It worsens track reconstruction accuracy, but improves the energy resolution due to enhanced calorimetric properties. If photons get scattered more often at a large absorption length, the probability to hit an OM increases[1]. An important observable is the effective scattering length which takes into account that small scattering angles do not affect to a great extent the direction of a photon. It is defined as via the mean scattering angle $< \cos(\theta_{scatt.}) >$:

[1]Note that this is only true for relatively "small" detectors like AMANDA-A.

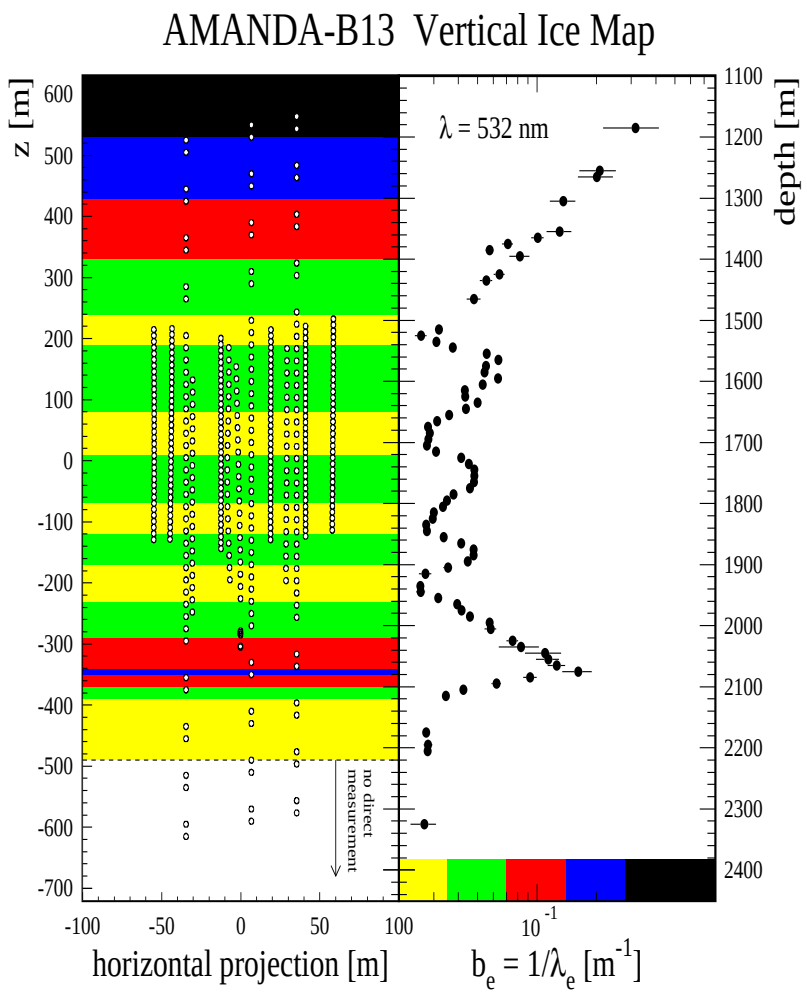

Figure 3.10: Depth vs. effective scattering coefficient measured with a dye laser at 532 nm wavelength. On the right side, depth-dependency of the effective scattering coefficient is plotted, the left side shows the ten strings of AMANDA-B10 and three additional strings deployed in 1998. Different shading corresponds to different scattering lengths. Figure taken from [67].

$$\lambda_{eff} = \frac{\lambda_{scatt.}}{1 - < cos(\lambda_{scatt.}) >} \tag{3.10}$$

For the case of AMANDA, additional complications arise due to vertically inhomogeneous ice properties. Figure 3.10 shows the variation of the scattering length with depth. At the location of AMANDA-B10, there is a variation of more than a factor 2. Both scattering and absorption coefficients are wavelength dependent.

3.3 Performance and Calibration

Each OM of AMANDA-B10 consists of a 30 cm diameter evacuated glass pressure sphere equipped with:

- an 8-inch Hamamatsu photomultiplier R5912-2 (14 dynodes), operated at individual gains of approximately 10^9,
- a voltage divider,
- silicon gel in order to ensure mechanical and optical contact between the photomultiplier and the glass sphere,
- an electrical penetrator into the sphere.

OMs are connected to the surface by coaxial (80 OMs) or twisted pair (222 OMs) cables to provide power supply and transmission of the analog signal.

The 80 OMs of the inner strings (AMANDA-B4) which are read out via coaxial cable, have an average noise rate of $\sim$ 300 Hz, the other 220 about $\sim$ 1.1 kHz after dead time suppression [68]. The major difference comes from the varying concentrations of K^{40} in the present sphere glass. Additionally, the OMs read out via twisted pair cables (strings 5-10) are subject to cross-talk [69]. The photomultipliers show strong afterpulsing at $\sim$ 6.2 μs [70].

3.3.1 The Data Acquisition System (1997)

The signals at the surface are amplified and decoupled from HV by SWAMPs ('SWedish AMPlifiers'). Prompt outputs are connected to discriminator inputs which feed the majority trigger logic (DMAD) and the multi-hits TDCs (Le Croy TDC3377). Another 2 μs delayed output is fed into a peak-sensing ADC (Phillips ADC7164).

The DMAD triggers on 16fold coincidence within a 2 μs time window. Additional triggers have been installed for coincidences with other experiments, e.g. AMANDA-A, and the South Pole Air Shower Array (SPASE II) on the ice surface.

TDCs record data over 32 μs and provide on trigger up to 16 egdes. Each pair of edges can be separated into a leading edge time (LE) and the corresponding trailing edge (TE) time. The width of the pulse (time-over-threshold TOT) is the time difference between LE and TE. The ADCs are gated for 4 μsec. TDC and ADC are read out via CAMAC bus and a controlling MacIntosh PC. The typical dead time of the DAQ was estimated to be $\sim$ 25% [71].

The whole event information thus consists of the LEs and TOTs for each pulse, one ADC value per OM, a GPS-time and information about which trigger was satisfied.

3.3.2 Calibration

The gain for each PMT was adjusted such that a 1-pe signal yields about 500 mV (400 mV for coax-connected OMs) at the amplifier output. This corresponds to a 1-pe trigger efficiency of 80-90%, assuming a discriminator threshold of 100 mV [57].

Precise timing calibration is essential for an underwater/-ice neutrino detector which relies on the knowledge of the photon arrival times in order to reconstruct a muon track. The measured arrival times of each OM have to be corrected for a time offset, called "t_0" and a time walk called "α" due to amplitude A dependent rise times. A corresponding correction factor for the LE of δt $\sim \frac{\alpha}{\sqrt{A}}$ has to be applied. The t_0 gives the time, the signal needs to propagate through the photomultiplier, the cable and to get digitized by the DAQ. For this reason, a YAG laser calibration system has been installed. The time offset can be calculated by sending laser pulses to isotropizer balls located below each OM and measuring the arrival times from the photomultiplier signal. Via OTDR (Optical Time Domain Reflectometer), the time it takes the signal to travel through the fiber, can be inferred and subtracted from the time distributions. Altogether, a 4-7 ns precision of the time offsets could be achieved [102].

A second calibration campaign was performed to determine the exact relative positions of each OM in the ice. From the time-of-flight of the photons between the YAG-laser and the OMs, their positions relative to the sources could be inferred with an accuracy of 1 m in the horizontal plane and 0.5 - 1.0 m in depth [102].

4 Simulation

An experiment working with a statistical approach to the data needs a correct detector and event simulation. In the case of AMANDA, this task is difficult, since the performance of the detector has to be derived from different in situ methods, Especially the exact ice properties which form an inherent part of the detector, cannot be translated into laboratory conditions in order to be measured and calibrated, there. Interpretation of measurements have to be disentangled from the effects of the detection medium. A full mass production of simulation was run in 1998, but analysis of the data revealed that new features e.g. vertical ice-structures and a more precise simulation of the detector hardware had to be included into the simulation. This led to a second improved effort in 2000 [70].

4.1 Atmospheric Muon Background Monte Carlo

Down-going muons have been simulated by a full atmospheric shower program called *basiev* [72]. This program generates isotropic primary protons with energies up to 1 PeV and simulates the muons produced in the shower occurring when the protons hit the atmosphere of the Earth. The muon propagation program *mudedx* [73] takes over and simulates full continuous (ionization) and stochastic energy loss (e^+e^-- and $\mu^+\mu^-$-pair production, bremsstrahlung, δ-electrons and nuclear interactions). Depending on the distance of an OM to the muon track, additionally Cherenkov radiation of the muon and the secondary showers is simulated. Not each generated photon is propagated through the ice but distributions of the expected number of photoelectrons and time delays as function of position and orientation of each OM to the track have been tabulated. Constants include the wavelength dependent quantum efficiency and the transmission coefficients of the glass spheres and the optical gel. Detailed modeling of the individual properties of each OM is included, such as pulse shapes, threshold, gain efficiencies and time delays. The ADC and TDC responses are generated and random noise hits added. Details are described in [70, 74], updated information about the detector simulation is available from [75].

4.2 Atmospheric Neutrino Signal Monte Carlo

Two independent MC samples have been produced. The first one produced muons from atmospheric neutrinos which have been simulated according to [76] and a program called *nu2mu* [77]. It uses ordinary sampling with a neutrino spectral index of $\gamma = 3.7$. The second neutrino simulation uses a program called *nusim* which allows simulation of neutrinos with an arbitrary energy spectrum and angular distribution by usage of importance sampling [78]. Muons produced in the rock below the detector are propagated separately until they reach the rock-ice boundary.

Additionally, samples containing muons with fixed energy and produced isotropically around the detector have been generated.

4.2.1 Mass Production 1998

Two MC signal and background simulation mass productions were run. The first one took place in 1998 [83]. 10 days of atmospheric muon background ($6.1 \cdot 10^7$ trigger) has been

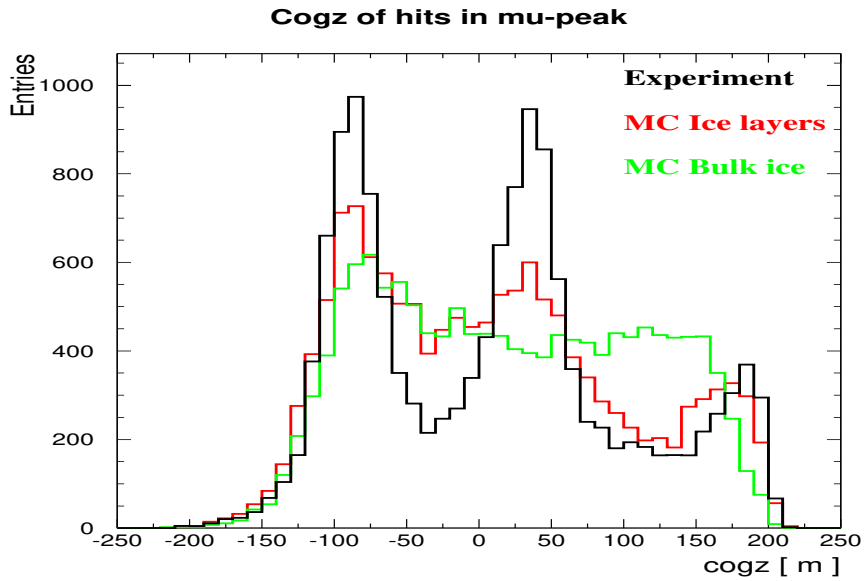

Figure 4.11: The center of gravity of hit OMs. Shown is the distribution predicted by the 1998 simulation of down-going muons which assumed homogeneous ice conditions. The dashed bold line shows a simulation assuming multiple ice-layers and the bold line the experimental behavior. Weak filters have been applied to all data (θ_{LF} >50°, θ_{like} >80 and $N_{dir}(-15:25\ ns)$ ≥3, see chapter 5). Figure taken from [79].

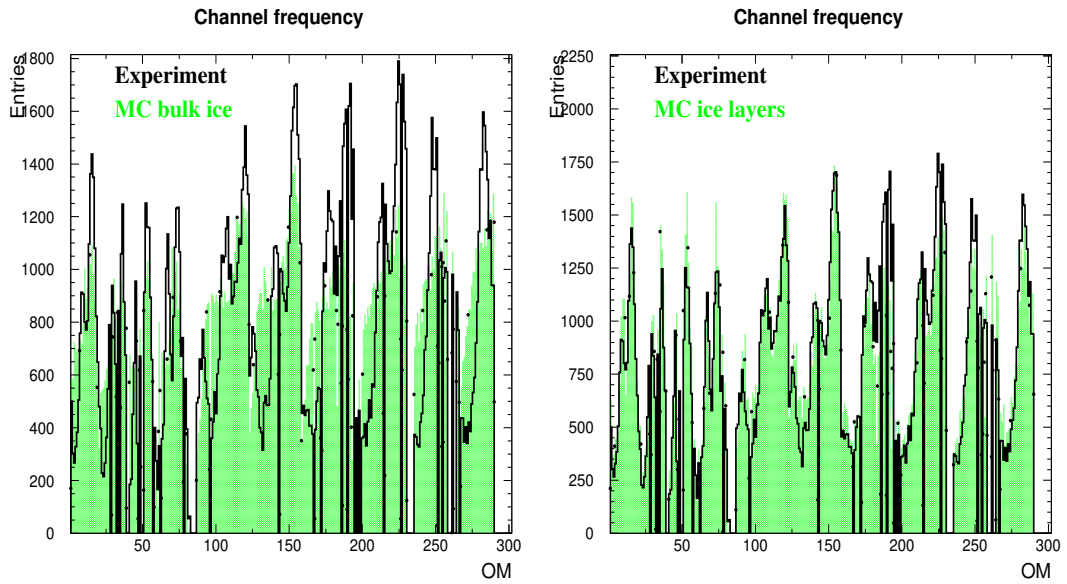

(a) Atmospheric muons simulation using homogeneous ice

(b) Atmospheric muons simulation with 17 horizontal ice-layers

Figure 4.12: The distribution of hit OMs. Weak filters have been applied to all data (θ_{LF} >50°, θ_{like} >80 and $N_{dir}(-15:25\ ns)$ ≥3, see chapter 5). Figure taken from [79].

created. This data has been used for the analysis described in chapter 8.

4.2.2 Mass Production 2000

A first analysis [80] revealed problems in the hardware simulation as well as non-simulated structures in the distributions of the center of gravity of hits within an event. This and several other indications led to the assumption that vertical structures of the photon scattering length in ice had not been fully understood. A campaign to measure the exact behavior was performed with the outcome described in chapter 3.2 and [81]. Another effect contributing to the observed structures is cross-talk [82, 69]. This effect is presently under investigation.

A new background simulation proved that some of the non-understood phenomena had in fact been due to vertical ice structures [84]. Figure 5.17 shows the center of gravity of hits at an intermediate cut level for a homogeneous ice model and a model simulating 16 horizontal ice-layers of different scattering length. Distributions agree better with experimental data, but still an improved understanding of the experimental behavior needs to be achieved.

Finally, a 17 ice-layers model and a more detailed description of the detector response have been incorporated in a new MC which was used for a second mass production effort in the summer of 2000 [85]. This simulation divides the ice around AMANDA-B10 into 17 horizontal layers (compare figure 3.10) of equal scattering length. Photons hitting an OM are treated as if they were produced in the same (scattering) environment [84]. This seems justified as long as layers do not differ too much and the average path length of photons does not become large compared to the thickness of a layer.

Background simulated with *basiev* was weighted by the square of the cosine of their generated zenith angle in order to get higher statistics for nearly horizontal directions. This is useful because most background events in the final data sample seem to originate from events with a direction close to the horizon.

Another, smaller background sample was produced with *corsika* air shower simulation instead of *basiev*. *corsika* simulates muons up to energies of 1 EeV and assumes a curved atmosphere, both of which is not simulated correctly with the *basiev* program. Additionally, *corsika* simulates the whole cosmic ray composition spectrum instead of only protons (like *basiev* does). Figure 4.13 shows that there are significant differences in the simulated muon multiplicity and the muon energies at higher filter levels. Events simulated with *corsika* are not zenith-angle weighted.

About 4.2 days of life time simulated with *basiev* and another 1.4 days simulated with *corsika* have been used for analysis B (chapter 9).

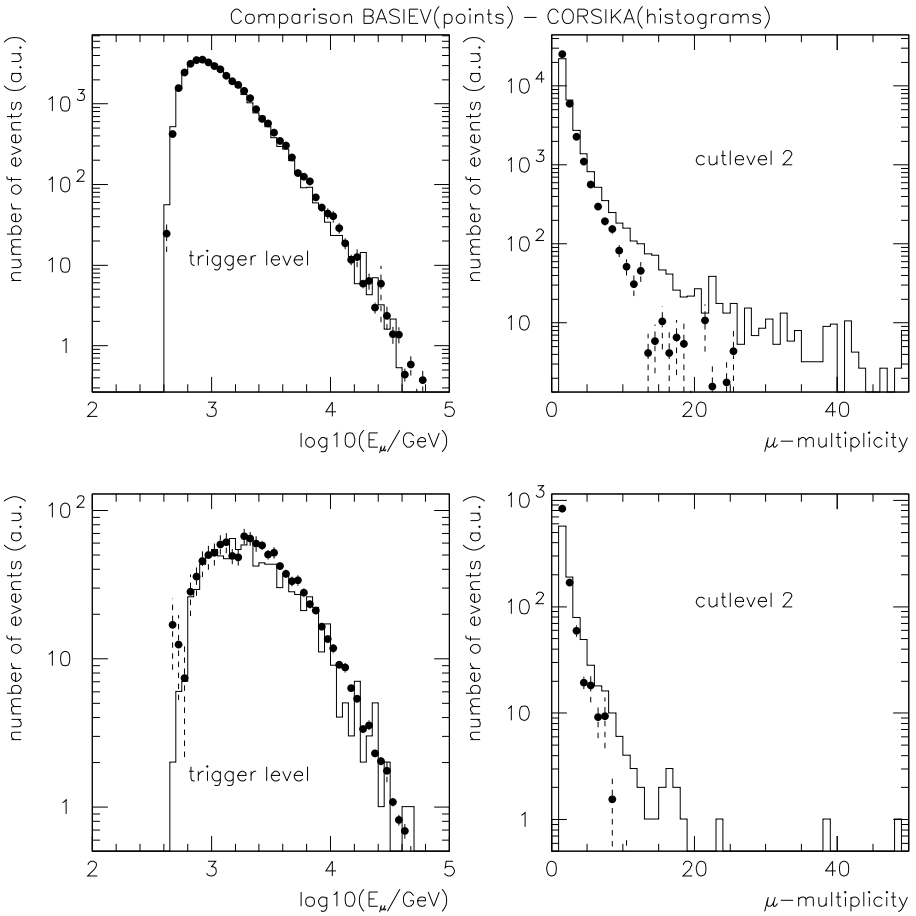

Figure 4.13: Comparison between the air shower simulation programs *basiev* and *corsika*: Shown are distributions of simulated muons which triggered the AMANDA-B10 array. The top left plot shows the distributions of the simulated energy for both air shower programs, the top right plot shows the muon multiplicity, both on trigger level. The bottom plots show the same distributions on cut level 2. Figure taken from [86].

5 Reconstruction and Filtering

One great challenge of running underwater/-ice neutrino telescopes is the rejection of a large amount of background. As pointed out in chapter 2.2, an underwater/-ice neutrino detector needs to reject muon tracks entering the array from above. A dead-time corrected trigger rate of about 100 Hz and therewith $O(10^7)$ triggers per day of this background has to be compared to a trigger rate due to atmospheric neutrinos of $O(30)$ per day [87]. This means that a rejection factor larger than 10^6 has to be achieved.

For the search for neutrino point sources or investigations of neutrino oscillations, determining the neutrino direction is essential. Equation 2.5 showed that at the energies needed to trigger the AMANDA array, neutrino and muon momentum are almost collinear. A good reconstruction of the muon track with an angular resolution down to the mean scattering angle is thus desirable. Muon tracks from below the horizon form a key signature for neutrino-induced events. Thus, one can select unambiguous neutrino-induced muons by accepting only events from below the horizon.

Due to the limited accuracy of the reconstruction, quality criteria have to be applied. They guarantee the quality of the determined direction. These quality criteria (compactly referred to as "cuts") will be investigated more thoroughly in this work.

Slow but accurate reconstruction algorithms can only be applied to a subsample of the overall data in order to account for available computer resources. The analysis usually uses an iterative approach where reconstruction and filtering alternate. First, fast but less accurate reconstruction algorithms are applied to the data. Filters based on these preliminary fits are used. Then, more sophisticated fits are calculated and cuts based on these fits applied. Subsequent filter-levels are thus created, each containing a reduced data sample with respect to the previous one. At each level, experimental data and MC are studied in detail and new cuts are developed based on the experience gained therewith. The analysis group at DESY Zeuthen has established four major filter levels at the end of which a final neutrino sample is obtained. I will present here the analysis chain and the corresponding reconstruction methods shortly and proceed to a more detailed description of the final cuts in chapter 6. Details about the basic reconstruction methods can be found in [89].

5.1 Preprocessing

Before filtering, a run selection has been performed. Only runs are accepted which contain at least 220 stable OMs. A stable OM was defined to have a noise rate deviating less than two (strings 1-4) or four (strings 5-10) standard deviations from its average noise rate [91]. After correction for dead time, the live time of the remaining runs was estimated to 130.1 days [87, 90]. The TDC and ADC values are calibrated. A run-based selection of reliable OMs is performed rejecting dead and unstable OMs as well as some lacking calibration information [87, 71].

In order to get rid of noise hits and cross-talk, a dedicated hit-cleaning procedure has been followed [87]:

- ADC requirements had to be fulfilled:
  - Only hits with ADC amplitudes above a 50 mV threshold were accepted.
  - Only hits with calibrated amplitudes between 0.1 and 1000 PE were accepted.
  - Hits occurring outside a trigger time window between 0 and 4,500 ns were removed.
- Several isolation criteria in time and space have been demanded:
  - Hits without neighboring hit channels of a distance $\leq$ 100 m were removed.
  - Hits without neighboring hit channels of a time difference $\leq$ 500 ns were removed.
- Only hits with a TOT between 125 and 2000 ns were taken. This cut removes 85% of cross-talk while keeping 98% of the real hits, as shown in [69, 82].

5.2 The Line Fit and Level 1 Filter

For a fast first guess, the "line fit" algorithm [92] was implemented. The method assumes a "time flow" of constant velocity $\vec{v}$ along a line. Thus, space points $\vec{r}_i$ of each hit OM i should follow the relation

$$\vec{r}_i \approx \vec{r}_0 + \vec{v} \cdot (t_i - t_0) \tag{5.11}$$

One can define a χ^2 for all hit photo-multipliers:

$$\chi^2 \equiv \sum_i (\vec{r}_i - \vec{r}_0 + \vec{v} \cdot t_i)^2 \tag{5.12}$$

The minimization of χ^2 can be solved analytically and yields:

$$\vec{v} = \frac{< \vec{r}_i t_i > - < \vec{r}_i >< t_i >}{< t_i^2 > - < t_i >^2}, \qquad \vec{r} =< \vec{r}_i > - \vec{v} < t_i > \tag{5.13}$$

Because this approximation is sensitive to distant noise hits with a long lever-arm, a stricter space isolation criteria (max. 70 m distance instead of 100 m) have been demanded for the hits used for the line fit.

The resulting vector $\vec{v}$ gives the direction of the fit and $|\vec{v}|$ its absolute "speed". The zenith angle of the line fit $\theta_{LF} \equiv acos(\frac{v_z}{|\vec{v}|})$ was used to separate signal and background. A particle traveling with the speed of light and emitting Cherenkov radiation which gets scattered in ice, does not necessarily produce a speed of the line fit equal to the speed of light. Nevertheless, $|\vec{v}|$ was proven to be a reasonable cut parameter in rejecting poor quality events.

Figure 5.14 shows the corresponding distributions[1] There is good agreement between experiment and simulation for the reconstructed angles. The zenith angle mismatch can

[1]Note that distributions shown in this paper are based on the mass production 2000 MC which includes vertical ice structures. Accordingly, there may be differences to ref. [87, 80].

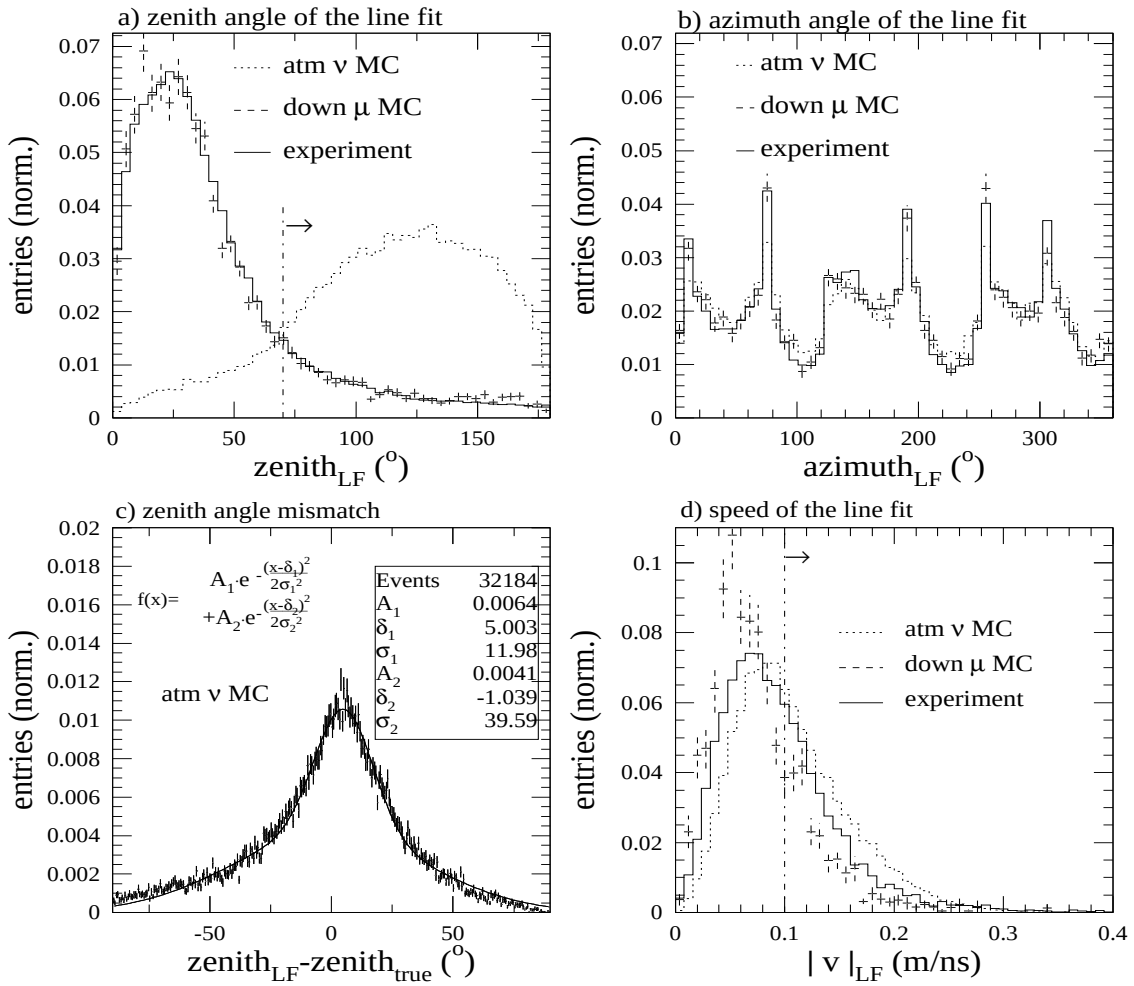

Figure 5.14: Line Fit reconstruction of AMANDA-B10 data. Shown are distributions of simulated atmospheric neutrino induced muons, simulated down-going muons from air showers and experimental data. The top left plot (a) shows distributions of the zenith angle, the top right plot (b) shows the azimuth angle, the bottom left plot (c) shows the zenith angle mismatch for simulated atmospheric neutrino events, which has been fitted by the sum of two Gaussians. Figure (d) shows the distributions of the speed of the line fit $|\vec{v}_{LF}|$. A cut on $\theta_{LF} > 70^\circ$ had been applied for the last plot.

be fitted by the sum of two Gaussians. One has a width of about 12°, the other one of 40°. During the analysis, badly reconstructed events will get reduced more with respect to the good one. The speed of the line fit distribution of the experiment is shifted towards higher values with respect to the background MC prediction. This is not understood yet.

Level 1 filtering consists of two cuts:

$$\begin{aligned} \theta_{LF} &> 70^\circ \\ |\vec{v}_{LF}| &> 0.1\ m/ns \end{aligned} \tag{5.14}$$

3.6% of the experimental data pass these cuts, 3.8% of the atmospheric muon simulation and 41% of the atmospheric neutrino simulation (both mass production 2000). Note that with the invention of further fast fits (see chapter 5.4 and 5.5), the need for a tight cut on the speed of the line fit has diminished. A future analysis would probably cut less tightly on this variable and has to investigate the remaining deviations between simulation and experiment.

5.3 The Maximum Likelihood Fits and Level 2 Processing

It is clear that an adequate reconstruction needs to incorporate the available knowledge about photon emission, propagation and detector response. The task is: find a probability density function for a registered Cherenkov photon to reach the OM from emission after a given time delay. Because of scattering, a photon can detour and thus arrive delayed with respect to a path along the straight line. It has been proven useful to define a term *time residual* t_{res} defined as [89]

$$t_{res} \equiv t_{hit} - t_{no\ scatt} = t_{hit} - d(OM, \mu - track)/(c_{light,ice} \cdot sin\theta_c) - t_{emission} \qquad (5.15)$$

The time residual gives the time difference between the actual photon arrival time and the one expected from a pure Cherenkov model without scattering. Thus, a distribution of time residuals is typically positive and asymmetric with large tails. Time residuals of $t_{res} \approx 0$ correspond to unscattered photons and are called *direct hits*. Photons emitted very close to the OM tend to have small time residuals, those emitted far away can have very large values because of multiple scattering. A time residual smaller than zero can occur in the following cases:

- The finite time resolution smears out the observed time residuals for unscattered photons around $t_{res} \approx 0$. Thus, slightly negative values can be observed.
- A noise hit or a cross-talk hit has occurred.
- The reconstruction has yielded a wrong result.

The AMANDA standard reconstruction procedure consists of defining a probability density function $p_i(d,t_{res})$ of time residuals t_{res} obtained by a muon track of distance d to the OM i. For isotropic, monochromatic photon emission from a point source, $p_i(d,t_{res})$ can be calculated analytically [93]

$$p_i(d, t_{res}) = \frac{1}{N} \cdot \frac{\tau^{(-d/\lambda)} \cdot t_{res}^{(d/\lambda - 1)}}{\Gamma(d/\lambda)} \cdot e^{-(t_{res}/\tau + c_{light,ice} \cdot t_{res}/\lambda_{abs} + d/\lambda_{abs})} \qquad (5.16)$$

This function is called after its inventor the *Pandel-function*. The two parameters $\tau(d,\theta)$ and $\lambda(d,\theta)$ are themselves functions of the distance d and the the orientation θ of the OM.

Equation 5.16 can be integrated analytically over all time residuals which gives the overall hit-probability P^{hit} for a "standard" OM. This is the normalization constant for the Pandel-function.

$$P_i^{hit}(d,\theta) = \int_0^\infty p_i(d, t_{res}) dt_{res} = e^{-d/\lambda_{abs}} \cdot (1 + \frac{\tau \cdot c_{light,ice}}{\lambda_{abs}})^{-d/\lambda} = N \qquad (5.17)$$

Equation 5.16 is not defined for negative times. In order to account for this and a finite PMT-resolution, it has been "patched" to a Gaussian around $t_{res} = 0$ ns with 15 ns width. The obtained *patched-Pandel* function $\hat{p}(d, t_{res})$ is then defined over the whole parameter space. For a given muon track guess, the distance d depends on the track parameters (x, y, z, θ, ϕ). Inserting these into the patched-Pandel function, one obtains a probability function for each hit OM $\hat{p}_i(x,y,z,\theta,\phi)$. The actual *maximum likelihood reconstruction* then tries to maximize the likelihood:

$$log(\mathcal{L}(x, y, z, \theta, \phi)) = log(\prod_{i=1}^{N_{hits}} \hat{p}_i(x, y, z, \theta, \phi) = \sum_{i=1}^{N_{hits}} log(\hat{p}_i(x, y, z, \theta, \phi)) \tag{5.18}$$

taking the result of the line-fit approximation as first guess. Implementation of the reconstruction and further details can be found in [89]. Figure 5.15a shows the zenith angle of the maximum likelihood reconstruction and figure 5.15b the zenith angle resolution. One can see that there is still a considerable amount of events reconstructed into the wrong hemisphere. A cut on $\theta_{like} > 70^\circ$ has been set.

The *iterative maximum likelihood reconstruction* improves the performance of the ordinary likelihood fit by iterating the minimum finding procedure M times. This time-consuming approach can be followed only after considerable reduction of the data, thus only at this stage of filtering. Figure 5.15c and d show data which had passed the level 1 filters 5.14 and the cut on the zenith angle of the ordinary likelihood fit. About 1/3 of the remaining background is reconstructed as upward moving.

The maximization procedure returns the likelihood $\mathcal{L}$ of the best found track hypothesis. In analogy to a reduced χ^2 value, a *likelihood parameter* can be defined:

$$L^{iter} \equiv= -\frac{log(\mathcal{L}(x, y, z, \theta, \phi))}{N_{hits} - 5} \tag{5.19}$$

This parameter has turned out to be a useful cut parameter. Its distribution is shown in figure 5.15e. Events which are not well reconstructed have a big value of L^{iter}. A cut was set at $L^{iter} < 8.7$[2].

A track reconstruction has five free fit parameters (x, y, z, θ, ϕ). Therefore, a reconstruction procedure needs at least five hits which have occurred with great probability. This is, for instance, the case for unscattered photons emitted very close to an OM. It is reasonable to cut out events with very few direct hits, because else one can assume that the reconstruction was poorly determined. Figure 5.15f shows the distributions of direct hits in a time residual window of -15 to +25 ns. Background simulation and experimental data show more events with few direct hits compared to the atmospheric neutrino simulation. A cut was therefore set at $N_{direct\ hits}$(-15ns:25ns) > 3. For the same reason, a cut on the number of hit OMs was set to $N_{hit\ OMs} > 11$. Filtering on the maximum likelihood reconstructions at this stage contained five cuts (level 2):

$$\begin{aligned} \theta_{like} &> 70^\circ \\ \theta_{iter} &> 90^\circ \end{aligned}$$

[2]Note that ref. [87, 80] set this cut at $L^{iter} < 9.5$ on filter level 2 and enforced it later.

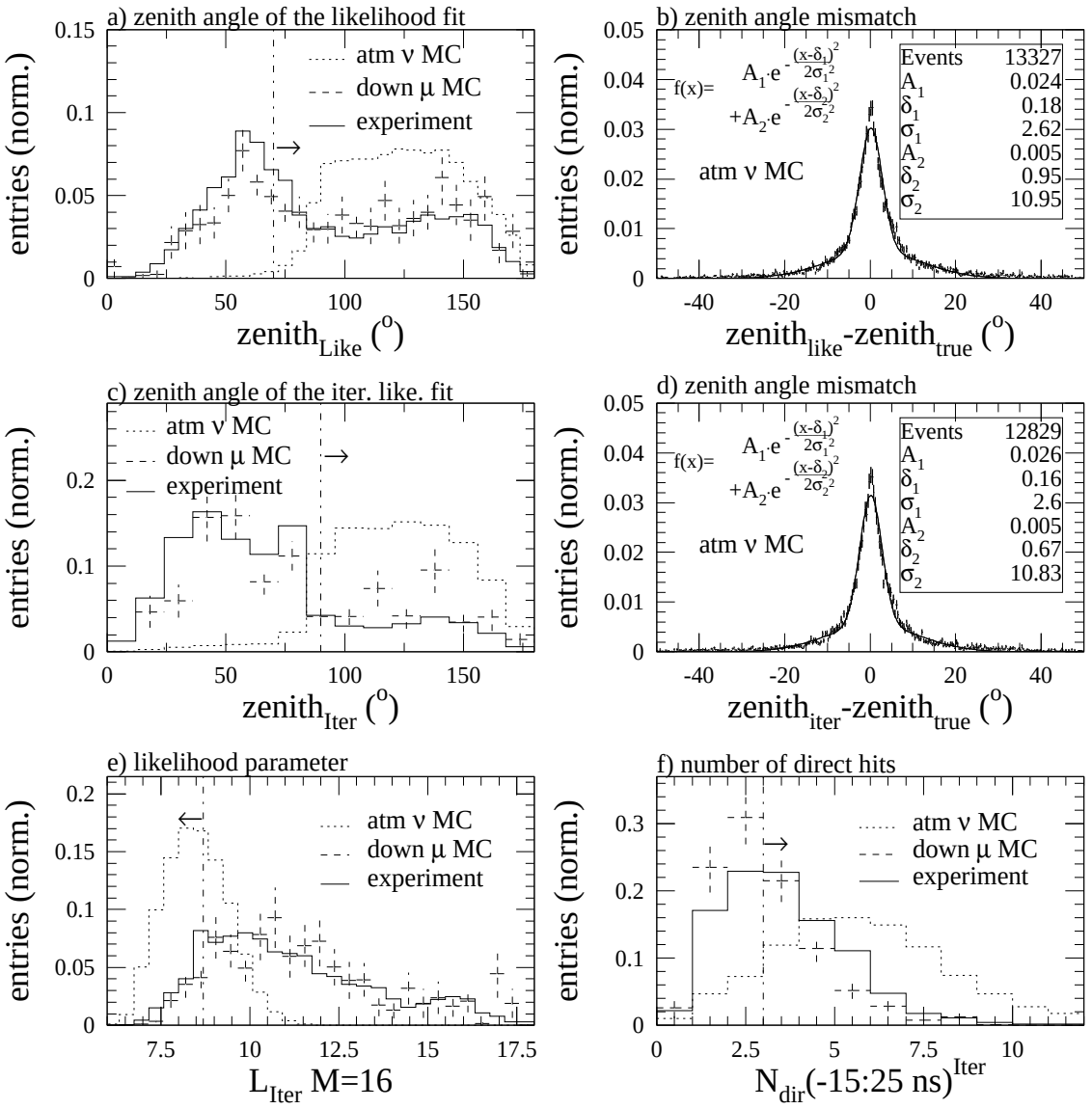

Figure 5.15: Maximum likelihood reconstructions of AMANDA-B10 data. Shown are distributions of simulated atmospheric neutrino induced muons, simulated down-going muons from air showers and experimental data after application of level 1 filters. The top left plot (a) shows distributions of the zenith angle of the likelihood fit. A cut at $\theta_{like} > 70^\circ$ was set as indicated by the dashed-dotted line. The top right plot (b) shows the zenith angle difference with respect to the true generated zenith angle of the muon. The sum of two Gaussians is fit to the data. The center left plot (c) gives the distributions of the iterative likelihood fit with 16 iterations, the cut on the zenith angle of the likelihood fit applied. The dashed-dotted line indicates that a cut at $\theta_{iter} > 80^\circ$ was set. Figure (d) shows the distribution of the reconstructed zenith angle mismatch of the iterative likelihood fit. Although the angular resolution has practically not improved, contribution of the badly reconstructed data sample has reduced considerable. The bottom left plot e) shows the likelihood parameter of the iterative likelihood fit. A cut was set keeping only data with $L^{iter} < 8.7$. Figure f) gives the distribution of direct hits within a time window of -15 ns and 25 ns. Only data containing more than 3 direct hits was kept.

$$\begin{aligned} L_{iter,M=16} &< 8.7 \\ N_{direct\ hits}(-15ns:25ns) &> 3 \\ N_{hit\ OMs} &> 11 \end{aligned} \tag{5.20}$$

Out of the line-fit filtered data (level 1), 0.9% of experimental data passed the maximum likelihood filters, 0.6% of the corresponding atmospheric muon simulation and 49.4% of the atmospheric neutrino simulation (both mass production 2000) pass these cuts. More detailed information about these filters can be found in [87, 88, 94][3].

5.4 Tensor of Inertia, Shower and Energy Fits

With the reduced data sample, more fits have been performed. First, a tensor of inertia of hit locations was calculated:

$$I^{k,l} = \sum_{i=1}^{N_{hits}} a_i \cdot (\delta^{kl} \cdot (\vec{r}_i^{\,2}) - r_i^k \cdot r_i^l) \tag{5.21}$$

with $\vec{r}_i$ the distance of hit i to the center of gravity of all hits and a_i an amplitude weight. The tensor of inertia has three eigenvalues I_1,I_2,I_3 and the corresponding three eigenvectors. The smallest eigenvalue (which was called I_1) corresponds to the longest axis of the event, its eigenvector is aligned to the direction of the track. For spherical events, the three eigenvalues should be of approximately equal size. Building ratios of I_1, I_2 and I_3 thus gives a handle on the spatial topology of an event. For track-like events, one expects a big difference between I_1 and (I_2,I_3). Figure 5.16a shows distributions of $3{\cdot}I_1/(I_1{+}I_2{+}I_3)$. One can see that background simulation as well as experimental data show an enhancement of spherical events. There is a shift for the experimental data towards larger values compared with the MC background prediction. This feature will be studied in further detail in chapters 5.4.1 and 9 where application of this cut will be described.

A complete reconstruction was performed using a cascade hypothesis. The procedure has been described in [41]. Just as with the maximum likelihood reconstruction described in chapter 5.3, the shower reconstruction returns a likelihood parameter, L_{shower}. For muon tracks, this parameter has to be worse than the one obtained for the track hypothesis fit. On the other hand, one important background to neutrino-induced muons consists of down-going high-energy muons passing close to the detector and emitting a bright shower due to stochastic energy loss. A cut has been invented to remove this background:

$$L_{shower}/L_{iter} > 0.95 \tag{5.22}$$

Figure 5.16b shows the distributions of this ratio. There is an enhancement of more cascade-like events visible for background simulation and experimental data.

Apart from the likelihood, the numbers of direct hits can be compared. We demand that data has more direct hits obtained via the track model than via the cascade model. In

[3] Note that the definitions of filter levels are slightly different, there.

this case, a time residual window of -15 to 75 ns has been proven more useful. Figure 5.16c shows that this cut seems reasonable removing more mis-reconstructed fake events than real signal.

An alternative approach using the muon-track as input can be described as follows: $P_i^{hit}(d,\theta)$ (equation 5.17) gives the overall probability for a reference OM to be hit by one single Cherenkov photon. If one expects μ photoelectrons to arrive within the time resolution window, one can calculate:

$$\begin{aligned} P_{i,\mu}^{no\ hit}(d) &= (1 - P_i^{hit}(d))^{\epsilon} \\ P_{i,\mu}^{hit}(d) = 1 - P_{i,\mu}^{no\ hit}(d) &= 1 - (1 - P_i^{hit}(d))^{\epsilon} \end{aligned} \tag{5.23}$$

with ϵ being related to the number of photoelectrons by a proportionality coefficient κ: $\epsilon = \kappa \cdot \mu$.

Again, a likelihood function can be constructed and maximized:

$$log(L(x,y,z,\theta,\phi,\mu) = \sum_{hit\ OMs} log(P_{i,\mu}^{hit}(d)) \quad + \sum_{not\ hit\ OMs} log(P_{i,\mu}^{no\ hit}(d)) \tag{5.24}$$

The procedure can be used as a second track reconstruction model which will be explained in chapter 9. At this stage, another approach has been followed: It takes the track found by the iterative maximum likelihood procedure and fits only ϵ as free parameter. This value depends (among others) on the photon intensity emitted by the muon and thus on the muon energy because of stochastic energy loss (see chapter 2.2) and additional Cherenkov radiation emitted by the showers along the track. One obtains therefore an energy estimate which is, however, only valid for muon energies above $\approx$ 700 GeV (that is when stochastic energy loss starts to dominate over the continuous one (see eq. 2.2)). A *likelihood parameter* L^{phit} can be calculated as

$$L^{phit} = -\frac{log(L(x,y,z,\theta,\phi,\mu))}{N_{OM,operating} - 1} \tag{5.25}$$

and further used as a quality parameter. Figure 5.16d shows distributions of this parameter. Experimental data and background simulation show greater values of L^{phit} than simulated neutrino induced muons, which seemingly can be reconstructed more easily by this method. Here also, a slight shift of experimental data to smaller values of L^{phit} (= better reconstructed data) can be seen. This feature is not understood, yet. A detailed description of the P^{hit}-P^{nohit}-method can be found in [89]. A cut was set at:

$$L^{phit} < 6 \tag{5.26}$$

The additional cuts introduced in this section are applied to the data (filter level 3):

$$\begin{aligned} L_{phit} &< 6.0 \\ L_{shower}/L_{iter} &> 0.95 \\ N_{direct\ hits}^{iter}(-15ns:75ns) - N_{direct\ hits}^{shower}(-15ns:75ns) &\geq 0 \end{aligned} \tag{5.27}$$

About 37% of previously filtered experimental data passes these cuts, 34% of atmospheric muon simulation and 87% of previously filtered atmospheric neutrino simulation (both mass production 2000).

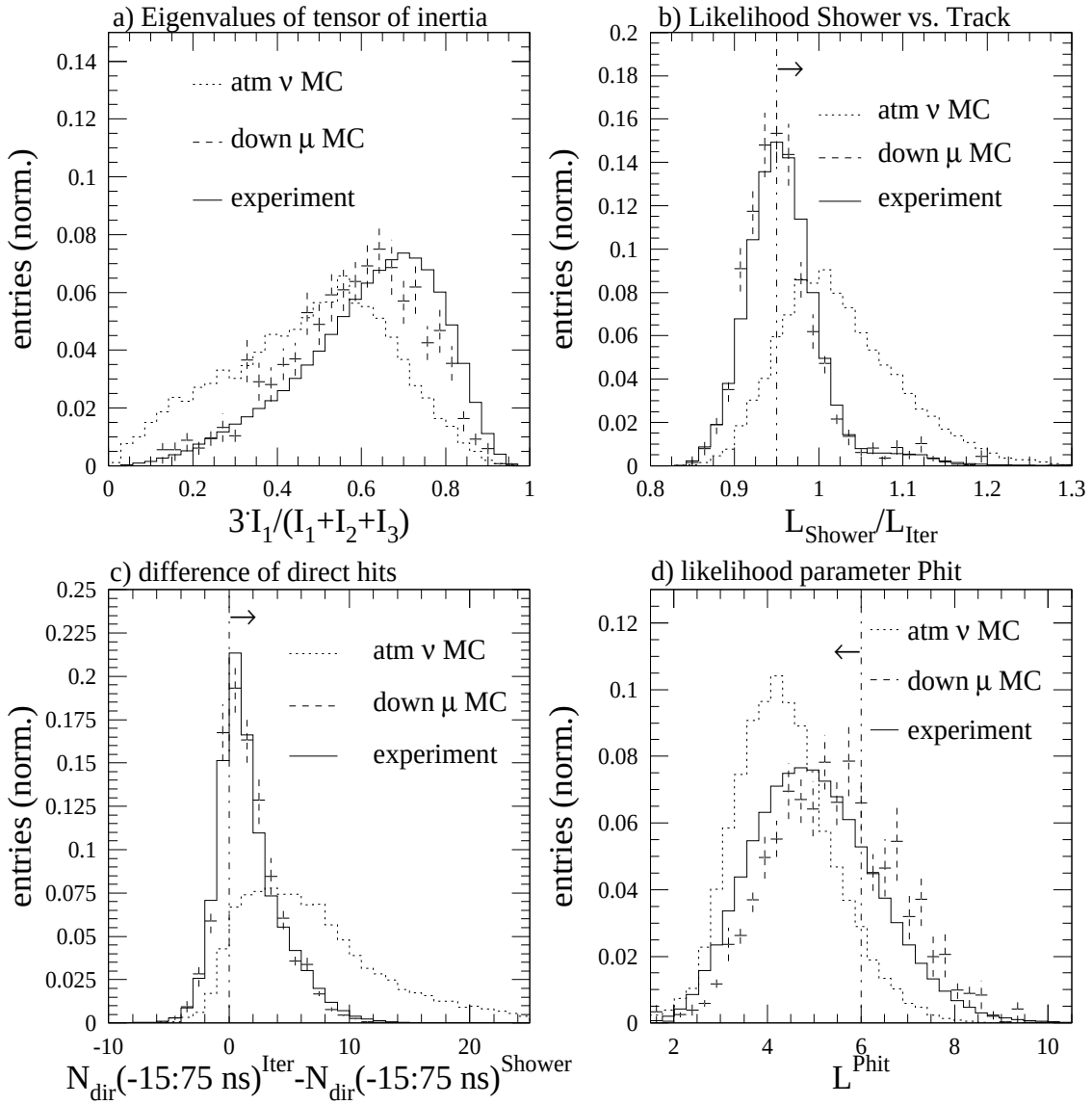

Figure 5.16: Tensor of inertia, shower and energy reconstructions of AMANDA-B10 data. Shown are distributions of simulated atmospheric neutrino induced muons, simulated down-going muons from air showers and experimental data filtered down to level 2 (eq. 5.14,5.20). The top left plot (a) shows distributions of the ratios of eigenvalues of the tensor of inertia. I_1 is the smallest eigenvalue. Events with a ratio towards 1 behave like emitted from spherical events with small ratios have a track-like topology of hits. The top right plot (b) shows the ratios of the returned likelihoods of the shower reconstruction and the iterative likelihood reconstruction. Events with a small ratio can be reconstructed better like a shower, events with large ratios behave more track-like. Figure c) shows the difference of direct hits within a time residual window of -25 to 75 ns between the shower reconstruction and the iterative likelihood fit. Events with large values have more unscattered photons assuming a track hypothesis than with a shower hypothesis. The bottom right picture d) gives the distribution of the likelihood parameter L^{phit} described in the text.

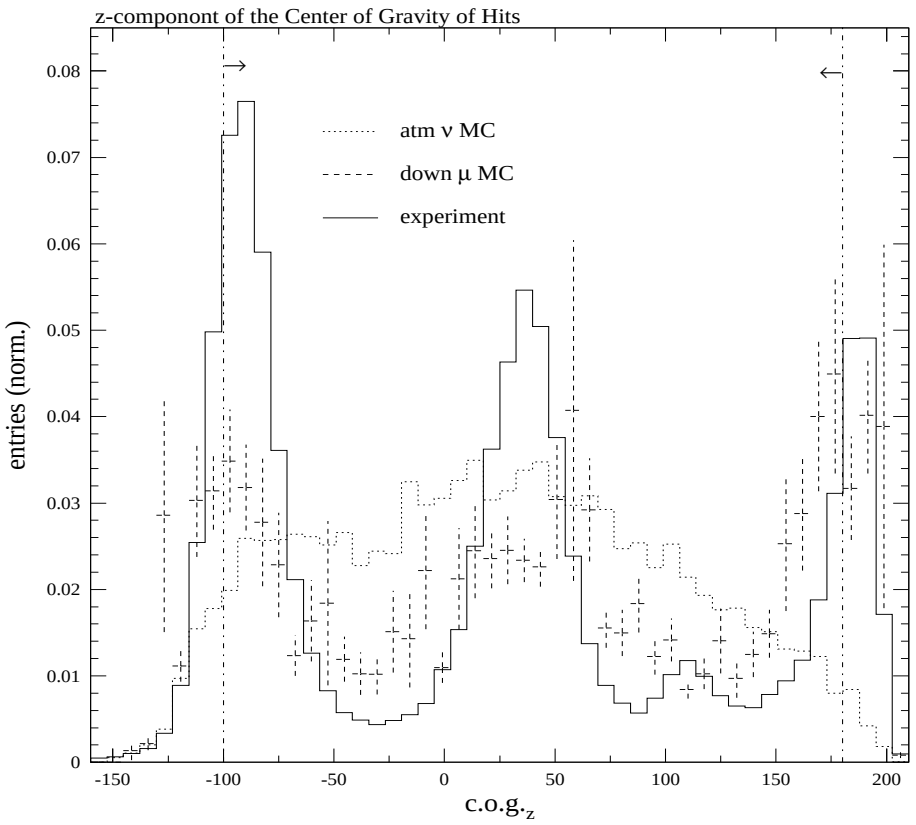

Figure 5.17: Vertical component of the center of gravity of hits. Shown are distributions of simulated atmospheric neutrino induced muons, simulated down-going muons from air showers and experimental data. The x-axis shows the z-component of the center of gravity of hits in meters, with 0 being the detector center. All data was filtered with the level 1 cuts (5.14), the likelihood-filters (5.20) and the level 3 filters (5.27).

5.4.1 Filtering on the "Center-of-Gravity"(c.o.g.)-Background

As already mentioned in chapter 4, at higher filter levels unsimulated structures in the center of gravity of hits appear. Figure 5.17 shows distributions of experimental data, simulated atmospheric muon background and simulated atmospheric neutrino-induced muons. Two peaks of events can be seen very high or very low in the detector. The upper peak is predicted by simulation and can be identified as "corner-clippers". These are muons passing aside lower or (as here) upper corners of the detector. Sometimes hit patterns occur favoring a track reconstructed as upward moving. These events can partly be rejected by simply cutting out the edges of the center of gravity distribution. At this stage of filtering, preliminary weak cuts have been set at -100 m $<$ c.o.g.$_z$ $<$ 180 m indicated by the dashed-dotted lines.

Figure 5.17 shows another peak in the middle which could partly, but not fully be simulated by taking vertical structures of the scattering length in ice into the simulation. The same is valid for the left peak. Reference [80] gives a lot of information about the

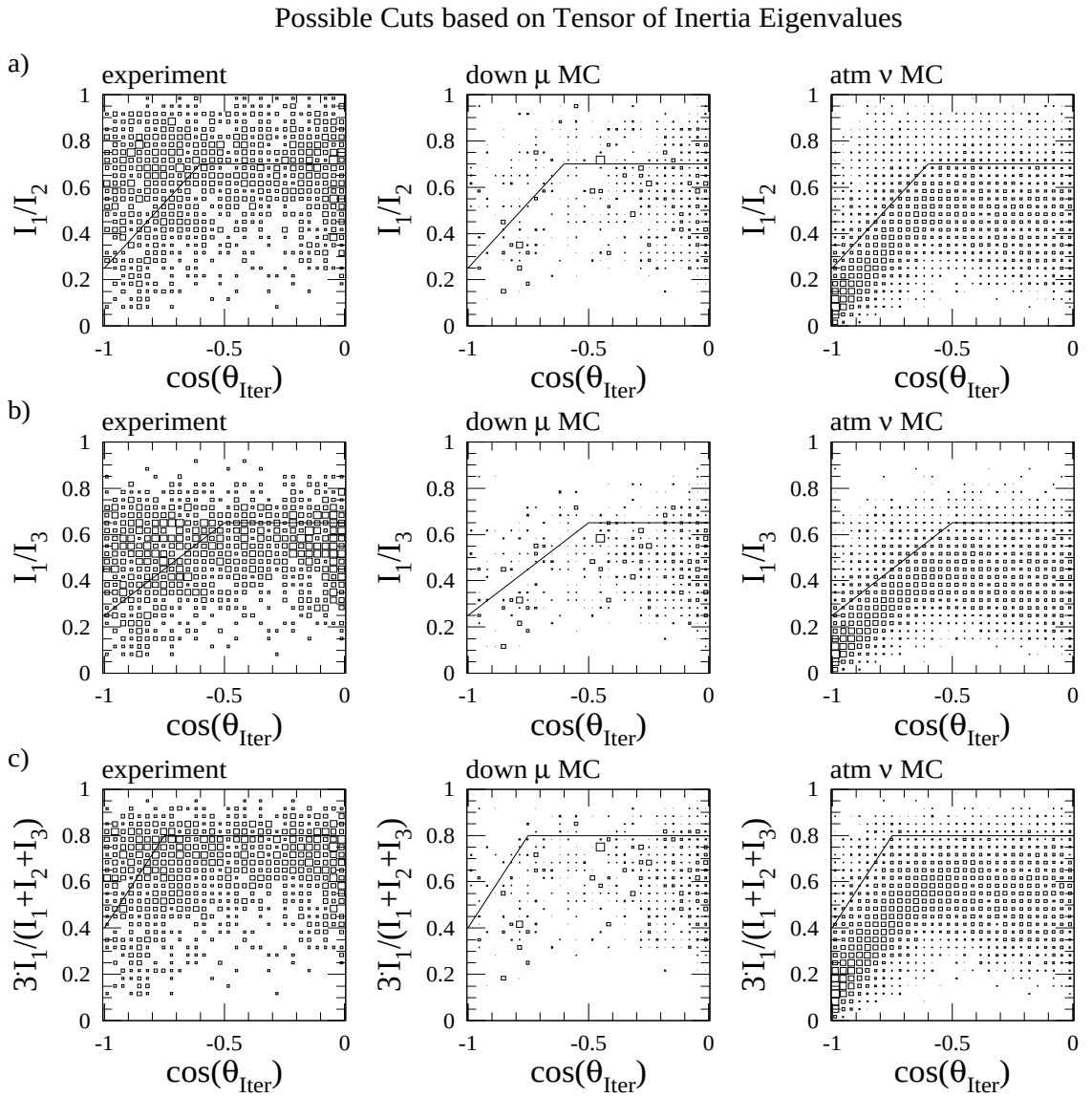

Figure 5.18: Center-of-gravity of hits - filters requiring angle-dependent cuts on ratios of the eigenvalues of the tensor of inertia of hits. Shown are neutrino induced muons, simulated downgoing muons from air showers and experimental data filtered to level 3 (5.14,5.20,5.27). All ratios are plotted against the cosine of the reconstructed zenith angle of the iterative likelihood fit. A cosine of -1 corresponds to tracks reconstructed as vertically upward moving, a cosine of 0 corresponds to horizontal events. Cuts are indicated by the full lines. Data below the line is kept. The top plots a) show the smallest eigenvalue divided by the largest one. Stronger cuts are applied for vertical tracks in order to remove the non-simulated part of experimental data clustering at the left side. Cuts indicated by the lines were applied previous to analysis A (see chapter 8). The medium plots b) show the ratio of the smallest eigenvalue and the medium one. Again non-simulated clustering of the experimental data is cut out (chapter 5.4.1). Cuts indicated by the lines were applied previous to analysis A (see chapter 8). The bottom plot c) shows the smallest eigenvalue divided by the sum of the three eigenvalues and normalized to one. Filtering was chosen to keep as much simulated signal as possible. Cuts indicated by the lines were applied previous to analysis B (see chapter 9).

behavior of the events found in the middle peak. They are generally like bright events and tend to be horizontally aligned. There is a tendency that these events occur closer to strings 9 and 10 than predicted. Reference [80] favors vertical ice structures to be responsible for this effect, possibly enhanced by small inaccuracies in the simulation of the muon propagation, the shower simulation or other effects. Meanwhile, there is strong indication for remaining events to be mostly due to residual cross-talk [95]. The way to deal with the problem chosen in [80] was to apply cuts which remove this non-understood background until new knowledge via simulation of depth-dependent scattering was acquired. With the help of high-quality down-going muon events (i.e. experimental data, reconstructed us down-going and having passed zenith-angle-inverted filters), the signal efficiency was verified and assured.

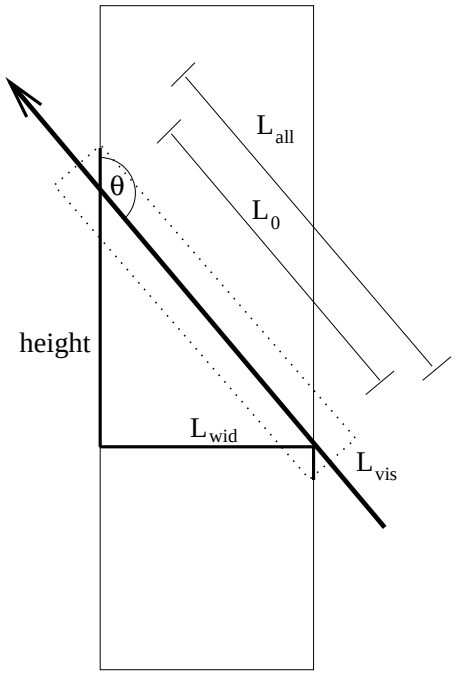

Figure 5.19: Geometrical model for the extension of an event versus the zenith angle θ. The following parameters are shown: L_{vis} gives the estimated visual range of Cherenkov light supposed to arrive within a time residual window of -15 to 75 ns. $height$ is the projected height of the muon track onto the detector array, L_{wid} the projected width. L_{all} gives the length of the muon track which is capable of emitting Cherenkov light detected within the time residual window and L_0 the part inside the detector. The angle θ is the reconstructed zenith angle. Figure taken from [80].

Used parameters are those reflecting the geometric extensions of an event. Because of the asymmetry of the detector which is more than four times as high than it is wide, cuts using the length of an event have to depend on the zenith angle. Otherwise, one would remove all horizontal events which is not desired. Figure 5.18 shows distributions of ratios of the eigenvalues of the tensor of inertia versus the cosine of the zenith-angle. There is an enhancement of events with nearly vertical tracks, but rather spherical topology. This feature is neither simulated by the background MC nor by the signal MC. Figures 5.18a

and 5.18b show two strong cuts aiming to filter out what is unsimulated. Plot 5.18c shows a cut which was taken after revision of the above two choices. This revision was done because analysis A suggested that cuts had been applied too strong at this filter level.

Figure 5.19 shows a simple model for the geometric extensions of an event. An event is thus required to have a certain length depending on the reconstructed zenith angle θ: In particular the *length of direct hits* L_{dir}. This parameter takes all hits occurring in a given time residual window and calculates the geometric distance between the two out-most ones. In our case, the length of direct hits of a time residual window of -15 to 75 ns has been chosen. Figure 5.20 shows the distributions for this parameter, again depending on the reconstructed zenith angle. There is a non-simulated enhancement visible of reconstructed events with a small length of direct hits and reconstructed as nearly vertically upward moving.

In the course of this thesis, two different data samples were used (analysis A and B). One sample had more stringent cuts applied (sample A) than the other. This "stringent" data sample is described in detail in [80]. The following "c.o.g.-cuts" were applied there:

$$\begin{aligned} -100\ m &< c.o.g._z < 180\ m \\ I_1/I_2 &< MIN(0.7, 1.375 - 1.125 \cdot |cos(\theta_{iter})|) \\ I_1/I_3 &< MIN(0.65, 1.05 - 0.8 \cdot |cos(\theta_{iter})|) \\ L_{dir}(-15:75\ ns) &> MIN(L_{max}, \frac{2 \cdot L_{vis} \cdot |cos(\theta_{iter})| + L_{wid}}{|sin(\theta_{iter})|}) \end{aligned} \tag{5.28}$$

with $L_{max} = 180$ m, $L_{vis} = 10$ m and $L_{wid} = 50$m. Reference [80] cites two more cuts:

$$\begin{aligned} height &> MIN(L_{max}, \frac{L_{wid} \cdot |cos(\theta_{iter})| + 2 \cdot L_{vis}}{|sin(\theta_{iter})|}) \\ L_{all} &> MIN(L_{max}, \frac{2 \cdot L_{vis} \cdot |cos(\theta_{iter})| + L_{wid}}{|sin(\theta_{iter})|}) \end{aligned} \tag{5.29}$$

with $L_{max} = 230$ m, $L_{vis} = 30$ m and L_{all} the length of all hits projected on the reconstructed track.

About 17% of previously filtered experimental data passes these "tight" cuts, 29% of atmospheric muon simulation and 73% of previously filtered atmospheric neutrino simulation (both mass production 2000).

As a result of analysis A (see chapter 8), the need for a data sample with more relaxed cuts arose (see chapter 8). Therefore, a second data sample (sample B) was created, with the following "c.o.g.-cuts":

$$\begin{aligned} -100\ m &< c.o.g._z < 170\ m \\ 3 \cdot I_1/(I_1 + I_2 + I_3) &< MIN(I_{max}, 2 - 1.6 \cdot |cos(\theta_{iter})|) \\ L_{dir}(-15:75\ ns) &> MIN(L_{max}, \frac{2 \cdot L_{vis} \cdot |cos(\theta_{iter})| + L_{wid}}{|sin(\theta_{iter})|}) \end{aligned} \tag{5.30}$$

with $L_{max} = 140$ m, $L_{vis} = 10$ m, $L_{wid} = 60$m and $I_{max} = 0.8$. Figure 5.18c and figure 5.20b show the corresponding distributions.

About 23% of previously filtered experimental data passed the "relaxed" cuts, 32% of atmospheric muon simulation and 83% of previously filtered atmospheric neutrino simulation (both mass production 2000).

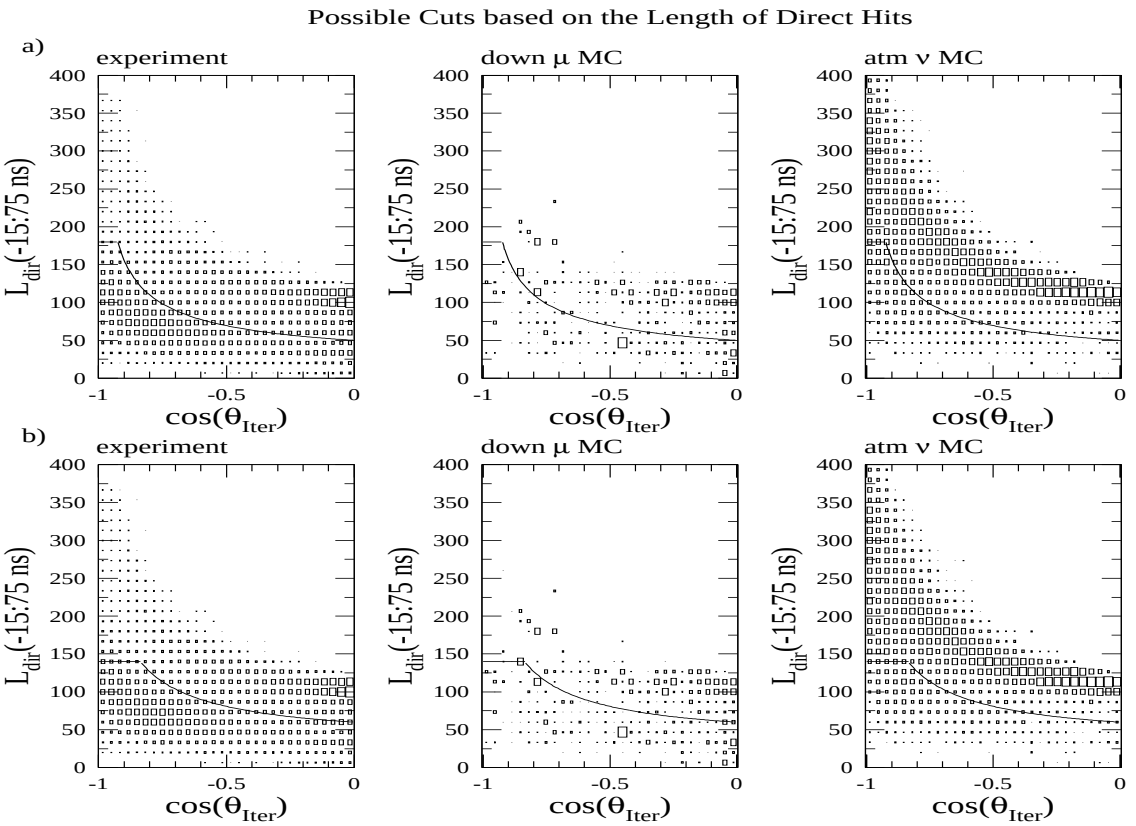

Figure 5.20: Length of direct hits - filters requiring angle-dependent cuts on the geometric extension of an event. Shown are neutrino induced muons, simulated down-going muons from air showers and experimental data filtered to level 3 (5.14,5.20,5.27) The length of direct hits within a time residual window of -15 to 75 ns is plotted against the cosine of the reconstructed zenith angle of the iterative likelihood fit. A cosine of -1 corresponds to tracks reconstructed as vertically upward moving, a cosine of 0 corresponds to horizontal events. Cuts are indicated by the full lines. Data above the line is kept. The top plots a) show the filter described in chapter 5.4.1. Stronger cuts are applied for vertical tracks in order to remove the non-simulated part of experimental data clustering at the left side. The lower plots b) show the filter used for the relaxed data sample.

5.5 The Dipole Fit, Multi-PE-Fits and Bayesian Approach

During visual inspection of the experimental data obtained by analysis A (chapter 8), we discovered a small contribution (about 3-4 events) of unsimulated background: Atmospheric muons from coincident air showers where one track goes through the detector bottom slightly earlier than the second one traversing the top of the detector. All fits introduced up to now were likely to identify the obtained signature as upward-moving. Multiple muons produced in air showers are not able to produce this pattern of hits as they arrive in bundles correlated in time. For this background and following an idea of W. Rhode [96], the dipole fit was implemented. It consists of two steps:

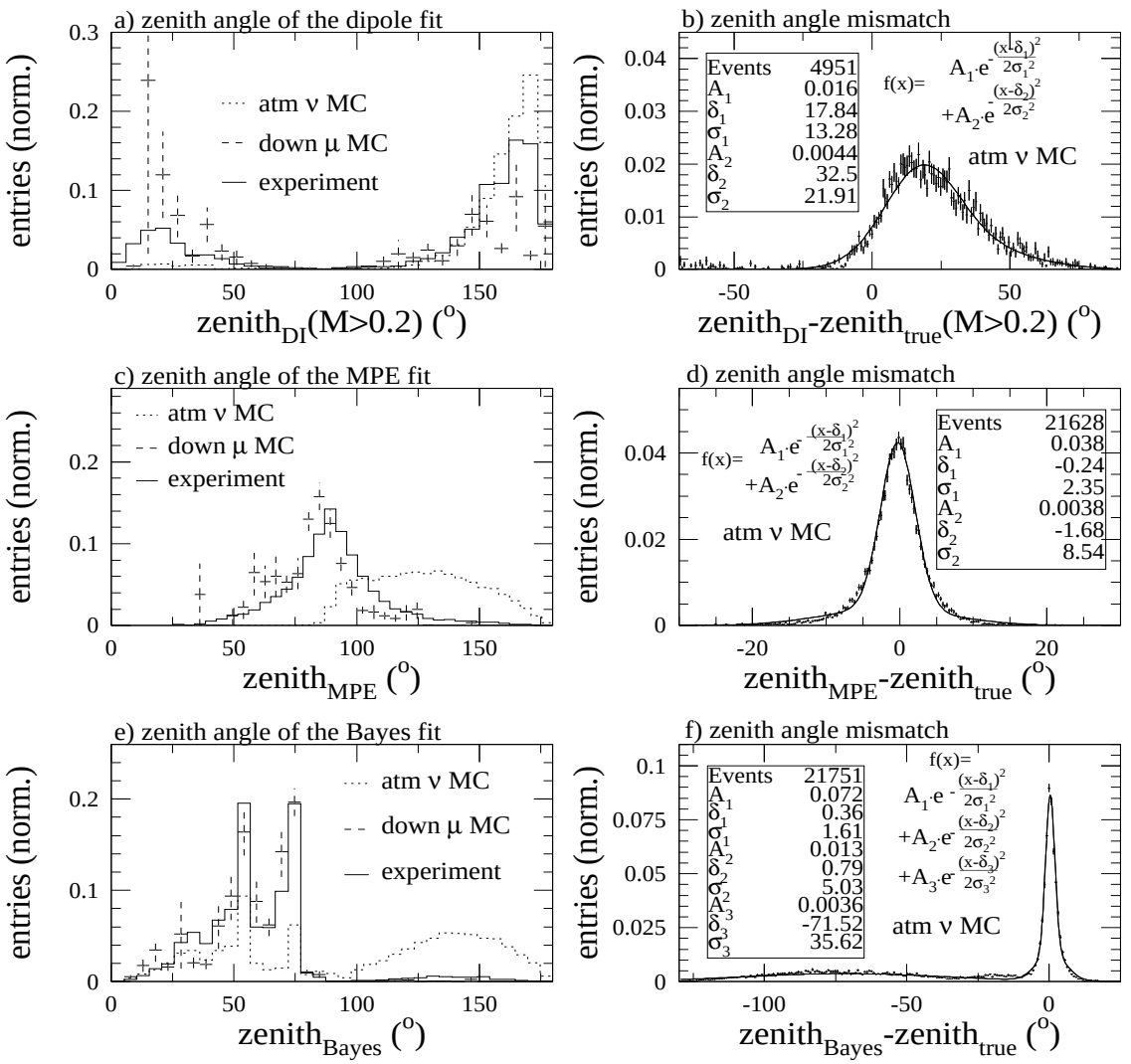

Figure 5.21: Dipole, MPE and Bayesian reconstructions of AMANDA-B10 data. Shown are distributions of simulated atmospheric neutrino induced muons, simulated down-going muons from air showers and experimental data, filtered to level 3 and the relaxed "c.o.g."'-cuts (sample B). The top left plot (a) shows distributions of the zenith angle of the dipole fit, only events with a magnetization $M > 0.2$ have been taken. Figure (b) shows the distribution of the reconstructed dipole zenith angle mismatch, again only for events with $M > 0.2$. A double Gaussian has been fitted to the data. The center left plot (c) gives the distributions of the multi-photoelectrons fit. Figure (d) shows the zenith angle mismatch for the multi-photoelectrons fit. The bottom left plot (e) shows the zenith angles of the Bayes fit. Nearly all background simulation events as well as experimental data is reconstructed as down-wards moving. Almost half of the signal atmospheric neutrino-induced muons, too. The corresponding zenith angle mismatch (f) has been fitted by a triple Gaussian due to about 4% of the events reconstructed with a very large error.

1. Sort all hits according to their calibrated times.

2. Calculate the Dipole-moment $\vec{M}$:

$$\vec{M} = \frac{1}{N_{hits} - 1} \cdot \sum_{i=2}^{N_{hits}} \frac{\vec{r}_i - \vec{r}_{i-1}}{|\vec{r}_i - \vec{r}_{i-1}|} \tag{5.31}$$

This fit takes each normalized pointing vector from one OM to the one fired next as little dipole moments, Averaging over all of them yields a global moment $\vec{M}$. Fits with a significant "magnetization" $|\vec{M}|$ (a value of 0.2 has been proven reasonable) are correlated with the true direction of the muon. About a quarter of the data passing the filters of chapter 9 fulfills this requirement. Figure 5.21a shows the corresponding zenith angle distributions of this sub-sample. Most simulated atmospheric neutrino-induced muons are fitted into the lower hemisphere. Experimental data events show a significant contribution of events fitted with low zenith angles, which is predicted by the background simulation. The corresponding zenith angle mismatch is shown in figure 5.21b. The angular resolution is poor.

Since an AMANDA-TDC can resolve different photons only if they arrive separated by more than some hundred nanoseconds, it is useful to define a probability function for the arrival time of the first photon out of N:

$$p^1_{i,N}(d, t_{res}) = N \cdot p_i(d, t_{res}) \cdot \left(\int_{t_{res}}^{\infty} p_i(d, t_{res}) dt_{res} \right)^{(N-1)} \tag{5.32}$$

One can therefore modify equation 5.18 by replacing $p_i(x, y, z, \theta, \phi)$ by $p^1_{i,N}(x, y, z, \theta, \phi)$. Maximization of the corresponding likelihood gives the *multi-photo-electron fit*. We chose to use a combined fit of time and hit probabilities by maximizing the product of the multi-photo-electron likelihoods (equation 5.32) and the P^{hit}-$P^{no\ hit}$ likelihood function $L(x, y, z, \theta, \phi, \mu)$ (equation 5.24). This will be referred to a multi-photo-electron (MPE) fit. Figure 5.21c shows the distributions of the reconstructed zenith angle for data which has passed all filters of chapter 9.

Experimental and background simulation data are both reconstructed towards smaller zenith angles with a mean of about 90°. A zenith angle cut seems to be reasonable. There is a slight shift however, between background simulation and experiment.

The zenith angle resolution has improved with respect to the previous fits and filter levels. The shift visible in figure c) seems not found back, here. Because of its capability to reject further mis-reconstructed events, we chose to use this fit for further filtering. However, one has to remain cautious keeping in mind that the simulation does not describe the data well and the involved systematics of this fit are complex.

The Madison analysis group has invented a fit based on Bayesian statistics. It multiplies the likelihood-function with a zenith-angle dependent prior. This prior-function is constant for up-going track hypotheses and grows to 10^6 above the horizon, according to the expected angular spectrum of down-going muons from air showers [97].

Figure 5.21e shows distributions of the reconstructed zenith-angle of this fit. Nearly all simulated background is reconstructed into the upper hemisphere, as well as a large fraction of experimental data. A considerable amount of atmospheric neutrino induced

muons signal however, is also reconstructed wrongly to smaller zenith angles. Figure 5.21f shows the zenith angle resolution of the Bayesian fit which was fitted by a triple Gaussian.

Analysis [97] relies completely on the large rejection capacities of the Bayesian approach. We have therefore included some parameters based on the Bayesian fit in analysis B (chapter 9).

5.6 Conclusions

From 10^9 triggers, experimental data has been reduced to about 16.500 events so far. This corresponds to a rejection factor of $5{\cdot}10^4$. 14% of simulated atmospheric neutrino-induced muon events survive these cuts.

Each applied filter had served different, specific purposes:

- The hit-cleaning procedure aimed at removing noise-hits and cross-talk.
- The line fit ensured fast, CPU-time saving rejection of more than 90% of the registered triggers.
- The maximum likelihood reconstruction rejects all events obviously reconstructed into the upper hemisphere.
- The time-consuming iterative maximum likelihood reconstruction further rejects downward moving events.
- Cuts on the likelihood parameter, the number of direct hits and the number of hit OMs reject events which, by fundamental principles, could not have been reconstructed well.
- Cuts using the shower reconstruction remove background looking more shower- than track-like, especially stochastic energy loss from downward moving high energetic muons.
- The likelihood parameter L^{phit} removes events with low combined hit-probabilities of each fired OM.
- Two cuts on the edges of the vertical component of the center of gravity of hits remove "corner-clippers".
- Filters based on the eigenvalues of the tensor of inertia remove events with a spherical topology, e.g. showers produced by muons passing aside the detector. Besides, they are tuned to remove all non-simulated, non-understood experimental events appearing in the middle peak of the c.o.g.$_z$-distribution.
- Finally, cuts derived from the geometrical extensions (especially the length) of a reconstructed track remove events with a short track (e.g. low-energy muons) and the non-simulated c.o.g.$_z$-events.

All cuts have thus been used for different sorts of background, in fact, all background, we could think of. What remains is still heavily dominated by mis-reconstructed fake events. However, no specific class of background can be identified with a single specific filter that could be developed for it. Instead, one has to go over to select what looks like a Cherenkov radiation emitting muon.

6 Cut Evaluation

The last filtering stage is different from previous ones for the following reasons:

- Lack of an easily identifiable class of remaining background. The choice of further filter parameters is therefore *not evident*. There is more than one combination of cut parameters conceivable.

- *Cuts are not independent*, i.e. filtering on one cut parameter can make another cut parameter redundant. Correlations between cut parameters have to be investigated in order to achieve an optimum signal passing rate and reduce systematic uncertainties.

Various quality cuts have been developed and amply used by different analyzes. The early Madison analysis has used 40 different cuts (although based on only 14 cut parameters) [97], whereas the previous DESY-Zeuthen muon neutrino analysis has converged to cut on about 20 quality parameters in total [80]. Major efforts of the analysis at DESY included the reduction of the number and the simplification of the cut parameters [98]. Another approach has been presented by the Madison group relying on a Bayesian track reconstruction which requires fewer quality cuts [99, 100].

However, systematic investigations on correlations and orthogonality between all those cuts becomes difficult at this stage. So far, methods of applying a discriminant analysis [101, 96] or neural nets have been investigated [35].

Before thinking about the best way to optimize cuts, one should define the tasks of a final analysis. I will define six main goals (in order of their priority):

1. High signal purity

2. High signal efficiency

3. An estimate about the final background contamination

4. An estimate about the statistical and systematic errors of points 1-3.

For the investigation of neutrino oscillations, two more items have to be added:

5. Large zenith angle range

6. Low energy threshold

Point 1 is not hard to achieve. Tightening of already introduced cut parameters can easily lead to a small neutrino sample of almost 100% purity. This approach has been followed with the smaller detector AMANDA-B4 [102] and by the first neutrino search with AMANDA-B10 [103] which yielded convincing neutrino candidates. In our case however, we want to optimize on points 2-6 as well. The systematic behavior of cut parameters play a major role. In this context it is important to simplify the systematics of the analysis by reducing the number of cuts.

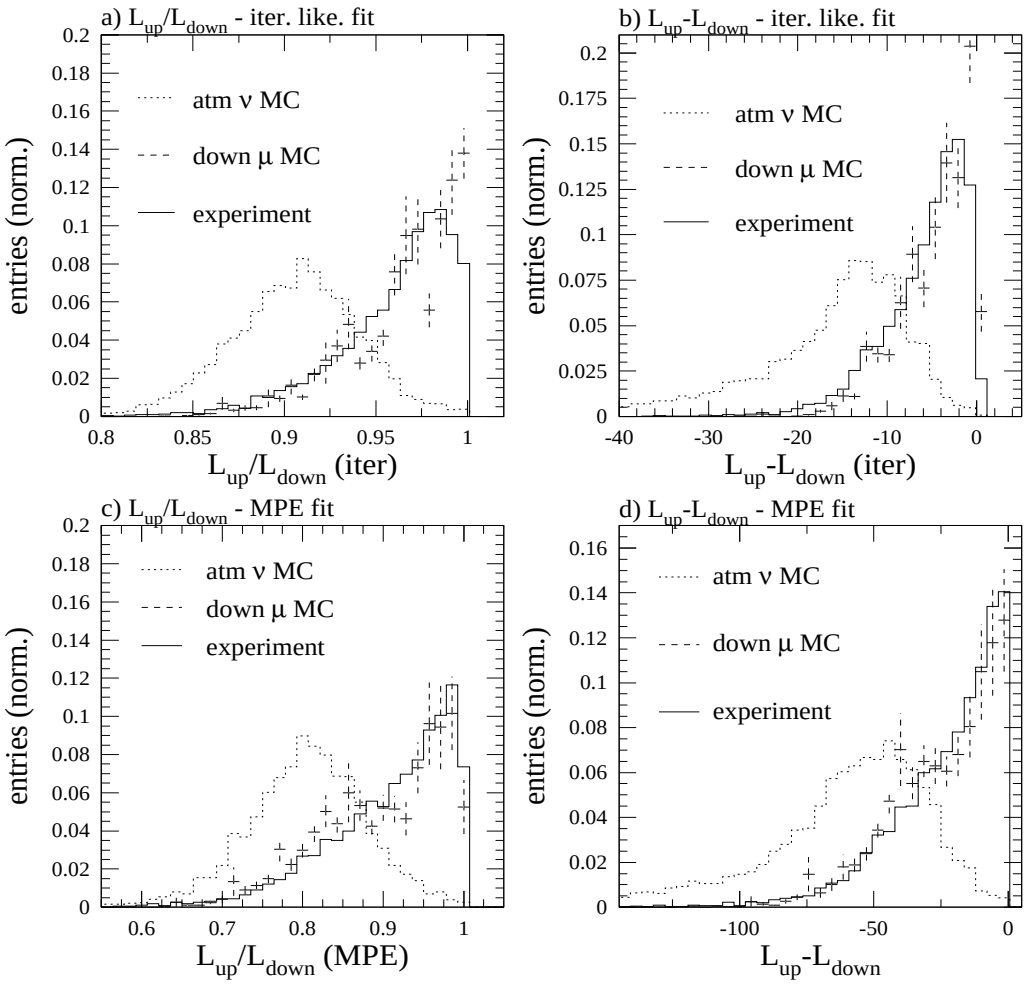

Figure 6.22: The parameters L_{up} and L_{down}. Shown are distributions of simulated atmospheric neutrino induced muons, simulated down-going muons from air showers and experimental data. All data was filtered up to level 3 with the relaxed set of "c.o.g."-cuts. The top left plot (a) shows distributions of the ratios of the likelihood parameters for the best found upward moving by the best downward moving track hypothesis obtained from the iterative likelihood reconstruction. The top right plot (b) shows the difference of both. Figures (c) and (d) show the the same variables obtained with the multi-photo-electron reconstruction.

6.1 Cut Parameters

In addition to the already introduced cut parameters (see chapter 5), other sensitive variables have been developed. I will introduce the important parameters for this analysis and explain the CUTEVAL-method, which allows to systematically investigate the rejection behavior of combinations of cut parameters.

6.1.1 L_{up} and L_{down}

One feature implemented in the iterative reconstruction algorithms is to store the best likelihood parameter, which the routine finds during its walk through the likelihood space for a *down-going* track hypothesis [80]. This parameter L_{down} is defined analogous to L_{up} (def. 5.19). One can then define:

$$L_{up} - L_{down} \equiv -\frac{log\frac{\mathcal{L}_{up}(x,y,z,\theta,\phi)}{\mathcal{L}_{down}(x,y,z,\theta,\phi)}}{N_{hits}-5} \tag{6.33}$$

$$\frac{L_{up}}{L_{down}} \equiv -\frac{log(\mathcal{L}_{up}(x,y,z,\theta,\phi))}{log(\mathcal{L}_{down}(x,y,z,\theta,\phi))} \tag{6.34}$$

Though the difference seems mathematically more justified (being based on the ratio of likelihoods), the ratio has been proven to be a better cut parameter in some cases (see chapter 8). Both parameters have different rejection behavior and have both been taken into the final analyzes. Figure 6.22a and 6.22b show the distributions of the two parameters obtained with the iterative likelihood fit, figures 6.22c and 6.22d the corresponding ones from the multi-photo-electron reconstruction. There is reasonable agreement between simulated atmospheric muon background and experiment. Separation between simulated signal and background seems good.

6.1.2 Differences between Reconstructed Directions

Except for cutting on the zenith angle of a certain reconstruction, the *difference of zenith angles between different reconstructions* is a good separator between signal and background predictions.

$$\Delta_\theta(fit_1, fit_2) \equiv |\theta_{fit_1} - \theta_{fit_2} + \text{offset}| \tag{6.35}$$

Especially, the zenith angle difference between the line fit and the iterative likelihood fit should be small in order to pass as a good reconstruction result. Figure 6.22a shows the corresponding distributions. A small shift of about 4° which is derived from the distribution of the atmospheric neutrino simulation is taken into account. In fact, zenith angle differences between all introduced reconstructions can be used as a cut parameter. Figure 6.23b shows one other example, the zenith-angle difference between the MPE-fit and the iterative likelihood fit.

An improved variant is the space angle between reconstructions which also takes the reconstructed azimuth angle into account:

$$\Psi(fit_1, fit_2) \equiv acos\left(\frac{\vec{r}_{fit1}\cdot\vec{r}_{fit2}}{|\vec{r}_{fit1}|\cdot|\vec{r}_{fit2}|}\right) \tag{6.36}$$

Figure 6.23c shows the distributions for the space angle between the iterative likelihood fit and the line fit. There is obvious separation between background and signal. The space angle difference between the line fit and the iterative likelihood fit shows a mean of about 17° for the simulated atmospheric neutrino sample. Figure 6.23d shows the space angle between the MPE fit and the iterative likelihood fit. Here, the separation is good, the mean space angle for the simulated atmospheric neutrino sample is much smaller (about 5°).

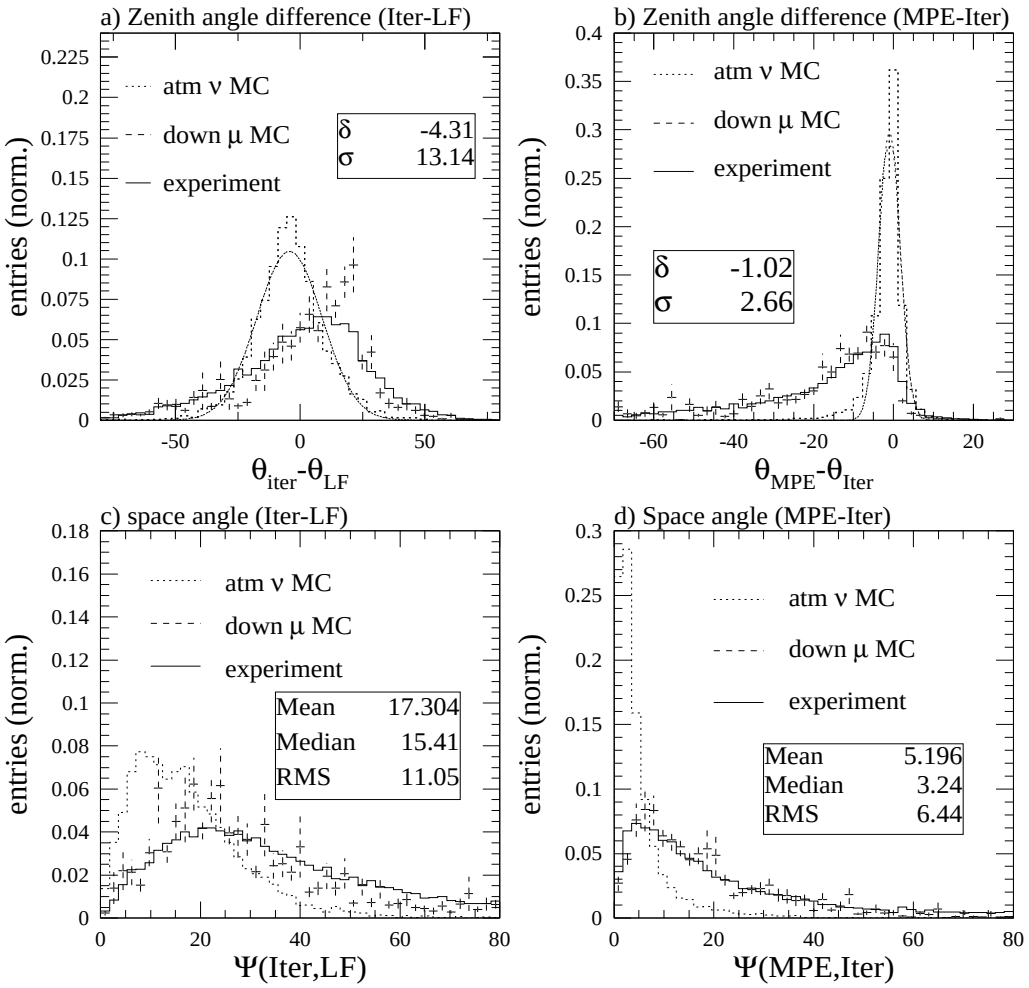

Figure 6.23: Differences of reconstructed directions: Shown are distributions of simulated atmospheric neutrino induced muons, simulated down-going muons from air showers and experimental data. All data was filtered up to level 3 with the relaxed set of "c.o.g."-cuts. The top left plot (a) shows the zenith angle difference between the iterative likelihood reconstruction and the line fit. A Gaussian was fitted to the simulated atmospheric neutrino sample resulting in an offset of 4.3° and a width of about 13°. Figure (b) shows the zenith angle difference between MPE-fit and iterative likelihood fit. A Gaussian was fitted to the atmospheric neutrino MC sample resulting in a mean of $\sim 1°$ and a width of 2.7°. The two bottom plots show the corresponding space angle differences. The mean, median and RMS of the atmospheric neutrino signal simulation are presented.

6.1.3 The Smoothness Parameters

In order to account for the continuous light emission pattern of Cherenkov radiation, a new set of cut parameters has been developed called *smoothness parameters*. The idea is to project onto the reconstructed track the longitudinal lengths between the points of closest approach to a hit OM and compare the cumulative of these pieces to a linear template

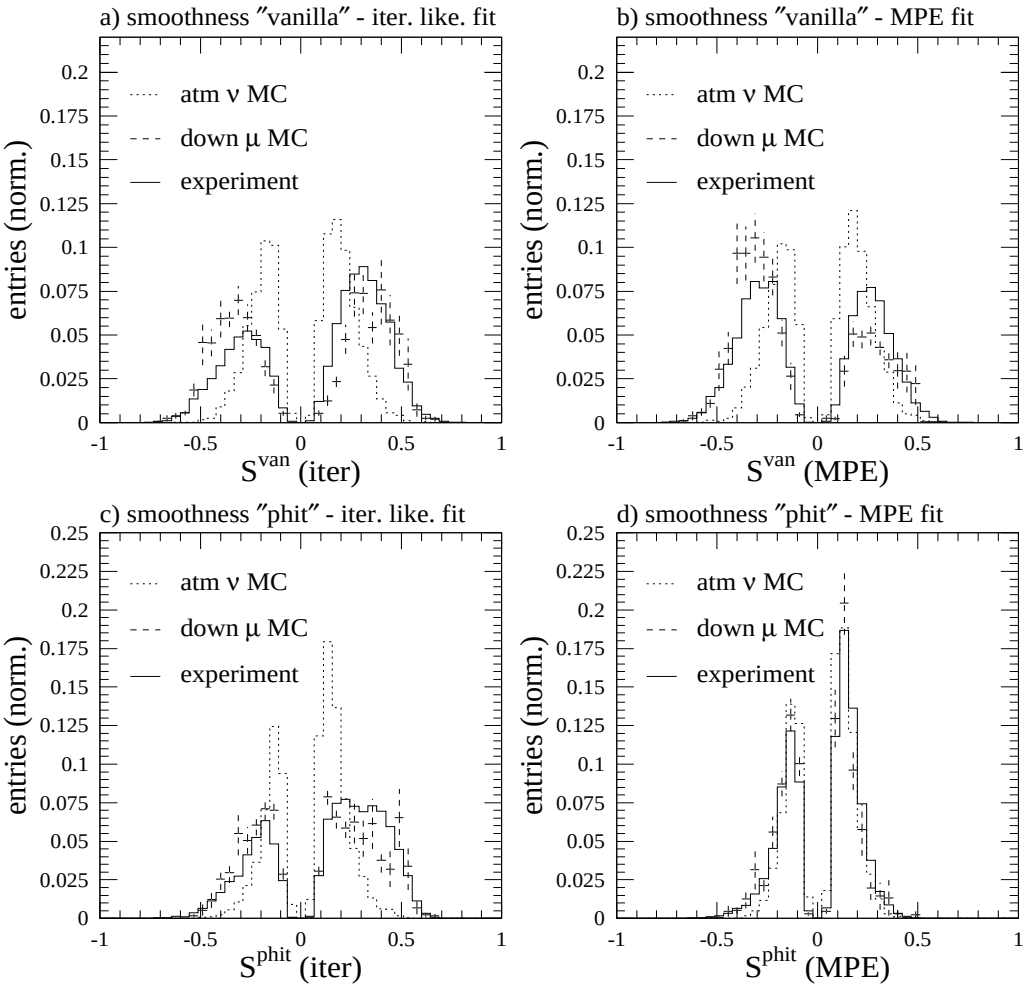

Figure 6.24: The smoothness parameters S^{van} and S^{phit}: Shown are distributions of simulated atmospheric neutrino induced muons, simulated down-going muons from air showers and experimental data. All data was filtered up to level 3 with the relaxed set of "c.o.g."-cuts. The top left plot (a) shows the S^{van} obtained from the iterative likelihood reconstruction track. Figure (b) shows the same parameter obtained from the MPE-fit. The two bottom plots show the smoothness parameter S^{phit}, again for both reconstructions.

of equal step width [104]. Both functions are normalized to one, the number of steps equals the number of hit OMs minus 2. The smoothness parameter S is defined as the maximum deviation of the two functions and can vary between -1 and 1. An hit pattern with longitudinal lengths of absolute equal size would have a $S = 0$. One can compare this approach to a Kolmogorov-Smirnov test for the "smoothness" of light emission. Various "flavors" of smoothness have been developed and described in reference [105]. The above described simplest flavor is called *vanilla smoothness* or S^{van}.

$$S^{van} = sup(S_j^{van}) \quad \text{with} \quad S_j^{van} = \frac{j-1}{N-1} - \frac{l_j}{l_N} \tag{6.37}$$

l_j is the distance between the points of closest approach (on the track) from the first hit OM to the j-th hit OM. N is the number of hits. Figure 6.24a shows the distributions of S^{van} obtained with the iterative likelihood fit. Atmospheric neutrino-induced signal tends to have much smaller smoothness parameters. There is a shift visible between experiment and background simulation. The MC slightly over-predicts negative values of S^{van} whereas it seems to under-predict small positive values. The same distributions obtained with the MPE-fit (figure 6.24b) show a similar behavior.

The presently most useful smoothness flavor is S^{phit} which takes into account the actual location of the OMs. It compares the pattern of hits not to a linear template, but to the actual, normalized hit-probabilities (equation 6.38):

$$S^{Phit} = sup(S_j^{Phit}) \quad \text{with} \quad S_j^{Phit} = \frac{\sum_{i=1}^{j} \Theta_i}{\sum_{i=1}^{N} \Theta_i} - \frac{\sum_{i=1}^{j} P_i^{hit}}{\sum_{i=1}^{N} P_i^{hit}} \tag{6.38}$$

with all channels sorted along the track. $\Theta_i = 1$ if the channel has a hit and 0 if not. ($\sum_{i=1}^{N} \Theta_i$ is thus the number of hit channels). Figures 6.24c and 6.24d show S^{phit} of the iterative likelihood reconstruction and the MPE reconstruction for atmospheric muon background, atmospheric neutrino-induced signal and experiment. Whereas S^{phit} of the iterative likelihood reconstruction shows separation between background and signal, the distributions of S^{phit} obtained from MPE fit agree for all samples. This result is surprising but could be due to fact that the MPE reconstruction makes use of the hit-probabilities. Agreement between background MC prediction and experiment seems better for S^{phit} compared to the parameter S^{van}.

Figures 6.25 show the absolute value $|S^{phit}|$ from different fits versus the reconstructed zenith angles. One can see that the background is accumulated above the separation line which is drawn into the three figures. A large part of the signal appears underneath the line. By choosing an adequate two-dimensional cut (indicated by the angle α) one can separate regions of simulated signal from background. The choice of parameters in the last row may appear less obvious: Because $|S^{phit}|$ of the MPE-fit has no separation power, it is reasonable to take $|S^{phit}|$ of the iterative likelihood fit. What concerns the reconstruction itself however, the MPE-fit gives much better results. A combination of $|S^{phit}|(iter.)$ with the zenith angle of the MPE-fit is a reasonable choice. Analysis B (chapter 9) tested three combinations shown in figure 6.25, the last one turned out to be superior.

6.2 Products of Direct Hits with Lengths of Direct Hits

Chapter 5.4.1 showed that the parameter $L_{direct\ hits}(-15\text{ns}: 75\text{ns})$ is zenith-dependent. A cut on this parameter as function of the reconstructed zenith angle has been applied to the data. Events from horizontal directions cannot have a large length of direct hits due to the detector geometry. There is another possibility to use this parameter: Multiplied with the number of direct hits $N_{direct\ hits}(-15\text{ns}: 75\text{ns})$, it can be used as a quality parameter which does not remove tracks with a relatively small length of direct hits if they have a large number of direct hits. Especially, one thus accepts muon tracks from horizontal directions if they have a large number of direct hits.

Figure 6.26a shows the distributions of $L_{direct\ hits}(-15\text{ns}: 75\text{ns}) \cdot (N_{direct\ hits}(-15\text{ns}: 75\text{ns}) - 2)$ [102]. Subtracting two direct hits comes from the assumption that a number of

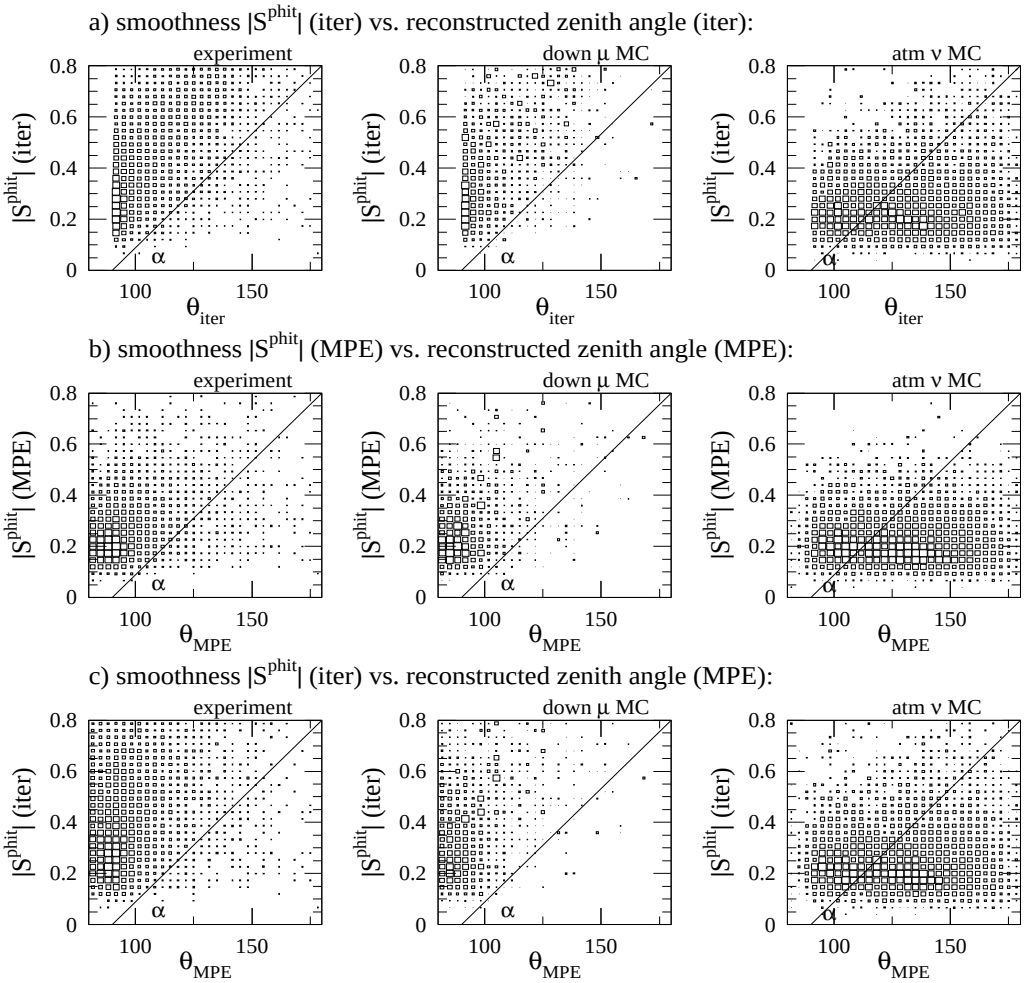

Figure 6.25: The absolute value of the smoothness parameter S^{phit} from different reconstructions versus the reconstructed zenith angles: Shown are distributions of simulated atmospheric neutrino induced muons, simulated down-going muons from air showers and experimental data. All data was filtered up to level 3 with the relaxed set of "c.o.g."-cuts. The three top plots (a) show $|S^{phit}|$ obtained from the iterative likelihood fit versus the reconstructed zenith angle of the same fit. The central figures (b) show $|S^{phit}|$ obtained from the MPE fit versus the reconstructed zenith angle of the same fit. The bottom figures (c) show the combinations of the two parameters with the best rejection behavior, respectively: $|S^{phit}|$ obtained from the iterative likelihood fit versus the reconstructed zenith angle of the MPE fit.

direct hits smaller than two would not define a corresponding length. Analysis B tested both combinations. Separation between signal and background seems reasonable, there however is a shift visible between simulated background and experiment. Figures 6.26b-d show the same parameter for different time residual windows and different reconstructions.

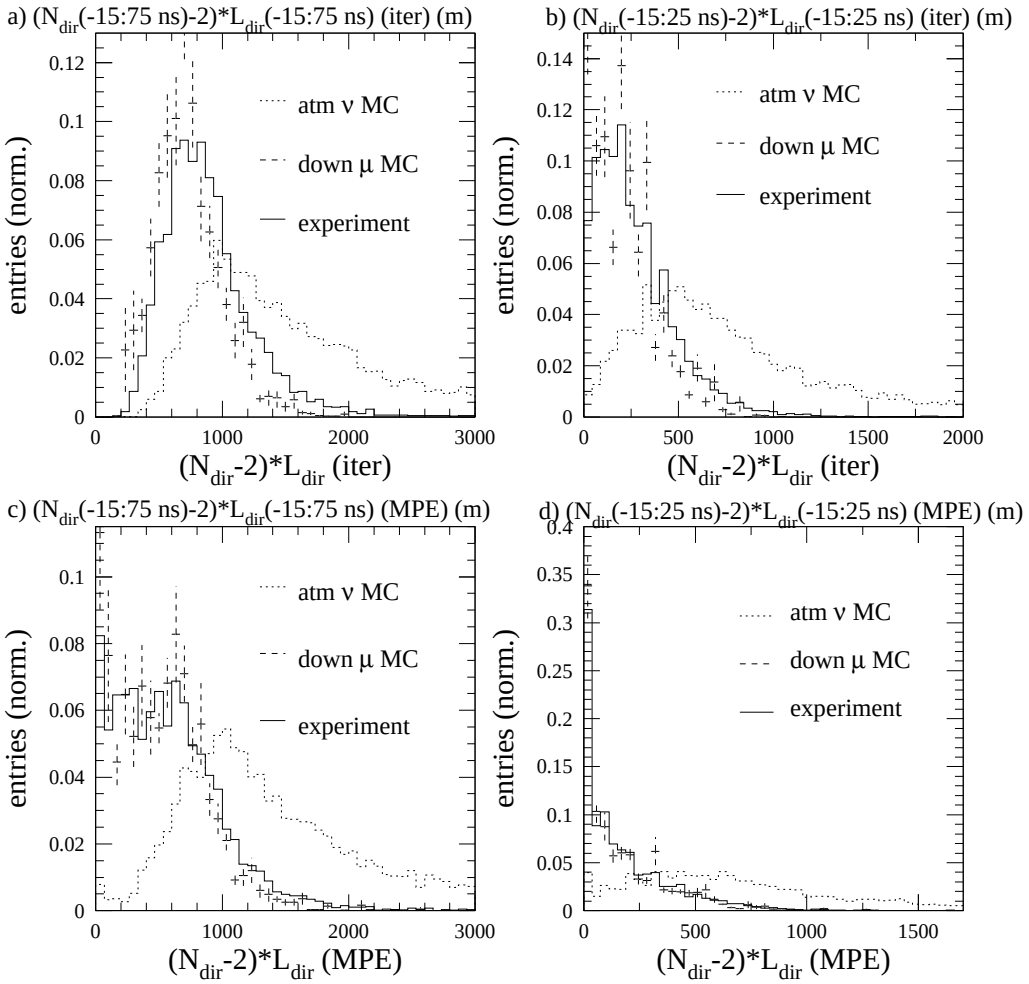

Figure 6.26: The products of $N_{dir} - 2$ with L_{dir}: Shown are distributions of simulated atmospheric neutrino induced muons, simulated down-going muons from air showers and experimental data. All data was filtered up to level 3 with the relaxed set of "c.o.g."-cuts. The top left plot (a) shows the distributions of the parameter $(N_{direct\ hits}(-15\text{ns}: 75\text{ns}) - 2) \cdot L_{direct\ hits}(-15\text{ns}: 75\text{ns})$ obtained from the iterative likelihood fit. The top right plot (b) shows the same parameter for a time residual window of $(-15\text{ns}: 25\text{ns})$. Figures (c) and (d) show the the same variables obtained with the multi-photo-electron reconstruction. The peak at 0 in figure (d) comes from events which have a number of direct hits smaller than two within the time residual window of (15ns:25ns) and thus do not define a length of direct hits.

6.3 The CUTEVAL Method

The CUTEVAL method tries to maximize the signal passing rate while minimizing background contamination *as function of the available cut parameters.* For this reason, a functional is defined:

$$F[S(\vec{x}^{cut}), B(\vec{x}^{cut})] = F(x_1^{cut}, x_2^{cut}, ..., x_i^{cut}, ...x_n^{cut}) \tag{6.39}$$

with $(x_1^{cut}...x_n^{cut})$ a sample of n *cut parameters filtering on the parameter value* x_i^{cut}. S stands for the signal content in analyzed event samples, B for the background content (i.e. everything which is not defined as signal). The functional can be for instance the signal passing rate divided by the background passing rate after cuts: $S(\vec{x}^{cut})/B(\vec{x}^{cut})$. A more general definition of functionals $F[S(\vec{x}^{cut}), B(\vec{x}^{cut})]$ of the form of equation 6.39 can be found in appendix A. $F[S(\vec{x}^{cut}), B(\vec{x}^{cut})]$ is chosen in a way that *maximization of* $F[S(\vec{x}^{cut}), B(\vec{x}^{cut})]$ yields *maximum achievable signal efficiency* for a given set of cut parameters with the largest possible rejection of background. Adequate choices of $F[S(\vec{x}^{cut}), B(\vec{x}^{cut})]$ will be discussed in chapter 6.4.

By comparing $F^{max}[\vec{x}]$ from different sets of cut parameters, we get a handle on the *independence* of cut parameters which is defined as follows:

Def.: A cut parameter (x_{n+1}) is called independent on a set of n existing cut parameters $(x_1, ..., x_n)$, if $F^{max}[(x_1, ..., x_n)]$ *can* be further maximized by adding (x_{n+1}) to $(x_1, ..., x_n)$.

$$F^{max}[(x_1, ..., x_{n+1})] \; > F^{max}[(x_1, ..., x_n)].$$

One can find a *complete sample of independent cut parameters* $(x_1...x_n)^{ind.}$ out of an investigated set of available cut parameters. This means that maximization of $F[(x_1...x_n)]^{ind.}$ yields the highest achievable value of $F[S(\vec{x}^{cut}), B(\vec{x}^{cut})]$ (e.g. the signal/background passing rates) for given signal and background (input) samples. Any further cut parameter cannot improve the signal efficiency, *even if the other parameters are relaxed.* The only way to improve signal efficiency further would be to *invent a new cut parameter* which must then be independent from $(x_1...x_n)^{ind.}$[1].

In order to get a handle on systematic and statistic uncertainties between simulation and experiment, I chose to optimize on different *signal samples*, e.g. taking different signal simulations as well as experimentally available data. This data set is obtained by applying zenith-angle inverted cuts to the experiment and thus filtering on well-reconstructed downward moving muon tracks. Every cut can be applied to this sample as a quality parameter if all zenith angles used by the reconstruction and the filtering procedure are reflected $\theta \rightarrow (180 - \theta)$.

I also took different *background samples*, like simulated atmospheric muons as well as *experimental data* on high filter levels, so that systematic cross-checks between the simulation and the experimental behavior at the highest filter levels are possible. This requires however a different functional $F[S(\vec{x}^{cut}), B(\vec{x}^{cut})]$ and will be explained in chapter 6.4.3.

I will first introduce possible functionals $F[S(\vec{x}^{cut}), B(\vec{x}^{cut})]$ used in the analyzes to follow and explain then the implementation of the maximum finding routines. The actual analyzes will be described in chapters 8 and 9.

6.4 The Functional $F[S(\vec{x}^{cut}), B(\vec{x}^{cut})]$

Usually, an analysis tries to maximize the significance which is the number of signal events passing after cuts, $S(\vec{x}^{cut})$, divided by the square root of remaining background events,

[1] A "new" cut parameter can also be a linear combination of old ones as these are *not* investigated. In that sense, the CUTEVAL method should not be confused with a discriminant analysis which searches the best linear combination of investigated cut parameters applied as one single cut.

$B(\vec{x}^{cut})$:

$$F[S(\vec{x}^{cut}), B(\vec{x}^{cut})] = \frac{S(\vec{x}^{cut})}{\sqrt{B(\vec{x}^{cut})}} \tag{6.40}$$

Application of this method without any modifications however, will only achieve reasonable signal purity if a sufficient statistics of *accurate background simulation* is available. This was not the case during this work for the following reason:

- The experiment needs a rejection factor of more than 10^7, perhaps 10^8 for background. This implies that accurate background simulation would have to agree with experimental data up this level. Chapters 4 and 5 have already shown that the AMANDA simulation has not yet reached a sufficient accuracy. The following results are only valid within these systematic uncertainties.
- Available computer resources limit the amount of simulated background events to less than about one tenth of AMANDA-B10 detector life-time. *We are thus also sensitive to statistical fluctuations within the background simulation data.*

First, I maximized $F[S(\vec{x}^{cut}), B(\vec{x}^{cut})]$ on the available background statistics as if it corresponded to the full detector life time and extrapolate obtained cut values to regions where too little background simulation statistics is available. The whole procedure of cut extrapolation will be explained in chapter 6.4.2.

A second, completely independent method compares different signal samples with experimental data. In chapter 6.4.3, I will show that for background samples containing a small amount of signal, the usual definition of significance is insufficient and has to be replaced by other functionals.

Results obtained by both methods are compared afterwards. Investigations on the relevance of deviations for systematic mis-understanding of data are made.

6.4.1 Signal vs. Background Distributions

Figures 6.27a and 6.27b show a the slope α of $|S^{phit}|$ versus the reconstructed zenith angle. An intersection point at 90° has been chosen. Shown are simulated atmospheric neutrino induced muons and simulated background muons from air showers,

An adequate cut on this variable improves the separation between signal and background. Due to the region of overlap between both distributions, it is not obvious where to place the cut exactly. A possible choice for $F[S(\vec{x}^{cut}), B(\vec{x}^{cut})]$ and pure signal and background distributions is:

$$\begin{aligned} F[S(\vec{x}^{cut}), B(\vec{x}^{cut})] &= \frac{S(x^{cut})}{\sqrt{B(x^{cut})}} \quad \text{for} \quad B(x^{cut}) \geq 1 \\ F[S(\vec{x}^{cut}), B(\vec{x}^{cut})] &= \frac{S(x^{cut})}{\sqrt{0.5}} \quad \text{for} \quad B(x^{cut}) = 0 \end{aligned} \tag{6.41}$$

For event weighted background samples, definition 6.41 can be modified to:

$$F[S(\vec{x}^{cut}), B(\vec{x}^{cut})] = \frac{S(x^{cut})}{\sqrt{B(x^{cut})}} \quad \text{for} \quad B(x^{cut}) \geq \frac{0.5 \cdot \sum_i w_i}{\bar{n}}$$

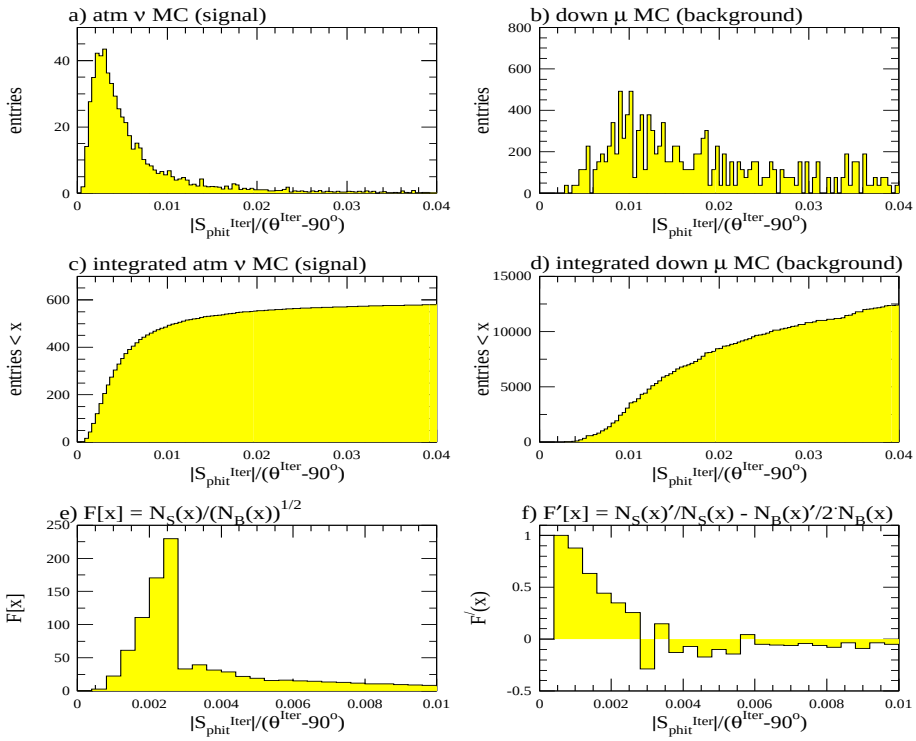

(i) Three years of simulated atmospheric neutrino-induced muons and 10 days of simulated cosmic ray induced muons (bulk ice). All data has previously passed the relaxed filters described in chapter 5. Only data for x values smaller than 0.04 is shown. For reasons of better visibility, figures (e) and (f) show only one forth of the previous parameter space. The whole distribution would extend to infinity.

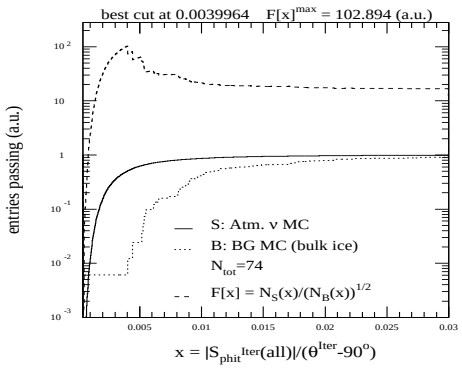

(ii) Background = mass production 1998 (bulk ice). Background has been set to 0.5 where it disappears.

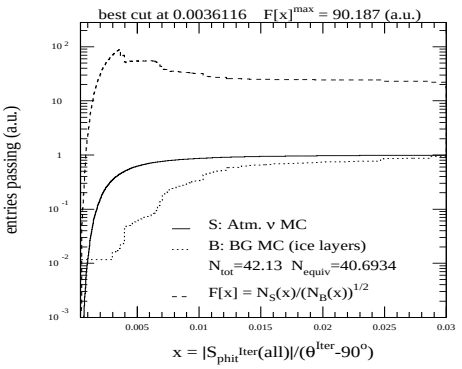

(iii) Background = mass production 2000 (ice layers). Background has been set to 0.52 where the sum weights would yield less.

Figure 6.27: $F[S(x^{cut}), B(x^{cut})] = \frac{S(x^{cut})}{\sqrt{B(x^{cut})}}$: Distributions of the slope of $smoothness^{phit}$ versus the reconstructed zenith angle (minus 90 degrees) (further referred to as x). Figures (i) (a) and (b) show differential distributions for signal and background MC, respectively. The corresponding integral distributions $S(x)$ and $B(x)$ are given in figures (i) (c) and (d). At places where $B(x)$ equals to zero, it has been set to 0.5. Figure (e) shows $F[S(x^{cut}), B(x^{cut})]$ and figure (f) the derivation of $F[S(x^{cut}), B(x^{cut})]$. Figures (ii) and (iii) show $F[S(x^{cut}), B(x^{cut})]$ with a smaller binning and automatic maximum search. $F[S(x^{cut}), B(x^{cut})]$ is represented by the dashed line. Signal and background distributions are shown normalized to one.

$$F[S(\vec{x}^{cut}), B(\vec{x}^{cut})] = \frac{S(x^{cut})}{\sqrt{\frac{0.5 \cdot \sum_i w_i}{\tilde{n}}}} \quad \text{for} \quad B(x^{cut}) < \frac{0.5 \cdot \sum_i w_i}{\tilde{n}} \tag{6.42}$$

with w_i the weight of each event and $\tilde{n}$ the equivalent number of events [106]:

$$\tilde{n} \equiv (\sum_i w_i)^2 / \sum_i w_i^2 \tag{6.43}$$

This means that the number of background events (the sum of weights) will be reduced to the number of events having the same relative statistical error as an unweighted sample of $\tilde{n}$ events[2] Figures 6.27c and 6.27d show the two integrated distributions and 6.27e the first one divided by the square root of the other: $F[x] = \frac{S(\vec{x}^{cut})}{\sqrt{B(\vec{x}^{cut})}}$. There is a clear peak at about 0.003 occurring at the place where the first entry of background appears. This is a specific feature of the insufficient background simulation statistic and has occurred in all following investigated background samples containing unweighted events.

The maximum condition writes as: (see equation B.58)

$$F'(\vec{x}^{cut}) = \frac{dF(\vec{x}^{cut})}{d\vec{x}}|^{best\ cut} = \frac{\frac{dS(\vec{x})}{dx}|^{best\ cut}}{S(\vec{x}^{best\ cut})} - \frac{1}{2}\frac{\frac{dB(x)}{d[\vec{x}}|^{best\ cut}}{B(\vec{x}^{best\ cut})} = 0 \tag{6.44}$$

$$= \frac{S(\vec{x}^{cut+\delta})}{S(\vec{x}^{cut-\delta})} - \sqrt{\frac{B(\vec{x}^{cut+\delta})}{B(\vec{x}^{cut-\delta})}} = 0 \tag{6.45}$$

with δ being the distance by which the background events are separated. There are a few things to say about equation 6.45:

- The mean result does not depend on the normalization nor the number of simulated events for signal, since a common factor in both the derivation of $S(x)$ and the value of $S(x)$ cancel out. However, it does influence the precision of the found solution.
- Stability of the maximum: The ratios in equation 6.45 are always greater or equal one because they contain integral distributions. Figure 6.27f shows the behavior of $F'(\vec{x}^{cut})$. It drops smoothly until it reaches the point where the first entry for background appears. At that point, $F'[\vec{x}]$ crosses the abscissa, as expected, and then grows again to reach zero at multiple intermediate places and at infinity. In more than one cut-parameter dimensions, the "point" where the first entry of background appears, becomes a hyper-plane.
- Samples of low background statistics: $F[S(\vec{x}^{cut}), B(\vec{x}^{cut})]$ will almost always yield a maximum at the place where the first entry of background appears, unless the relative increase of $S(x)$ in the overlap region is higher than the one for $B(x)$. This behavior has not been observed in the maximization procedures described in the following chapters.

[2]Note that this is only true if the relative accuracy of the MC is about the same throughout the whole parameter space under consideration. This is definitely not the case for the weighted atmospheric muons simulation used in this analysis which was sampled (and reconstructed) with higher accuracy around the horizon than for vertical tracks. Most of the used cuts however have sensitivities very much dependent on the zenith angle. The above choice reflects more a reasonable a priori choice justified by the stability and consistency of the results than a correct statistical treatment.

- Wrong global maximum: In multi-dimensional cut-parameter space, a wrong global maximum can be obtained if fluctuations of the signal distribution generate local maxima in the hyper-plane where background appears. This scenario becomes more probable as one proceeds to higher dimensions and less probable with higher statistics of signal events. Therefore, this analysis chose that much signal simulation as was possible to process with the available computer resources. Additionally, several consistency-checks were performed.

6.4.2 Cut Extrapolation

Equations 6.41 and 6.42 contain an offset constant (0.5 events for the unweighted background samples and $0.5 \cdot \frac{\tilde{n}}{\sum w_i}$ for the weighted samples) which is arbitrary because it depends on the amount of simulated statistics. If one assumes that background falls off exponentially in its tails. For cut parameters (or sets of cut parameters) which separate signal from background well, one can try to get *hints* for the behavior of background in neighboring regions.

Equation 6.45 and the discussion thereafter showed that $F[S(\vec{x}^{cut}), B(\vec{x}^{cut})] = \frac{S(\vec{x}^{cut})}{\sqrt{B(\vec{x}^{cut})}}$ applied on background samples with much less statistics as the signal sample, will find a set of cut parameters which maximize signal passing rate while reducing the entire background *down to the chosen offset*. The last can be used to *parameterize* the maximum achievable signal passing rate by the number of retained background events as function of a set of cut parameters

$$F[\vec{x}^{cut}, \text{offset}]^{max} = \frac{S(\vec{x}^{cut})^{max}}{\sqrt{\text{offset}(\vec{x}^{cut})}} \tag{6.46}$$

The dependence of the offset on $\vec{x}^{cut}$ comes from the fact that any combination of background events may sum up the offset, depending on the chosen cut values.

Figure 6.28 illustrates the cut extrapolation procedure. First, one plots the obtained cut values as function of the logarithm of the chosen offset. In the case of only one cut parameter (1-dimensional cut parameter space), this is equivalent to plotting the cut value as function of the logarithm of the integrated background distribution. With more cut parameter dimensions, $F[\vec{x}^{cut}, offset]^{max}$ will yield a *path through the cut parameter space* parameterized by the different offset values. One has to plot the projections of that path onto every single parameter. The obtained cut parameter values can then be parameterized typically by an exponential. The correlation can be obtained between the expected number of background events and a proposed set of cut parameter values needed to reject it.

I want to stress however, that an exponential fall-off is a an assumption which by no means is bound to have anything to do with reality.

. One has not simulated in that region, therefore one does not know if the background changes behavior with respect to the background simulation. Furthermore, cut parameters have been fitted in a region of background simulation which is limited by systematic uncertainties. It can easily be that the found path through the parameter space is wrong, even where background simulation is still available.

However, if one compares the results to those obtained with experimental data alone,

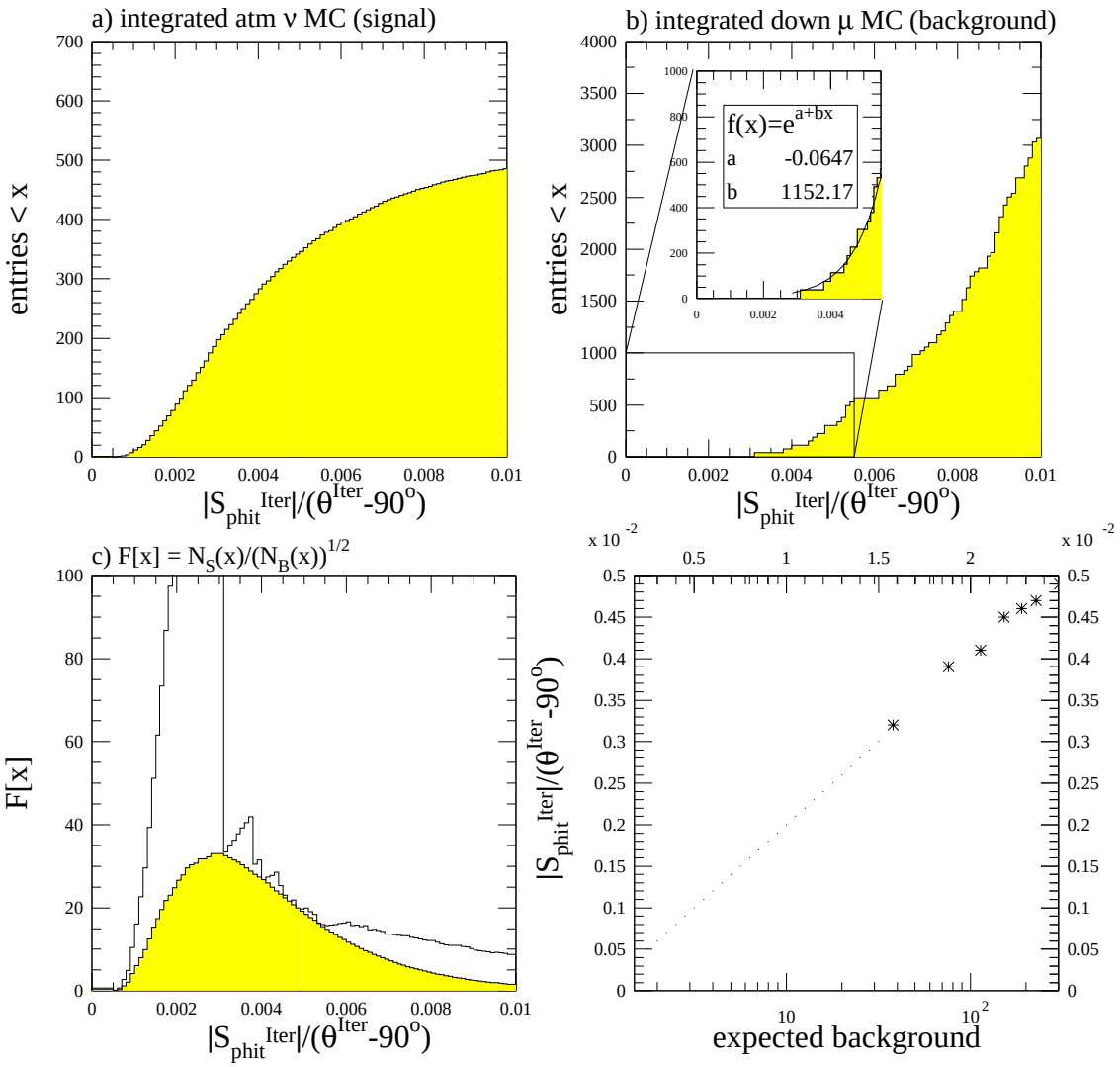

Figure 6.28: Extrapolation of cuts using $F[S(x^{cut}), B(x^{cut})] = \frac{S(x^{cut})}{\sqrt{B(x^{cut})}}$: Distributions of the slope of $smoothness^{phit}$ versus the reconstructed zenith angle (minus 90 degrees) (further referred to as x). Figures (a) and (b) show integral distributions for three years of simulated atmospheric neutrino-induced muons and 10 days of simulated cosmic ray induced muons, respectively. The last part of the spectrum is fitted by an exponential. Figure (d) shows the same data (stars) with inverted axes and logarithmic coordinates. The line shows the fit result from figure (b), identically they can be obtained by a straight line fit to the stars. Figure (c) shows the behavior of $F[S(x^{cut}), B(x^{cut})] = \frac{S(x^{cut})}{\sqrt{B(x^{cut})}}$ (white histogram, see also figure 6.4.1e and the one obtained by replacing the background distribution by the fitted exponential (dashed histogram).

or other simulated background, one can study the systematic behavior of cut parameters. Furthermore, in case of strong disagreement between both methods, unsimulated background has been found and can be further investigated.

6.4.3 Signal vs. (Background+Signal) Distributions

For the above reasons, it is desirable not to rely on the (unprecise) background simulation alone, but to incorporate experimental data into the investigations. The experimental data sample at low cut levels (E) is dominated by mis-reconstructed fake events (background=B) and a small part of atmospheric neutrino-induced muons (signal=S). This background-dominated sample would define $F[S(\vec{x}^{cut}), B(\vec{x}^{cut})] = S(\vec{x})/\sqrt{E(\vec{x})}$ $= S(\vec{x})/\sqrt{(B+S)(\vec{x})}$. Optimizing on $F[S(\vec{x}^{cut}), E(\vec{x}^{cut})]$ would mean to try cut out the background as well as the signal with the result the maximum is located in the background-contaminated region. Too weak cut values would be found. The maximum condition writes as (see equation C.63):

$$\begin{aligned} S'(\vec{x})|^{cut} &- B'(\vec{x})|^{cut} \cdot \frac{1-\epsilon}{1+\epsilon} = 0 \\ \epsilon &= \frac{B(\vec{x}^{cut})}{S(\vec{x}^{cut})} \end{aligned} \tag{6.47}$$

ϵ is small for cut parameters which show a good separation between the signal and the background. The maximum would be found at a place where the number of entries of background in the differential distribution is a bit higher than that for signal. This is not compatible with the demand of a high signal purity and therefore unacceptable.

The analysis A (see chapter 8) optimized on the difference between signal and experiment:

$$F[S(\vec{x}^{cut}), B(\vec{x}^{cut})] = \alpha \cdot S(x) - (B+S)(\vec{x}) \tag{6.48}$$

with α being the number of events in the signal sample divided by the number of signal events in the experimental sample (which is unknown a priori). Equation C.65 gives the maximum condition:

$$(\alpha - 1)\frac{dS(\vec{x})}{dx}|^{cut} = \frac{dB(\vec{x})}{dx}|^{cut} \tag{6.49}$$

A normalization constant of $\alpha \to 1$ is preferable in order to get all background rejected.

Figures 6.29a and 6.29b show the distributions of experimental data reconstructed as downward moving (down-going muons), filtered with the relaxed set of cuts described in chapter 5, but zenith-angle inverted cut parameters. This means that muons (or muon bundles) of high reconstruction quality have been obtained. Shown is again the slope of S^{phit} divided by the reconstructed zenith angle (or the inverted reconstructed zenith angle, correspondingly). An intersection point at 90° has been chosen. The distributions agree well with 6.27a and 6.27b except for the tail of the signal distribution. The difference comes from the non-isotropic zenith-angle spectrum of down-going muons produced in air showers. Figures 6.29c and 6.29d show the integrated distributions and figure 6.29e $F[S(\vec{x}^{cut}), B(\vec{x}^{cut})]$ defined as eq. 6.48. There is a clear peak visible, but at a smaller value than expected from the background simulation (figure 6.27e). This tighter cut is expected because the experiment contains more background than was ever simulated.

The functional $F[S(\vec{x}^{cut}), B(\vec{x}^{cut})] = \alpha \cdot S(x) - (B+S)(\vec{x})$ has been used in the first analysis which will be described in chapter 8. For values of $\alpha \gtrapprox 1.5$, stable results could be reached, albeit obtaining too weak cut values. It is not possible to decrease it further

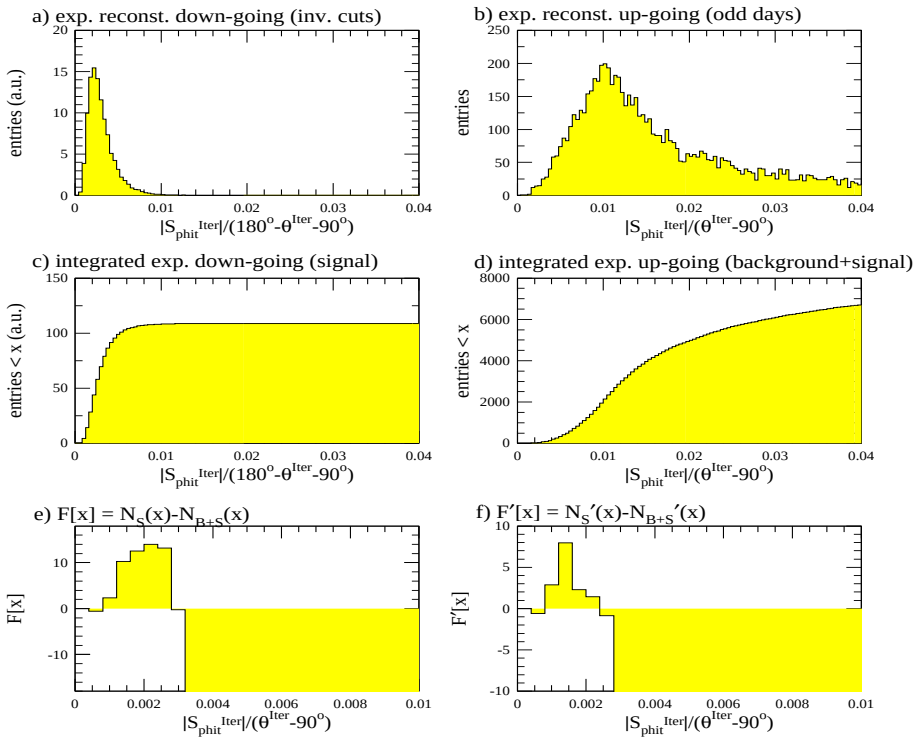

(i) 3 minutes of experimental cosmic ray induced muons (normalized to about 200 events) and 65 days of triggered muons reconstructed as upward moving. Data labeled as up-going has previously passed the relaxed filters described in chapter 5, data labeled as down-going has passed the corresponding filters with inverted zenith angles ($\theta \rightarrow 180^\circ - \theta$).

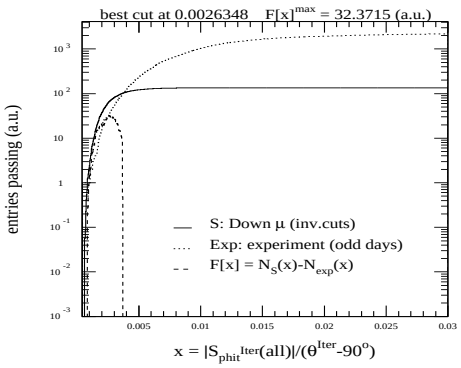

(ii) Signal = experimental data reconstructed as downward moving.

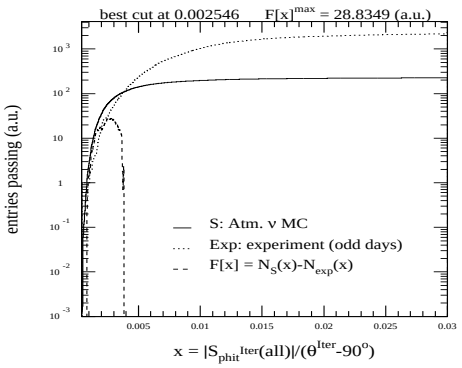

(iii) Signal = simulated atmospheric neutrino induced muons, mass production 2000 (ice layers).

Figure 6.29: $F[S(x^{cut}), B(x^{cut})] = \alpha S(x^{cut}) - (S+B)(x^{cut})$: Distributions of the slope of S^{phit} divided by the reconstructed zenith angle (minus 90 degrees) or the reflected zenith angle ($\theta \rightarrow 180^\circ - \theta$) (further referred to as x). Figures (a) and (b) show differential distributions for signal and experiment. The corresponding integral distributions are given in figures (c) and (d). Figure (e) shows $F[S(x^{cut}), B(x^{cut})]$ and figure (f) the derivation of $F[S(x^{cut}), B(x^{cut})]$.

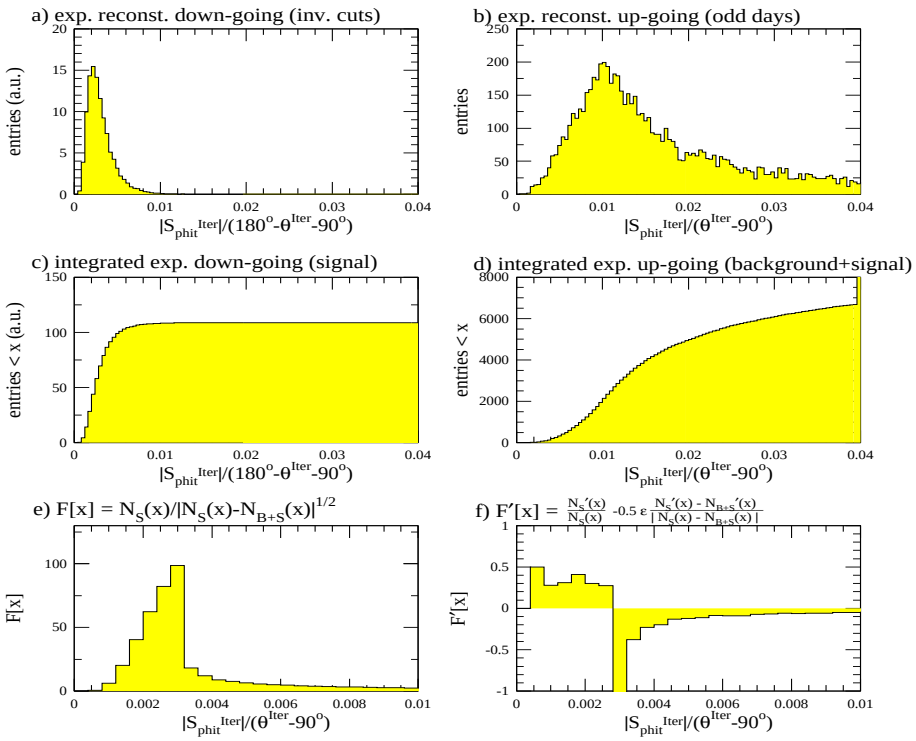

(i) 3 minutes of cosmic ray induced muon signatures obtained experimentally (normalized to about 200 entries) and 65 days of triggered muons reconstructed as upward moving. Data labeled as up-going has previously passed the relaxed filters described in chapter 5, data labeled as down-going has passed the corresponding filters with inverted zenith angles ($\theta \rightarrow 180^\circ - \theta$). Only data for x values smaller than 0.04 is shown.

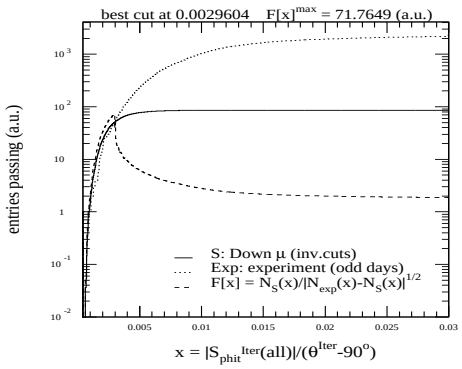

(ii) Signal = experimental data reconstructed as downward moving.

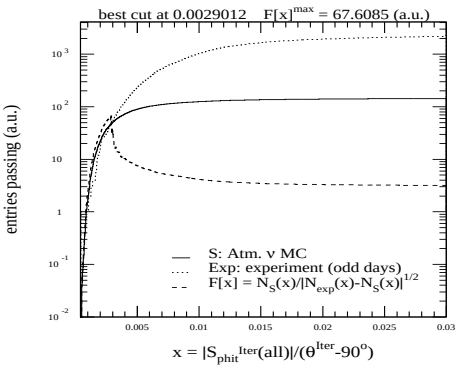

(iii) Signal = simulated atmospheric neutrino induced muons, mass production 2000 (ice layers).

Figure 6.30: $F[S(x^{cut}), B(x^{cut})] = \alpha S(x^{cut})/|\alpha S(x^{cut}) - (S(x^{cut}) + B(x^{cut}))|^{\frac{1}{2}}$: Distributions of the slope of S^{phit} versus the reconstructed zenith angle (minus 90 degrees) or the reflected zenith angle ($\theta \rightarrow 180^\circ - \theta$) (further referred to as x). Figures (a) and (b) show differential distributions for signal and experiment, respectively. The corresponding integral distributions are given in figures (c) and (d). Figure (e) shows $F[S(x^{cut}), B(x^{cut})]$ and figure (f) the derivation of $F[S(x^{cut}), B(x^{cut})]$.

due to statistical fluctuations which start to influence the results. It would be desirable to have a functional with a maximum condition of the form 6.45.

in chapter 9, the following functional has been taken:

$$F[S(\vec{x}^{cut}), B(\vec{x}^{cut})] = \frac{\alpha \cdot S(x^{cut})}{\sqrt{|(B+S)(x^{cut}) - \alpha S(x^{cut})|}} \quad \text{if} \quad |(B+S)(x^{cut}) - \alpha S(x^{cut})| \geq 1$$
$$F[S(\vec{x}^{cut}), B(\vec{x}^{cut})] = \frac{\alpha \cdot S(x^{cut})}{\sqrt{0.5}} \quad \text{if} \quad |(B+S)(x^{cut}) - \alpha S(x^{cut})| < 1 \tag{6.50}$$

This functional behaves relatively stable around $\alpha \approx 1$, compared to eq. 6.48 (see eq. C.72) and yields the required form of equation 6.45 for $\alpha = 1$. Figures 6.30 show the behavior of $F[S(x^{cut}), B(x^{cut})]$. There is a clear maximum found at cut value weaker than the one obtained with the functional 6.48, but still much stronger than the one from the background sample alone.

The exact value of the flux normalization is not known (see chapter 2.3). It is however desirable to work at exactly $\alpha = 1$ or at least at $\alpha \lessapprox 1$. Figure 6.31 illustrates this.

A relative normalization constant which over-predicts the atmopheric neutrino rate is expected to yield too weak cut values (figure 6.31a). Background would still be leaking into the signal sample. When choosing α too low (figure 6.31d), strong cut values will be obtained which remove also parts of the signal regions. There is an intermediate part around $\alpha \approx 1$ (figure 6.31c) which is dominated by statistical fluctuations especially in the experimental data sample[3] (if the signal is simulated with much higher statistical accuracy). A normalization constant slightly smaller than 1 would be optimal. In chapter 9, I will show how a correct α can be obtained experimentally.

[3]These fluctuations become more pronounced in multi-dimensional cut-parameter space.

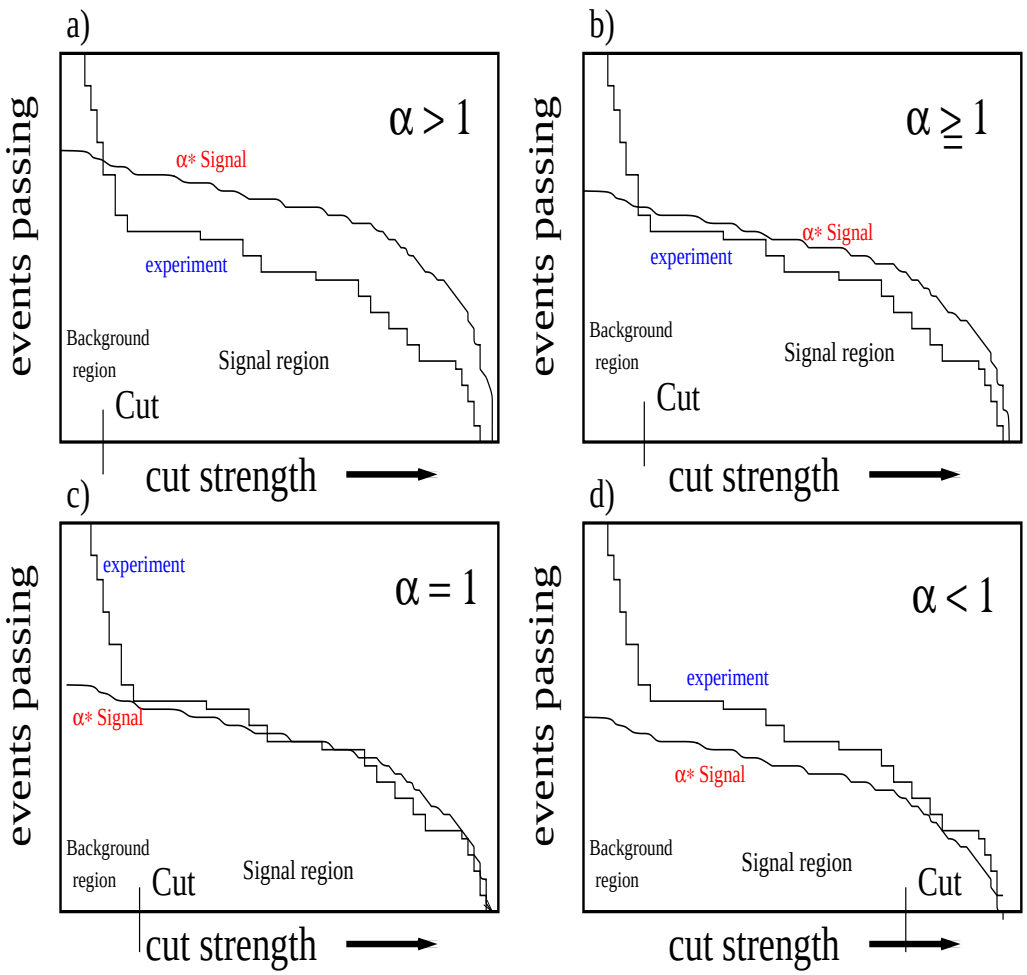

Figure 6.31: $F[S(x^{cut}), B(x^{cut})] = \frac{\alpha S(x^{cut})}{|\alpha S(x^{cut}) - (S+B)(x^{cut})|^{\frac{1}{2}}}$: Variation of the normalization constant α. The pictures show a hypothetical cut parameter. Two integral distributions are drawn: A signal simulation and experimental data containing signal and background. If the simulation over-predicts the flux (picture (a)), $F[S(x^{cut}), B(x^{cut})]$ will become maximal at the crossing point between the two distributions. A too weak cut value will be obtained. As α approaches one (pictures (b) and (c)), fluctuations will dominate the place where $F[S(x^{cut}), B(x^{cut})]$ becomes maximal. This is especially true for multidimensional cut-parameter spaces. If the simulation under-predicts the flux (picture (d)), too strong cut parameters are found.

7 Computing $F^{max}[S(\vec{x}^{cut}), B(\vec{x}^{cut})]$

7.1 The Downhill-Simplex Algorithm with Simulated Annealing

The implemented maximum-finding algorithm was taken from reference [107] and is described in more detail in [109]. It used the Downhill Simplex method[1] which gradually moves up the "hill" of a multidimensional function and converges at the top. A short description of the algorithm can be found in appendix D.

A first try was undertaken in 2-dimensional parameter space using the parameters $|S^{phit}|$ and L_{dir}(-15ns:75ns)^{Iter}. Among 70 tries with random initialization, only 3 converged at the global maximum. Apparently, the parameter "landscape" was too rough. The simplex stopped at local maxima and could not find the global one.

In this case, reference [107] proposes an extension of the downhill simplex method using "simulated annealing". The idea is the following:

Replace $F(x_i)$ by $(F(x_i) - T * ln([0,1]))$ and decrease T slowly during execution of the downhill simplex algorithm.

[0,1] is a random number between 0 and 1 and T stands for a "temperature". For $T \to 0$, the algorithm converges against the previously defined downhill simplex method. In the limit $T \to \infty$, $F(\vec{x})$ will fluctuate completely randomly and for a finite T, fluctuations are weighted with a Boltzmann factor $e^{-\frac{1}{T}}$. The idea has been taken from nature: When temperature is decreased very slowly at the phase transition between liquid and solid state, the Boltzmann weighted energy distribution of molecules will even out local solidifications. At the end, the whole macroscopic body will turn into the state of *global* energy minimum, the crystal.

Ref. [107] suggests to parameterize the temperature decrease as:

$$T = T_0(1 - \frac{k}{K})^{\alpha} \tag{7.51}$$

T_0 is a start temperature, k is a counting index that ranges from 0 to K and gets increased by one every time the downhill simplex algorithm evaluates the functional $F[S(\vec{x}^{cut}), B(\vec{x}^{cut})]$. K gives the total number of iterations and is limited by the available CPU-time. The parameter α tells how fast temperature decreases, high α corresponds to fast decrease at the beginning and slow one at the end of the optimization procedure.

7.2 Adjusting Parameters

Sensitive parameters are T_0 and K. α, in contrary, seems to give no visible effect. I tried $\alpha's$ 1,2 and 4, but could not find any difference. I chose $\alpha = 1$[2].

Three different initializations were tested, one random initialization, one initializing at the corners of the parameter box which contains the strong cuts and a third one initializing

[1] The actual algorithm is a minimum finding routine, therefore the name "Downhill Simplex". In our case however, it is used to find the maximum of a function, (as an "Uphill Simplex" method).

[2] Experience showed that once a simplex resides on the right "mountain", it will easily find the correct maximum. The aim is thus to avoid smaller hills at the beginning. Thus, a slower decrease of temperature at the beginning is justified.

at the weak corners. The last on corresponds to the initialization proposed by ref. [107] and yielded the most stable results. It can be written as:

$$\begin{aligned} \vec{x}_0 &= \vec{x}^{\,weak\ borders} \\ \vec{x}_i^{\,start} &= \vec{x}_0 + \vec{e}_i(border_i^{strong} - border_i^{weak}) \end{aligned} \tag{7.52}$$

with $i = 1 \ldots n$

In order to test T_0 and K, a grid search was performed for every cut parameter dimension from 2 to 5. The grid search used the following cut parameters:

1. $S^{phit}/(\theta^{iter} - 95^\circ)$
2. $\frac{L_{up}}{L_{down}}$
3. $\Delta_\theta(LF, Iter) = |\theta_{LF} - \theta_{iter} + 6^\circ|$
4. $|S^{phit}|$
5. $\mathrm{N}_{direct\ hits}$(-15ns:75ns)·$\mathrm{L}_{direct\ hits}$(-15ns:75ns)

Cuts 1-4 constitute the complete sample of independent cut parameters obtained in the first analysis (chapter 8). Cut parameter 5 is thus redundant. For signal, three years of simulated atmospheric neutrino-induced events (bulk ice) were taken. This sample showed a mean of 6° for the difference of zenith angles. The background sample contained 82 events of atmospheric muons (bulk ice simulation) which had passed the tight set of cuts introduced in chapter 5 and chapter 8. Signal contained 2698 events, thus the maximum possible value for $F[S(\vec{x}^{cut}), B(\vec{x}^{cut})]^{max}$ is ≈ 3815 (equation 6.41).

T_0 varied between 5° to 50° in steps of 5° for dimensions 2 and 3, between 5° and 200° for dimensions 4 and 5. A total number of iterations from 10^3 to 10^4 was investigated with equal step size in the logarithm.

A first try gave very poor results with only about 10% of the tries finding the global maximum. A closer investigation revealed that the borders (appendix D item 1.) have been set too loose. Cuts had fluctuated at planes of equal $F[S(\vec{x}^{cut}), B(\vec{x}^{cut})]^{max}$ after initialization. After tightening of the borders, all 99 tries found the global maximum at $F[S(\vec{x}^{cut}), B(\vec{x}^{cut})]^{max}$=3504. The same result was obtained in the 3-dimensional search. Only at four dimensions, significant differences have been found, illustrated in figure 7.32.

Appendix E (equation E.79) gives an guideline found analytically for a possible choice of the four parameters T_0, K, α and the number of dimensions n. Based on the experience gained from the grid search, temperature and total number of iterations were chosen in the following way:

$$\begin{aligned} T_0 &= \frac{N_{signal}}{\mathrm{offset}^{\frac{1}{2}} \cdot 150} \quad \text{for} \quad F[S(\vec{x}^{cut}), B(\vec{x}^{cut})] = \frac{S(\vec{x})}{B(\vec{x})^{\frac{1}{2}}} \\ T_0 &= \frac{N_{signal} \cdot 0.9}{150} \quad \text{for} \quad F[S(\vec{x}^{cut}), B(\vec{x}^{cut})] = (\alpha S(\vec{x}) - (B+S)(\vec{x})) \\ T_0 &= \frac{N_{signal}}{100} \quad \text{for} \quad F[S(\vec{x}^{cut}), B(\vec{x}^{cut})] = \frac{S(\vec{x})}{|\alpha S(\vec{x}) - (B+S)(\vec{x})|^{\frac{1}{2}}} \\ N_{iteration} &= 550(n+1) \cdot e^{(n+1)\cdot 0.15} \end{aligned} \tag{7.53}$$

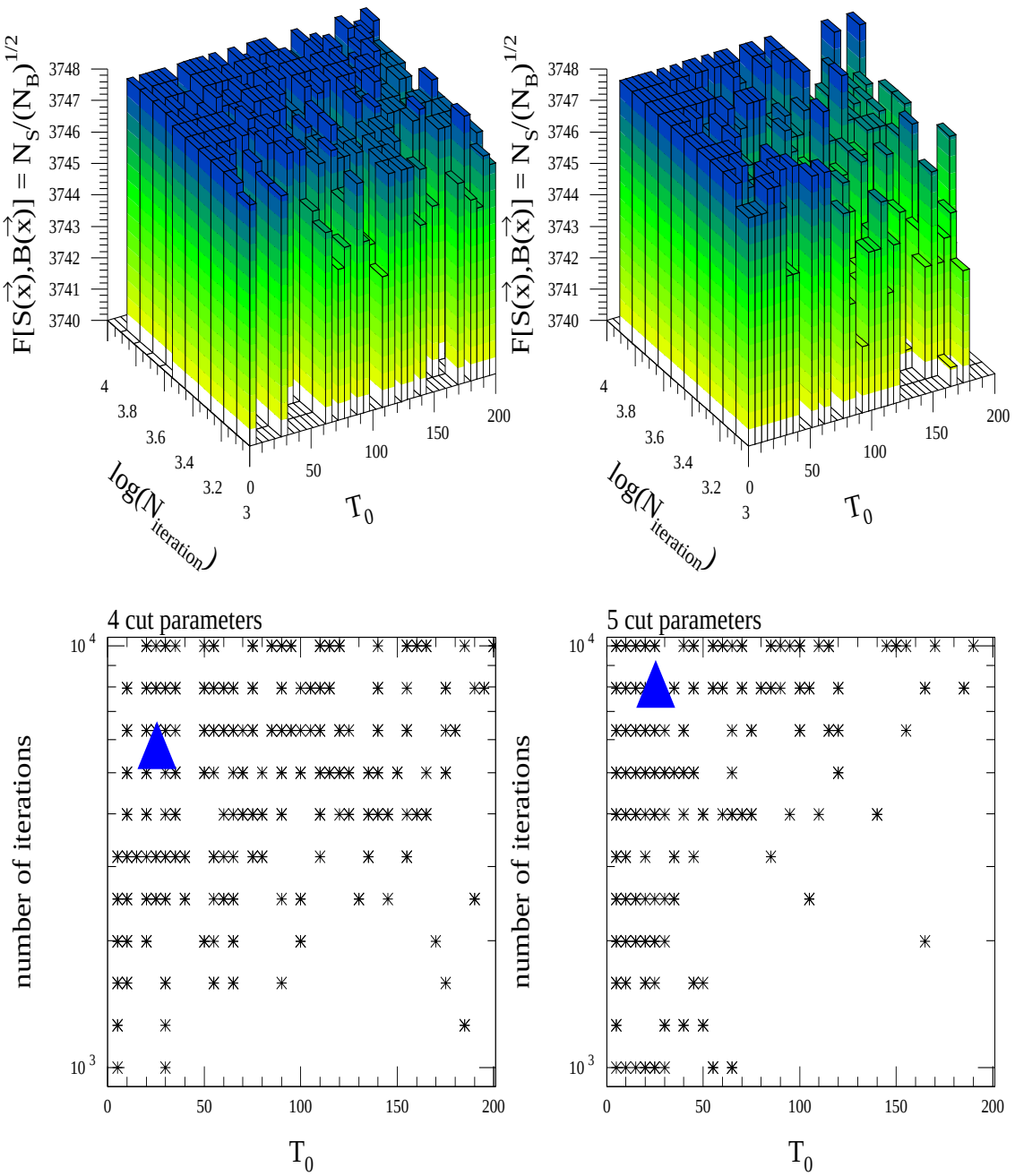

Figure 7.32: Results of the grid search. On the left side, results of the 4-dimensional maximum search are shown, on the right side the 5-dimensional search. The two bottom plots show only combinations which found the global maximum. The triangles indicate the parameter set chosen. Note that entries of a same temperature are correlated because the same initialization for the random number generator has been used for all combinations.

This choice is also influenced by experience gained through variation of the parameters and available CPU-time. The triangles in figure 7.32 mark the corresponding values. Appendix F gives additional results obtained with the 5-dimensional grid search.

A better grid search is certainly desirable. Samples using other functionals need to be cross-checked for right choice of the parameters. This task is very CPU-consuming and could not be performed during this analysis. Instead, I referred to consistency-checks between results obtained in different parameter dimensions. I assume that a good choice of borders is more efficient than variation of temperature and number of iterations. Note that an almost 100% efficiency of the maximum finding procedure (as obtained with dimensions two and three) is only feasible with a much higher number of iterations. This was (yet) not obtainable with available CPU-resources.

8 Results - Analysis A

A first analysis was performed with data filtered with the whole level 1-3 filter-chain plus the tight "c.o.g."-cuts (sample A) described in chapter 5. The following filters had been applied additionally to the data[1]:

1. $N_{hit\ OMs} > 15$
2. $N^{iter}_{direct\ hits}$(-15ns:75ns) > 6
3. $L^{iter}_{direct\ hits}$(-15ns:25ns) > 60m
4. $L^{iter}_{direct\ hits}$(-15ns:75ns) > 80m
5. $L^{iter}_{direct\ hits}(-1)$(-15ns:25ns) > 50m
6. $L_{iter,M=16} < 8.5$
7. $\frac{L_{up}}{L_{down}}(iter) \leq 0.97$

Cut parameter 5 has not been introduced yet: It calculates the geometric distance between the two out-most lying direct hits neglecting the one with the greatest distance to the rest (in order not to get faked by noise hits).

Because background from horizontal directions or with a center of gravity of hits at the higher or lower edge of the detector seemed not separable from signal with the above set of cuts, I added two more selection criteria:

8. $\theta^{iter} > 105^\circ$
9. -70 m$< c.o.g._z <$ 150 m

These cuts lead to the following data samples:

- 2698 with *nu2mu* simulated atmospheric neutrino-induced muon events corresponding to 3 years of detector life time.
- 2484 muons of 1 TeV energy, simulated isotropically over the lower hemisphere. This corresponds to 15.5% of the generated triggers.
- 18 events of atmospheric muon background MC out of 10 days of simulated detector life time (entire background simulation produced during the mass production 1998).
- 406 experimental data events registered on odd numbered days. This corresponds to half the entire data sample ($\sim$ 65 days life time).
- 1631 triggers from experiment, reconstructed as down-going and having passed all corresponding zenith-angle inverted filters. The number corresponds to about 75 seconds life time.

[1]The entire set of filters make up the data sample called "level 3 final", described in [80].

The three MC samples were simulated with homogeneous ice properties (mass production 1998). These samples were compared in five independent optimization modes (see table 8.2):

- Two MC vs. MC optimization modes, taking the 18 remaining simulated fake events as background $B(\vec{x}^{cut})$ and either the atmospheric neutrino simulation or 1 TeV isotropic muons as signal $S(\vec{x}^{cut})$. The functional $F[S(\vec{x}^{cut}), B(\vec{x}^{cut})]$ as defined in 6.41 was maximized.

- Two further modes used the 406 events from experiment as "background plus signal" and either the simulated 1 TeV isotropic muons or the 1631 down-going muons from experiment as signal. The functional $F[S(\vec{x}^{cut}), (B+S)(\vec{x}^{cut})]$ as defined in 6.48 was maximized. For the down-going muon sample, all investigated cut parameters were zenith-angle inverted, except for the parameter L_{down} which was not implemented at that time. Therefore the down-going muon sample could not be used to study this parameter.

- A fifth sample comparing simulated atmospheric neutrino-induced muons with experimental data was used to investigate some systematic behavior of the optimization functional. This combination was not used during the search for linear independent cut parameters.

Opt. mode	Signal	Background	$F[S(\vec{x}^{cut}), B(\vec{x}^{cut})]$
atm. ν % BG MC	atm. ν simulation	background MC	$S(\vec{x}^{cut})/\sqrt{B(\vec{x}^{cut})}$
1 TeV μ % BG MC	1 TeV isotr. muon MC	background MC	$S(\vec{x}^{cut})/\sqrt{B(\vec{x}^{cut})}$
1 TeV μ % exp.	1 TeV isotr. muon MC	experiment	$S(\vec{x}^{cut}) - (B+S)(\vec{x}^{cut})$
exp.(inv.cuts)% exp.	(exp., inv. cuts)	experiment	$S(\vec{x}^{cut}) - (B+S)(\vec{x}^{cut})$
atm. ν % exp.	atm. ν simulation	experiment	$S(\vec{x}^{cut}) - (B+S)(\vec{x}^{cut})$

Table 8.2: Optimization modes

Table 8.3 shows the tested cut parameters. The first column gives the name of the parameter, the second the cut value already applied to the data during previous filtering and the third column shows the range within which the parameter was allowed vary (if used as a cut).

8.1 Pre-Study

First, $F[S(\vec{x}^{cut}), B(\vec{x}^{cut})]$ was maximized for the parameter $|S^{phit}|/(\theta_{iter} - \Delta)$ with four different intersection points Δ. Figure 8.33a shows the corresponding distributions. The results are shown in table 8.4. The two samples optimizing on background MC show a maximum signal passing rate for an intersection point of 95°, whereas the optimization modes using experimental data prefer 90°. The obtained results appear independent from the taken signal sample.

Cut parameter name	previous filters	allowed range of variation
$N^{iter}_{direct\ hits}$(-15ns:25ns)	$\geq$4	$4-10$
$N^{iter}_{direct\ hits}$(-15ns:75ns)	$\geq$7	$7-20$
$L^{iter}_{direct\ hits}$(-15ns:25ns)	$>$60m	60m $-$150m
$L^{iter}_{direct\ hits}$(-15ns:75ns)	$>$80m	80m $-$180m
$L^{iter}_{direct\ hits}(-1)$(-15ns:25ns)	$>$50m	50m $-$150m
L^{iter}	$<$8.5	$7.0-8.5$
L^{phit}	$<$6.0	$3.0-6.0$
$L^{iter}_{up}/L^{iter}_{down}$	≤ 0.97	$0.9-0.97$
L^{shower}/L^{iter}	≥ 0.95	$0.95-1.1$
$N^{iter}_{direct\ hits}$(-15ns:75ns) - $N^{shower}_{direct\ hits}$(-15ns:75ns)	≥ 0	$0-10$
$\lvert\vec{v}_{LF}\rvert$	$>$0.1m/ns	$0.1-0.19$
L^{iter}_{up}-L^{iter}_{down}	not used	$(-18.0)-(-3.0)$
L^{shower}-L^{iter}	not used	$(-5.0)-1.5$
$\lvert\theta_{iter}-\theta_{LF}+6^\circ)\rvert$	not used	$5^\circ-70^\circ$
$\lvert S^{phit}\rvert$	not used	$0.15-0.6$
$\lvert S^{van}\rvert$	not used	$0.15-0.6$
$\lvert S^{phit}\rvert/(\theta_{iter}-105^\circ)$	not used	$0.0004-0.03$
$\lvert S^{phit}\rvert/(\theta_{iter}-100^\circ)$	not used	$0.0004-0.03$
$\lvert S^{phit}\rvert/(\theta_{iter}-95^\circ)$	not used	$0.0004-0.03$
$\lvert S^{phit}\rvert/(\theta_{iter}-90^\circ)$	not used	$0.0004-0.03$

Table 8.3: Analyzed Cut Parameters

	atm. ν % *BG MC*		1 *TeV* μ % *BG MC*		1 *TeV* μ % *exp.*		*exp.*(*inv.cuts*)% *exp.*	
	$\frac{\lvert S^{phit}\rvert}{(\theta-\Delta)}$	F^{max}	$\frac{\lvert S^{phit}\rvert}{(\theta-\Delta)}$	F^{max}	$\frac{\lvert S^{phit}\rvert}{(\theta-\Delta)}$	F^{max}	$\frac{\lvert S^{phit}\rvert}{(\theta-\Delta)}$	F^{max}
$\Delta = 90^\circ$	0.0055	2995.3	0.0055	3037.7	0.009	2250	0.0067	1492
$\Delta = 95^\circ$	0.0076	3167.8	0.0076	3160.8	0.011	2217	0.0077	1490
$\Delta = 100^\circ$	0.0090	3047.6	0.0090	3080.2	0.018	2170	0.0092	1484
$\Delta = 105^\circ$	0.0110	2933.1	0.0110	2985.4	0.023	2098	0.0110	1475

Table 8.4: Optimization modes

Two experimental modes have found weaker cut values. This is not unexpected because a high normalization constant α (see chapter 6.4.3) of $\frac{1631}{signal\ content\ in\ experiment}$ for the mode (*exp.*(*inv.cuts*)% *exp.*) and $\frac{2484}{signal\ content\ in\ experiment}$ for the mode (1 *TeV* μ & *exp.*) was used. This feature will be further investigated in chapter G.

tested	*atm. ν % BG MC*			*1 TeV μ % BG MC*			*1 TeV μ % exp.*			*exp.(inv.ctus)% exp.*		
cut	$\frac{\lvert S^{phit}\rvert}{(\theta-90°)}$	value	F^{max}	$\frac{\lvert S^{phit}\rvert}{(\theta-90°)}$	value	F^{max}	$\frac{\lvert S^{phit}\rvert}{(\theta-90°)}$	value	F^{max}	$\frac{\lvert S^{phit}\rvert}{(\theta-90°)}$	value	F^{max}
$\lvert\theta_{iter}-\theta_{LF}+6°\rvert$	0.0091	40.7°	3609	0.0091	40.3°	3413	0.009	41°	2268	0.0067	47.4°	1503
$L_{up}^{iter}/L_{down}^{iter}$	0.0091	0.941	3336	0.0091	0.941	3246	0.01	0.954	2263	n.a.	n.a.	n.a.
L^{phit}	-	-	3168	-	-	3162	0.009	5.9	2252	-	-	1492
$\lvert S^{van}\rvert$	-	-	3168	-	-	3162	0.011	0.34	2271	0.007	0.4	1495
$L_{dir}(-15\text{ns}:75\text{ns})$	-	-	3168	-	-	3162	-	-	2250	0.007	121m	1496
cut	$\frac{\lvert S^{phit}\rvert}{(\theta-95°)}$	value	F^{max}	$\frac{\lvert S^{phit}\rvert}{(\theta-95°)}$	value	F^{max}	$\frac{\lvert S^{phit}\rvert}{(\theta-95°)}$	value	F^{max}	$\frac{\lvert S^{phit}\rvert}{(\theta-95°)}$	value	F^{max}
$\lvert\theta_{iter}-\theta_{LF}+6°\rvert$	0.01	41°	3504	0.01	41°	3347	-	-	2250	0.008	48°	1502
$L_{up}^{iter}/L_{down}^{iter}$	-	-	3168	0.01	0.941	3183	-	-	2250	n.a.	n.a.	n.a.
$\lvert S^{van}\rvert$	-	-	3168	-	-	3162	0.0133	0.34	2265	-	-	1492
$L_{dir}(-15\text{ns}:75\text{ns})$	-	-	3168	-	-	3162	-	-	2250	0.008	96m	1495
cut	$\frac{\lvert S^{phit}\rvert}{(\theta-100°)}$	value	F^{max}	$\frac{\lvert S^{phit}\rvert}{(\theta-100°)}$	value	F^{max}	$\frac{\lvert S^{phit}\rvert}{(\theta-100°)}$	value	F^{max}	$\frac{\lvert S^{phit}\rvert}{(\theta-100°)}$	value	F^{max}
$\lvert\theta_{iter}-\theta_{LF}+6°\rvert$	0.012	41.1°	3329	0.012	40.4°	3243	-	-	2250	0.009	48°	1496
L^{iter}	0.0121	8.3	3253	0.0121	8.3	3199	-	-	2250	-	-	1492
L^{phit}	0.121	5.4	3192	0.0121	5.4	3176	-	-	2250	-	-	1492
$N_{dir}(-15\text{ns}:75\text{ns})$	0.012	8	3244	0.0118	8	3176	-	-	2250	-	-	1492
$\lvert\vec{v}_{LF}\rvert$	0.012	0.103	3244	0.12	0.103	3182	-	-	2250	-	-	1492

Table 8.5: 2-dimensional optimization: Cut parameters which were able to increase $F[S(\vec{x}^{cut}), B(\vec{x}^{cut})]^{max}$ together with $|S^{phit}|/(\theta_{iter}-\Delta)$. Four different intersection points Δ were tested ($\Delta = 90°$, 95°, 100° and 105°), but only the three listed above could further maximize $F[S(\vec{x}^{cut}), B(\vec{x}^{cut})]$ in combination with another cut parameter.

8.2 2-Dimensional Optimization

All other parameters of table 8.5 were tested together with the four cut parameters $|S^{phit}|/(\theta_{iter}-\Delta)$ in a 2-dimensional search ($\Delta = 90°$, 95°, 100° and 105°). Those combinations which could not further increase $F[S(\vec{x}^{cut}), B(\vec{x}^{cut})]$, were rejected. Samples using experimental data yield more combinations of successful cut parameters for smaller values of Δ. This could give a hint for more residual background in the experimental sample leaking into the signal distribution. In this case, additional cuts are necessary to guarantee relatively low values of $|S^{phit}|$ while keeping a high signal passing rate. The argument is supported by the fact that the parameter $|S^{van}|$ gives good results for $\Delta = 90°$. This parameter is correlated to $|S^{phit}|$ (see figure 8.35b).

The hierarchy in $|S^{phit}|/(\theta_{iter}-\Delta)$ between samples using background MC and those optimizing on experiment is now inverted: In most of the cases, experimental samples produce a tighter cut on $|S^{phit}|/(\theta_{iter}-\Delta)$, but a less tight cut on the accompanying parameter.

8.3 3- and 4-Dimensional Optimization

In order to investigate more thoroughly the region of overlap between signal and background distributions (to which a possible choice of Δ is sensitive), I optimized $F[S(\vec{x}^{cut}), B(\vec{x}^{cut})]$ with the following parameters:

- $|S^{phit}|$

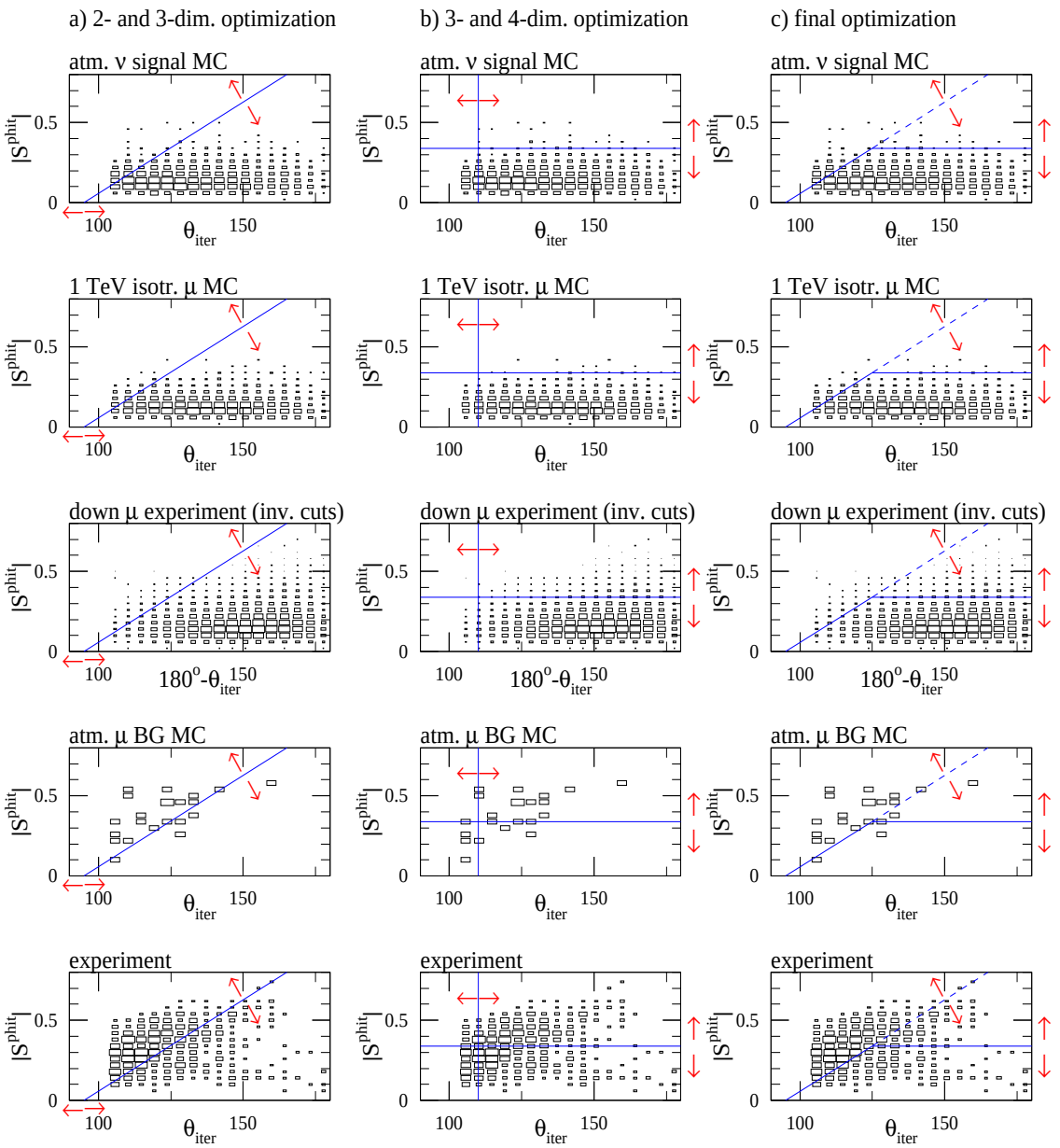

Figure 8.33: Analysis A: Basic cut parameters were combinations of $|S^{phit}|$ and θ^{iter}. In a first try, $F[S(\vec{x}^{cut}), B(\vec{x}^{cut})]$ was maximized for the parameters $|S^{phit}|/(\theta_{iter} - \Delta)$ with varying intersection points Δ plus one parameter out of table 8.3 (first column (a)). In order to investigate which parameters are sensitive to the overlap region between signal and background distributions, the parameters $|S^{phit}|$ and θ^{iter} were tested together with one additional parameter (3-dimensional analysis) or with a combination of two parameters out of table 8.5 (4-dimensional analysis). This is indicated by figures in the middle column (b). The cut parameter $|\theta_{iter} - \theta_{LF} + 6^{\circ}|$ is best suited to further maximize $F[S(\vec{x}^{cut}), B(\vec{x}^{cut})]$. The final analysis ($3^{rd}$ column (c)) aimed at finding a minimum sample of independent cut parameters together with the parameters $|S^{phit}|/(\theta_{iter} - 95^{\circ})$, $|S^{phit}|$ and $|\theta_{iter} - \theta_{LF} + 6^{\circ}|$. Results are listed in table 8.5.

- θ^{iter}
- Parameters listed at least once in table 8.5.

The combination is indicated by the boxes drawn into figures 8.33b. The top left corner of the box is susceptible to background contamination which cannot easily be rejected by $|S^{phit}|/(\theta_{iter} - \Delta)$ while keeping a high signal passing rate. Thus, additional cut parameters have a good possibility to become active. Table 8.6 shows the combinations of cut parameters which were able to increase $F[S(\vec{x}^{cut}), B(\vec{x}^{cut})]^{max}$ with respect to $|S^{phit}|$ and θ^{iter} alone.

One can see, that the parameter $|\theta_{iter} - \theta_{LF} + 6^\circ|$ gives the best results with all four combinations of data samples. Additionally, four-parameter combinations were tested, but only combinations containing the zenith angle difference could further increase $F[S\vec{x}^{cut}, B(\vec{x}^{cut})]^{max}$ obtained by the 3-dimensional analysis. Table 8.7 gives the obtained parameter names and values. The parameter $L_{up}^{iter}/L_{down}^{iter}$ improves $F[S\vec{x}^{cut}, B(\vec{x}^{cut})]^{max}$ for both background samples, the closely related parameter $L_{up}^{iter} - L_{down}^{iter}$ is favored by the sample maximizing 1 TeV isotropic muons against experimental data. Both parameters were not available for the experimental sample filtered with inverted cuts. The corresponding combination of pure experimental samples chose $N_{dir}^{iter} - N_{dir}^{shower}$ as best additional cut parameter.

8.4 Final Optimization and Extrapolation

A further addition of parameters to a five-dimensional ensemble could not increase efficiency any more. This defines the minimum set of independent cut parameters. It is however useful to rearrange parameters in a reasonable way.

1. $|S^{phit}|/(\theta - 95^\circ)$
2. $|S^{phit}|$
3. $|\theta_{iter} - \theta_{LF} + 6^\circ|$
4. $L_{up}^{iter}/L_{down}^{iter}$ or $L_{up}^{iter} - L_{down}^{iter}$, according to the sample
5. N_{dir}^{iter}(-15ns:75ns)-N_{dir}^{shower}(-15ns:75ns) for the down-going muons with inverted cuts which could not use the parameter L_{down}.

Figure 8.33c illustrates the final choice of two of the cut parameters:

These 4-parameter combinations were tested together with every parameter out of table 8.7 in a 5-dimensional optimization, but the functional $F[S(\vec{x}^{cut}), B(\vec{x}^{cut})]$ could not be improved.

The two samples containing background simulation were extrapolated as described in chapter 6.4.2. Figure 8.34 shows the results. All cut parameters reach the limits of the phase space at about 15 events offset. The parameter $|S^{phit}|/(\theta - 95^\circ)$ seems to saturate at 0.023 for the atmospheric neutrino sample. The same feature is found in the 1 TeV isotropic muons sample, except for the last entry. It is not clear whether this is just a fluctuation or a change in the background behavior. A similar behavior can be observed with the parameter $|\theta_{iter} - \theta_{LF} + 6^\circ|$. The parameter $L_{up}^{iter}/L_{down}^{iter}$ cannot be extrapolated.

tested third cut	*atm. ν % BG MC*				*1 TeV μ % BG MC*				*1 TeV μ % exp.*				*exp.(inv.cuts)% exp.*			
	$\lvert S^{phit}\rvert$	θ^{iter}	value	F^{max}	$\lvert S^{phit}\rvert$	θ^{iter}	value	F^{max}	$\lvert S^{phit}\rvert$	θ^{iter}	value	F^{max}	$\lvert S^{phit}\rvert$	θ^{iter}	value	F^{max}
without	0.22	105.8°	-	3325	0.22	105.8°	-	3233	0.3	105°	-	2276	0.34	118°	-	1470
$\lvert\theta_{iter} - \theta_{LF} + 6°\rvert$	0.38	105°	28°	3690	0.34	108.5°	41°	3456	0.3	105°	33°	2309	0.34	115°	43°	1488
$L_{up}^{iter}/L_{down}^{iter}$	0.24	105°	0.96	3449	0.34	105.5°	0.94	3291	0.3	105°	0.96	2281	n.a.	n.a.	n.a.	n.a.
$L_{up}^{iter} - L_{down}^{iter}$	-	-	-	3325	-	-	-	3233	0.34	105°	-6.6	2283	n.a.	n.a.	n.a.	n.a.
L^{phit}	0.38	108.4°	5.3	3427	0.38	108.4°	5.3	3314	0.3	105°	5.9	2280	-	-	-	1470
L^{iter}	0.36	105.8°	8.2	3472	0.36	105.9°	8.1	3321	-	-	-	2276	-	-	-	1470
$L_{dir}(-15\text{ns}: 75\text{ns})$	0.34	105.9°	117m	3425	0.34	105.9°	117m	3305	-	-	-	2276	0.34	115°	120m	1484
$N_{dir}(-15\text{ns}: 75\text{ns})$	-	-	-	3325	0.36	108.5°	8	3316	-	-	-	2276	-	-	-	1470
$\lvert\vec{v}^{LF}\rvert$	0.37	106°	0.109	3364	0.3	108.5°	0.102	3270	-	-	-	2276	-	-	-	1470
$N_{dir}^{iter} - N_{dir}^{shower}$	-	-	-	3325	-	-	-	3233	-	-	-	2276	0.34	115°	2	1485
L^{shower}/L^{iter}	-	-	-	3325	-	-	-	3233	0.3	105°	0.96	2282	-	-	-	1470
$\lvert S^{van}\rvert$	-	-	-	3325	-	-	-	3233	0.3	105°	0.41	2279	-	-	-	1470

Table 8.6: 3-dimensional optimization: Shown are cut parameters which could increase $F[S_{\vec{x}}^{cut}, B(\vec{x}^{cut})]^{max}$ with respect to cuts on $\lvert S^{phit}\rvert$ and θ_{iter} alone. Obtained differences in the cut parameter values are sometimes too small to be visible in this list. The parameter $\lvert\theta_{iter} - \theta_{LF} + 6°\rvert$ gives the best result for all compared samples.

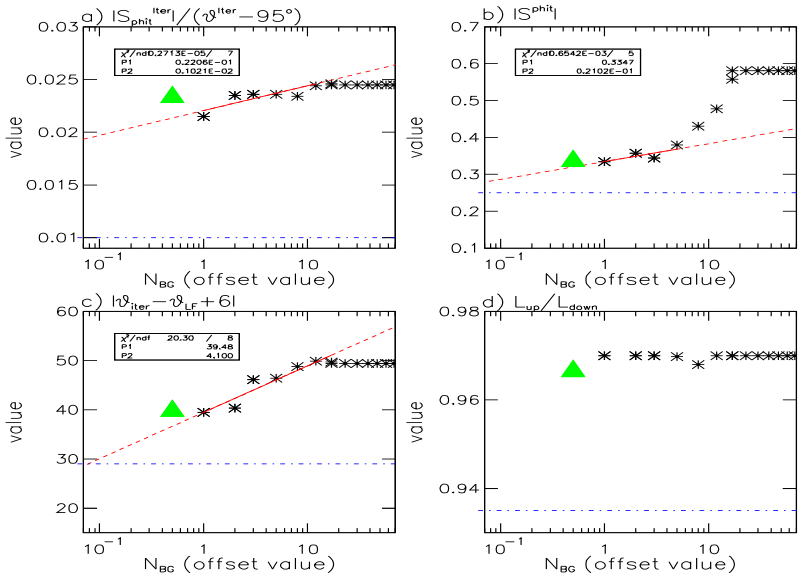

(a) 1 TeV isotropic muons optimized vs. background MC.

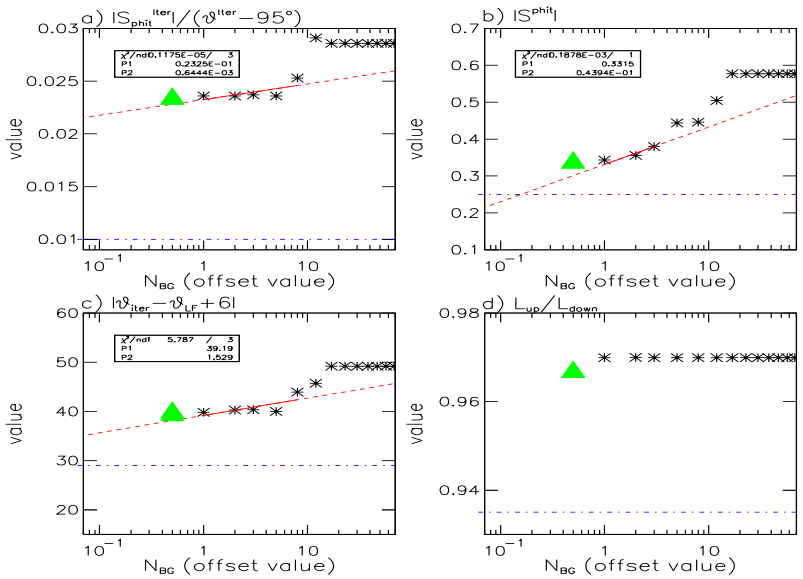

(b) Atmospheric neutrino-induced muon MC vs. background MC.

Figure 8.34: Extrapolation of cuts: Shown are the four parameters $|S^{phit}|$, $|S^{phit}|/(\theta-95°)$, $|\theta_{iter}-\theta_{LF}+6°)|$ and $L_{up}/L_{down}(iter)$ used for variation of the offset parameter N_{BG} (x-axis). The y-axis shows the cut value yielding the highest signal passing rate while reducing background until the offset value is reached. The dashed-dotted line represents the final choice of parameters as listed in table 8.5. One parameter ($L_{up}/L_{down}(iter)$) appeared to be redundant. Only setting the offset parameter to 0 passing background events, a tightening of the value used by the previous applied filter can be observed. This is indicated by the triangle (arbitrarily placed at $N_{BG} = 0.5$). This parameter could not be extrapolated and has been set by studying the experimental distribution (see figure 8.35a).

Parameter	*atm. ν % BG MC*		*1 TeV μ % BG MC*		*1 TeV μ % exp.*		*exp.(inv.cuts)% exp.*	
	value	F^{max}	value	F^{max}	value	F^{max}	value	F^{max}
$L^{iter}_{up}/L^{iter}_{down}$	0.967	3733	0.967	3462	-	2309	n.a.	n.a.
$L^{iter}_{up} - L^{iter}_{down}$	-	3690	-	3456	-6.3	2314	n.a.	n.a.
$N^{iter}_{dir} - N^{shower}_{dir}$	-	3690	-	3456	-	2309	2	1497
$L^{iter}_{direct\ hits}$(-15ns:75ns)	-	3690	-	3456	-	2309	120m	1494
L_{iter}	8.47	3701	-	3456	-	2309	-	1488
L_{phit}	5.99	3693	-	3456	-	2309	-	1488
S_{van}	0.34	3691	-	3456	-	2309	-	1488
L^{shower}/L^{iter}	-	3690	-	3456	0.96	2310	-	1488

Table 8.7: Results of the 4-dimensional analysis. The shown parameters were able to increase $F[S\vec{x}^{cut}, B(\vec{x}^{cut})]^{max}$ obtained by the 3-dimensional analysis. They were tested together with $|S^{phit}|$, θ_{iter} and $|\theta_{iter} - \theta_{LF} + 6^\circ|$. The obtained cut values of these three parameters are not shown here.

It is only needed if the background MC last event has to be cut out. Note that a cut at 0.97 had already been set. The point corresponding to zero events offset has been indicated by the triangle arbitrarily placed at 0.5. Extrapolation seems not feasible, but an approximate behavior can estimated. This is indicated by the dotted lines in figures 8.34.

8.5 Results

Parameter	*atm. ν% BG MC*	*1 TeV μ % BG MC*	*1 TeV μ % exp.*	*exp.(inv.cuts)% exp.*	final choice
$\|S^{phit}\|/(\theta^{iter} - 95^\circ) \leq$	0.022	0.019	0.016	0.0095	0.01
$\|S^{phit}\| \leq$	0.22	0.28	0.34	0.36	0.25
$\|\theta_{iter} - \theta_{LF} + 6^\circ)\| \leq$	35°	29°	38°	39°	30°
$L^{iter}_{up}/L^{iter}_{down} \leq$	0.967 (no extr.)	0.967 (no extr.)	-	n.a.	0.935
$L^{iter}_{up} - L^{iter}_{down} \leq$	-	-	-4.0	n.a.	-
$N^{iter}_{dir} - N^{shower}_{dir} \geq$	-	-	-	2	2
$F[S(\vec{x}^{cut}), B(\vec{x}^{cut})]^{max}$	3748 (offset=0)	3482 (offset=0)	2324	1509	-

Table 8.8: Results of the final optimization: The first column gives the cut parameters which could increase $F[S(\vec{x}^{cut}), B(\vec{x}^{cut})]$ in any of the four optimization modes. The next two columns show the extrapolation results of the two modes using background simulations, the third and forth columns show the cut values which yielded $F[S(\vec{x}^{cut}), B(\vec{x}^{cut})]^{max}$ for the two modes using experimental data. The last column gives a possible final choice of cut values.

Table 8.5 gives a summary of obtained cut values. The right column shows the cut values applied for the final sample of analysis A. The value of $L^{iter}_{up}/L^{iter}_{down} = 0.935$ for the background samples was not obtained by extrapolation of cuts, but by closer inspection of the distributions (see figure 8.35a). The obtained value of $S^{phit} < 0.25$ and $S^{phit} < 0.22$ is

not found in the modes using experimental data as background. One possible explanation for this effect could be that the extrapolation suggests a wrong background behavior. Supporting evidence for this assumption can be found in figure G.56a (see appendix G). Here the fifth (cross-check) sample has been optimized with varying signal normalization α. Approaching $\alpha = 1$ from above, ideally cut values should be reached which reduce the entire background in the experiment (see chapter 6.4.3). Here a value of about 0.28 is approached before fluctuations dominate.

The cut $|S^{phit}|/(\theta^{iter} - 95^\circ) \leq 0.01$ might also be set too strong. It has been set due to the results from the *exp.*(*inv.cuts*)% *exp.* mode. Figure 8.33 shows that the down-going muons sample obtained from experiment with inverted cuts is shifted towards higher values of $(180 - \theta_{iter})$. This is due to the fact that the angular spectrum of atmospheric muons does not extend further than to about 80°. We do not know however, if this is the only reason for the obtained strong cut value. This combination of samples is the only one which does not contain MC simulation. In order to keep systematic uncertainties between simulation and experiment as low as possible, it is reasonable to keep this strong cut value. Generally, cut values found by extrapolation with the mode 1 $TeV\ \mu\ \%\ BG\ MC$ are found to be stronger than those obtained with the same signal sample optimized versus experimental data. This result may be due to an overestimation of background via the extrapolation procedure or an underestimation by the modes using experimental data. Variation of the normalization parameter α in these modes supports the second assumption (see chapter G) as α had been set too high. In total, 127 events of experimental data pass these cuts (130.1 days lifetime). Figure 8.35c-f show some relevant distributions for these events.

One can now interpret the extrapolation results (atmospheric neutrino MC vs. background MC) as a proposed path through the cut parameter space parameterized by the offset parameter N_{BG}. Following that path, tighter and tighter cut values are obtained of the four (orthogonal) parameters $|S^{phit}|$, $|S^{phit}|/(\theta_{iter}-95^\circ)$, $|\theta_{iter}-\theta_{LF}+6|$ and L_{up}/L_{down}. Figure 8.36a shows the obtained passing rates for atmospheric neutrino-induced muon simulation, background MC and experiment. One can see that the experimental data follows first (at the right side) the simulated background and then the signal prediction. This becomes even clearer in figure 8.36b. It shows possible ratios of the obtained passing rates. The signal/experiment ratio flattens out and reaches a constant value of about 0.65. Note that the ratio (signal MC + background MC)/experiment fluctuates only little around the expected value of 1.

8.6 Conclusions

The following conclusions can be made for analysis A:

- The four optimization modes found 4 independent cut parameters out of the pool of investigated observables. The two modes using background simulation found exactly the same minimum set of independent variables, the two modes using experimental data differ only by one parameter which is very closely related in the case of signal simulation. For the optimization mode using only experimental data, conclusions about consistency with the last independent parameter cannot be drawn because the relevant parameter was not available.

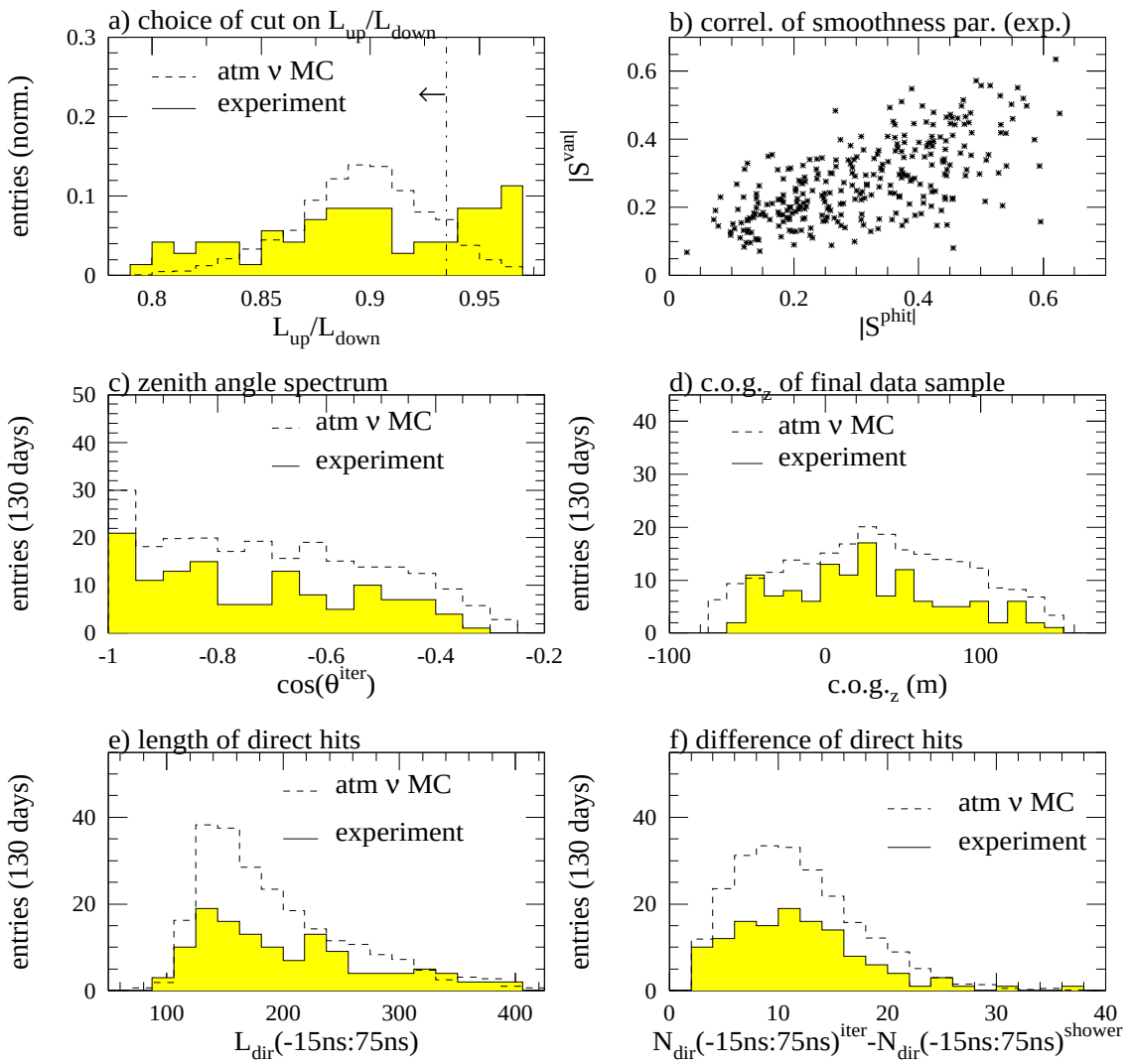

Figure 8.35: Results of analysis A: Figure (a) shows the distribution for the parameter $L_{up}^{iter}/L_{down}^{iter}$ with all cuts of table 8.5 applied except for this parameter. The cut of 0.935 is indicated by the dashed-dotted line. There is a deficit of medium quality events visible ($L_{up}^{iter}/L_{down}^{iter} > 0.85$) with respect to the atmospheric neutrino MC prediction. Figure (b) shows the correlation of the parameters $|S^{phit}|$ and $|S^{van}|$ before application of the final cuts. Figure (c) gives the zenith angle distribution with all cuts applied (included the cut which is shown in figure (a)). Except for a general deficit of experimental data with respect to the signal prediction, the distribution agrees within statistical errors. The same holds for the distribution of the z-component of the center-of-gravity of hits (figure (d)). Figure (e) shows the length of direct hits within a time residual window of (-15ns:75ns). Here also, the simulation predicts too many medium-quality events with a length of direct hits smaller than about 220 m. The last plot (f) shows the difference of direct hits between the iterative likelihood reconstruction and the cascade reconstruction.

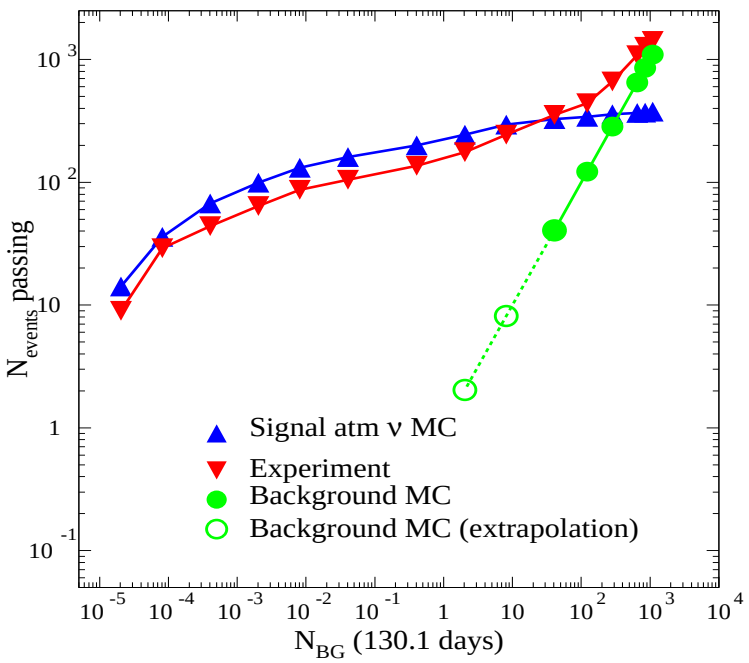

(a) Passing rates.

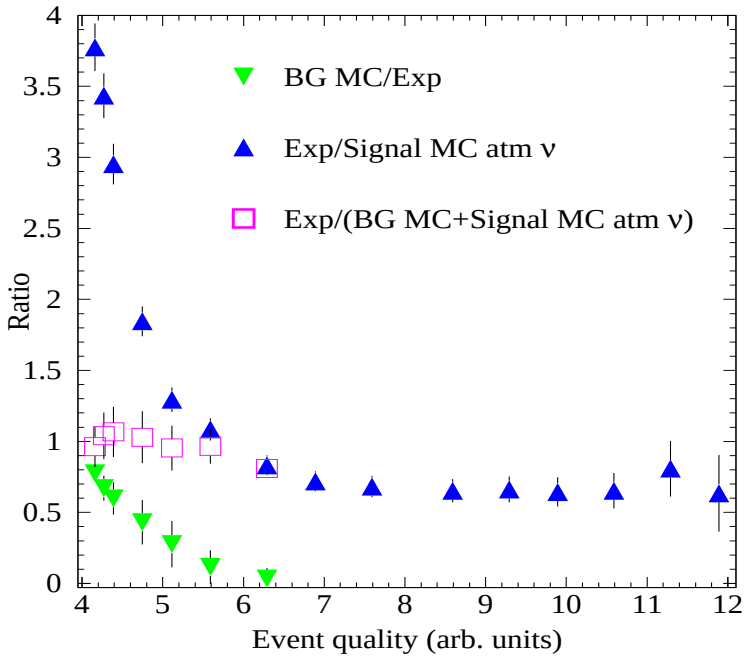

(b) Ratios of passing rates

Figure 8.36: The cut values obtained by maximization of $F[S(\vec{x}^{cut}), B(\vec{x}^{cut}), \text{offset}]$ and extrapolation of the offset-parameter. The x-axis in figure (a) gives the offset-value (from 10^3 down to 15 as input-parameter for the functional F, from 15 downwards as input parameter for the assumed extrapolation function). Cuts get stronger from right to left. The background simulation samples and the offset parameter were multiplied by a factor 3 according to their relative normalization with respect to the experiment on filter level 3. The bottom plot (b) shows the ratios of passing rates. The above x-axis has been relabeled into the more adequate notation of "event quality" ($quality = -log(N_{BG}) + 7.2$). Quality does not start from 1 because data has already been pre-filtered. Cuts get now stronger from left to right.

- A first try to extrapolate cut values has been made. All parameters reached the borders of their phase space (previous filters or borders implemented in the optimization routine) at an offset value of about 15, one parameter already at 1 event. This parameter could not be extrapolated. The other three parameters show large intrinsic uncertainties in the extrapolation procedure. Apparently, the phase space was too restricted because some parameters have already been used in previous filter levels.

- Gradual tightening of cuts along the path proposed by the extrapolation function converged against a constant ratio of passing rates for atmospheric neutrino-induced muon simulation and experiment at about 0.6-0.7.

- Taking the strongest cut values found by the four optimization modes yields 127 neutrino candidates in 130.1 days life time.

- The functional $F[\alpha \cdot S(\vec{x}^{cut}), (B+S)(\vec{x}^{cut})] = \alpha \cdot S(\vec{x}^{cut}) - (B+S)(\vec{x}^{cut})$ behaves stable against variation of α for $\alpha > 1$, but finds in general too weak cut values. α was probably chosen too high for the search of independent cut parameters.

- Compared to the simulation (bulk ice), the experiment shows a deficit of lower quality quality in the length of direct hits and the ratio of likelihood parameters (L_{up}/L_{down}).

- Visual inspection of data revealed that fake events have not only large differences in zenith angle between different reconstructions, but also in azimuth. The implementation of a space angle parameter is useful. This will be done in analysis B.

- Comparison with the analysis performed by the Madison group showed that a poor overlap of of the found neutrino candidates was reached. Closer inspection revealed that several events were lost due to the tighter "c.o.g."-cuts (see chapter 5.4.1) and the filters applied previous to this analysis. As a result, the "c.o.g"-cuts were redesigned in order to get the "relaxed" set of cuts explained in chapter 5.4.1.

9 Results - Analysis B

9.1 Changes with Respect to Analysis A

With better confidence in the stability of the CUTEVAL-approach, a second enlarged analysis (analysis B) was performed. Apart from the addition of new cut parameter, also systematic improvements relative to analysis A were achieved. The following modifications have thus been made:

- Loosening of previously applied cuts: The complete set of additionally applied filters (see 7 and 9) in analysis A was omitted. Additionally, "c.o.g."-cuts were reworked (see chapter 5.4.1) and weaker adjusted. The parameters $L_{vis}, L_{wid}, L_{max}$ and I_{max} the slope of $3 \cdot I_1/(I_1 + I_2 + I_3)$ with respect to the reconstructed zenith angle were incorporated in the list of tested cut parameters.

- The dipole fit, multi-PE-reconstruction and the Bayesian reconstruction were calculated for the data sets. Variables depending on these fits were added to the list of tested cut parameters.

- The parameter L_{down} was implemented also for zenith-angle inverted cuts (i.e. L_{up} was calculated for down-going tracks).

- The simulations containing vertical ice structures were added. *Basiev*- and *corsika*-generated muons from air showers were compared and added together to form one common background sample.

- The functional to find the minimum set of independent cut parameters was $F[\alpha S(\vec{x}^{cut}), (B+S)(\vec{x}^{cut})] = \frac{\alpha S(\vec{x}^{cut})}{\sqrt{|(B+S)(\vec{x}^{cut}) - \alpha S(x^{cut})|}}$. Before starting, the correct normalization factor α was determined.

- Because of the larger list of tested parameters, a different procedure was followed to find the minimum set of independent cut parameters:

  - Add the cut which yields the highest value of $F[\alpha S(\vec{x}^{cut}), B(\vec{x}^{cut})]^{max}$ to the list of independent cut parameters.
  - Reject all parameters which could not improve $F[\alpha S(\vec{x}^{cut}), B(\vec{x}^{cut})]^{max}$.
  - Perform the optimization one dimension higher with the list of independent cut parameters plus each parameter which was not rejected.

- Two additional selection criteria were added:

  - $\theta^{iter} > 95^\circ$
  - $\theta^{MPE} > 95^\circ$

The data samples obtained with these filters and the new "c.o.g"-cuts were compared in four optimization modes:

atm ν%BG MC (00): 25047[1] with *nusim* simulated atmospheric neutrino-induced muon events (weighted) were used as signal. The simulation included vertical ice-structures. The number of events normalized to 65 days of detector life time was 207.0. This sample was optimized against the entire background simulation (including vertical ice structures) available during this work. This was a combination of 3960 (weighted) *basiev* and 14 (unweighted) *corsika* background muon simulation from air showers. The *basiev* sample corresponded to about 4.2 days and the *corsika* sample to about 1.4 day detector life time.

atm ν%BG MC (98): 56466 with *nusim* simulated atmospheric neutrino-induced muon events (weighted) were used as signal. This was the same sample as in the previous mode with twice the statistics. The number of events normalized to 65 days of detector life time was 206.7. This sample was optimized against the entire background simulation (without vertical ice structures) produced during the mass production 1998 and is identical to the one used in analysis A. Because of weaker cuts applied previous to the optimization procedure, it contained more events than in analysis A, namely 82, corresponding to a total detector life time of about 10 days at trigger level.

atm ν%experiment: 56466 with *nusim* simulated atmospheric neutrino-induced muon events (weighted) including vertical ice layers were used as signal (same as in the previous modes). This sample was optimized against the experimental data having been registered on odd numbered days ($\sim$ 65 days life time). The number of experimental events was 2333.

exp (inv.cuts)%experiment: 4727 triggers from experiment, reconstructed as down-going and having passed all corresponding zenith-angle inverted filters, were used as signal. This corresponds to about 2.5 minutes detector life time. The sample was optimized against the experimental data having been registered on odd numbered days ($\sim$ 65 days life time).

9.2 The Correct Normalization α

The choice was made to use the functional $F(x) = \frac{\alpha S(\vec{x}^{cut})}{\sqrt{|(B+S)(\vec{x}^{cut}) - \alpha S(\vec{x}^{cut})|}}$ (equation 6.50) for analysis B. The value α is the ratio between the number of events in the signal sample divided by the signal content in the experiment. Figure 9.37 shows the results of an optimization run with the four parameters used for extrapolation in analysis A. The signal sample consisted of the atmospheric neutrino simulation (bulk ice) which was optimized against the experimental data sample. The obtained cut values are more sensitive to variations of the normalization of the signal sample than those obtained with the functional used in analysis A (see figure G). According to analysis A, a value of 0.65 corresponds to $\alpha = 1$. The obtained cut values at $\alpha \approx 1$ give results comparable to the choice of final cut values (dashed blue lines). Values corresponding to relative normalizations greater than about 2 are not representative because of phase space limitations.

[1]The used statistics was limited by the available CPU-resources at the time when the optimization of this mode was performed.

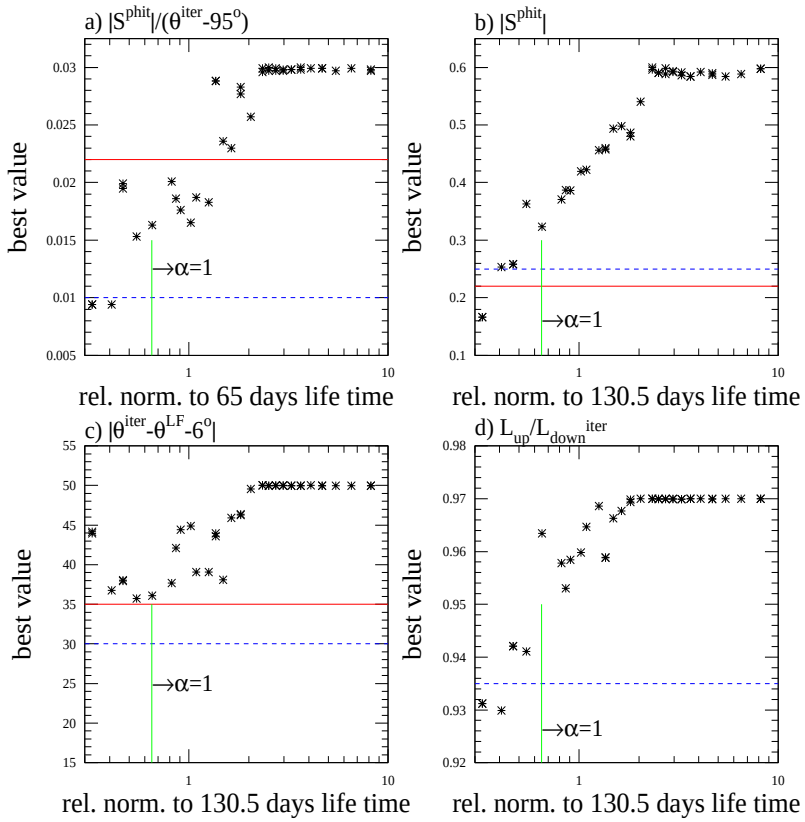

Figure 9.37: Obtained cut values through maximization of $F[S(\vec{x}^{cut}), B(\vec{x}^{cut})] = \frac{\alpha S(\vec{x}^{cut})}{\sqrt{|(B+S)(\vec{x}^{cut}) - \alpha S(\vec{x}^{cut})|}}$ with the four cut parameters used for the extrapolation in analysis A. The fifth optimization mode used for test purposes was investigated: Atmospheric neutrino simulation was compared to the experimental data. The atmospheric neutrino simulation sample (normalized to 65 days life time) was multiplied with varying factors (x-axis). The red lines (dotted lines) show the cut values obtained by extrapolation of the sample which compared the atmospheric neutrino-induced muon simulation with the background simulation, the dashed lines show the final choice of cut values in analysis A.

It would be nice to know the position of $\alpha = 1$ previous to searching for the set of independent cut variables. Test runs showed that not only the cut values vary with the signal normalization, but also the cut parameters themselves. A wrong signal normalization can yield different sets of independent cut parameters.

The following steps were thus undertaken: First, the signal samples were normalized according to the theoretical prediction for 65 days life time for the atmospheric neutrino simulation sample. The experimental sample was multiplied with the number of events of the atmospheric neutrino simulation (normalized to 65 days life time) and divided by the number of events in the experimental sample. This gave a factor of 0.031. Then an optimization was performed up to 3 dimensions. The three cut parameters obtained were kept and optimized with varying signal normalizations. The geometric mean was taken

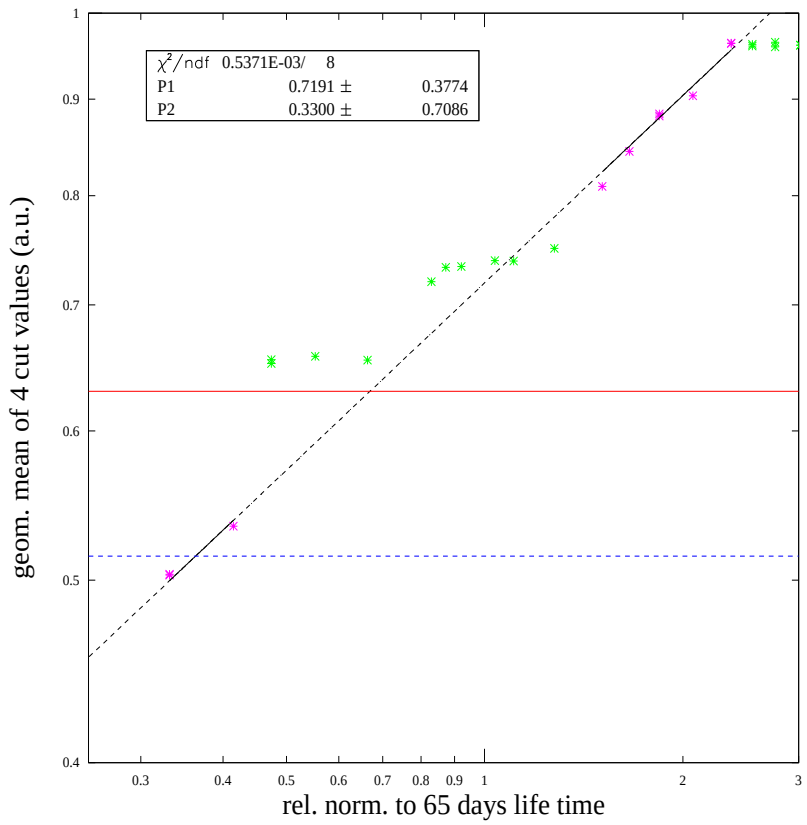

Figure 9.38: Variation of the signal normalization for the mode $atm\ \nu\%experiment$ (analysis A). The four cut parameters used for extrapolation in analysis A have been optimized with the functional $F[S(\vec{x}^{cut}), B(\vec{x}^{cut})] = \frac{\alpha S(\vec{x}^{cut})}{\sqrt{|(B+S)(\vec{x}^{cut}) - \alpha S(\vec{x}^{cut})|}}$ (same as figure 9.37). The relative normalization of the atmospheric neutrino simulation (compared to the predictions for 65 days life time) has been varied (x-axis). The geometric mean of the obtained cut values is plotted against the normalization of the signal sample. Small fluctuations area averaged out and a larger structure appears.

from the obtained cut values:

$$\bar{x}^{cut} = (\prod_{i=1}^{3} x_i^{\epsilon})^{\frac{1}{3}} \tag{9.54}$$

with $\epsilon = 1$ if the corresponding cut parameter keeps events smaller than the returned cut value and ϵ = -1 otherwise. Figures 9.39 and 9.40 show the results obtained for the modes using simulated atmospheric neutrino-induced muons and experimentally obtained down-going muons, respectively, tested against experimental data. Figure 9.38 shows the result of the same procedure performed with the test sample of analysis A and the cut parameters used for the extrapolation there. There is a zone of fluctuations visible below and above the place, where one expects $\alpha \approx 1$. This is expected (see discussion in chapter 6.4.3 and figure 6.31). and most probably corresponding to statistical fluctuations of the experimental data sample More stable regions can be seen which were fitted with a

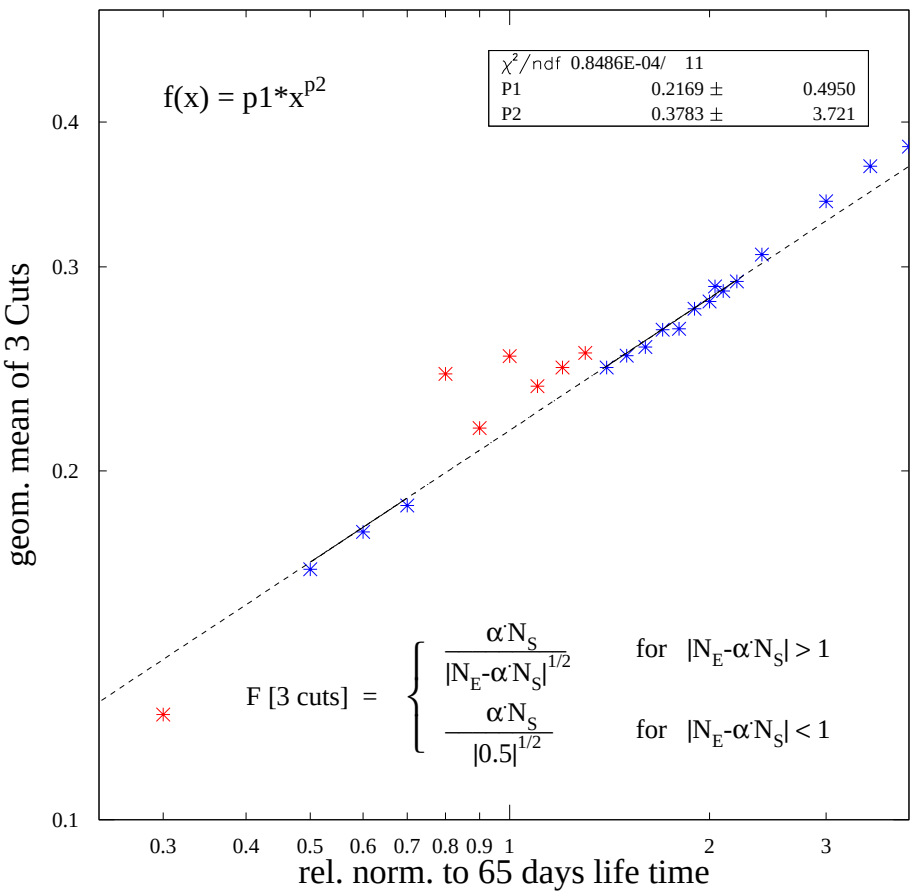

Figure 9.39: Variation of the signal normalization for the mode $atm\ \nu\%experiment$. Three cut parameters $(\Psi(MPE, Bayes), |S^{van}(MPE)|$ and $L_{dir}(-15:75\text{ns})^{Iter} \times N_{dir}(-15:75\text{ns})^{Iter})$ have been optimized with $F[S(\vec{x}^{cut}), B(\vec{x}^{cut}), \alpha]$ as defined in eq. 6.50. The relative normalization of the atmospheric neutrino simulation (compared to the predictions for 65 days life time) has been varied. The x-axis gives the factor with which the simulated atmospheric neutrino sample (normalized to 65 days life time) was multiplied. The geometric mean of the returned cut values which maximize $F[S(\vec{x}^{cut}), B(\vec{x}^{cut}), \alpha]$ has been taken and defines the y-axis. A power law was fitted to the more stable regions (blue markers).

power law. In order to avoid the zone of fluctuations, I chose the region at *smaller* signal normalizations. This region tends to produce too tight cut values. It is thus a conservative choice.

Therefore, a normalization correction of 0.7 for the simulated atmospheric neutrino-induced muon signal was thus chosen (see figure 9.39). The sample consisting of down-going muons from experimental data was multiplied with a factor of 0.018 (see figure 9.40).

Note that the presence of these fluctuations is a first (though very indirect) indication that atmospheric neutrinos are present in the experimental data sample at about the expected rate and with properties in agreement with the MC simulation.

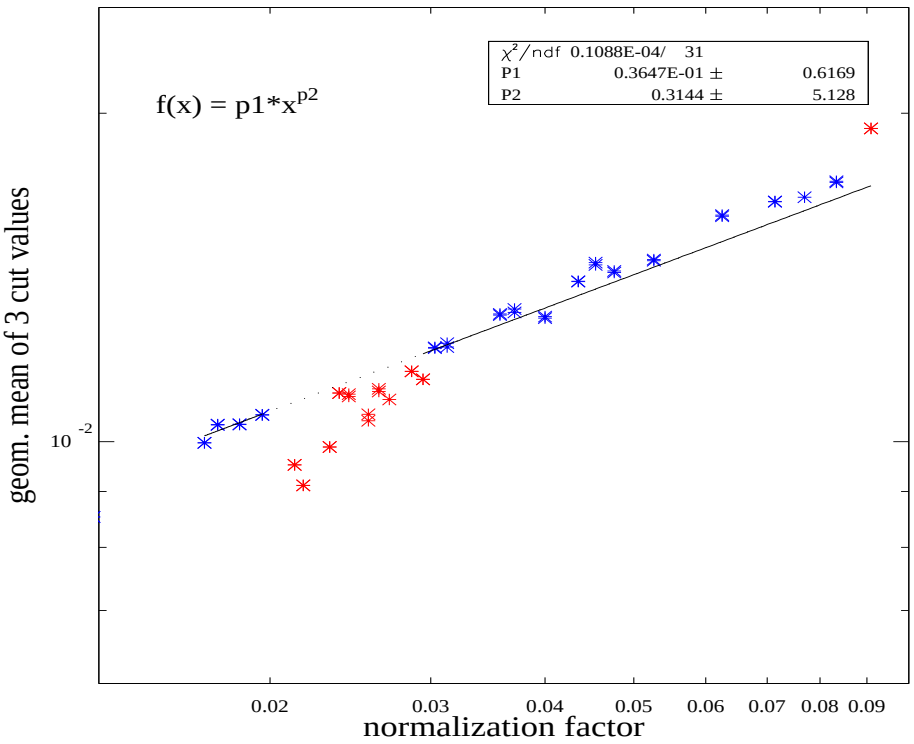

Figure 9.40: Variation of the signal normalization for the mode $exp\ (inv.cuts)\%experiment$. Three cut parameters ($|S^{van}(MPE)|$, $L_{dir}(-15\ :\ 75\text{ns})^{Iter} \times N_{dir}(-15\ :\ 75\text{ns})^{Iter}$ and $|S^{phit}(Iter)|/(\theta^{MPE} - 90°)$) have been optimized with $F[S(\vec{x}^{cut}), B(\vec{x}^{cut}), \alpha]$ as defined in eq. 6.50. The x-axis gives the absolute normalization factor of the experimentally obtained sample of down-going muons. The geometric mean of the returned cut values which maximize $F[S(\vec{x}^{cut}), B(\vec{x}^{cut}), \alpha]$ has been taken and defines the y-axis. A power law was fitted to the more stable regions (blue markers).

9.3 The Minimum Set of Independent Cut Parameters

First, a 1-dimensional search was performed for all four optimization modes. 76 cut parameters were investigated. The atmospheric muon background simulation from the mass production 2000 consisted of weighted events, therefore an offset of ~ 0.3 had been calculated according to equation 6.42. Background was reduced to this value within the optimization mode $atm\ \nu\%BG\ MC$ (00). Specifically in the 1-dimensional search, the simulated background consisted only of the muons simulated with $basiev$. This is equivalent to about 4/5 of the total amount of background used in the later analysis steps. For each mode, table 9.9 shows the single parameter which yielded the highest value of $F[S(x^{cut}), B(x^{cut})]$.

Together with these parameters, 2-dimensional searches were performed. Those cut parameters which yielded the highest achievable value of $F[S(\vec{x}^{cut}), B(\vec{x}^{cut})^{max}]$ were added to the list of independent parameters. The 3-dimensional optimization tested the obtained two parameters together with those which had improved $F[S(\vec{x}^{cut}), B(\vec{x}^{cut})^{max}]$ in the 2-

Opt. mode	$F[S(\vec{x}^{cut}), B(\vec{x}^{cut})]$	cut parameter	cut value	F^{max}
atm. ν $\%BG\ MC(00)$	$\frac{S(\vec{x}^{cut})}{\sqrt{B(\vec{x}^{cut})}}$	$\lvert S^{phit}(Iter)\rvert /$ $(\theta^{MPE} - 90^{\circ})$	0.0052	128.46
atm. ν $\%BG\ MC(98)$	$\frac{S(\vec{x}^{cut})}{\sqrt{B(\vec{x}^{cut})}}$	$\lvert S^{phit}(Iter)\rvert /$ $(\theta^{MPE} - 90^{\circ})$	0.0054	129.32
atm. ν $\%experiment$	$\frac{S(\vec{x}^{cut})}{\sqrt{\lvert S(\vec{x}^{cut}) - (B+S)(\vec{x}^{cut})\rvert}}$	$L_{dir}(-15:75)^{MPE} \times$ $(N_{dir}(-15:75)^{MPE} - 2)$	1768.93	79.21
exp (inv.cuts) $\%experiment$	$\frac{S(\vec{x}^{cut})}{\sqrt{\lvert S(\vec{x}^{cut}) - (B+S)(\vec{x}^{cut})\rvert}}$	$\lvert S^{phit}(Iter)\rvert /$ $(\theta^{MPE} - 90^{\circ})$	0.003	72.15

Table 9.9: 1-dimensional optimization: Listed are the four optimization modes together with the chosen optimization functional F and the parameters which yielded F^{max}. The first column shows the name of the optimization mode, the second column the the optimization functional used for that mode. The next two columns give the name of the cut parameter and its best setting for F^{max}. The last column shows the obtained maximum achievable value of F within this 1-dimensional search. The result of optimization mode *atm* $\nu\%BG\ MC$ (00) is shown only for background simulated with *basiev*.

dimensional search (with respect to $F_{1-dim}[S(x^{cut}), B(x^{cut})^{max}]$, as listed in table 9.9.). Analogously, a 3-,4-,5- and 6-dimensional search was performed, until $F[S(\vec{x}^{cut}), B(\vec{x}^{cut})^{max}]$ could not be improved further.

All results can be found in appendix H. Tables 9.10 and 9.12 present the cut parameters tested and the dimension n where they became dependent on the rest of the $(n-1)$ parameters. A bold number surrounded by a box marks the number of dimensions n where the corresponding cut parameter yielded the best result of all tested ones and was thus added to the list of independent parameters. Table 9.11 shows a summary of the best cuts obtained in each optimization mode.

One can see that the two cut parameters which were obtained first are the same for all modes. The only exception is the parameter $L_{dir}(-15:75)^{Iter} \times N_{dir}(-15:75)^{Iter}$ which was obtained in the mode *exp (inv.cuts)%experiment*. A closer inspection of the tables (appendix H.4) shows that the corresponding cut parameter found in the other modes, $L_{dir}(-15:75)^{MPE} \times (N_{dir}(-15:75)^{MPE} - 2)$, yielded a signal passing rate of only 0.2 events less. The obtained difference can thus be due to statistical fluctuations.

Starting with the third dimension, results of the different modes diverge. To get a feeling for the order of magnitude and thus the relevance of the other differences, the corresponding passing rates are listed in table 9.11. The following observations can be made:

1. A comparison of the optimization modes *atm* $\nu\%BG\ MC$ (00) and *atm* $\nu\%experiment$ shows that the signal passing rate within the first mode is lower than the one obtained with the second mode. The obtained cut parameters are essentially the same except for $|S^{van}(MPE)|$ which was found in mode *atm* $\nu\%experiment$ but not in

Cut	dim. of optimization			
	exp (inv.cuts)% *experiment*	*atm ν %* *experiment*	*atm ν %* *BG MC* (00)	*atm ν %* *BG MC* (98)
Topology of Hits				
N_{ch}	2	3	3	2
$c.o.g._z <$	3	2	3	2
$c.o.g._z >$	**4**	2	4	2
I_1/I_2	3	2	4	2
I_1/I_3	3	3	3	2
$3I_1/(I_1+I_2+I_3)$	3	3	4	2
$(I_1/I_2)/cos(\theta^{Iter})$	3	2	3	2
$(I_1/I_3)/cos(\theta^{Iter})$	3	2	3	2
$(3I_1/(I_1+I_2+I_3))/cos(\theta^{Iter})$	2	2	4	2
$(I_1/I_2)/cos(\theta^{MPE})$	3	2	3	2
$(I_1/I_3)/cos(\theta^{MPE})$	3	2	3	2
$(3I_1/(I_1+I_2+I_3))/cos(\theta^{MPE})$	3	3	4	2
$\|\vec{v}\|_{LF}$	3	2	3	2
$c.o.g._\rho$	2	2	3	2
Reconstructed direction				
θ^{LF}	3	2	4	2
θ^{Iter}	3	3	5	2
θ^{MPE}	3	3	5	2
θ^{Bayes}	n.a.	3	3	2
θ^{dipole}	3	4	3	2
$\Psi(Iter, LF)$	3	**4**	**5**	2
$\Psi(MPE, LF)$	3	4	5	2
$\Psi(MPE, Iter)$	3	2	3	2
$\Psi(Bayes, LF)$	n.a.	3	3	2
$\Psi(Bayes, Iter)$	n.a.	3	3	2
$\Psi(Bayes, MPE)$	n.a.	3	3	2
$\Psi(MPE, dipole)$	2	3	2	2
Likelihood				
L^{Iter}	2	2	3	3
$L^{phit}(Iter)$	3	2	5	3
L^{MPE}	3	4	4	3
$L^{phit}(MPE)$	3	3	3	3
$\theta^{dipole} > 60$ *or* $M^{dipole} > q$	3	4	4	2
L^{shower}/L^{Iter}	3	5	5	3
L^{shower}/L^{MPE}	2	2	4	3
$L^{shower} - L^{Iter}$	3	3	5	3
$L^{shower} - L^{MPE}$	3	5	4	3
$L_{up}/L_{down}(Iter)$	3	5	5	3
$L_{up}/L_{down}(MPE)$	2	3	4	2
$L_{up} - L_{down}(Iter)$	3	5	5	2
$L_{up} - L_{down}(MPE)$	3	**5**	**3**	3

Table 9.10: Tested cut parameters: The columns for each optimization mode give the number of cut parameter dimensions until which the parameter still improved $F[S(\vec{x}^{cut}), B(\vec{x}^{cut})]$. A bold number surrounded by a box indicates that the cut parameter has yielded the highest achievable value of $F[S(\vec{x}^{cut}), B(\vec{x}^{cut})]$ and has been added to the list of independent cut parameters.

	Exp. (inv.cuts)% experiment			*atm. ν% experiment*			*atm. ν% BG MC(00)*			*atm. ν% BG MC(98)*		
Cut Parameter	nr	signal passing (2.7 sec.)	exp. passing (65 days)	nr	signal passing (65 days)	exp. passing (65 days)	nr	signal passing (65 days)	BG passing (65 days)	nr	signal passing (65 days)	BG passing (10 days)
$\lvert S^{phit}(Iter)\rvert/(\theta^{MPE}-90^\circ)$	1	50.9	51	2	110.3	78	1	75.3	3.5	1	130.6	0
$L_{dir}(-15:75)^{MPE}\times(N_{dir}(-15:75)^{MPE}-2)$		-	-	1	80.0	57	2	104.4	3.5	2	154.7	0
$L_{dir}(-15:75)^{Iter}\times N_{dir}(-15:75)^{Iter}$	2	65.5	66		-	-		-	-		-	-
$\lvert S^{van}(MPE)\rvert$	3	67.9	68	3	120.4	85		-	-		-	-
$\Psi(Iter, LF)$		-	-	4	123.6	87	5	119.1	3.5		-	-
$L_{up}-L_{down}(MPE)$		-	-	5	138.4	97	3	114.4	3.5		-	-
$\lvert S^{phit}(Iter)\rvert/(\theta^{Iter}-95^\circ)$		-	-		-	-	4	118.3	3.5		-	-
$L_{dir}(-1)(-15:25)^{Iter}$		-	-		-	-	(5)	(119.1)	3.5		-	-
$c.o.g._z >$	4	68.6	69		-	-		-	-		-	-
$\lvert S^{phit}(Iter)\rvert/(\theta^{Iter}-90^\circ)$	5	69.2	70		-	-		-	-		-	-
$\lvert S^{phit}(MPE)\rvert/(\theta^{MPE}-85^\circ)$		-	-		-	-		-	-	3	161.9	0
							(offset=0.3/5.6 days)			(offset=0/10 days)		

Table 9.11: Results of the search for a minimum set of independent parameters: The first column gives the cut parameters which could increase $F[S(\vec{x}^{cut}), B(\vec{x}^{cut})]$ in any of the four optimization modes. The following columns show: The dimension where the addition of that parameter yielded the highest value of $F[S(\vec{x}^{cut}), B(\vec{x}^{cut})]$, the obtained numbers of passing signal and background events. The normalization correction (chapter 9.2) was omitted for the atmospheric neutrino simulation sample.

Smoothness				
Cut	dim. of optimization			
	exp (inv.cuts)% % *experiment*	*atm ν*% % *experiment*	*atm ν*% % *BG MC* (00)	*atm ν*% % *BG MC* (98)
$\lvert S^{phit}(like)\rvert$	3	4	4	2
$\lvert S^{van}(like)\rvert$	4	4	4	2
$\lvert S^{van}(mpe)\rvert$	**3**	**3**	4	2
$\lvert S^{phit}(Iter)\rvert/(\theta^{Iter}-95^\circ)$	3	3	**4**	2
$\lvert S^{phit}(MPE)\rvert/(\theta^{MPE}-95^\circ)$	3	3	2	2
$\lvert S^{phit}(Iter)\rvert/(\theta^{MPE}-90^\circ)$	**1**	**2**	**1**	**1**
$\lvert S^{phit}(Iter)\rvert/(\theta^{Iter}-90^\circ)$	**5**	3	4	3
$\lvert S^{phit}(MPE)\rvert/(\theta^{MPE}-90^\circ)$	2	3	2	2
$\lvert S^{phit}(Iter)\rvert/(\theta^{MPE}-85^\circ)$		3	3	2
$\lvert S^{phit}(Iter)\rvert/(\theta^{Iter}-85^\circ)$	3	3	3	2
$\lvert S^{phit}(MPE)\rvert/(\theta^{MPE}-85^\circ)$	3	3	2	**3**
$(\lvert S^{phit}(Iter)\rvert \times \lvert S^{van}(Iter)\rvert)^{(1/2)}$	3	4	4	2
$(\lvert S^{phit}(MPE)\rvert \times \lvert S^{van}(MPE)\rvert)^{(1/2)}$	3	3	5	3
Direct hit observables				
$N_{dir}(-15:25\text{ns})^{Iter}$	3	2	4	3
$N_{dir}(-15:75\text{ns})^{Iter}$	2	2	4	3
$N_{dir}(-15:25\text{ns})^{MPE}$	2	2	3	2
$N_{dir}(-15:75\text{ns})^{MPE}$	2	2	4	3
$L_{dir}(-15:25\text{ns})^{Iter}$	3	4	3	2
$L_{dir}(-15:75\text{ns})^{Iter}$	3	3	4	2
$L_{dir}(-15:25\text{ns})^{MPE}$	3	3	3	2
$L_{dir}(-15:75\text{ns})^{MPE}$	3	3	3	2
$L_{dir}(-1)(-15:25\text{ns})^{Iter}$	3	4	**5**	2
$L_{dir}(-1)(-15:25\text{ns})^{MPE}$	3	2	4	2
$L_{dir}(-15:75\text{ns})^{Iter} > 140$ *or* $L_{wid}(-15:75\text{ns})^{Iter}$	3	3	4	2
$L_{dir}(-15:75\text{ns})^{MPE} > 140$ *or* $L_{wid}(-15:75\text{ns})^{MPE}$	3	2	3	2
$L_{dir}(-15:75\text{ns})^{Iter} > 140$ *or* $L_{vis}(-15:75\text{ns})^{Iter}$	3	2	3	2
$L_{dir}(-15:75\text{ns})^{MPE} > 140$ *or* $L_{vis}(-15:75\text{ns})^{MPE}$	3	2	3	2
$L_{dir}(-15:25\text{ns})^{Iter} \times N_{dir}(-15:25\text{ns})^{Iter}$	3	4	5	2
$L_{dir}(-15:75\text{ns})^{Iter} \times N_{dir}(-15:75\text{ns})^{Iter}$	**2**	3	3	3
$L_{dir}(-15:25\text{ns})^{MPE} \times N_{dir}(-15:25\text{ns})^{MPE}$	3	4	4	2
$L_{dir}(-15:75\text{ns})^{MPE} \times N_{dir}(-15:75\text{ns})^{MPE}$	3	2	3	3
$L_{dir}(-15:75\text{ns})^{Iter} \times (N_{dir}(-15:75\text{ns})^{Iter}-2)$	3	3	4	3
$L_{dir}(-15:75\text{ns})^{MPE} \times (N_{dir}(-15:75\text{ns})^{MPE}-2)$	3	**1**	**2**	**2**
$L_{dir}(-15:25\text{ns})^{Iter} \times (N_{dir}(-15:25\text{ns})^{Iter}-2)$	3	3	5	2
$L_{dir}(-15:25\text{ns})^{MPE} \times (N_{dir}(-15:25\text{ns})^{MPE}-2)$	2	3	4	2
$N_{dir}(-15:75)^{Iter}/N_{ch}$	3	3	3	2
$N_{dir}(-15:75)^{MPE}/N_{ch}$	3	3	3	3

Table 9.12: Tested cut parameters (continued): The columns for each optimization mode give the number of cut parameter dimensions until which the parameter still improved $F[S(\vec{x}^{cut}), B(\vec{x}^{cut})]$. A bold number surrounded by a box indicates that the cut parameter has yielded the highest achievable value of $F[S(\vec{x}^{cut}), B(\vec{x}^{cut})]$ and has been added to the list of independent cut parameters.

the other one. Nonetheless, parameter $|S^{van}(MPE)|$ made it up to dimension 4 within the mode *atm* ν%*BG MC* (00), but a discrepancy remains. The difference could be due to the fact that $|S^{van}(MPE)|$ does not describe the data as well as needed (see figure 6.24b).

2. The optimization mode using background MC simulation without ice layers (last column) shows only three independent cut parameters, the other modes yielded five. In order not to get fooled by errors in the maximum search, I tested all parameters which had been proven independent to higher dimensions within the other modes. These tests were performed with different start conditions (T_0, number of iterations), the result remained stable.

3. On the contrary, the parameter $|S^{phit}(Iter)|/(\theta^{Iter} - 95^\circ)$ was found in the mode *atm* ν%*BG MC* (00) only. This difference could not be further investigated, but it is a minor effect since this parameter helps increase the signal passing rate only by 3.9 events (≈3.5%)

4. The difference between the mode *exp* (*inv.cuts*)%*experiment* and *atm* ν%*experiment* is larger: First, a completely different cut parameter was found: $c.o.g._z$. This can be easily explained with the intrinsic systematic difference of the down-going muon signal sample, obtained with zenith angle-inverted cuts in comparison with the atmospheric neutrino simulation. Because of the lack of muons from horizontal directions, events with a very low center of gravity of hits become unlikely. Figure 9.41 shows the distributions of this variable for simulated atmospheric neutrino-induced events and for the experimentally obtained down-going muons sample. The latter shows a different shape for events with low values of $c.o.g._z$.

5. More important are the cut parameters found by the mode *atm* ν%*experiment*, instead of the pure experimental samples: $\Psi(Iter, LF)$ and $L_{up} - L_{down}(MPE)$. Both parameters were tested with different start conditions, but again, no increase of $F[S(\vec{x}^{cut}), B(\vec{x}^{cut})]$ could be reached. The shape of the two parameters for the resulting neutrino candidates in experiment and the atmospheric neutrino simulation was investigated in chapter 9.6 (figure 9.45). No significant deviation from the MC prediction could be derived there[2]. A last cut parameter of the optimization mode *exp* (*inv.cuts*)%*experiment* is not found in the other samples: $|S^{phit}(Iter)|/(\theta^{Iter} - 90^\circ)$. It helps increase the signal passing rate by 0.6 events and brings only minor improvement. The same parameter with a different offset of $\Delta = 95^\circ$ has been found by the mode *atm* ν%*experiment*. Generally, the mode consisting of pure experimental samples seems to prefer variables based on the iterative likelihood reconstruction. This different behavior from the mode which used atmospheric neutrino simulation should be investigated further.

[2] A Kolmogorov-Smirnov test yielded ≈ 4% probability of agreement for both variables. Taking into account the residual background contamination, this is a good value

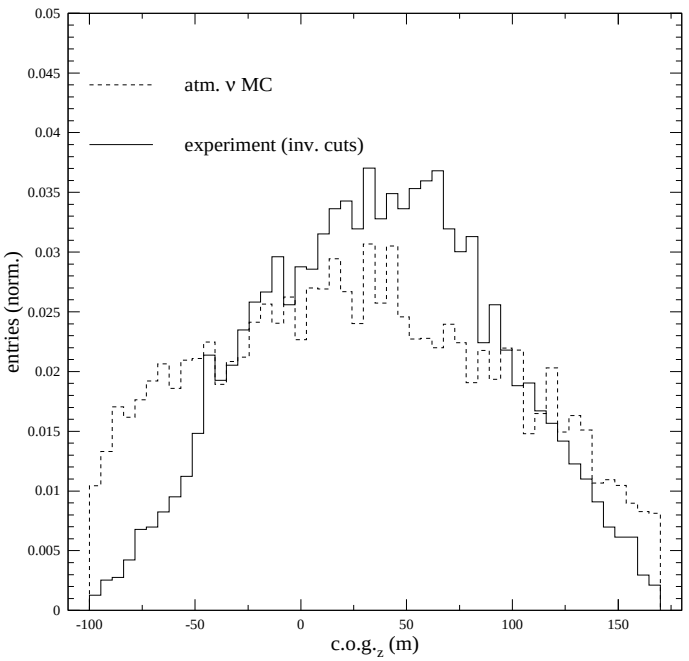

Figure 9.41: The center of gravity of hits between two signal samples used for the optimization: The dashed line shows the atmospheric neutrino-induced muon simulation (ice layers), the full line shows experimental data, filtered with zenith-angle-inverted cuts. The last sample consists thus of high-quality down-going muons from air-showers.

9.4 Selection of Final Cut Parameters

Because of the good agreement of cut parameters between the modes *atm* ν%*experiment* and *atm* ν%$BG\ MC$, it seems reasonable to include these parameters in the final set of cuts. Most of the deviating cut parameters from the mode *exp.* (*inv.cuts*)%*experiment* could be related to systematic differences in the experimental signal sample obtained with inverted cuts. Because the effects of these differences on the obtained cut parameters have not been studied in detail, it seemed safer to include only the parameters obtained with the mode *atm* ν%*experiment*. However, a closer study of the differences between these two samples containing experiment is desirable for a further investigation of our systematic understanding of the experiment.

9.5 Extrapolation of Cuts

The five cut parameters obtained with the mode *atm* ν%*experiment* were extrapolated with the help of the background simulation (00). Taking these cuts gave the possibility to compare the extrapolation results with the cut values found between experiment and background MC We know however that these five cut parameters have not been shown independent in the mode *atm* ν%$BG\ MC$ (00). At least one parameter or a combination parameters will be redundant with respect to the other parameters. Stronger fluctuations

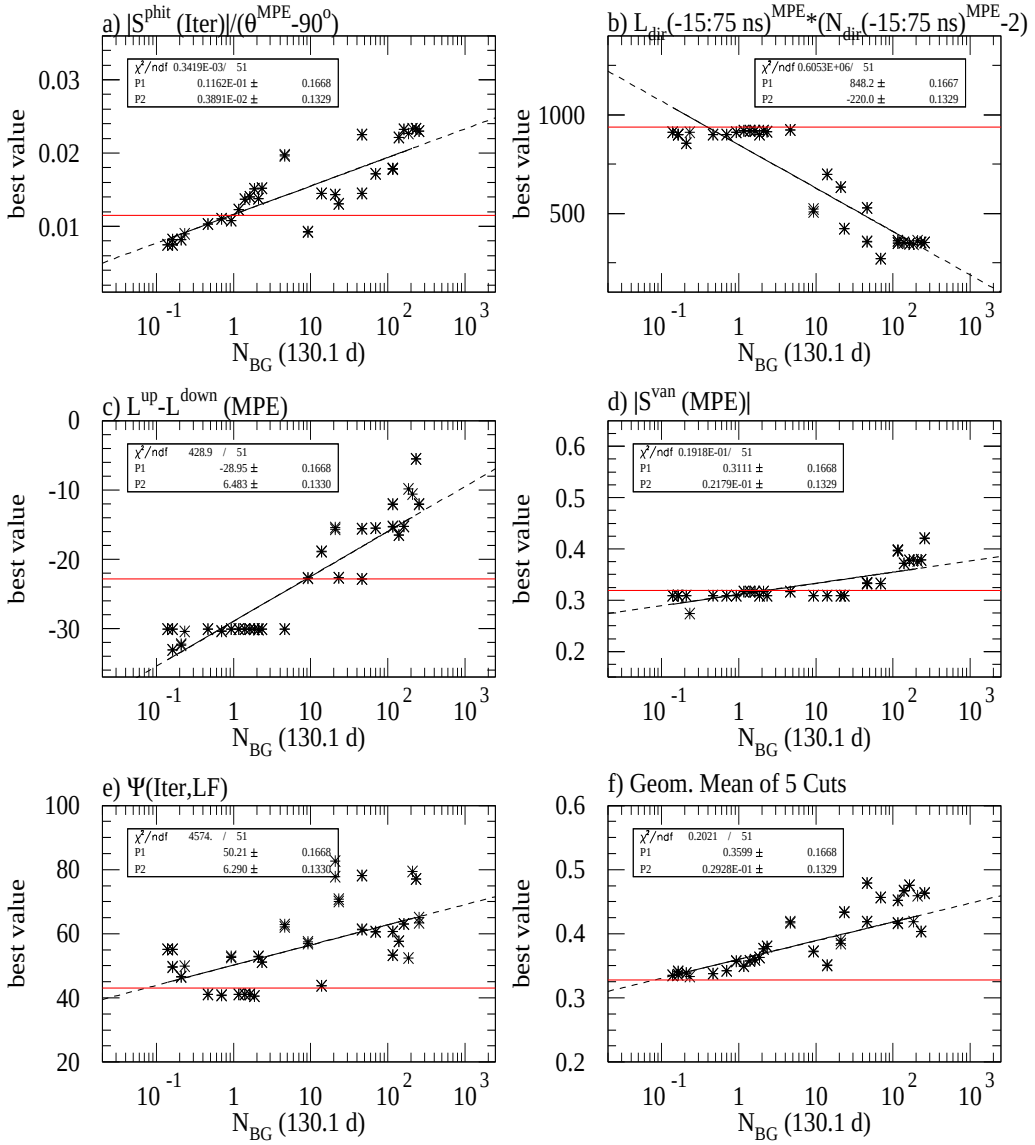

Figure 9.42: Parameterization of cuts: Shown are the five parameters $|S^{phit}|/(\theta^{MPE} - 90°)$, $(N_{direct\ hits}(-15 : 75) - 2) \times L_{direct\ hits}(-15 : 75)$, $L_{up}^{MPE} - L_{down}^{MPE}$, S^{van} and $\Psi(iter, LF)$ under variation of the offset parameter N_{BG} (x-axis). The y-axis shows the cut value yielding the highest signal passing rate while reducing background until the offset value is reached. The dashed-dotted line indicates the cut values found by the optimization mode $atm\ \nu\%experiment$. The last plot (f) shows the geometric mean of the obtained cut values.

are thus expected. This can be seen in figure 9.42 which shows the results[3] of the ex-

[3] If one wants to compare the results of these plots to figure 8.34, one has to multiply the x-axis there with the life time of the experiment (130.1 days) divided by the simulated life time of the background simulation used there (10 days). The cut values at $N_{BG} = 1$ obtained there correspond to $N_{BG} = 13$ here.

trapolation. Surprisingly, the only parameter which behaves stable is $|S^{van}(MPE)|$, the one which was taken to replace the fifth independent cut parameter. The parameters $L_{up} - L_{down}(MPE)$ and $L_{dir}(-15:75\text{ns})^{MPE} \times (N_{dir}(-15:75\text{ns})^{MPE} - 2)$ seem to saturate below offset values of $N_{BG} \sim 5$. Some parameters fluctuate stronger than others: $\Psi(Iter, LF)$ and $|S^{phit}(Iter)|/(\theta^{MPE} - 90^{\circ})$. In order to try to cancel out the effect of correlated fluctuations, the geometric mean of the five cut values (see equation 9.54) was taken and is shown in figure 9.42f. The values were fitted with a straight line according to an exponential fall-off assumption of the background (see chapter 6.4.2). Figure 9.43a shows the number of passing events obtained after application of the combination of cut values obtained with the fits. There is an obvious change of behavior of the background MC simulated with *basiev* visible at $N_{BG} \sim 3$. This behavior could be a specific feature of the weighted sampling in the MC simulation and needs further investigation. The two background simulation samples obtained with *basiev* and *corsika* have been multiplied by a factor 3. This corresponds roughly to the number of experimental events on filter level 3 divided by the corresponding number of remaining background events (normalized to 130.1 days life time). The number of events passing from experiment and atmospheric neutrino simulation show a rapid decrease at $N_{BG} \approx 10^{-2}$. This behavior is due to the chosen extrapolation of the cut parameter $|S^{phit}(Iter)|/(\theta^{MPE} - 90^{\circ})$ which reaches zero at $N_{BG} = 10^{-3}$. The region of $N_{BG} \lessapprox$ a few, is not of practical importance for the final result.

Figure 9.43b shows the ratios of the above passing rates. The number of passing events from experiment divided by the number of passing events from the atmospheric neutrino simulation flattens out gradually and converges against a constant of about 0.65. This convergence behavior is less pronounced than in the corresponding plot of analysis A (figure 8.36b), a slight decrease is still observable. As in figure 8.36b, a reasonable choice for a final set of cut values would be an event quality of about 8.

9.6 Results of Analysis B

Together with the results of the two modes using experimental data, final cut parameters and the corresponding cut values were determined. In figure 9.42 the obtained cut values (full red lines) can be compared with the extrapolation results. There is an overall agreement at $N_{BG} = 1$, except for the cut parameter $L_{up}^{MPE} - L_{down}^{MPE}$. The extrapolation result would demand a stronger cut on this parameter than the optimization mode *atm. ν%experiment*. It is interesting that this parameter was also rejected by the pure experimental mode. Table 9.6 shows the obtained cut values and a possible choice for the final cuts of analysis B. As in analysis A, the choices were made conservatively, i.e. in case of doubt, the stronger cut values were taken. These cuts were further investigated by studying their distributions with all other cuts applied (figures 9.44, 9.45 and 9.46). All obtained cut values seem to be placed correctly and cannot be relaxed. A further tightening seems unjustified as well. The distributions agree on the side which keeps the data. On the other side background appears. Figure 9.44 shows the distributions of the zenith angles of the iterative likelihood reconstruction and the multi-photo-electron reconstruction. Cuts on $cos(\theta^{iter}) < -0.087$ and $cos(\theta^{MPE}) < -0.087$ had been applied previous to the optimization procedure which were both left out for figure 9.44. One can see the sharp rise

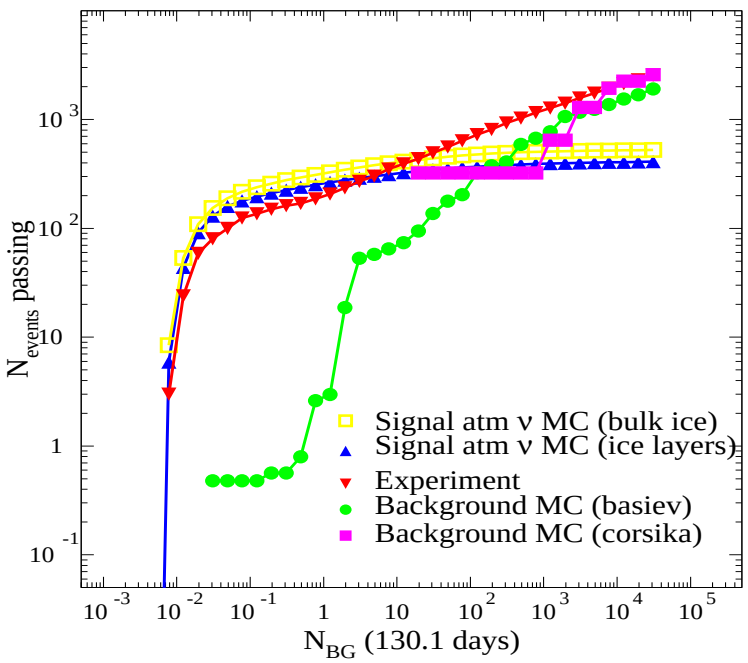

(a) Passing rates

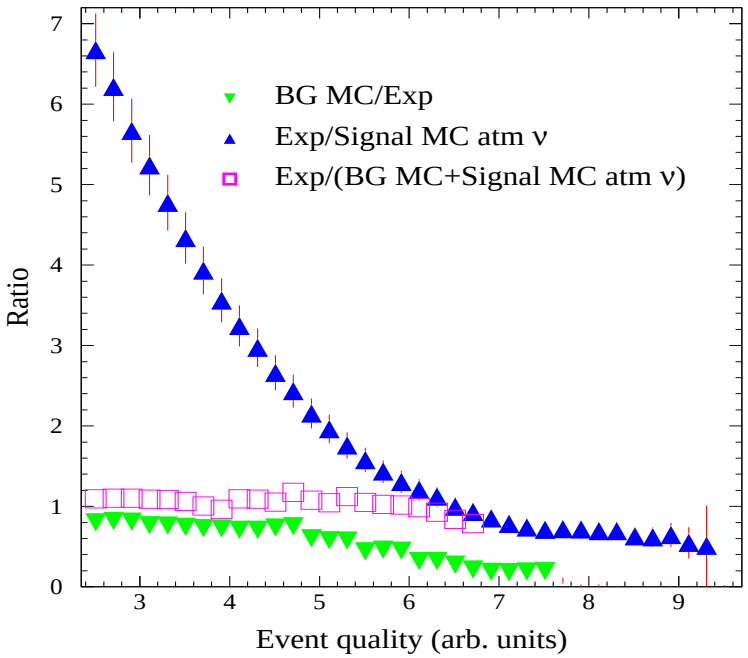

(b) Ratios of passing rates

Figure 9.43: The cut values obtained by maximization of $F[S(\vec{x}^{cut}), B(\vec{x}^{cut}), \text{offset}]$ and extrapolation of the offset-parameter. The fit results of figure 9.42 were used to calculate the cut values parameterized by the offset-parameter N_{BG} (x-axis). The resulting cuts were applied to the different data samples and the number of passing events counted (a). The background simulation samples and the offset parameter were multiplied by a factor 3 according to their relative normalization with respect to the experiment on filter level 3. The bottom plot (b) shows the ratios of passing rates. The above x-axis has been relabeled into the more adequate notation of "event quality" ($quality = -log(N_{BG}) + 7.2$). Quality does not start from 1 to indicate that the data has already been filtered before.

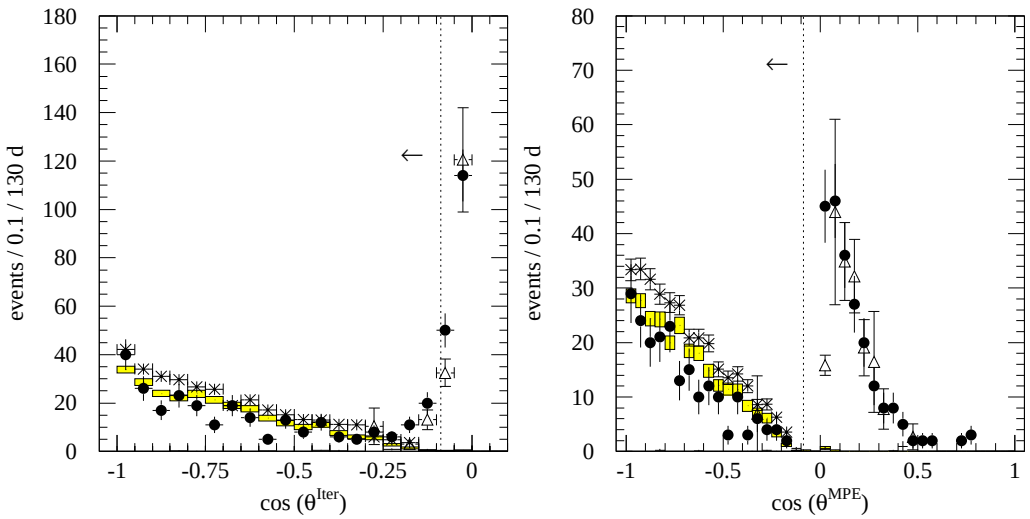

Figure 9.44: Distributions of the reconstructed zenith angles. Shown are atmospheric neutrino simulation generated with *nusim* (grey areas), atmospheric neutrino simulation generated with *nu2mu* (both including ice layers) and experimental data (points). The triangles represent the atmospheric muon background simulation generated with *basiev* (ice layers included). All cuts listed in the last column of table 9.6 were applied except for *both* cuts on the zenith angles ($\theta^{Iter} > 95°$ and $\theta^{Iter} > 95°$). At filter level 2, a cut on $\theta^{Iter} > 90°$ had been used. The dashed line marks the cut value applied in analysis B.

of background above $cos(\theta^{iter}) \sim -0.2$. The cut on the zenith angle of the multi-photo-electron fit seems to remove residual background between $-0.2 < cos(\theta^{iter}) < -0.087$ (see also figure 9.47). Note that a cut at $cos(\theta^{iter}) < -2.59$ was set in analysis B. The cut on the variable θ^{MPE} could be varied generously without big effects. Note that the experiment follows the slope of the simulated background nicely.

Figures 9.45 show the parameters $L_{up} - Ldown(MPE)$, $L_{dir}(-15 : 75\text{ns})^{MPE} \times (N_{dir}(-15 : 75\text{ns})^{MPE} - 2)$, $|S^{van}(MPE)|$ and $\Psi(Iter, LF)$ with all final cuts applied except for the one which is plotted. One can see that all four cuts remove background independently from the others. The order by which the cut parameters were found is also visible: $L_{dir}(-15 : 75\text{ns})^{MPE} \times (N_{dir}(-15 : 75\text{ns})^{MPE} - 2)$ was found at the beginning because it seems to remove the largest part of background. $\Psi(Iter, LF)$ was the last independent cut parameter and removes only little additional background. The parameter $L_{up} - Ldown(MPE)$ shows an enhancement of experimental events for values greater than about -40. This is an indication that this cut could have been set too weak.

Application of the cuts listed in the last column of table 9.6 yields 209 neutrino candidates in 130.1 days of life time. All variables which were rejected by the optimization procedure could now be used for further studies. Figure 9.47 shows the reconstructed zenith angles with different binnings. Apart from an overall deficit, no significant deviation in shape can be observed. The same holds for the reconstructed azimuth angles (figure 9.48). The length of direct hits (which showed significant deviations in the results of analysis A) are plotted in the bottom part of figure 9.48. Again, a deficit for lower

Parameter	*Exp.* (*inv.cuts*)% *experiment*	*atm.* ν% *experiment*	*atm.* ν% *BG MC*(00) extrapol.	*atm.* ν% *BG MC*(00) ind.par.	*atm.* ν% *BG MC*(98)	final choice
$\lvert S^{phit}(Iter)\rvert/(\theta^{MPE}-90^\circ) \leq$	0.0048	0.0115	0.0116	0.0075	0.0296	0.01
$\lvert S^{phit}(MPE)\rvert/(\theta^{MPE}-85^\circ) \leq$	-	-	-	-	0.0076	-
$\lvert S^{phit}(Iter)\rvert/(\theta^{Iter}-90^\circ) \leq$	0.028	-	-	-	-	-
$\lvert S^{phit}(Iter)\rvert/(\theta^{Iter}-95^\circ) \leq$	-	-	-	-	0.0099	-
$L_{dir}(-15:75)^{MPE} \times (N_{dir}(-15:75)^{MPE}-2)$	-	937 m	848 m	474 m	757 m	950 m
$L_{dir}(-15:75)^{Iter} \times N_{dir}(-15:75)^{Iter}$	1196 m	-	-	-	-	-
$L_{dir}(-1)(-15:25)^{Iter}$	-	-	-	-	(30 m)	-
$L_{up}-L_{down}(MPE) \leq$	-	-23	-29	-13	-	-30
$\lvert S^{van}(Iter)\rvert$	0.32	0.32	0.31	-	-	0.32
$\Psi(Iter, LF)$	-	43°	50°	78°	-	40°
$c.o.g._z >$	-69 m	-	-	-	-	-
θ^{Iter}	95°	95°	95°	95°	95°	95°
θ^{MPE}	95°	95°	95°	95°	95°	95°
			(offset=0.04)	(offset=0.3)	(offset=0)	

Table 9.13: The cut values obtained by the different optimization modes and the final choice of cut values (last column). The cuts on the zenith angle of two reconstructions at 95° was applied to all data previous to optimization.

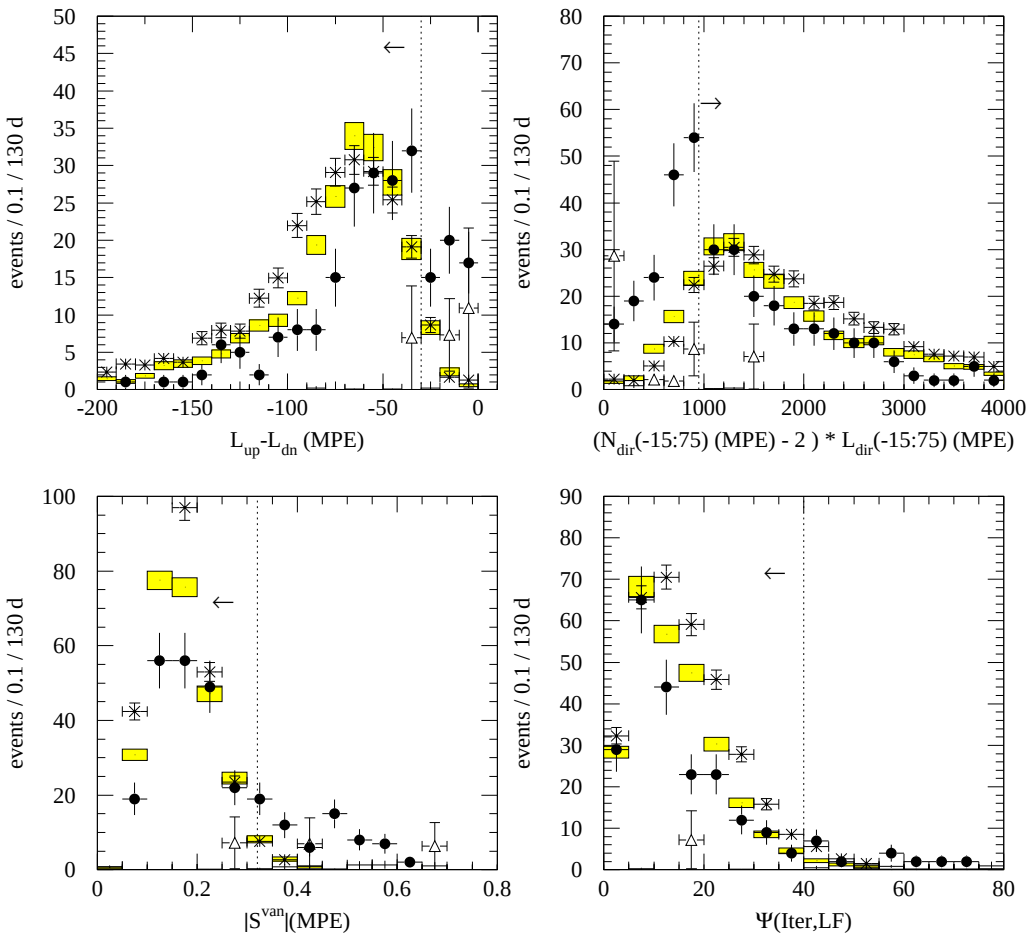

Figure 9.45: Distributions of the cut parameters used for final filtering. Shown are atmospheric neutrino simulation generated with *nusim* (grey areas), atmospheric neutrino simulation generated with *nu2mu* (both including ice layers) and experimental data (points). The triangles represent the atmospheric muon background simulation generated with *basiev* (ice layers included). All cuts listed in the last column of table 9.6 were applied except for the cut on the corresponding parameter. No cut on these variables had been applied previous to analysis B. The dashed line marks the final cut value.

quality events can be observed at 100 m $< L_{dir}(-15:75\text{ns}) <$ 200 m. There is also a discrepancy visible between the two atmospheric neutrino generators *nusim* (shaded areas) and *nu2mu* (stars).

The top part of figure 9.49 shows the zenith angles of the Bayesian reconstruction and the line fit. There is a small enhancement of experimental data visible for directions reconstructed into the upper hemisphere by the Bayesian fit. A cut on this variable however (e.g. at $\theta^{bayes} > 90°$) would remove about 50 signal events as well. The bottom plots in figure 9.49 show the space angles between the multi-photo-electron fit, the iterative likelihood fit and the line fit, respectively. Deviations of the shapes are statistically not significant.

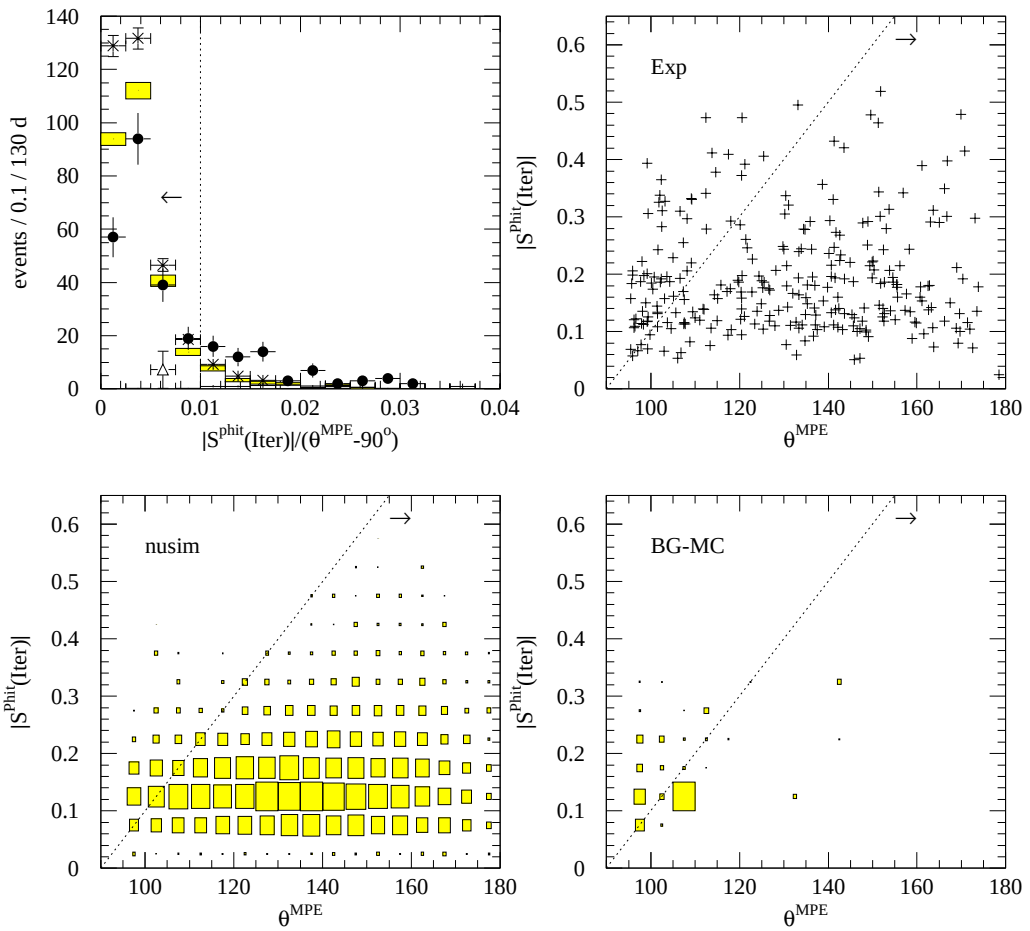

Figure 9.46: Distributions of the strongest cut parameter found by the optimization procedure: $|S^{phit}(Iter)|/(\theta^{MPE} - 90°)$. Shown are atmospheric neutrino simulation generated with *nusim* (grey areas), atmospheric neutrino simulation generated with *nu2mu* (both including ice layers) and experimental data (points). The triangles represent the atmospheric muon background simulation generated with *basiev* (ice layers included). All cuts listed in the last column of table 9.6 were applied except for this cut The dashed line marks the cut value proposed in the last column of table 9.6.

Figure 9.50 shows distributions of topological parameters of events. The top left plot gives the distribution of the vertical component of the center of gravity of hits. There is no significant deviation of the shapes visible. This is an important result since the distributions of this parameter disagreed in previous filter levels and the cut parameters used to reject parts of the unknown background were reworked especially for analysis B (see chapter 5.4.1). Also the azimuthal component $c.o.g._\phi$ shows no disagreement of shape between the experimental data and the atmospheric neutrino simulation prediction. Only the radial component $c.o.g._\rho$ shows a significant enhancement of experimental events with values of $c.o.g._\rho > 45$ m. A Kolmogorov-Smirnov test showed only a 0.5% probability that the *nusim* atmospheric neutrino distribution and the experimental one are compatible.

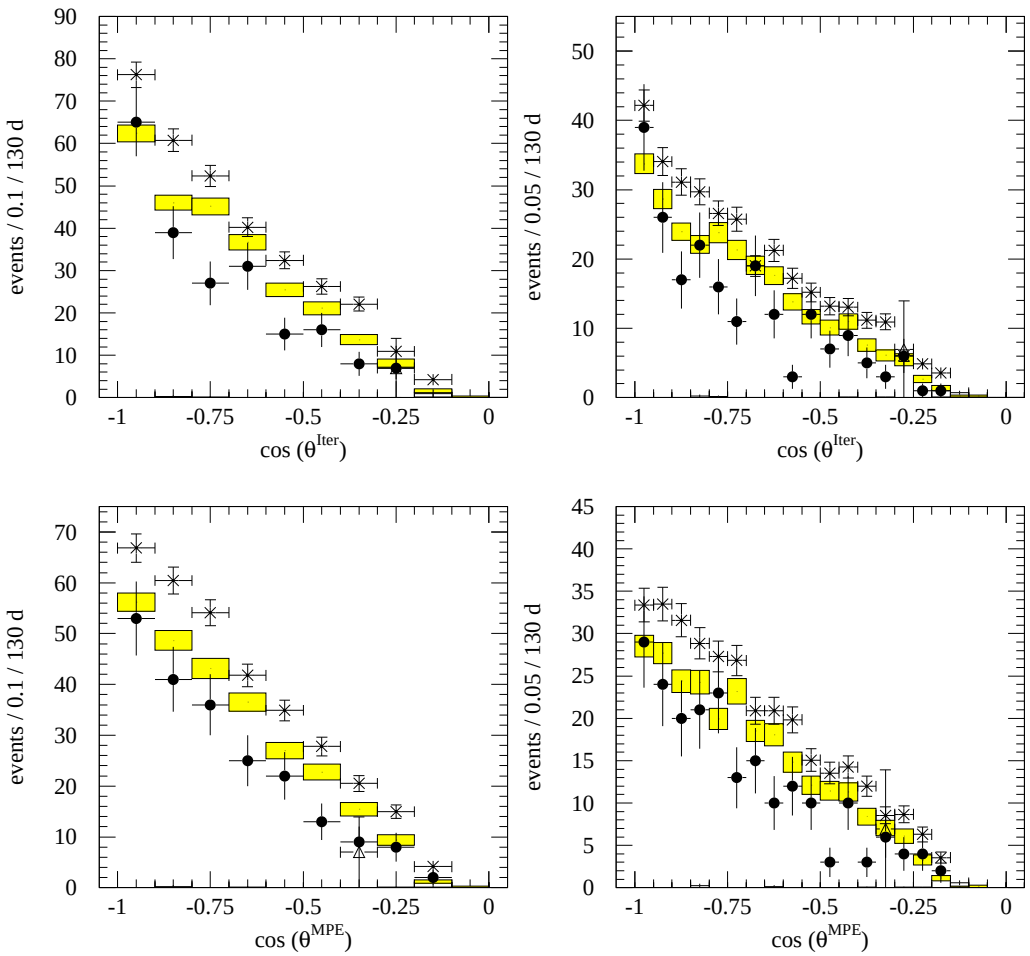

Figure 9.47: Distributions of the reconstructed zenith angles with different binnings. Shown are atmospheric neutrino simulation generated with *nusim* (grey areas), atmospheric neutrino simulation generated with *nu2mu* (both including ice layers) and experimental data (points). The triangles represent the atmospheric muon background simulation generated with *basiev* (ice layers included).

The bottom right plot shows the speed of the line fit which shows the most obvious deviation from the atmospheric neutrino simulation prediction. This feature is not new, already at trigger level (figure 5.14d), the distributions between (background) simulation and experiment disagreed[4].

Figure 9.51 (top left plot) shows the number of hit OMs N_{ch}. The distribution of experimental data is shifted towards lower channel-multiplicities which is not understood yet. This feature is further investigated in [113, 112]. Figures 9.51 show deviations from the atmospheric neutrino simulation prediction. These are the parameters $N_{dir}(-15:75\text{ns})$ from both reconstructions and the likelihood of the multi-photo-electron fit L^{MPE} which

[4]There is however indication that the background muons simulated with *corsika* describe the data much better within this variable [111].

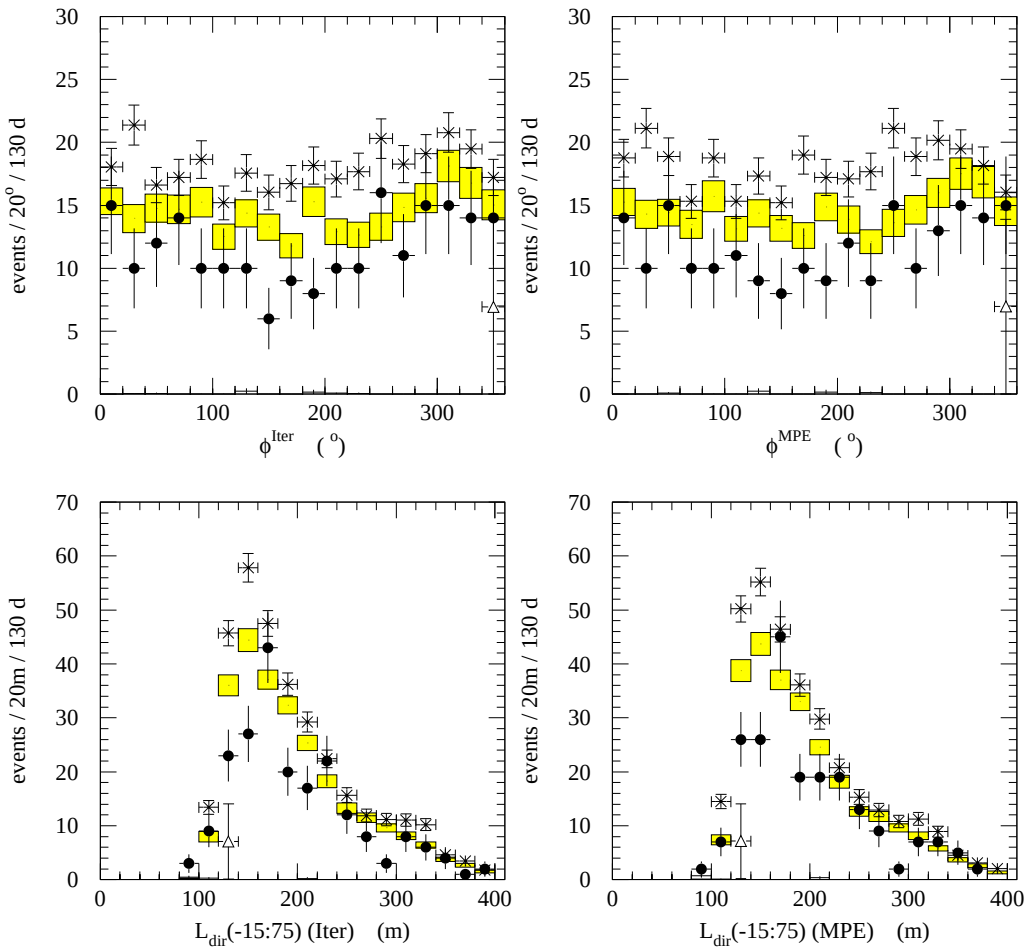

Figure 9.48: Distributions of the reconstructed azimuth angles and the length of direct hits. Shown are atmospheric neutrino simulation generated with *nusim* (grey areas), atmospheric neutrino simulation generated with *nu2mu* (both including ice layers) and experimental data (points). The triangles represent the atmospheric muon background simulation generated with *basiev* (ice layers included).

included the hit-probabilities (see eq. 5.24). This is an indication that not sufficiently understood OM sensitivities and need further investigation.

9.7 Conclusion

Analysis B investigated 76 different cut parameters on samples filtered to level 3 and two cuts on reconstructed zenith angles applied ($\theta^{Iter} > 95°$ and $\theta^{MPE} > 95°$) The resulting experimental data contained 4727 events.

As in analysis A, four different optimization modes were investigated:

1. One mode investigated the behavior of 5.6 days of atmospheric muon background (ice layers), simulated partly with the air program *basiev*, partly with *corsika*, with

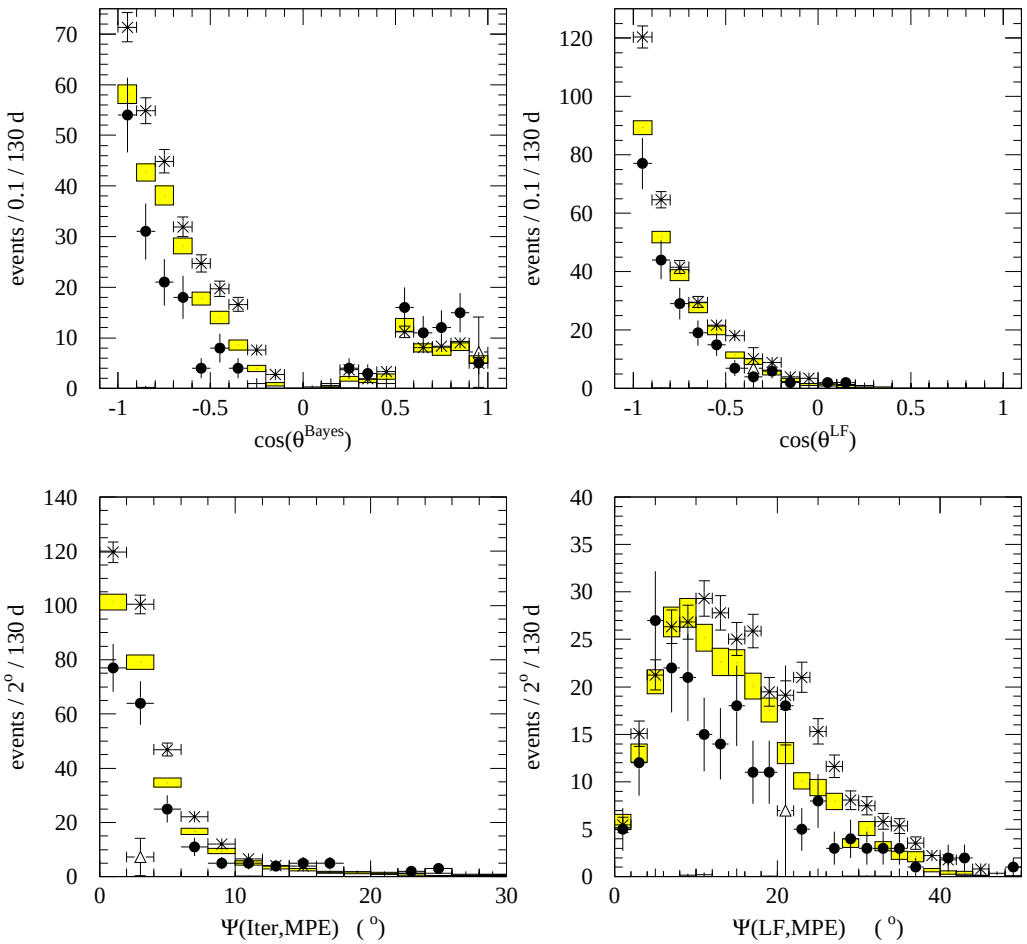

Figure 9.49: Distributions of the reconstructed zenith angle of the Bayesian reconstruction and the line fit (top figures). The bottom plots show the space angle between different reconstruction directions. Shown are atmospheric neutrino simulation generated with *nusim* (grey areas), atmospheric neutrino simulation generated with *nu2mu* (both including ice layers) and experimental data (points). The triangles represent the atmospheric muon background simulation generated with *basiev* (ice layers included).

respect to atmospheric neutrino-induced muons signal simulation (*nusim*, ice layers).

2. Another mode investigated the background simulation used in analysis A (bulk ice) compared to the atmospheric neutrino simulation (same as in point 1)

3. Two other modes investigated experimental data from 65 days life time. This data was compared once to down-going muons observed with the detector during 2.5 seconds of life time and filtered with zenith-angle inverted cuts and a second time to atmospheric neutrino-induced muons signal simulation (*nusim*, ice layers).

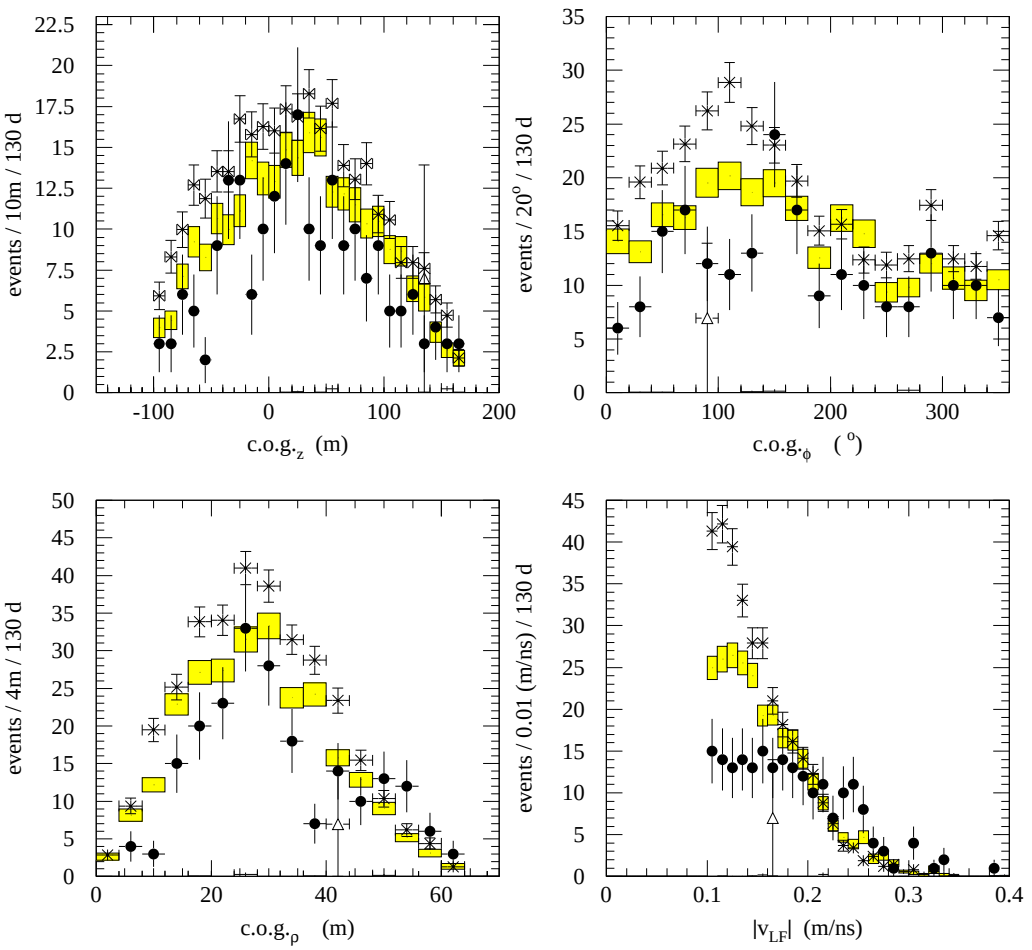

Figure 9.50: Distributions of the topological observables: Center of gravity of hits (c.o.g.) (cylindrical coordinates) and the speed of the line fit. Shown are atmospheric neutrino simulation generated with *nusim* (grey areas), atmospheric neutrino simulation generated with *nu2mu* (both including ice layers) and experimental data (points). The triangles represent the atmospheric muon background simulation generated with *basiev* (ice layers included).

The following results were obtained:

- A new functional $F[\alpha S(\vec{x}^{cut}), (B+S)(\vec{x}^{cut})] = \frac{\alpha S(\vec{x}^{cut})}{\sqrt{|(B+S)(\vec{x}^{cut}) - \alpha S(x^{cut})|}}$ was tested for the modes containing experimental data.

- The two most important cut parameters: $|S^{phit}(Iter)|/(\theta^{MPE} - 90°)$ and $L_{dir}(-15 : 75\text{ns})^{MPE} \times (N_{dir}(-15 : 75\text{ns})^{MPE} - 2)$ were found commonly within all four optimization modes. For the sample based on bulk ice background simulation, only one third parameter was needed in order to obtain the minimum set of independent cut parameters.

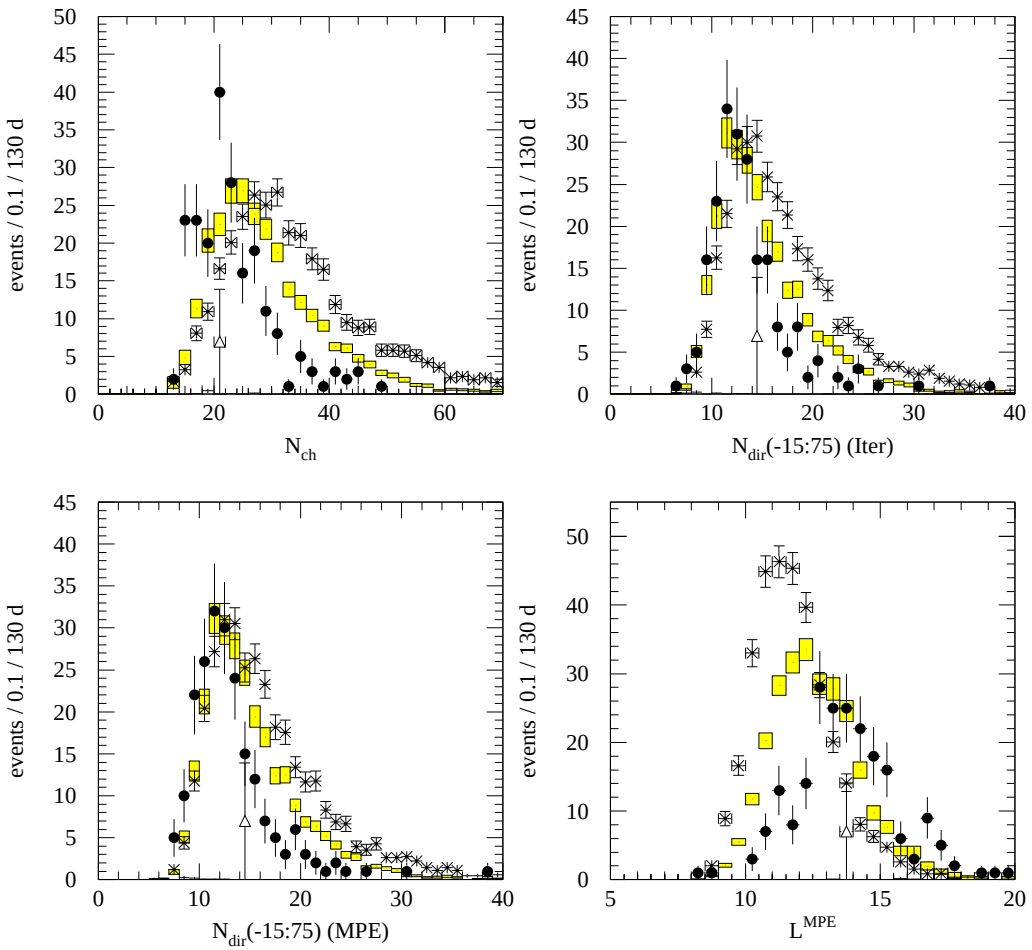

Figure 9.51: Distributions of the number of hit OMs (N_{ch}, top left figure) and the number of direct hits in a time residual window of -15:75 ns, obtained with the iterative likelihood fit, (top right figure) and the multi-photo-electron fit (bottom left figure). The bottom right figure shows the likelihood parameter of the multi-photo-electron fit. Shown are atmospheric neutrino simulation generated with *nusim* (grey areas), atmospheric neutrino simulation generated with *nu2mu* (both including ice layers) and experimental data (points). The triangles represent the atmospheric muon background simulation generated with *basiev* (ice layers included).

- The other three modes resulted each in five independent parameters. The modes $atm\ \nu\%BG\ MC$ (00) and $atm\ \nu\%experiment$ agreed within four parameters. Differences in the fifth parameter could be due to small systematic differences in the experiment and the MC simulations.

- The mode comparing only experimental data found three variables differing from the other modes and seems to avoid variables depending on the multi-photo-electron fit. A cut on the center of gravity of hits found can be explained by the apparent differences in this signal sample (e.g. the different angular spectrum).

- Extrapolation of cuts turned out to be interpolation between the results found with the help of background simulation and experiment, respectively. This is however not true for the parameter $L_{up} - L_{down}(MPE)$ which was proposed stronger by the extrapolation.

- A closer inspection of the behavior of cut values and the passing rates obtained by application of to fitted cut values showed that the background MC simulation with the *basiev* air shower program shows a change of behavior at ~ 3 events per 130.1 days life time.

- The ratio of experimental data divided by the atmospheric neutrino simulation gives a value of $\sim$0.65. This analysis thus observes 35% fewer events than expected.

- Cuts on the five variables obtained with the mode *atm ν%experiment* and the extrapolation were defined yield 209 neutrino candidates. The shapes of important distributions like the zenith angles of different reconstructions and the center of gravity of hits agree with the atmospheric neutrino signal prediction except for an overall deficit of about 35%. Some parameters, e.g. $N_{hit\ OMs}$, $N_{direct\ hits}(-15\text{ns}: 75\text{ns})(MPE\ fit)$ and the corresponding $N_{direct\ hits}(-15\text{ns}: 75\text{ns})(MPE\ fit)$, $L_{dir}(-15\text{ns}: 75\text{ns})$, L^{MPE} as well as $|v_{LF}|$ and $c.o.g._{\rho}$ show significant deviations from the simulation predictions. The deficit seems not to be due to a plain overall normalization.

Some comparisons can be made between analysis B and analysis A:

- Analysis B found almost twice as many neutrino candidates as analysis A. An investigation of the different filters applied previous to analysis A revealed that the earlier "c.o.g."-cuts remove 22% of the events found in analysis B. The filters applied previous to analysis A (eq. 7) remove 12% of the remaining signal. Applying both cut combinations to the 209 events leaves 144. The rest can be explained by the tighter cuts on θ^{iter} and $c.o.g._z$ (eq. 9). The possibility to relax these cuts also connected to the improved cut parameters in analysis B. (The four strongest cuts have not been used there.)

- Both analysis A and B found commonly deviations from the atmospheric neutrino signal prediction in the variable $L_{dir}(-15 : 75\text{ns})$ and an overall deficit of 35-40%.

- The background simulation used for analysis A showed different results in analysis B when compared to the more accurate simulation used there.

- Both functionals used for the modes containing experimental data showed reasonable results. A direct comparison was made only for the cut parameters obtained with analysis A and could be reiterated analogously for analysis B. This was beyond the time limit of this thesis and could be done at a later step.

- The cut extrapolation did not always succeed in both analyzes. In analysis A, too tight filters had been applied previous to the optimization procedure, especially on one cut parameter which was found independent there. Analysis B revealed a not

understood behavior of the background simulation and yielded unreliable saturation effects for the cut values. Another extrapolation with increased statistics is therefore planned [94].

10 Summary and Outlook

In 1997, the AMANDA-B10 neutrino detector has taken data corresponding to 130.1 days of dead-time corrected life time. Filters reduced the data from 10^9 triggers to 16600 events which have been reconstructed as upward moving muons.

An analysis was performed with the aim to reduce the number of final cut parameters to a minimum set of independent variables. For this reason, the CUTEVAL-method was developed. It investigates systematically correlations between cut parameters and rejects variables which cannot improve the signal passing rate while keeping background contamination as low as possible. Cut parameters are thought of as coordinates in a multi-dimensional hyper-space. Each point in this space $\vec{x}$ defines a combination of cut values. With the additional information about the direction of the cut, the application of a combination of cut values is represented by the coordinates of the point $\vec{x}^{cut}$.

The central idea is to maximize a functional $F[S(\vec{x}^{cut}), B(\vec{x}^{cut})]$ which depends on the investigated data samples. Simulated neutrino-induced muons together with the background simulation can be used as well as combinations of experimentally obtained data samples. Different functionals $F[S(\vec{x}^{cut}), B(\vec{x}^{cut})]$ have been developed. They maximize the passing rate of a signal sample while reducing the background contained in a reference sample. This can be a pure background simulation (consisting entirely of background) which maximizes $F[S(\vec{x}^{cut}), B(\vec{x}^{cut})] = N_{signal}/\sqrt{N_{background}}$ or combined samples containing signal and background (usually experimental data). For the last one, new functionals have been developed and investigated.

Cut parameters were tested with respect to their potential to increase the maximum achievable value of $F[S(\vec{x}^{cut}), B(\vec{x}^{cut})]$ in combination with other cut parameters. Those which failed were classified as redundant and rejected. By rejecting more and more redundant parameters, a set of independent cut variables remained which could not be reduced further.

In order to investigate the systematic differences between data samples, different optimization modes were created: Those which optimized on the MC background simulation data were used for an extrapolation procedure based on the obtained minimum set of independent cut parameters. Other modes optimized on experimental data. Obtained cut parameters and the corresponding cut values could be compared afterwards.

Two analyzes have been performed. The first one (analysis A) investigated 20 possible cut parameters. It started from a high filter level (rejection factor: 10^7). Four independent cut parameters were found by each of the four different optimization modes. Three of these resulting parameters agreed within all modes. The cut extrapolation, investigated on the pure MC simulation mode, yielded consistent results with the experimental modes albeit with large errors because of limited statistics and too tight cuts applied previous to analysis A.

The path through the cut parameter space proposed by the cut extrapolation was used to investigate passing rates of the atmospheric muon neutrino simulation and the experimental data. A deficit of about 40% in the observed total flux compared to the signal prediction was found.

Investigations were performed on the stability of the obtained cut parameter values with respect to the absolute normalization of the signal sample S. For this purpose, a

fifth optimization mode using atmospheric neutrino simulation compared to experimental data was created. Variation of the normalization factor showed no inconsistencies with the previous results. A conservative combination of cut values proposed by the four optimization modes ("final cuts") yielded 127 neutrino event candidates. Investigation of some distributions of this sample showed moderate inconsistencies with the atmospheric neutrino signal prediction.

A second analysis B was performed which used an improved detector simulation and investigated 86 cut parameters, partly based on new reconstructions. Analysis B started from a lower filter level than analysis A (rejection factor: $2 \cdot 10^5$). Again, four different optimization modes were investigated, cut parameters obtained with pure MC simulation samples were extrapolated and compared to the values obtained with experimental data. The two first cut parameters were consistent within all four optimization modes, later some differences arose. A set of five cut parameters was extrapolated and gave comparable results to the values obtained with the help of experimental data. A conservative combination of cut parameters yielded 209 neutrino candidates for 130.1 days of detector life time. Agreement between experiment and atmospheric neutrino-induced muon simulation is better with the new detector simulation used for analysis B.

The obtained sample of 209 neutrino candidates has to be investigated further. Some small inconsistencies which appeared in the course of this analysis are not understood yet.

There are also limitations of the method which have to addressed:

- The efficiency to find the global maximum of $F[S(\vec{x}^{cut}), B(\vec{x}^{cut})]$ is not 100% and decreases with the number of dimensions. A lower limit would be the number of cut parameters which did not even reach the best result of the one obtained a dimension lower (which should have been achieved though, because the maximization routine has always the possibility to neglect the additional cut parameter by setting it on its weakest value). This estimate gives a rough upper limit of 75% for two cut parameter dimensions, 64% for three dimensions and 50% for higher dimensions. Iteration of the maximum finding routine with different start values (as has been done in important cases) can increase these limits. A higher number of iterations (possible with increase CPU resources) would also help.

- For this reason, the set of independent cut parameters could be slightly different, certainly for the parameters found in higher dimensions. Corresponding deviations between the optimization modes become less significant with the investigated cut parameter dimension.

- The correct handling of the functionals used for the modes optimizing on experiment should be investigated with a combined sample of signal and background simulation. Systematic errors of the method itself could be studied that way.

- The straight line fit used in the extrapolation of the cut values could be replaced by more adequate functions which would improve the possibility to investigate passing rates and ratios of passing rates. Also, redoing the extrapolation with higher statistics would increase the significance of the found results.

- In that sense, the intention of this work was to develop the method and show that it can be applied to the AMANDA data. Although new results have been obtained, a more profound inspection of the subtleties of the method itself will be done in the future.

The CUTEVAL method and the corresponding package of computer programs is available on demand [108]. In a following step, the atmospheric neutrino analysis should be pursued with increased statistics and a better MC simulation which describes the detector as well as ice more accurately. It has to be mentioned that the optimization functional $F[S(\vec{x}^{cut}), B(\vec{x}^{cut})]$ not necessarily has to maximize on signal to background. Instead the optimization can be performed for any desired enhancement of data characteristics as function of combinations of cut parameters. Examples are the selection of events with higher energy or the improvement of the angular resolution.

Acknowledgements

I would like to thank Christopher Wiebusch for his guidance and the amount of time and commitment, he invested in this work, further Alexander Biron and Marek Kowalski for detailed proof-reading and always being available with a helping hand. I thank Christian Spiering without whom this work would not have been possible for all the support he provided. Many thanks to Matthias Leuthold who used and critisized the CUTEVAL package and helped to debug it. I also thank Peter Steffen and Stefan Hundertmark who provided important plots and Peter Niessen who showed me how to work with PAW. In general, I would like to thank the whole Zeuthen-Group which was always cooperative and helpful to me.

Vielen, vielen Dank meinen beiden Eltern, die mich bisher in allem, was ich tat, unterstützten, so auch während der Gesamtzeit meines Studiums. Diese Diplomarbeit, entstanden weit entfernt von zuhause, bedeutete für sie zugleich lange Zeiten meiner Abwesenheit. Ohne ihre Hilfe wäre ich auch finanziell nicht in der Lage gewesen, hier mein Studium abzuschließen.

Außerdem möchte ich an meinen verstorbenen Großvater erinnern, welcher sich sehr gewünscht hätte, diese Arbeit zu lesen. Leider kann ich ihm diese Freude nicht mehr bereiten,

Merci à Pauline Desnuelles qui étais fascinée par et qui as su maintenir mon enthousiasme pour la recherche en physique. Tu étais présente au cours entier de la création de ce travail.

References

[1] Y. Fukuda et al., Evidence for oscillation of atmospheric neutrinos, Phys.Rev.Lett.81 (1998), p. 1562-1567 Y. Fukuda et al., Measurement of a small atmospheric ν_μ/ν_e ratio, Phys.Lett.B433 (1998), p. 9-18

[2] Y. Fukuda et al., Study of the atmospheric neutrino flux in the multi-GeV energy range, Phys.Lett. B436 (1998), p. 33-41
see also: http://www.phys.hawaii.edu:80/~jgl/sk_release.html

[3] Y. Fukuda et al., Measurement of the flux and zenith-angle distribution of upward through-going muons by Super-Kamiokande, Phys.Rev.Lett.82 (1999), p. 2644

[4] T.J. Haines et al., Calculation of Atmospheric Neutrino-Induced Backgrounds in a Nucleon-Decay Search, Phys.Rev.Lett.57 (16), 1986, p.1986-1989

[5] T. Kafka, Recent atmospheric neutrino results from Soudan 2, Nucl. Phys. Proc. Suppl. 87 (2000), p. 186-188

[6] K.S. Hirata, Experimental Study of the Atmospheric Neutrino Flux, Phys.Lett.B205, 1988, p. 416-420 K.S. Hirata, Observation of a small atmospheric ν_μ/ν_e ratio in Kamiokande, Phys.Lett.B280 (1992), p. 146-152

[7] M.Ambrosio et al., Low energy atmospheric muon neutrinos in MACRO, Phys.Lett.B478, 2000, p. 5-9

[8] see e.g.: M. Punch et al., Detection of TeV photons from the active galaxy Markarian 421, Nature 358, p. 477, 1992 A.D. Kerrick et al., Outburst of TeV photons from Markarian 421, Ap.J.L438, 1995, L59; J. Quinn et al., Detection of Gamma Rays with E>300 GeV from Markarian 501, Astroph.J.456, p. 83-86, 1996; M. Catanese et al., Discovery of Gamma-Ray Emission above 350 GeV from BL Lacertae Object 1ES 2344+514, Astrophys.J.501, 1998, p. 616-623

[9] see e.g.: F.A. Aharonian et al., Measurement of the flux, spectrum and variability of TeV gamma-rays from Mkn 501 during a state of high activity, Astron. and Astroph. 327, p. 5-8, 1997 F.A. Aharonian et al., The time averaged TeV energy spectrum of Mkn 501 of the extraordinary 1997 outburst as measured with the stereoscopic Cherenkov telescope system of HEGRA, Astron. and Astroph. 349, 1999, p. 11-28 F.A. Aharonian et al., Observations of Mkn 421 during 1997 and 1998 in the energy range above 500 GeV with the HEGRA stereoscopic Cherenkov telescope system, Astron. and Astroph. 350, 1999, p. 757-764

[10] D.J. Bird et al., detection of a cosmic ray with measured energy well beyond the expected spectral cutoff due to cosmic microwave radiation, astro-ph/9410067, 1994

[11] S. Weinberg, Phys.Rev.Lett.19, 1967, p. 1264; A. Salam, Elementary Particle Theory, ed. N. Svantholm (Almquist and Wiksell, Stockholm, 1968); Glashow S.L., Nucl.Phys.22, 1961, p. 579

[12] J.G. Learned, K. Mannheim, High-Energy Neutrino Astrophysics, submitted to Annual Reviews of Nuclear Science, 2000 (see http://www.phys.hawaii.edu/∼jgl/)

[13] Maki Z., Nakagawa M., Sakata S., Prog.Theor.Phys.28, 1962, p. 247

[14] A. Rostovtsev, The Neutrino Telescope ANTARES, talk given at MERIDA99, Nov.10-19, 1999, Merida, Mexico

[15] see e.g. Halzen F., Tau Neutrino Appearance with a 1000 Megaparsec Baseline, Phys.Rev.Lett.81, 1998, p. 4305-4308

[16] see e.g. J.G. Learned, Intermediate-size DUMAND detectors, 1979 Summer Workshop at Khabarovsk and Lake Baikal, 1979, August 22-31

[17] Ch.H.V. Wiebusch, The Detection of Faint Light in Deep Underwater Neutrino Telescopes, RWTH Aachen, PhD-thesis, RWTH Aachen, PITHA 95/37, 1995

[18] T.K. Gaisser, F. Halzen, T. Stanev, Phys. Rep. 258, 1995, p. 173

[19] I.A. Belolaptikov et al., Astroparticle Phys. 7, 1997, p. 263

[20] The AMS Collaboration, Leptons in near earth orbit, Phys.Lett.B484, 2000, p. 10-22

[21] Physikalische Blätter 3, 56. Jahrgang, March 2000

[22] L. Nellen, K. Mannheim, P.L. Biermann, Phys.Rev.D 47, 1993, p. 5670-5274

[23] W. S. Paciesas et al., The Fourth BATSE Gamma-Ray Burst Catalog (Revised), to appear in Ap. J. Suppl, astro-ph/9903205, 1999

[24] T.K. Gaisser, Atmospheric Neutrino Flux: A Review of Calculations, Nucl.Phys.Proc.Suppl. 87, p. 145-151

[25] http://hires.physics.utah.edu/general/detect.html

[26] Particle Data Group, Europ. Phys. Journal C15, 2000, p. 132

[27] K.H.Kampert for the KASCADE Collaboration, The KASCADE Air Shower Experiment : Composition Analyzes and Energy Spectrum, proc. of the 26th International Cosmic Ray Conference, Salt Lake City, Utah, August 17-25, 1999

[28] Particle Data Group, Europ. Phys. Journal C15, 2000, p. 154-155

[29] G.R. Farrar, P.L. Biermann, Phys.Rev.Lett.81, 1998

[30] K.Mannheim, R.J.Protheroe, J.P.Rachen, astro-ph/9812398

[31] E. Waxman and J. Bahcall, High Energy Neutrinos from Cosmological Gamma-Ray Burst Fireballs, Phys.Rev.Lett.78, 1997, p. 2292-2295

[32] For an overview of existing Cosmic Ray experiments see: http://www-hfm.mpi-hd.mpg.de/CosmicRay/CosmicRaySites.html

[33] A. Lazzarini, Gravitational Wave Detection II, Proc. of the 2nd TAMA International Workshop on Gravitational Wave Detection, Oct. 19-22, Tokyo, Japan, 1999

[34] http://cossc.gsfc.nasa.gov/cossc/

[35] A. Biron, On the Rejection of Atmospheric Muons in the AMANDA Detector, DESY-THESIS-1998-014, diploma thesis, Humboldt-Universität Berlin, DESY-THESIS-1998-014, 1998.

[36] K. Hirata et al., Observation of a Neutrino Burst from Supernova SN1987A, Phys.Rev.Lett.58, 1987, p. 1490-1493

[37] R.M.Bionta et al., Observation of a Neutrino Burst in Coincidence with Supernova SN1987A in the Large Magellanic Cloud, Phys.Rev.Lett.58, 1987, p. 1494-1496

[38] M.A. Markov, I.M. Zheleznykh, On High Energy Neutrino Physics in Cosmic Rays, Nucl.Phys.27, 1961, p.385-394

[39] The DUMAND Collaboration, DUMAND II, Proposal to Construct a Deep-Ocean Laboratory for the study of High Energy Neutrino Astrophysics and Particle Physics, Hawaii DUMAND Center, Univ. of Hawaii, 1988.

[40] R. Gandhi, Ch. Quigg, M. Hall Reno, I. Sarcevic, Ultrahigh-Energy Neutrino Interactions, Astropart.Phys.5, 1996, p. 81-110

[41] M. Kowalksi, On the Reconstruction of Cascade-Like Events in the AMANDA Detector, Humboldt-Universität, diploma thesis, Humboldt Universität, Berlin, 1999.

[42] Particle Data Group, Europ. Phys. Journal C15, 2000, p. 152, p.171

[43] P. Lipari, T. Stanev, Propagation of multi-TeV muons, Phys.Rev.D44, 1991, p. 3543-3554

[44] F.W. Stecker, M.H. Salomon, Sp.Sci.75, 1996, p. 341

[45] K. Mannheim, High-energy neutrinos from extra-galactic jets, Astropart.Phys.4, 1995, p. 295-302

[46] Propagation of ultra high energy protons and gamma rays over cosmological distances and implications for topological defect models, Astropart.Phys. 4, 1996, p. 253-269

[47] G. Sigl et al., Probing grand unified theories with cosmic-ray, gamma-ray and neutrino astrophysics, Phys.Rev.D59, 043504, 1998, hep-ph/9809242

[48] W. Rhode et al., Limits on the flux of very high energy neutrinos with the Fréjus detector, Astropart.Phys. 4, 1996, p. 217-225

[49] R.M.Blatrusaitis et al., Limits on deeply penetrating particles in the $> 10^{17}$ eV cosmic-ray flux, Phys.Rev.D31, 1985, p.2191-2198

[50] M. Thunmann, G. Ingelmann, P. Gondolo, Charm Production and High Energy Atmospheric Muon and Neutrino Fluxes, Astropart.Phys.5, 1996, p. 309-322

[51] T.K. Gaisser, Cosmic Rays and Particle Physics, Cambridge University Press, 1990

[52] Ch. Wiebusch et al., Supplementary Proposal to Complete Construction of a Deep-Ocean Laboratory for the study of High Energy Neutrino Astrophysics and Particle Physics. Hawaii DUMAND Center, Univ. of Hawaii, 1994.

[53] V.A. Balkanov et al., Registration of Atmospheric Neutrinos with the BAIKAL Neutrino Telescope NT-96, Astropart.Phys.12 (1999), 1999, p. 75-86

[54] F. Halzen, Ice Fishing for Neutrinos, http://amanda.berkeley.edu/www/ice-fishing.html

[55] P. Amram et al., Background Light in Potential Sites for the ANTARES Undersea Neutrino Telescope, Astropart.Phys.13, 2000, p. 127-136

[56] P. Askebjer et al., Optical Properties of the South Pole Ice at Depths Between 0.8 and 1 Kilometer, Science 267, p. 1147-1150, 1995

[57] A. Biron et al., Upgrade of AMANDA-B towards AMANDA-II, DESY-Zeuthen, 1997

[58] L. Moscoso, The ANATARES Project, proc. of 8^{th} Int. Workshop on Neutrino Telescopes, Venice, Feb. 23-26, 1999, p. 99-109

[59] S.A. Sotiriou, Nestor: A Status Report, Proc. of Workshop on Simulation and Analysis Methods for Large Neutrino Telescopes, DESY Zeuthen, Germany, July 6-9, 1999, DESY-PROC-1999-01 p. 61
http://www.roma1.infn.it/nestor/win97/espcrc2.html

[60] C. De Marzo, NEMO, A km^3 NEutrino Meditarrenean Observatory, Talk presented at NOW 2000, Europhysics Neutrino Oscillations Workshop, Conca Specchiulla, Italy, Sept. 9-16, 2000

[61] Zh. Djilkibaev, Proc. of Workshop on Simulation and Analysis Methods for Large Neutrino Telescopes, DESY Zeuthen, Germany, July 6-9, 1999, DESY-PROC-1999-01, 1999, p. 132

[62] Particle Data Group, Europ. Phys. Journal C15, 2000, p. 80

[63] J.D. Jackson, Klass. Elektrodynamik, 2. Auflage, de Gruyter, Berlin, 1983, p. 762-766

[64] Particle Data Group, Europ. Phys. Journal C15, 2000, p. 172

[65] N.M. Budnev, R.R. Mirgazov,A.V.Rzhetshizki, B.A. Tarashansky, Proc. of Workshop on Simulation and Analysis Methods for Large Neutrino Telescopes, DESY Zeuthen, Germany, July 6-9, 1999, DESY-PROC-1999-01, 1999, p. 165

[66] A. Kouchner, Rencontres de Moriond, March 2000

[67] K. Woschnagg, http://amanda.berkeley.edu/kurt/ice2000/hq.html

[68] A. Silvestri, Search for Neutrino Bursts from Supernovae with the AMANDA Detector, diploma thesis, Humboldt Universität Berlin, 2000.

[69] K.D. Hanson, Crosstalk in 1997 AMANDA raw data, AMANDA Internal Report 20000801, 2000

[70] S. Hundertmark, Simulation und Analyse von Myonereignissen im AMANDA-B4-Neutrinoteleskop, PhD-thesis submitted to the Humboldt Universität Berlin, 1999, DESY-THESIS-1999-010

[71] 1997 Diagnostics Data Analysis
http://grimm.berkeley.edu/~ped/datastat/

[72] S.N. Boziev et al., INR-Preprint P-0630, 1989

[73] W. Lohmann, R. Kopp, R. Voss, Energy Loss of Muons in the Energy Range 1-10000 GeV, CERN-85-03, Geneva 1985

[74] S. Hundertmark , AMASIM Neutrino Detector Simulation Program, Proc. of Workshop on Simulation and Analysis Methods for Large Neutrino Telescopes, DESY Zeuthen, Germany, July 6-9, 1999, DESY-PROC-1999-01, 1999 p. 276-286

[75] St. Hundertmark, AMASIM - Simulation tool for AMANDA.
http://www.ps.uci.edu/~hundert/amanda/irvine/amasim.html

[76] P. Lipari, Astropart.Phys. 1., 1993, p. 195-227

[77] E. Dalberg, A Search for Neutralino Dark Matter with the AMANDA-B10 Detector, PhD-thesis, Stockholm University, 1999

[78] G. Hill, Detecting neutrinos from AGN: New fluxes and cross sections Astropart.Phys. 6, p. 215-227, 1997

[79] St. Hundertmark, private communication

[80] A. Biron, M. Leuthold, Ch.H. Wiebusch, Separation of ν_μ event candidates in AMANDA-B10, AMANDA Internal Report 19990902, 1999

[81] K. Woschnagg, Optical Properties of South Pole Ice at Depths from 140 to 2300 Meters, Proc. of the 23^{rd} International Cosmic Ray Conference, July 19-30, 1993, Vol. 2, p. 200

[82] J. Klug, Enhancement of the Up/Down Signal Ratio and Crosstalk Studies in AMANDA, Diploma thesis, Uppsala University, Sweden, 1997

[83] The Zeuthen MC mass production
http://www.ifh.de/~biron/mc/

[84] S. Hundertmark, Vertical Ice Properties for the AMANDA-Simulation, AMANDA Internal Report, 2000

[85] AMANDA B10 mass00 production http://www.ps.uci.edu/~hundert/amanda/mass00/mass00main.html

[86] P. Steffen, private communication

[87] A. Biron, M. Leuthold, C. Wiebusch , First and Second Level Reconstruction of 97 Muon Data, AMANDA Internal Report 19990701, update 19990901, 1999

[88] A. Biron, M. Leuthold, Ch.H. Wiebusch, Update on Level 1+2 processing of 97 muon data, AMANDA Internal Report 19990901, 1999.

[89] Ch. Wiebusch, Muons reconstruction with AMANDA, Proc. of Workshop on Simulation and Analysis Methods for Large Neutrino Telescopes, DESY Zeuthen, Germany, July 6-9, 1999, DESY-PROC-1999-01, p. 302-316

[90] On the run-selection in 1997 data http://www.ifh.de/~wiebusch/rundat/rundat.html

[91] A. Bouchta, private communication

[92] V.J.Stenger, Track fitting for the DUMAND Octagon, HDC-1-90, Hawaii, 1990

[93] D. Pandel, Measurement of water and detector parameters and reconstruction of muons to energies of 100TeV with the Baikal Neutrino Telescope NT-72. Diploma thesis, Humboldt Universität Berlin, 1996.

[94] A. Biron, M. Gaug, W. Rhode, Ch. Wiebusch, R. Wischnewski, Detection of Atmospheric Neutrinos in 97 data, AMANDA Internal Report, in preparation

[95] T. de Young, Talk presented at the AMANDA meeting, Sept. 19-24, Irvine, USA.

[96] W. Rhode, private communication

[97] G. Barouch et al., Search for Atmospheric Neutrino Events in AMANDA-B10, AMANDA Internal Report 20000101, 2000

[98] Ch. Wiebusch, talk presented at the AMANDA analysis meeting, Zeuthen, Germany, March 10-12, 2000

[99] G. Hill, Status of the search for high energy neutrinos with the AMANDA B10 detector, AMANDA Internal Report, 2000

[100] G. Hill and T. Deyoung, talks presented at the AMANDA analysis meeting, Zeuthen, Germany, March 10-12, 2000

[101] P. Loriza, O. Botner, A. Hallgren, C. Perez de los Heros, Search for vertically up-going muons with the AMANDA-B10 detector, AMANDA Internal Report 20000302, 2000

[102] E. Andres et al., DESY-99-073, astro-ph/9906203, Astropart. Phys. 13, 2000, p. 1-20

[103] A. Karle, Observation of Atmospheric Neutrino Events with AMANDA, Proc. of the 26th International Cosmic Ray Conference, Salt Lake City, Utah, August 17-25, 1999

[104] G. Hill and T. Deyoung, Status of UW neutrino search, talk presented at the AMANDA meeting, Philadelphia, USA, Oct. 4-6, 1999

[105] M. Gaug, P. Niessen, Ch. Wiebusch, Investigations on Smoothness observables, Amanda Internal Report 20000201, 2000.

[106] G. Zech, Comparing Statistical Data to Monte Carlo Simulation - Parameter Fitting and Unfolding, DESY-PROC-1995-03, 1995 ISSN 0418-9833

[107] W.H. Press, S.A. Teucholsky, W.T. Vetterling, B.P.Flannery, Numerical Recipes in FORTRAN, 2nd edition, Cambridge Univ. Press, 1992, p. 402-406

[108] The CUTEVAL homepage: http://www.ifh.de/∼gaug/cutev.html

[109] M. Gaug, CUTEVAL, A library for Cut-Evaluation of the AMANDA cut sets, Installation and user's guide, http://www.ifh.de/∼gaug/cuteval.ps.gz

[110] Ch. Wiebusch, private communication

[111] P. Steffen, Ch. Wiebusch, private communication

[112] M. Leuthold, Derivation of limits for high-energy neutrino fluxes with the AMANDA-B10 detector. PhD thesis, in preparation.

[113] M. Leuthold, Systematics on signal expectation, AMANDA Internal report, in preparation.

[114] Ch. Spiering, Workshop on Simulation and Analysis Methods for Large Neutrino Telescopes, DESY Zeuthen, Germany, July 6-9, 1999, DESY-PROC-1999-01, 1999

A Definitions Used to Work with Step-Wise Defined Functions

Each event has a well-defined set of n pre-calculated parameters which can be thought of as coordinates $x_1, x_2, ..., x_i, .., x_n$ in an n-dimensional parameter space. Cutting on one of these parameters has to imply two informations:

- A cut value x_i^{cut} which is the coordinate of x_i
- Information about which side (coordinates of x_i higher or lower than x_i^{cut}) be removed or kept in the data sample.
- A "weakest" value x_i^0 which keeps any event in the data sample [1]

Let us now assume a distribution $F(\vec{x})$ of N events - each with well-defined parameters $\{x_i\}$. Each set of cut-values $\vec{x}^{cut}$ then defines:

$$F(\vec{x}^{cut}) = \int_{x_1^0}^{x_1^{cut}} dx_1 \int_{x_2^0}^{x_2^{cut}} dx_2 \ldots \int_{x_n^0}^{x_n^{cut}} dx_n \sum_{j=1}^{N_S} \delta(\vec{x} - \vec{x}^j) + \varepsilon \tag{A.55}$$

which is the number of events remaining after cut plus a small number ε. This number was set to 0.5 for background samples without weighting and $\frac{0.5*\tilde{n}}{\sum_i w_i}$ for events weighted with a factor w_i. $\tilde{n}$ is the equivalent number of events, defined as $\tilde{n} = (\sum_i w_i)^2 / \sum_i w_i^2$, which is the number of unweighted events that would have the sum relative error as the weighted sum [106].

If there is a signal distribution $S(\vec{x})$ and a background one $B(\vec{x})$, every point $\vec{x}^{cut}$ in the cut parameter hyperspace defines a value

$$R(\vec{x}^{cut}) = S(\vec{x}^{cut}) / \sqrt{B(\vec{x}^{cut})} \tag{A.56}$$

$R(\vec{x}^{cut})$ will look like a multidimensional step function.

In the following, I will give a possible definition for the "derivation" of a function $F(\vec{x})$ defined in A.55. This will allow to find maximum conditions without having to deal with an ensemble of delta-functions spread over the whole space. Let us define a "bin" $\Delta_i^{12}\vec{x} = \vec{x}_i^2 - \vec{x}_i^1$ in cut parameter space. Then, $F'(\frac{\vec{x}^1+\vec{x}^2}{2})$ is defined as:

$$\begin{aligned} \frac{\partial F(\vec{x})}{\partial \vec{x}_i} &= lim_{\Delta_i^{12}\vec{x} \to min.binsize} \frac{F(x_1, \ldots, x_i^2, \ldots, x_n) - F(qx_1, \ldots, x_i^1, \ldots, x_n)}{|\Delta_i^{12}\vec{x}|} \\ F'(\frac{\vec{x}^1 + \vec{x}^2}{2}) &= \sum_{i=1}^{n} \frac{\partial F(\vec{x})}{\partial \vec{x}_i} \end{aligned} \tag{A.57}$$

Min. Binsize is defined as the binsize that makes F not change at all over the whole range of the bin.

[1] Usually, this value is given in a natural way: It is e.g. 0 for lenghts or numbers of "direct hits" or 1 for Smoothness and ratios of eigenvalues of the tensor of intertia.

B Maximum Conditions for S vs. B Distributions

B.1 Derivation of the Maximum Condition for $F[\vec{x}^{cut}] = \alpha S(\vec{x})/(B(\vec{x}))^{\beta}$

Following the error propagation yields:

$$\begin{aligned} F'[\vec{x}^{cut}] &= \frac{\alpha S'(\vec{x})}{(B(\vec{x}))^{\beta}} - \beta\frac{\alpha S(\vec{x})}{B(\vec{x})^{\beta+1}}B'(\vec{x}) = 0 \\ \frac{S'(\vec{x})}{S(\vec{x})} - \beta\frac{B'(\vec{x})}{B(\vec{x})} &= 0 \\ ln(S(\vec{x}))' &= \beta ln(B(\vec{x}))' \\ ln(S(\vec{x}^{cut+\epsilon})) - ln(S(\vec{x}^{cut-\epsilon})) &= \beta \cdot ln(B(\vec{x}^{cut+\epsilon})) - ln(B(\vec{x}^{cut-\epsilon})) \\ lim_{|\vec{x}^2-\vec{x}^1|\to min.binsize}\frac{S(\vec{x}^2)}{S(\vec{x}^1)} &= \frac{B(\vec{x}^2)^{\beta}}{B(\vec{x}^1)} \end{aligned} \tag{B.58}$$

C Maximum Conditions for S vs. $(S+B)$ Distributions

C.1 The Maximum Condition for $F[\vec{x}^{cut}] = \alpha S(\vec{x})/(S(\vec{x}) + B(\vec{x}))^{\gamma}$

$$\begin{aligned} F'[\vec{x}^{cut}] &= \frac{\alpha S'(\vec{x})}{(S(\vec{x})+B(\vec{x}))^{\gamma}} - \gamma\frac{\alpha S(\vec{x})}{(S(\vec{x})+B(\vec{x}))^{\gamma+1}}(S'(\vec{x})+B'(\vec{x})) = 0 \\ S'(\vec{x}) &\approx \gamma(S'(\vec{x})+B'(\vec{x}))(1-\frac{B(\vec{x})}{S(\vec{x})}) \\ S'(\vec{x})(1-\gamma+\gamma\frac{B(\vec{x})}{S(\vec{x})}) &\approx \gamma B'(\vec{x}))(1-\frac{B(\vec{x})}{S(\vec{x})}) \qquad \text{(C.59)} \\ \to_{\gamma=\frac{1}{2}}\ S'(\vec{x})(1+\frac{B(\vec{x})}{S(\vec{x})}) &= B'(\vec{x})(1-\frac{B(\vec{x})}{S(\vec{x})}) \qquad \text{(C.60)} \\ \to_{\gamma\to 0}\ S'(\vec{x}) &= 0 \qquad \text{(C.61)} \\ \to_{\gamma\to 1}\ \frac{S'(\vec{x})}{S(\vec{x})} &= \frac{B'(\vec{x})}{B(\vec{x})}(1-\frac{B(\vec{x})}{S(\vec{x})}) \qquad \text{(C.62)} \\ \to_{\gamma<1} & \quad \text{no solution} \qquad \text{(C.63)} \end{aligned}$$

C.2 The Maximum Condition for $F[\vec{x}^{cut}] = \alpha S(\vec{x}) - (S(\vec{x}) + B(\vec{x}))$

$$\begin{aligned} F'[\vec{x}^{cut}] &= \alpha S'(\vec{x}) - (S'(\vec{x}) + B'(\vec{x})) = 0 \\ (\alpha-1)S'(\vec{x}) &= B'(\vec{x})) \\ \to_{\alpha\to 1}\ B'(\vec{x}) &= 0 \qquad \text{(C.64)} \\ \to_{\alpha<1} & \quad \text{no solution} \qquad \text{(C.65)} \end{aligned}$$

C.3 The Maximum Condition for $F[\vec{x}^{cut}] = \frac{\alpha S(\vec{x})}{((S+B)(\vec{x})-\alpha S(\vec{x}))^{\gamma}}$

$$F'[\vec{x}^{cut}] = \frac{\alpha S'(\vec{x})}{((1-\alpha)S(\vec{x})+B(\vec{x}))^{\gamma}} - \gamma\frac{\alpha S(\vec{x})}{((1-\alpha)S(\vec{x})+B(\vec{x}))^{\gamma+1}}((1-\alpha)S'(\vec{x})+B'(\vec{x})) = 0$$

$$\frac{S'(\vec{x})}{S(\vec{x})} - \gamma\frac{((1-\alpha)S'(\vec{x})+B'(\vec{x}))}{((1-\alpha)S(\vec{x})+B(\vec{x}))} = 0 \tag{C.66}$$

$$\rightarrow_{\alpha\rightarrow 1} \quad \frac{S'(\vec{x})}{S(\vec{x})} = \gamma\frac{B'(\vec{x})}{B(\vec{x})} \tag{C.67}$$

$$\begin{aligned}
\rightarrow_{\alpha<<1} \quad S'(\vec{x}) &= \frac{\gamma}{(1-\alpha)}\frac{((1-\alpha)S'(\vec{x})+B'(\vec{x}))}{(1+\frac{B(\vec{x})}{(1-\alpha)S(\vec{x})})} \\
S'(\vec{x}) &\approx \frac{\gamma}{(1-\alpha)}((1-\alpha)S'(\vec{x})+B'(\vec{x}))(1-\frac{B(\vec{x})}{(1-\alpha)S(\vec{x})}) \\
S'(\vec{x})(1-\gamma+\frac{B(\vec{x})}{(1-\alpha)S(\vec{x})}) &\approx B'(\vec{x})\cdot\frac{\gamma}{(1-\alpha)}(1-\frac{B(\vec{x})}{(1-\alpha)S(\vec{x})}) \\
S'(\vec{x})(1-\gamma+\frac{B(\vec{x})}{S(\vec{x})}) &\approx B'(\vec{x})\cdot\gamma(1-\frac{B(\vec{x})}{S(\vec{x})}) \qquad (C.68)
\end{aligned}$$

$$\rightarrow_{\alpha>1}^{\beta=\alpha-1>0} \frac{S'(\vec{x})}{S(\vec{x})} = \gamma\frac{-\beta S'(\vec{x})+B'(\vec{x})}{-\beta S(\vec{x})+B(\vec{x})} \quad \text{(fluctuating solution)} \tag{C.69}$$

$$\tag{C.70}$$

C.4 The Maximum Condition for $F[\vec{x}^{cut}] = \frac{\alpha S(\vec{x})}{|(S+B)(\vec{x})-\alpha S(\vec{x})|^{\gamma}}$

$$\begin{aligned}
F'[\vec{x}^{cut}] = \frac{\alpha S'(\vec{x})}{|(1-\alpha)S(\vec{x})+B(\vec{x})|^{\gamma}} &- \gamma\frac{\epsilon\cdot\alpha S(\vec{x})}{|(1-\alpha)S(\vec{x})+B(\vec{x})|^{\gamma+1}}((1-\alpha)S'(\vec{x})+B'(\vec{x})) = 0 \\
\frac{S'(\vec{x})}{S(\vec{x})} &- \gamma\frac{(1-\alpha)S'(\vec{x})+B'(\vec{x})}{(1-\alpha)S(\vec{x})+B(\vec{x})} = 0 \\
\rightarrow_{\alpha\rightarrow 1} \quad \frac{S'(\vec{x})}{S(\vec{x})} &= \gamma\frac{B'(\vec{x})}{B(\vec{x})} \qquad (C.71)
\end{aligned}$$

$$\tag{C.72}$$

D The Downhill-Simplex Algorithm

If the dimension of the parameter space is $n \geq 2$, the algorithm performs the following steps:

1. Define a "box" within which cut parameters are allowed to vary.
2. Define a simplex of n orthogonal vectors plus one.
3. Evaluate the functions $F(\vec{x}^i)$ at every corner i of the simplex.
4. Store the points:
   - $\vec{x}^{low}$ with the lowest value of F,
   - $\vec{x}^{low-1}$ with the seconed lowest value of F,
   - $\vec{x}^{high}$ with the highest value of F.
5. Calculate $\vec{x}^{center} = \frac{1}{n} \sum_{i \neq low} \vec{x}^i$
6. Reflect the point x^{low} through the center of the rest of the simplex and get a trial point x^{try}: $\vec{x}^{try} = 2 \cdot \vec{x}^{center} - \vec{x}^{low}$
7. If a coordinate x_j^{try} lies outside the box, the corresponding coordinate of the box border is taken as $\vec{x}^{try}$ instead.
8. Evaluate $F(\vec{x}^{try})$.
9. If $F(\vec{x}^{try}) > F(\vec{x}^{high})$, expand by a factor of 2 point $\vec{x}^{try}$ with respect to the center of the rest of the simplex: $\vec{x}^{new} = 2 \cdot \vec{x}^{try} - \vec{x}^{center}$ Check 6) and goto 3).
10. If $F(\vec{x}^{try}) < F(\vec{x}^{high})$ and $F(\vec{x}^{try}) \geq F(\vec{x}^{low-1})$ replace $\vec{x}^{low}$ by $\vec{x}^{try}$ and goto 3).
11. If $F(\vec{x}^{try}) \leq F(\vec{x}^{low-1})$, shrink by a factor of $1/2$ point $\vec{x}^{try}$ with respect to the center of the rest of the simplex and replace $\vec{x}^{low}$ by $\vec{x}^{newtry}$: $\vec{x}^{newtry} = \frac{1}{2} \cdot (\vec{x}^{try} + \vec{x}^{center})$
    - If $F(\vec{x}^{newtry}) \leq F(\vec{x}^{low})$ contract the whole simplex by a factor of $1/2$ around $\vec{x}^{high}$: $\vec{x}^i = \frac{1}{2}(\vec{x}^i + \vec{x}^{high})$

    Goto 3).

E Relation between T_0, K, α and Number of Dimensions n

To motivate the calculation of T_0, I calculated the probability that all (n+1) points of the simplex jump by more than a certain value ΔF in one calculation loop. Since the evaluated function value is modified by -T*ln([0,1]), this probability gives:

$$\begin{aligned} P_{n+1} &= exp(-x) \\ x &= \frac{\Delta F \cdot (n+1)}{T} \end{aligned} \tag{E.73}$$

Since T is $T(k, K, \alpha, T_0)$, P_{n+1} will become $P(k, K, \alpha, T_0, n+1)$

$$\begin{aligned} P_{n+1} &= exp(\frac{-x}{(1-\frac{k}{K})^{\alpha}}) \\ x &= \frac{\Delta F \cdot (n+1)}{T_0} \end{aligned} \tag{E.74}$$

Now, the probability that during K loops, once all points of the simplex jump by more than ΔF gives

$$\begin{aligned} P_{n+1}^K &= 1 - \prod_{k=1}^{K} (1 - P_{n+1}^k(k, K, \alpha, T0, n+1)) \\ &= 1 - (1-P_1)(1-P_2)(1-P_3)\cdots \\ &= \sum_{k=1}^{K} P_k - \sum_{k \neq l}^{K,L} P_k P_l + \sum_{k \neq l \neq m}^{K,L,M} P_k P_l P_m - \cdots \end{aligned} \tag{E.75}$$

Now, assuming that x is much bigger then 1 (which will have to be verified later), we will take only the leading first term in the last equation. Only terms with low k will contribute to the remaining sum, so we can make an approximation:

$$\frac{1}{(1-\frac{k}{K})^{\alpha}} = 1 + \frac{\alpha * k}{K} - \cdots \qquad \text{for} \frac{k}{K} \ll 1 \tag{E.76}$$

and thus

$$\begin{aligned} P_{n+1}^K &= exp(-x) \sum_{k=1}^{K} exp(-\frac{\alpha * x}{K})^k + \cdots \\ &\approx exp(-x) \frac{1 - exp(-\frac{\alpha * x * (K+1)}{K})}{1 - exp(-\frac{\alpha * x}{K})} \\ &\approx exp(-x) \frac{1}{1 - exp(-\frac{\alpha * x}{K})} \end{aligned} \tag{E.77}$$

A second assumption is that $\alpha \frac{x}{K}$ is much smaller than 1:

$$P_{n+1}^K \approx exp(-x) \frac{K}{\alpha x} \tag{E.78}$$

If we want to keep this probability equal for all dimensions and initial number of entries, we get:

$$\begin{aligned} \frac{\alpha * const}{K} &\approx \frac{1}{x} exp(-x) \\ ln(K) &\approx \frac{(n+1)\cdot \Delta F}{T} + ln(\frac{(n+1)\cdot \Delta F}{T}) + const. \end{aligned} \tag{E.79}$$

F Results from the Grid Search in 5 Cut Parameter Dimensions

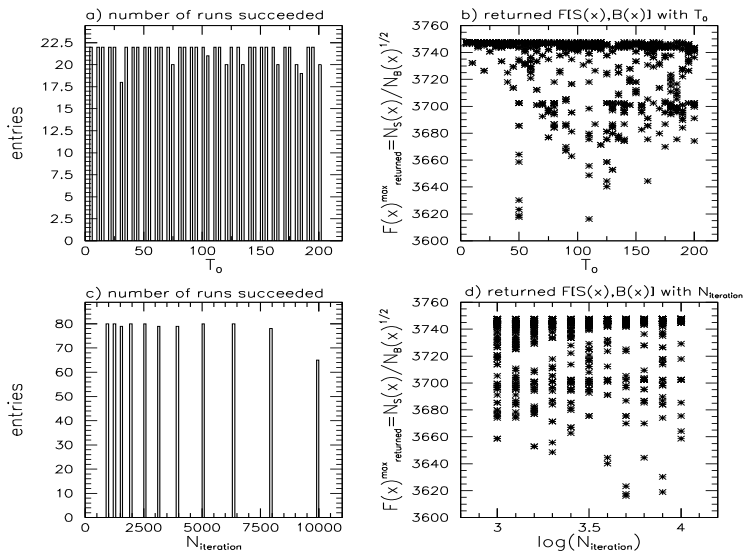

Figure F.52: Run statitistics: Figure a) shows the number of runs which succeeded starting with temperature T_0 and figure c) the corresponding numbers for $N_{iteration}$. A major source of instability was discovered (memory overload) for $N_{iteration} > 8500$. Figures b) and d) show the stability of the returned maximum depending on the chosen parameters.

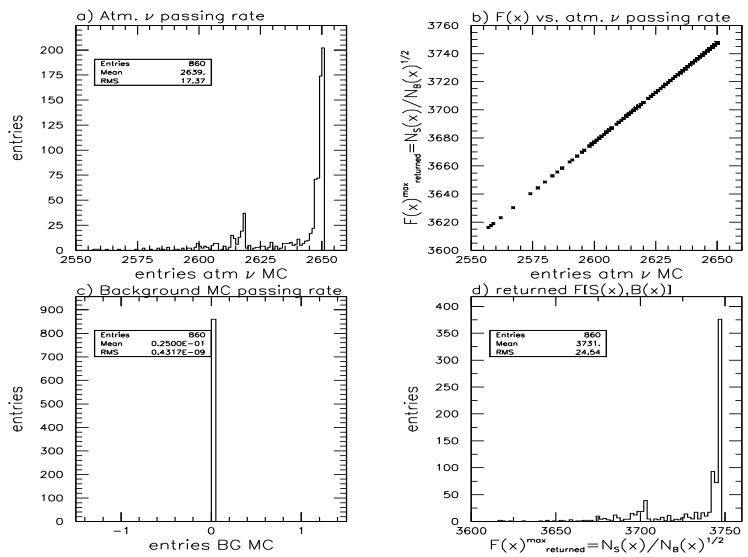

Figure F.53: Passing rates: Figure a) gives the returned atmospheric neutrino simulation passing rate. Figure b) shows that the passing rate corresponds to the returned value of $F[S(x^{cut}), B(x^{cut})]$, since all background was removed (figure c)). Figure d) shows the number of runs having returned a given value of $F[S(x^{cut}), B(x^{cut})]$.

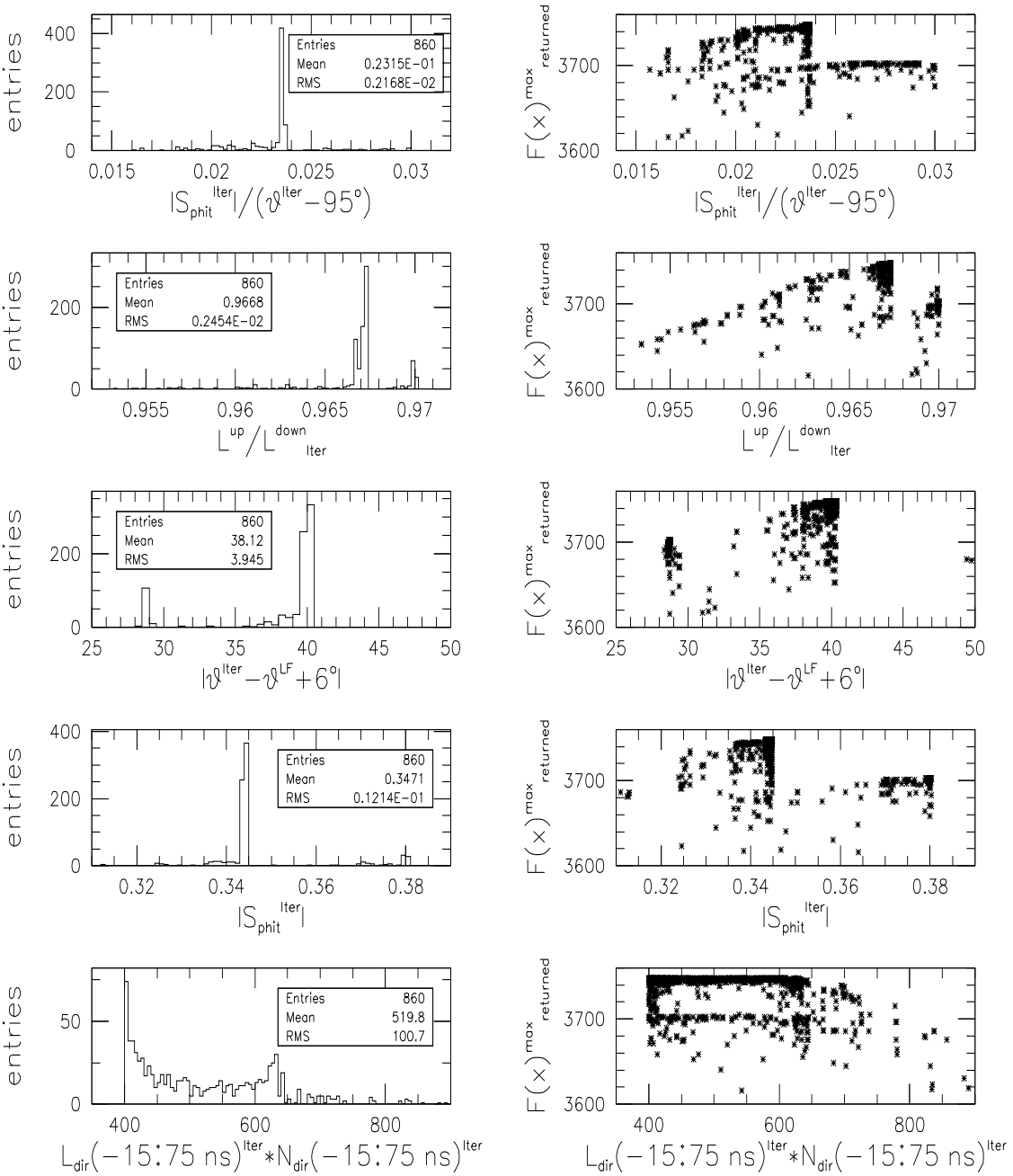

Figure F.54: Returned maximum and the corresponding cut parameters. The plots on the left side show the variations of each single parameter, those on the right side the returned maximum versus returned cut parameter values. Returned values of different parameters are strongly correlated. The two bottom plots show a redundant cut parameter. Values between 400 and 600 are too weak to reject neither signal nor background events (on the chosen filter level). Some plots on the right side reflect also an alternative combination of parameters indicated by a second branch. This second "valley" however, has a lower signal passing rate.

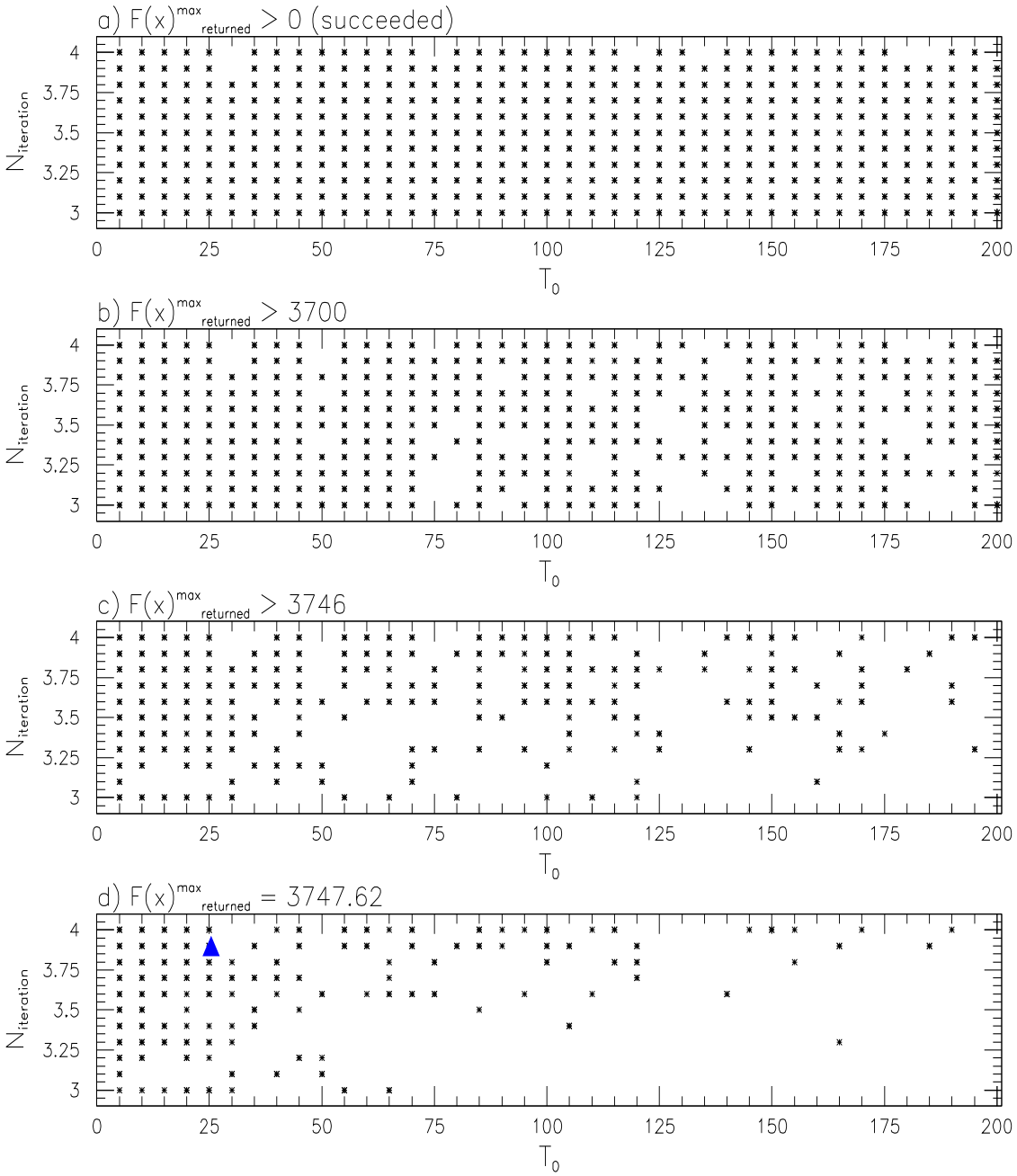

Figure F.55: Number of iterations versus start temperature. Figure a) shows parameter combinations which returned a result at all, figure b) gives those which returned a reasonable value, figure c) shows combinations very close to the global maximum and figure d) only those having returned the global maximum. The triangle shows the chosen working point.

G Stability Cross-Check for Analysis A

At the beginning of chapter 8, a fifth combination of samples was mentionned (atmospheric neutrino simulation vs. experiment) which was kept for cross-checks at the end. The four independent cut parameters were optimized with this combination and varying normalization of the signal sample. This factor α stands gives the normalization relative to the MC prediction. A too high value of α should yield too weak cut values and leaves background in the experiment (see equation 6.49), approaching $\alpha \to 1$, fluctuations should start to dominate. Figures G.56 show the obtained cut parameters depending on α. The dotted lines indicate the extrapolation results obtained from the optimization mode comparing neutrino-induced muon simulation with experimental data, dashed lines indicate the final cut value. There is a smooth tightening of cuts from high values of α down to about 1. With smaller α, fluctuations start to dominate. There is indication that the parameters $|S^{phit}|/(\theta_{iter} - 95^\circ)$ and $|\theta_{iter} - \theta_{LF} + 6|$ have been chosen too tight and the parameter $S^{phit}|$ too loose.

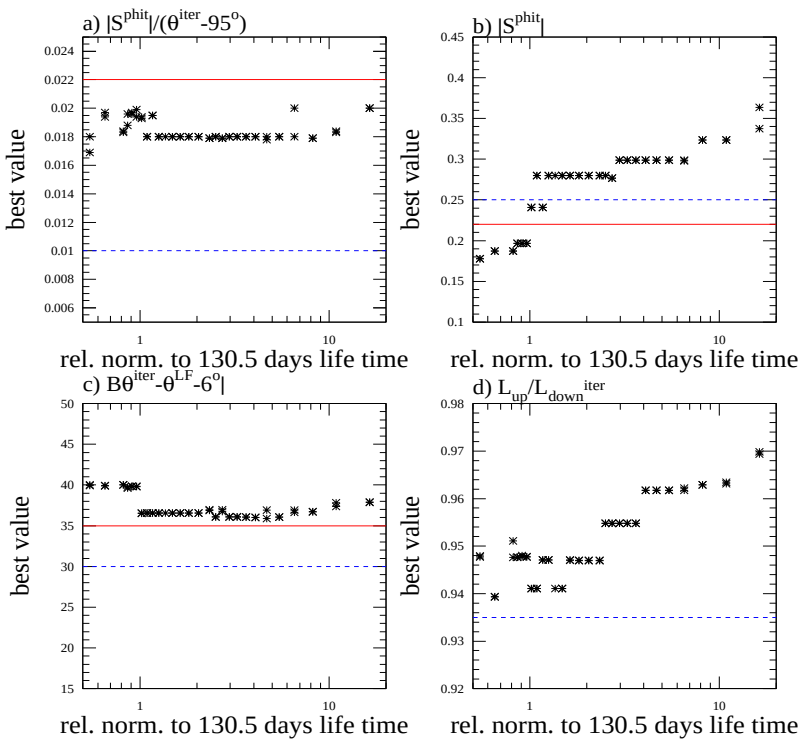

Figure G.56: Obtained cut values through maximization of $F[\alpha \cdot S(\vec{x}^{cut}), (B+S)(\vec{x}^{cut})]$ with the four parameters used for extrapolation (analysis A). The functional $F(x) = \alpha \cdot S(\vec{x}^{cut}) - (B+S)(\vec{x})$ was taken for maximization. The atmospheric neutrino simulation sample (normalized to 130.5 days life time) was multiplied with a varying factors which are represented by the x-axis. The obtained values behave relatively stable with a small fall-off until fluctuations dominate. This happens before the absolute normalizations between signal prediction and experiment agree. The full lines show the cut values obtained by extrapolation of the sample which compared the atmospheric neutrino-induced muon simulation with the background simulation, the dashed lines show the final choice of cut values in analysis A. Note that these plots were made after the choice of final cut values and did not influence their settings.

H CUTEVAL Results for Analysis B

The following lists show the results for all tested cut parameter combinations. Together with a start parameter obtained in a 1-dimensional search (not shown), combinations of parameters were tested if they could further maximize $F[S(\vec{x}^{cut}), B(\vec{x}^{cut})]$, i.e. obtain a higher signal passing rate while keeping background contamination equally low. Parameters which could improve $F[S(\vec{x}^{cut}), B(\vec{x}^{cut})]$ were taken as test parameters for the next cut parameter dimension, parameters which yielded the highest value of $F[S(\vec{x}^{cut}), B(\vec{x}^{cut})]$, were added to the set of independent parameters. All further combinations consisted then of the new set of independent parameters plus another test parameter. The tables are sorted by the optimization mode and therewithin by cut parameter dimension. The triple line marks the best value of $F[S(\vec{x}^{cut}), B(\vec{x}^{cut})]$ obtained one dimension lower.

H.1 The Optimization Mode $atm\ \nu\ \%BG\ MC$ (00)

The entries in the column $atm\ \nu\ MC$ have to multiplied by a factor of 1.43 to give the correct normalization corresponding to 65 days of detector life time as proposed by the simulation[1]. Entries in the column $BG\ MC$ corresponds to about 5.6 days life time of simulated background on trigger level. This sample consists of 1.4 days life time of unweighted events simulated with the air shower program *corsika* and 4.2 days weighted events, simulated with the air shower program *basiev* [110]. An offset value of 0.3 has been chosen.

[1] The same normalization correction of 0.7 as in the mode $atm\ \nu\%experiment$ has been applied

tested cut	$\lvert S^{phit}(Iter)\rvert/$ $(\theta_{MPE} - 90^\circ)$	tested cut (values)	$atm.\ \nu\ MC$ $(ice\ layers)$	$BG\ MC$ $(ice\ layers)$	F^{max}
$L_{dir}(-15:75)^{MPE} * (N_{dir}(-15:75)^{MPE} - 2) >$	0.0062	756.7300	73.08	0.3	133.29
$L_{dir}(-15:25)^{MPE} * N_{dir}(-15:25)^{MPE} >$	0.0063	351.2600	72.72	0.3	132.678
$L_{dir}(-15:25)^{MPE} * (N_{dir}(-15:25)^{MPE} - 2) >$	0.0063	192.1770	72.36	0.2	132.264
$L^{Iter} <$	0.0083	7.9616	72.36	0.3	132.102
$L_{dir}(-15:75)^{Iter} * (N_{dir}(-15:75)^{Iter} - 2) >$	0.0063	1021.1700	71.1	0.2	129.69
$N_{dir}(-15:75)^{Iter} - N_{dir}(-15:75)^{shower} >$	0.0066	4.0076	70.92	0.3	129.348
$N_{dir}(-15:75)^{MPE} >$	0.0065	8.1135	71.28	0.3	129.204
$L_{dir}(-15:75)^{MPE} * N_{dir}(-15:75)^{MPE} >$	0.0066	1260.2500	70.02	0.2	127.746
$L_{dir}(-15:25)^{Iter} * (N_{dir}(-15:25)^{Iter} - 2) >$	0.0072	436.9950	68.58	0.3	125.298
$N_{dir}(-15:75)^{Iter} >$	0.0056	8.0939	68.22	0.2	124.578
$L_{dir}(-1)(-15:25)^{MPE} >$	0.0065	92.3335	68.94	0.3	124.2
$(I_1/(I_1 + I_2 + I_3))/cos(\theta^{Iter}) <$	0.0050	-1.7398	66.6	0.3	121.536
$L^{shower} - L^{MPE} >$	0.0080	-5.8018	65.88	0.3	120.366
$\lvert\theta_{MPE} - \theta_{LF} + 6^\circ\rvert <$	0.0050	23.3711	65.52	0.1	119.484
$\lvert\theta_{MPE} - \theta_{Iter} + 1^\circ\rvert <$	0.0047	12.4042	64.8	0.2	118.188
$N_{dir}(-15:75)^{MPE}/N_{ch} >$	0.0047	0.2111	64.44	0.3	117.774
$L_{max}(-15:75)(MPE) >$	0.0047	116.9330	64.26	0.1	117.486
$L_{dir}(-15:75)^{MPE} > 140\ or\ L_{wid}(-15:75)^{MPE} >$	0.0047	50.0835	64.26	0.2	117.45
$N_{dir}(-15:25)^{MPE} >$	0.0066	5.6213	64.08	0.2	116.946
$L_{dir}(-15:25)^{MPE} >$	0.0065	116.8950	64.08	0.3	116.892
$L_{dir}(-15:75)^{MPE} > 140\ or\ L_{vis}(-15:75)^{MPE} >$	0.0047	10.0224	63.9	0.1	116.73
$\Psi(MPE, Iter) <$	0.0047	18.5120	63.9	0.2	116.676
$N_{dir}(-15:25)^{Iter} >$	0.0085	6.3316	63.18	0.1	115.272
$L_{dir}(-15:75)^{MPE} >$	0.0047	116.9040	62.82	0.1	114.804
$L_{dir}(-15:75)^{Iter} * N_{dir}(-15:75)^{Iter} >$	0.0047	1127.1600	62.46	0.0	114.066
$L_{dir}(-15:25)^{Iter} * N_{dir}(-15:25)^{Iter} >$	0.0050	489.0800	62.28	0.0	113.616
$N_{ch} >$	0.0053	19.9281	60.12	0.2	109.746
$\Psi(Bayes, Iter) <$	0.0063	0.6649	59.58	0.2	108.63
$L_{dir}(-1)(-15:25)^{Iter} >$	0.0050	94.6690	59.22	0.0	108.216
$L_{Phit}(Iter) <$	0.0050	4.8453	58.14	0.1	105.984
$(\lvert S^{phit}(MPE)\rvert \cdot \lvert S^{van}(MPE)\rvert)^{(1/2)} <$	0.0053	0.1806	57.96	0.3	105.948
$log(energy^{Iter}) <$	0.0050	1.5727	66.96	0.4	103.554
$\lvert S^{van}(MPE)\rvert <$	0.0085	0.1876	56.52	0.3	103.104
$\lvert\theta_{MPE} - \theta_{Bayes}\rvert <$	0.0047	74.9470	55.8	0.1	101.898
$COG_\rho <$	0.0050	49.6920	64.26	0.4	101.052
$\lvert\theta_{Bayes} - \theta_{Iter}\rvert <$	0.0047	69.9700	54.9	0.1	100.314
$N_{dir}(-15:75)^{Iter} - N_{dir}(-15:75)^{shower} >$	0.0088	8.9999	54.54	0.0	99.576
$\lvert\theta_{Bayes} - \theta_{LF}\rvert <$	0.0047	69.7055	54.36	0.0	99.162
$\theta^{Bayes} >$	0.0047	65.0555	53.64	0.1	97.794
$L_{up} - L_{down}(Iter) <$	0.0046	-12.3639	53.46	0.0	97.452
$\Psi(Bayes, LF) <$	0.0047	80.0000	53.1	0.0	97.056
$\Psi(MPE, Bayes) <$	0.0047	69.9792	53.1	0.0	96.912
$L_{up}/L_{down}(MPE) <$	0.0039	0.9972	52.74	0.2	96.228
$(I_1/I_2)/cos(\theta^{MPE}) <$	0.0039	-0.8171	52.74	0.2	96.21
$L_{up} - L_{down}(MPE) <$	0.0039	-5.0218	52.74	0.2	96.21

tested cut	$\lvert S^{phit}(Iter)\rvert/$ $(\theta_{MPE}-90°)$	tested cut (values)	*atm. ν* (*ice layers*)	*BG MC* (*ice layers*)	F^{max}
$\Psi(Iter,LF)<$	0.0039	77.3870	52.74	0.2	96.21
$L_{dir}(-15:75)^{Iter}>140$ *or* $L_{wid}(-15:75)^{Iter}>$	0.0039	60.6625	52.74	0.0	96.192
$L_{dir}(-15:75)^{Iter}>140$ *or* $L_{vis}(-15:75)^{Iter}>$	0.0039	10.3102	52.74	0.2	96.192
$(I_1/I_3)/cos(\theta^{MPE})<$	0.0039	-0.5871	52.74	0.2	96.156
$I_1/I_2<$	0.0039	0.7810	52.74	0.2	96.156
$L_{dir}(-15:75)^{Iter}>$	0.0039	88.0208	52.74	0.2	96.138
$3\cdot I_1/(I_1+I_2+I_3)<$	0.0039	0.7755	52.74	0.2	96.138
$(I_1/I_2)/cos(\theta^{Iter})<$	0.0039	-0.9221	52.56	0.2	96.12
$I_1/I_3<$	0.0039	0.6265	52.56	0.2	95.832
$L^{shower}/L^{MPE}>$	0.0039	0.4935	52.56	0.2	95.814
$L^{phit}(MPE)<$	0.0039	5.7932	52.38	0.2	95.796
$\Psi(MPE,LF)<$	0.0039	49.1155	52.38	0.2	95.724
$L^{MPE}<$	0.0039	17.5872	52.38	0.2	95.724
$(I_1/I_3)/cos(\theta^{Iter})<$	0.0039	-0.6671	52.38	0.2	95.598
$(3\cdot I_1/(I_1+I_2+I_3))/cos(\theta^{MPE})<$	0.0039	-1.6975	52.38	0.2	95.49
$COG_z<$	0.0039	152.6690	52.2	0.2	95.454
$L^{shower}/L^{Iter}>$	0.0039	0.9757	52.2	0.2	95.31
$L^{shower}-L^{Iter}>$	0.0039	-0.2007	52.2	0.2	95.256
$N_{dir}(-15:75)^{Iter}/N_{ch}>$	0.0039	0.2636	52.2	0.2	95.148
$L_{dir}(-15:25)^{Iter}>$	0.0039	42.3030	52.02	0.1	94.932
$\lvert S^{phit}(MPE)\rvert/(\theta_{MPE}-85°)$	0.0039	0.0035	51.84	0.1	94.536
$\lvert S^{phit}(Iter)\rvert/(\theta_{MPE}-85°)$	0.0047	0.0035	55.08	0.3	94.158
$\lvert S^{van}(Iter)\rvert<$	0.0039	0.4707	52.74	0.3	93.528
$(\lvert S^{phit}(Iter)\rvert\cdot\lvert S^{van}(Iter)\rvert)^{(1/2)}<$	0.0039	0.3304	52.74	0.3	93.528
$L_{up}/L_{down}(Iter)<$	0.0039	0.9557	51.12	0.2	93.474
$\lvert S^{phit}(MPE)\rvert/(\theta_{MPE}-95°)<$	0.0039	0.0044	51.12	0.1	93.474
$\theta^{dipole}>$	0.0039	18.3180	52.38	0.3	93.006
$\theta^{LF}>$	0.0039	117.9360	50.76	0.1	92.808
$\theta^{dipole}>60$ *or* $M^{dipole}<$	0.0039	0.1492	52.56	0.3	92.592
$COG_z>$	0.0039	-78.4205	50.76	0.2	92.52
$\lvert\theta_{Iter}-\theta_{dipole}+2°\rvert<$	0.0039	129.6760	52.56	0.3	92.484
$\Psi(MPE,dipole)<$	0.0039	145.6610	52.38	0.3	92.358
$\lvert v\rvert_{LF}$(m/ns)>	0.0038	0.1039	50.58	0.2	92.358
$\lvert S^{phit}(Iter)\rvert/(\theta_{Iter}-95°)<$	0.0039	0.0055	52.56	0.3	91.638
$\lvert\theta_{Iter}-\theta_{LF}+4°\rvert<$	0.0039	43.3449	52.38	0.3	91.512
$\lvert S^{phit}(Iter)\rvert/(\theta_{Iter}-90°)$	0.0039	0.0042	52.56	0.3	91.35
$\theta^{Iter}>$	0.0039	111.8790	52.38	0.3	91.152
$log(energy^{MPE})<$	0.0039	1.1859	52.74	0.3	91.116
$\lvert S^{phit}(Iter)\rvert/(\theta_{Iter}-85°)$	0.0039	0.0228	52.74	0.3	91.116
$\lvert S^{phit}(Iter)\rvert<$	0.0039	0.3389	52.74	0.3	91.116
$\theta^{MPE}>$	0.0039	95.7040	52.74	0.3	91.116
$\lvert S^{phit}(Iter)\rvert/(\theta_{MPE}-90°)$	0.0102	0.0039	52.74	0.3	91.116
$\lvert S^{phit}(MPE)\rvert/(\theta_{MPE}-90°)$	0.0205	0.0028	42.12	0.1	76.932

tested cut	$\lvert S^{phit}(Iter)\rvert /$ $(\theta_{MPE} - 90°)$	$L_{dir}(-15:75)^{MPE} \cdot$ $(N_{dir}(-15:75)^{MPE} - 2)$	tested cut (values)	$atm.\ \nu$ $(ice\ layers)$	$BG\ MC$ $(ice\ layers)$	F^{max}
$L_{up} - L_{down}(MPE) <$	0.0075	541.8690	-30.0891	80.1	0.3	146.214
$\lvert S^{phit}(Iter)\rvert /(\theta_{Iter} - 95°) <$	0.0075	756.0350	0.0099	79.2	0.3	144.504
$\theta^{Iter} >$	0.0075	756.0150	106.8790	78.66	0.3	143.514
$L^{shower} - L^{Iter} >$	0.0075	756.0870	-0.1185	78.48	0.3	143.406
$L^{shower}/L^{Iter} >$	0.0075	756.0250	0.9853	78.48	0.3	143.28
$COG_z <$	0.0081	761.3240	135.4280	78.48	0.3	143.208
$\theta^{MPE} >$	0.0075	756.0830	107.9900	77.94	0.3	142.398
$L_{up}/L_{down}(MPE) <$	0.0066	541.9520	0.9338	77.94	0.3	142.38
$L_{up} - L_{down}(Iter) <$	0.0075	756.8000	-7.1186	77.94	0.2	142.164
$L_{up}/L_{down}(Iter) <$	0.0075	756.2450	0.9507	77.04	0.2	140.724
$L_{dir}(-15:25)^{Iter} * (N_{dir}(-15:25)^{Iter} - 2) >$	0.0066	473.4360	161.6880	76.5	0.3	139.77
$(\lvert S^{phit}(MPE)\rvert \cdot \lvert S^{van}(MPE)\rvert)^{(1/2)} <$	0.0066	700.3500	0.3225	76.5	0.3	139.68
$L_{dir}(-1)(-15:25)^{Iter} >$	0.0066	475.4890	52.7681	76.5	0.2	139.662
$\lvert S^{van}(MPE)\rvert <$	0.0065	699.7050	0.4158	76.68	0.3	139.464
$(\lvert S^{phit}(Iter)\rvert \cdot \lvert S^{van}(Iter)\rvert)^{(1/2)} <$	0.0066	700.3590	0.3374	76.32	0.3	139.428
$\lvert S^{van}(Iter)\rvert <$	0.0066	699.6040	0.3878	76.32	0.3	139.32
$N_{dir}(-15:75)^{Iter} >$	0.0065	653.1090	7.9046	76.68	0.3	138.87
$L^{Phit}(Iter) <$	0.0066	661.4390	5.6336	75.78	0.3	138.492
$L^{MPE} <$	0.0065	750.2600	17.2723	75.42	0.3	137.7
$L_{dir}(-15:75)^{Iter} >$	0.0066	755.9700	104.0890	75.42	0.3	137.682
$L^{shower} - L^{MPE} >$	0.0065	756.0620	-8.8677	75.42	0.3	137.556
$L_{dir}(-15:25)^{Iter} * N_{dir}(-15:25)^{Iter} >$	0.0065	699.6810	189.1030	75.6	0.3	137.43
$\lvert\theta_{MPE} - \theta_{LF} + 6°\rvert <$	0.0061	385.1270	29.2071	75.24	0.3	137.25
$L_{dir}(-15:75)^{Iter} * (N_{dir}(-15:75)^{Iter} - 2) >$	0.0065	756.0850	531.0560	75.6	0.3	137.034
$\lvert S^{phit}(Iter)\rvert <$	0.0065	670.2670	0.2980	74.7	0.3	136.53
$L^{shower}/L^{MPE} >$	0.0065	756.0910	0.5149	74.7	0.3	136.512
$\theta^{LF} >$	0.0066	757.2650	97.8428	74.7	0.2	136.26
$\Psi(Iter, LF) <$	0.0064	756.1410	55.1719	74.34	0.3	135.846
$L_{dir}(-15:25)^{MPE} * (N_{dir}(-15:25)^{MPE} - 2) >$	0.0065	473.3310	175.6050	74.34	0.3	135.594
$(3 \cdot I_1/(I_1 + I_2 + I_3))/cos(\theta^{Iter}) <$	0.0062	670.2430	-1.6397	74.16	0.3	135.342
$log(energy^{MPE}) <$	0.0065	756.4050	1.5824	74.52	0.3	135.216
$L_{dir}(-15:25)^{MPE} * N_{dir}(-15:25)^{MPE} >$	0.0065	476.8470	351.2370	73.98	0.3	135.018
$I_1/I_2 <$	0.0064	756.2080	0.7295	73.98	0.3	134.928
$N_{dir}(-15:75)^{Iter} - N_{dir}(-15:75)^{shower} >$	0.0062	566.5760	2.0220	74.16	0.3	134.928
$(3 \cdot I_1/(I_1 + I_2 + I_3))/cos(\theta^{MPE}) <$	0.0061	700.1450	-1.6650	73.8	0.3	134.766
$N_{dir}(-15:75)^{Iter} - N_{dir}(-15:75)^{shower} >$	0.0061	699.5500	0.6760	73.8	0.3	134.748
$3 \cdot I_1/(I_1 + I_2 + I_3) <$	0.0066	756.1800	0.6993	74.16	0.3	134.676
$N_{dir}(-15:75)^{MPE} >$	0.0061	701.6500	6.7334	73.62	0.3	134.55
$log(energy^{Iter}) <$	0.0064	699.7320	1.5507	73.98	0.3	134.37

tested cut	$\lvert S^{phit}(Iter)\rvert/$ $(\theta_{MPE} - 90°)$	$L_{dir}(-15:75)^{MPE}$. $(N_{dir}(-15:75)^{MPE} - 2)$	tested cut (values)	*atm.* ν *(ice layers)*	*BG MC (ice layers)*	F^{max}
$N_{dir}(-15:25)^{Iter} >$	0.0066	541.8720	4.3500	73.62	0.3	134.244
$L_{dir}(-15:75)^{Iter} > 140$ *or* $L_{wid}(-15:75)^{Iter} >$	0.0065	758.6600	88.9033	73.44	0.3	133.938
$L_{dir}(-1)(-15:25)^{MPE} >$	0.0062	699.5570	10.0414	73.26	0.3	133.866
$\Psi(MPE, LF) <$	0.0066	473.3190	29.6868	73.26	0.3	133.704
$COG_z >$	0.0062	755.9700	-99.9679	73.08	0.3	133.29
$I_1/I_3 <$	0.0062	756.1350	0.7322	73.08	0.3	133.29
$(I_1/I_3)/cos(\theta^{Iter}) <$	0.0062	755.9950	-0.5193	73.08	0.3	133.29
$(I_1/I_3)/cos(\theta^{MPE}) <$	0.0062	756.1120	-0.5027	73.08	0.3	133.29
$\lvert S^{phit}(Iter)\rvert/(\theta_{MPE} - 85°)$	0.0062	755.9670	0.0178	73.08	0.3	133.29
$\lvert S^{phit}(Iter)\rvert/(\theta_{MPE} - 90°)$	0.0062	756.0650	0.0084	73.08	0.3	133.29
$(I_1/I_2)/cos(\theta^{MPE}) <$	0.0062	756.2210	-0.7312	73.08	0.3	133.29
$\theta^{dipole} >$	0.0062	756.0930	0.2705	73.08	0.3	133.29
$\lvert\theta_{MPE} - \theta_{Iter} + 1°\rvert <$	0.0062	756.0750	52.3695	73.08	0.3	133.29
$\theta^{dipole} > 60$ *or* $M^{dipole} <$	0.0062	756.9070	0.9493	73.08	0.3	133.29
$L_{dir}(-15:75)^{MPE} * (N_{dir}(-15:75)^{MPE} - 2) >$	0.0062	755.9650	680.8020	73.08	0.3	133.29
$N_{ch} >$	0.0062	756.0830	11.1108	73.08	0.3	133.29
$N_{dir}(-15:75)^{MPE}/N_{ch} >$	0.0062	756.0600	0.1024	73.08	0.3	133.29
$N_{dir}(-15:75)^{Iter}/N_{ch} >$	0.0062	756.0260	0.1140	73.08	0.3	133.29
$\Psi(MPE, Iter) <$	0.0061	757.3100	52.5999	72.9	0.3	133.254
$\lvert\theta_{Bayes} - \theta_{dipole}\rvert <$	0.0066	755.9770	122.2860	72.9	0.3	133.146
$(I_1/I_2)/cos(\theta^{Iter}) <$	0.0061	757.7830	-0.7505	72.9	0.3	132.984
$\lvert\theta_{Iter} - \theta_{dipole} + 2°\rvert <$	0.0065	755.9920	85.0363	72.9	0.3	132.804
$L_{dir}(-15:75)^{MPE} > 140$ *or* $L_{wid}(-15:75)^{MPE} >$	0.0061	755.9580	50.0552	72.72	0.3	132.732
$L_{dir}(-15:75)^{MPE} * N_{dir}(-15:75)^{MPE} >$	0.0066	770.8620	1168.0400	72.72	0.3	132.678
$L_{dir}(-15:75)^{MPE} > 140$ *or* $L_{vis}(-15:75)^{MPE} >$	0.0061	762.4250	10.3161	72.18	0.3	131.778
$N_{dir}(-15:25)^{MPE} >$	0.0066	385.2080	4.8415	72	0.2	131.418
$COG_\rho <$	0.0062	699.5930	49.9894	69.84	0.3	127.53
$\lvert\theta_{MPE} - \theta_{Bayes}\rvert <$	0.0079	756.0070	74.9913	69.48	0.3	126.972
$\lvert\theta_{Bayes} - \theta_{LF}\rvert <$	0.0076	756.0270	79.9502	68.4	0.3	124.92
$L^{phit}(MPE)(<$	0.0084	955.8430	4.8572	68.4	0.3	123.678
$\lvert\theta_{Bayes} - \theta_{Iter}\rvert <$	0.0079	755.9750	69.9570	67.68	0.3	123.57
$\lvert v\rvert_{LF}$(m/ns)>	0.0066	755.9460	0.1100	67.68	0.2	123.48
$L_{dir}(-15:75)^{Iter} * N_{dir}(-15:75)^{Iter} >$	0.0075	1177.0200	760.9650	65.52	0.3	119.754
$L_{dir}(-15:75)^{MPE} >$	0.0075	1208.3800	48.7070	64.26	0.3	117.414
$L^{Iter} <$	0.0156	706.9590	7.7039	64.26	0.3	117.198
$L_{dir}(-15:25)^{Iter} >$	0.0112	1221.2200	38.3932	67.5	0.3	117.054
$\Psi(MPE, Bayes) <$	0.0079	756.1000	89.9988	63.72	0.3	116.442
$\Psi(Bayes, Iter) <$	0.0079	756.0840	89.9468	63.54	0.3	116.118
$\Psi(Bayes, LF) <$	0.0249	1183.8200	33.1563	58.14	0.2	106.272
$\theta^{Bayes} >$	0.0104	1361.5300	55.0141	55.08	0.3	100.458
$L_{dir}(-15:25)^{MPE} >$	0.0062	1421.2300	36.9135	52.38	0.0	95.67

tested cut	$\lvert S^{phit}(Iter)\rvert/$ $(\theta_{MPE}-90°)$	$L_{dir}(-15:75)^{MPE}\cdot$ $(N_{dir}(-15:75)^{MPE}-2)$	$L_{up}-$ $L_{down}(MPE)$	tested cut (values)	$atm.\ \nu$ $(ice\ layers)$	$BG\ MC$ $(ice\ layers)$	F^{max}
$\lvert S^{phit}(Iter)\rvert/(\theta_{Iter}-95°)<$	0.0075	473.9700	-17.8353	0.0099	82.8	0.2	151.2
$\theta^{Iter}>$	0.0075	541.8680	-12.9837	106.8860	82.26	0.3	150.066
$\theta^{Iter}>$	0.0075	541.8810	-12.9816	106.8780	82.26	0.3	150.066
$L^{shower}/L^{Iter}>$	0.0075	473.4590	-13.0011	0.9853	82.26	0.3	150.03
$L^{shower}-L^{Iter}>$	0.0075	473.8110	-12.9918	-0.1183	82.08	0.3	150.012
$L_{dir}(-15:25)^{Iter}*(N_{dir}(-15:25)^{Iter}-2)>$	0.0075	481.2290	-19.1683	145.4080	82.08	0.3	149.814
$L_{dir}(-15:25)^{Iter}*N_{dir}(-15:25)^{Iter}>$	0.0075	476.8260	-18.8439	291.1450	81.9	0.3	149.418
$\theta^{MPE}>$	0.0075	473.5970	-17.8195	108.0210	81.72	0.3	149.22
$L_{up}-L_{down}(Iter)<$	0.0075	473.3160	-12.9774	-7.1223	81.54	0.3	148.986
$L_{dir}(-1)(-15:25)^{Iter}>$	0.0075	474.9030	-18.8307	52.7664	81.18	0.3	148.248
$L_{up}/L_{down}(Iter)<$	0.0075	473.3030	-12.9908	0.9507	81	0.3	147.78
$\Psi(Iter,LF)<$	0.0075	473.4190	-30.1093	79.9098	80.82	0.3	147.492
$\Psi(MPE,LF)<$	0.0075	473.3150	-30.1029	78.9456	80.82	0.3	147.456
$(\lvert S^{phit}(MPE)\rvert\cdot\lvert S^{van}(MPE)\rvert)^{(1/2)}<$	0.0102	934.9150	-18.9183	0.3160	80.46	0.3	146.916
$L_{dir}(-15:75)^{MPE}*N_{dir}(-15:75)^{MPE}>$	0.0075	541.8750	-30.1012	713.8950	80.1	0.3	146.214
$L_{dir}(-15:75)^{Iter}>140\ or\ L_{wid}(-15:75)^{Iter}>$	0.0075	541.8570	-30.0984	60.0380	80.1	0.3	146.214
$\lvert S^{phit}(Iter)\rvert/(\theta_{Iter}-90°)<$	0.0075	541.8590	-30.1081	0.0214	80.1	0.3	146.214
$M^{dipole}/\theta^{dipole}<$	0.0075	541.8570	-30.0878	5.9494	79.92	0.3	145.962
$(\lvert S^{phit}(Iter)\rvert\cdot\lvert S^{van}(Iter)\rvert)^{(1/2)}<$	0.0102	934.9260	-17.3413	0.3149	79.92	0.3	145.854
$\theta^{dipole}>$	0.0075	474.9790	-12.9895	60.6126	79.2	0.3	144.738
$\lvert S^{van}(MPE)\rvert<$	0.0102	919.0290	-18.8761	0.3321	79.2	0.3	144.738
$L_{dir}(-15:25)^{Iter}>$	0.0066	475.8000	-10.9400	29.1901	79.2	0.3	144.504
$I_1/I_2<$	0.0066	475.3370	-19.4673	0.7369	78.66	0.3	143.478
$L_{dir}(-15:75)^{Iter}*(N_{dir}(-15:75)^{Iter}-2)>$	0.0066	474.1660	-17.8191	598.9500	78.66	0.3	143.46
$log(energy^{Iter})<$	0.0066	541.8790	-17.8243	1.2006	78.3	0.3	143.064
$L^{Iter}<$	0.0066	541.8800	-17.8404	8.7000	78.3	0.3	143.064
$N_{dir}(-15:75)^{Iter}-N_{dir}(-15:75)^{shower}>$	0.0066	541.8880	-17.8386	-2.4822	78.3	0.3	143.064
$L^{phit}(MPE)<$	0.0066	541.8840	-17.8419	7.9295	78.3	0.3	143.064
$I_1/I_2<$	0.0066	541.8670	-17.8501	0.8962	78.3	0.3	143.064
$L_{up}/L_{down}(MPE)<$	0.0066	541.8780	-17.8419	1.8898	78.3	0.3	143.064
$L_{up}-L_{down}(MPE)<$	0.0066	541.8800	-12.8264	-17.8196	78.3	0.3	143.064
$(3\cdot I_1/(I_1+I_2+I_3))/cos(\theta^{MPE})<$	0.0066	541.8880	-17.8464	-1.6011	78.3	0.3	143.028
$3\cdot I_1/(I_1+I_2+I_3)<$	0.0066	479.6860	-18.9526	0.7334	78.3	0.3	142.974
$L_{dir}(-15:75)^{MPE}*(N_{dir}(-15:75)^{MPE}-2)>$	0.0066	352.3550	-18.2925	543.1960	78.3	0.3	142.902
$\theta^{LF}>$	0.0065	582.5040	-12.9882	70.6337	78.3	0.3	142.848
$\lvert\theta_{MPE}-\theta_{LF}+6°\rvert<$	0.0066	582.8010	-12.9975	79.5441	78.3	0.3	142.848
$log(energy^{MPE})<$	0.0066	582.2790	-12.9961	1.2639	78.3	0.3	142.848
$L^{shower}/L^{MPE}>$	0.0066	582.4450	-12.9965	0.4420	78.3	0.3	142.848
$L_{dir}(-15:75)^{MPE}>$	0.0066	582.2760	-12.9958	30.7957	78.3	0.3	142.848
$L^{MPE}<$	0.0066	582.3320	-13.0069	26.2038	78.3	0.3	142.848
$\Psi(MPE,Iter)<$	0.0066	582.9090	-12.9934	64.1530	78.3	0.3	142.812

tested cut	$\lvert S^{phit}(Iter)\rvert/$ $(\theta_{MPE}-90°)$	$L_{dir}(-15:75)^{MPE}\cdot$ $(N_{dir}(-15:75)^{MPE}-2)$	$L_{up}-$ $L_{down}(MPE)$	tested cut (values)	*atm. ν* (*ice layers*)	*BG MC* (*ice layers*)	F^{max}
$\lvert S^{phit}(Iter)\rvert <$	0.0101	955.9170	-17.3356	0.3410	78.48	0.3	142.65
$L_{dir}(-1)(-15:25)^{MPE} >$	0.0066	473.3010	-10.9486	26.7655	77.76	0.3	142.128
$L_{dir}(-15:75)^{Iter} * N_{dir}(-15:75)^{Iter} >$	0.0075	476.7810	-22.7572	1158.7200	78.12	0.3	139.068
$(3\cdot I_1/(I_1+I_2+I_3))/cos(\theta^{Iter}) <$	0.0063	606.2490	-12.9971	-1.6029	75.96	0.3	138.6
$L_{dir}(-15:75)^{Iter} >$	0.0075	918.4880	-18.8253	67.7730	75.24	0.3	137.376
$L^{phit}(Iter) <$	0.0088	955.8940	-14.3331	5.4793	74.88	0.3	136.818
$N_{dir}(-15:75)^{Iter} - N_{dir}(-15:75)^{shower} >$	0.0075	700.6090	-14.0709	4.9164	74.88	0.3	136.584
$\lvert\theta_{Bayes}-\theta_{Iter}\rvert <$	0.0078	549.9270	-19.3360	85.2122	73.98	0.3	135.072
$L^{shower}-L^{MPE} >$	0.0102	926.6790	-12.5162	-6.5433	73.98	0.3	134.748
$\lvert\theta_{Bayes}-\theta_{Iter}\rvert <$	0.0079	545.5830	-17.8620	85.2457	74.34	0.3	134.712
$\lvert\theta_{Bayes}-\theta_{LF}\rvert <$	0.0076	475.7470	-15.5066	79.9739	70.56	0.3	128.97
$\lvert S^{van}(Iter)\rvert <$	0.0153	1183.8100	-10.9520	0.4008	70.2	0.3	128.322
$N_{dir}(-15:75)^{Iter} >$	0.0119	1185.3900	-14.0684	7.0635	69.48	0.3	126.81
$COG_z <$	0.0212	1183.7700	-6.5643	135.4720	68.94	0.3	125.73
$L_{dir}(-15:25)^{MPE} * N_{dir}(-15:25)^{MPE} >$	0.0121	926.6750	-20.5682	743.1670	67.32	0.3	122.76
$N_{dir}(-15:75)^{MPE} >$	0.0153	1242.7900	-20.5669	8.2700	66.6	0.3	121.482
$\theta^{Bayes} >$	0.0079	477.2080	-13.0025	65.5058	65.16	0.3	119.106
$\Psi(Bayes, Iter) <$	0.0079	474.4410	-12.9914	81.3187	64.98	0.3	118.62
$\Psi(MPE, Bayes) <$	0.0079	473.4850	-17.0966	79.6837	64.8	0.3	118.242
$L_{dir}(-15:25)^{MPE} * (N_{dir}(-15:25)^{MPE}-2) >$	0.0223	931.7720	-20.8041	609.8440	63.36	0.3	115.488
$N_{dir}(-15:25)^{Iter} >$	0.0249	351.3460	-5.2745	7.2776	57.24	0.2	104.454

tested cut	$\lvert S^{phit}(Iter)\rvert/$ $(\theta_{MPE}-90°)$	$L_{dir}(-15:75)^{MPE}\cdot$ $(N_{dir}(-15:75)^{MPE}-2)$	$L_{up}-$ $L_{down}(MPE)$	$\lvert S^{phit}(Iter)\rvert/$ $(\theta_{Iter}-95°)$	tested cut (values)	$atm.\ \nu\ MC$ $(ice\ layers)$	$BG\ MC$ $(ice\ layers)$	F^{max}
$L_{dir}^{-1}(-15:25)^{Iter}>$	0.0076	350.8480	-12.2523	0.0099	29.5867	83.34	0.3	152.28
$\Psi(Iter,LF)<$	0.0075	473.9680	-13.0044	0.0099	77.6104	83.34	0.2	152.172
$L_{dir}(-15:75)^{MPE}*(N_{dir}(-15:75)^{MPE}-2)>$	0.0075	474.3470	-17.8415	0.0099	441.6500	82.8	0.2	151.2
$L_{up}-L_{down}(MPE)<$	0.0075	473.6390	-17.8436	0.0099	-8.0487	82.8	0.2	151.2
$\lvert S^{phit}(Iter)\rvert/(\theta_{MPE}-90°)$	0.0119	541.8730	-12.9875	0.0099	0.0075	82.62	0.3	150.804
$\theta^{MPE}>$	0.0075	541.8830	-12.9792	0.0099	98.7903	82.62	0.3	150.804
$L_{dir}(-15:25)^{Iter}*N_{dir}(-15:25)^{Iter}>$	0.0075	477.2600	-17.6690	0.0105	189.0500	82.26	0.3	150.318
$L^{shower}-L^{Iter}>$	0.0075	473.7170	-13.0012	0.0270	-0.1171	82.08	0.3	149.958
$L^{shower}/L^{Iter}>$	0.0075	474.4090	-13.0033	0.0289	0.9853	82.08	0.3	149.886
$L_{dir}(-15:25)^{Iter}*(N_{dir}(-15:25)^{Iter}-2)>$	0.0075	474.2790	-19.0187	0.0239	145.4380	81.9	0.3	149.688
$(\lvert S^{phit}(MPE)\rvert\cdot\lvert S^{van}(MPE)\rvert)^{(1/2)}<$	0.0102	934.9160	-17.3772	0.0291	0.3161	80.28	0.3	146.718
$M^{dipole}*\theta^{dipole}>$	0.0075	475.1400	-14.9389	0.0089	0.0500	78.84	0.2	143.784
$L_{up}/L_{down}(Iter)<$	0.0238	541.8750	-12.9998	0.0080	0.9565	77.58	0.3	141.48
$\Psi(MPE,LF)<$	0.0125	759.1800	-5.0105	0.0080	75.1046	76.86	0.3	140.49
$\theta^{Iter}>$	0.0163	759.5200	-10.9568	0.0079	99.1739	76.68	0.3	139.878
$L_{up}-L_{down}(Iter)<$	0.0090	1183.8000	-5.0604	0.0292	-11.8990	59.94	0.3	109.476

tested cut	$\lvert S^{phit}(Iter)\rvert /$ $(\theta^{MPE} - 90^\circ)$	$L_{dir}(-15:75)^{MPE} \cdot$ $(N_{dir}(-15:75)^{MPE} - 2)$	$L_{up} - L_{down}(MPE)$	$\lvert S^{phit}(Iter)\rvert /$ $(\theta^{Iter} - 95^\circ)$	$\Psi(Iter, LF)$	tested cut (value)	$atm\ \nu\ MC$ $(ice\ layers)$	$BG\ MC$ $(ice\ layers)$	F^{max}
$L_{dir}(-1)(-15:25)^{Iter} >$	0.0075	474.5190	-19.1671	0.0300	78.2293	52.7648	81.2	0.3	148.14
$L_{dir}(-1)(-15:25)^{Iter} >$	0.0075	474.4600	-19.3240	0.0299	78.1188	52.7254	81.2	0.3	148.14

H.2 The Optimization Mode $atm\ \nu\ \%BG\ MC$ (98)

The entries in the column $atm\ \nu\ MC$ have to multiplied by a factor of 1.43 to give the correct normalization corresponding to 65 days of detector life time, as proposed by the simulation. Entries in the column $BG\ MC$ correspond to about 10 days life time of simulated background on trigger level [87] which corresponds to 2-3 times less on filter level 3 because of the insufficient simulation of horizontal events with *basiev* [110]. An offset value of 0 has been chosen.

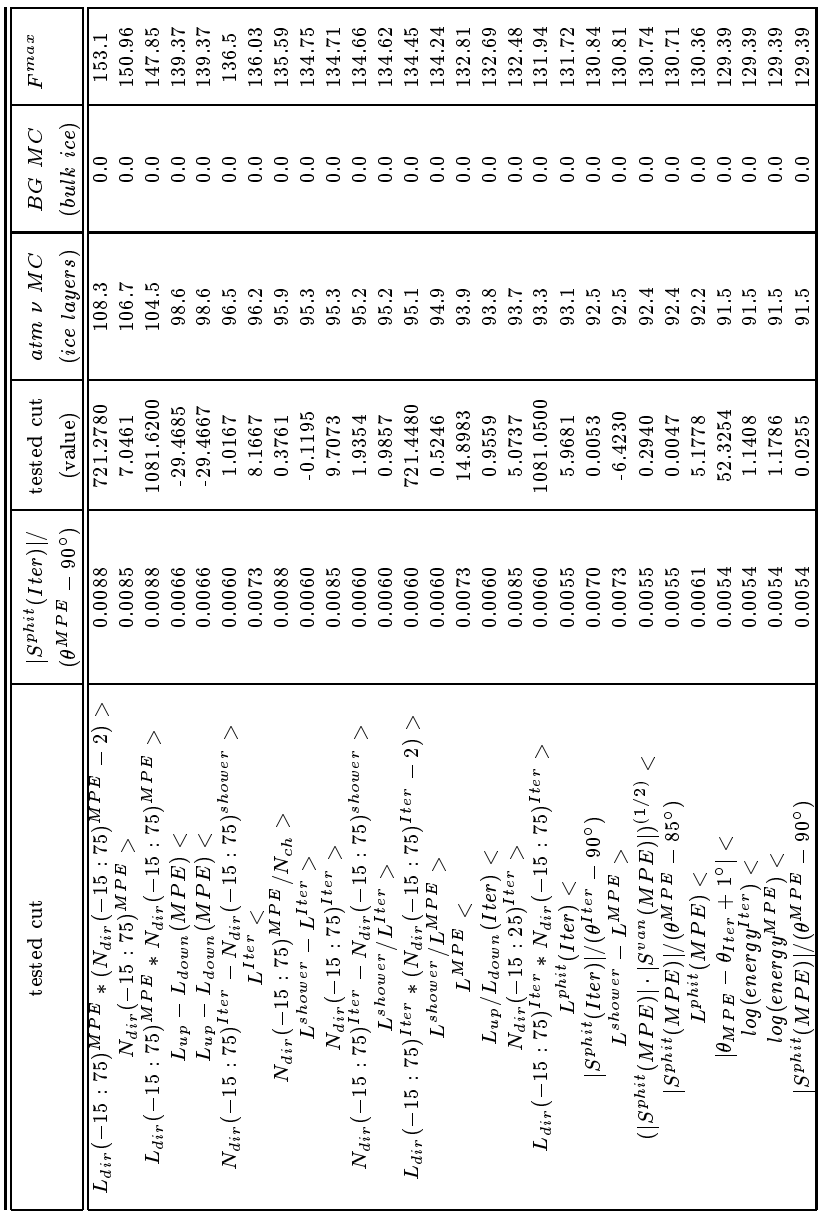

tested cut	$\lvert S^{phit}(Iter)\rvert/(\theta^{MPE}-90^\circ)$	tested cut (value)	$atm\ \nu\ MC$ (*ice layers*)	$BG\ MC$ (*bulk ice*)	F^{max}
$L_{dir}(-15:75)^{MPE} * (N_{dir}(-15:75)^{MPE} - 2) >$	0.0088	721.2780	108.3	0.0	153.1
$N_{dir}(-15:75)^{MPE} >$	0.0085	7.0461	106.7	0.0	150.96
$L_{dir}(-15:75)^{MPE} * N_{dir}(-15:75)^{MPE} >$	0.0088	1081.6200	104.5	0.0	147.85
$L_{up} - L_{down}(MPE) <$	0.0066	-29.4685	98.6	0.0	139.37
$L_{up} - L_{down}(MPE) <$	0.0066	-29.4667	98.6	0.0	139.37
$N_{dir}(-15:75)^{Iter} - N_{dir}(-15:75)^{shower} >$	0.0060	1.0167	96.5	0.0	136.5
$L^{Iter} <$	0.0073	8.1667	96.2	0.0	136.03
$N_{dir}(-15:75)^{MPE}/N_{ch} >$	0.0088	0.3761	95.9	0.0	135.59
$L^{shower} - L^{Iter} >$	0.0060	-0.1195	95.3	0.0	134.75
$N_{dir}(-15:75)^{Iter} >$	0.0085	9.7073	95.3	0.0	134.71
$N_{dir}(-15:75)^{Iter} - N_{dir}(-15:75)^{shower} >$	0.0060	1.9354	95.2	0.0	134.66
$L^{shower}/L^{Iter} >$	0.0060	0.9857	95.2	0.0	134.62
$L_{dir}(-15:75)^{Iter} * (N_{dir}(-15:75)^{Iter} - 2) >$	0.0060	721.4480	95.1	0.0	134.45
$L^{shower}/L^{MPE} >$	0.0060	0.5246	94.9	0.0	134.24
$L^{MPE} <$	0.0073	14.8983	93.9	0.0	132.81
$L_{up}/L_{down}(Iter) <$	0.0060	0.9559	93.8	0.0	132.69
$N_{dir}(-15:25)^{Iter} >$	0.0085	5.0737	93.7	0.0	132.48
$L_{dir}(-15:75)^{Iter} * N_{dir}(-15:75)^{Iter} >$	0.0060	1081.0500	93.3	0.0	131.94
$L^{phit}(Iter) <$	0.0055	5.9681	93.1	0.0	131.72
$\lvert S^{phit}(Iter)\rvert/(\theta^{Iter}-90^\circ)$	0.0070	0.0053	92.5	0.0	130.84
$L^{shower} - L^{MPE} >$	0.0073	-6.4230	92.5	0.0	130.81
$(\lvert S^{phit}(MPE)\rvert \cdot \lvert S^{vap}(MPE)\rvert)^{(1/2)} <$	0.0055	0.2940	92.4	0.0	130.74
$\lvert S^{phit}(MPE)\rvert/(\theta^{MPE}-85^\circ)$	0.0055	0.0047	92.4	0.0	130.71
$L^{phit}(MPE) <$	0.0061	5.1778	92.2	0.0	130.36
$\lvert\theta_{MPE} - \theta_{Iter} + 1^\circ\rvert <$	0.0054	52.3254	91.5	0.0	129.39
$log(energy^{Iter}) <$	0.0054	1.1408	91.5	0.0	129.39
$log(energy^{MPE}) <$	0.0054	1.1786	91.5	0.0	129.39
$\lvert S^{phit}(MPE)\rvert/(\theta^{MPE}-90^\circ)$	0.0054	0.0255	91.5	0.0	129.39

tested cut	$\lvert S^{phit}(Iter)\rvert/$ $(\theta^{MPE}-90^\circ)$	tested cut (value)	$atm\ \nu\ MC$ $(ice\ layers)$	$BG\ MC$ $(bulk\ ice)$	F^{max}
$3\cdot I_1/(I_1+I_2+I_3)<$	0.0054	0.7996	91.5	0.0	129.39
$\lvert S^{phit}(Iter)\rvert<$	0.0054	0.5148	91.5	0.0	129.39
$(I_1/I_2)/cos(\theta^{MPE})<$	0.0054	-0.6213	91.5	0.0	129.39
$N_{ch}>$	0.0054	10.8297	91.5	0.0	129.39
$\lvert\theta_{MPE}-\theta_{LF}+6^\circ\rvert<$	0.0054	68.6975	91.5	0.0	129.38
$(I_1/I_3)/cos(\theta^{MPE})<$	0.0054	-0.5260	91.5	0.0	129.38
$N_{dir}(-15:75)^{Iter}/N_{ch}>$	0.0054	0.1351	91.5	0.0	129.37
$\lvert S^{phit}(MPE)\rvert<$	0.0054	0.4663	91.4	0.0	129.32
$COG_z>$	0.0054	-99.9350	91.4	0.0	129.32
$COG_z<$	0.0054	169.9000	91.4	0.0	129.32
$(\lvert S^{phit}(Iter)\rvert\cdot\lvert S^{van}(Iter)\rvert)^{(1/2)}<$	0.0054	0.4962	91.4	0.0	129.32
$\lvert S^{phit}(MPE)\rvert/(\theta^{MPE}-95^\circ)<$	0.0054	0.0216	91.4	0.0	129.32
$\lvert S^{phit}(Iter)\rvert/(\theta^{MPE}-90^\circ)$	0.0054	0.0093	91.4	0.0	129.32
$\lvert S^{MPE}(van)\rvert<$	0.0054	0.5868	91.4	0.0	129.32
$\lvert S^{Iter}(van)\rvert<$	0.0054	0.5926	91.4	0.0	129.32
$\theta^{dipole}>$	0.0054	1.0639	91.4	0.0	129.32
$\theta^{LF}>$	0.0054	70.2745	91.4	0.0	129.32
$\theta^{MPE}>$	0.0054	97.6169	91.4	0.0	129.32
$\theta^{Iter}>$	0.0054	95.8665	91.4	0.0	129.32
$\lvert\theta_{MPE}-\theta_{Iter}+3^\circ\rvert<$	0.0054	169.9480	91.4	0.0	129.32
$(3\cdot I_1/(I_1+I_2+I_3))/cos(\theta^{Iter})<$	0.0054	-1.5349	91.4	0.0	129.32
$(I_1/I_2)/cos(\theta^{Iter})<$	0.0054	-0.5887	91.4	0.0	129.32
$(I_1/I_3)/cos(\theta^{Iter})<$	0.0054	-0.5004	91.4	0.0	129.32
$I_1/I_2<$	0.0054	0.8980	91.4	0.0	129.32
$M^{dipole}>$	0.0054	0.0020	91.4	0.0	129.32
$L_{up}/L_{down}(MPE)<$	0.0054	1.7752	91.4	0.0	129.32
$L_{dir}(-15:75)^{Iter}>140$ *or* $L_{vis}(-15:75)^{Iter}>$	0.0054	10.0022	91.4	0.0	129.32
$L_{dir}(-15:75)^{Iter}>140$ *or* $L_{wid}(-15:75)^{Iter}>$	0.0054	60.0944	91.4	0.0	129.32
$\theta^{dipole}>60$ *or* $M^{dipole}<$	0.0054	0.8890	91.4	0.0	129.32
$L_{dir}(-15:75)^{Iter}>$	0.0054	60.4230	91.4	0.0	129.32

tested cut	$\lvert S^{phit}(Iter)\rvert/$ $(\theta^{MPE}-90^\circ)$	tested cut (value)	$atm\ \nu\ MC$ $(ice\ layers)$	$BG\ MC$ $(bulk\ ice)$	F^{max}
$I_1/I_3 <$	0.0054	0.7440	91.4	0.0	129.32
$\lvert S^{phit}(MPE)\rvert <$	0.0054	0.5998	91.4	0.0	129.32
$\lvert\theta_{Iter}-\theta^{\circ}_{Like}\rvert <$	0.0054	63.7765	91.4	0.0	129.31
$\lvert\theta_{Iter}-\theta_{LF}+4^\circ\rvert <$	0.0054	70.0790	91.4	0.0	129.31
$\lvert\theta_{dipole}-\theta_{LF}+5^\circ\rvert <$	0.0054	146.4930	91.4	0.0	129.31
$\Psi(MPE,dipole) <$	0.0054	169.0320	91.4	0.0	129.3
$\lvert\theta_{dipole}-\theta_{LF}\rvert <$	0.0054	169.8800	91.4	0.0	129.3
$\lvert S^{phit}(Iter)\rvert/(\theta^{Iter}-95^\circ) <$	0.0054	0.0296	91.4	0.0	129.29
$(3\cdot I_1/(I_1+I_2+I_3))/cos(\theta^{MPE}) <$	0.0054	-1.6006	91.4	0.0	129.28
$\Psi(dipole,LF) <$	0.0054	169.9420	91.4	0.0	129.27
$\Psi(Iter,LF) <$	0.0054	79.4444	91.4	0.0	129.25
$\Psi(MPE,Iter) <$	0.0054	54.2740	91.4	0.0	129.25
$\Psi(MPE,LF) <$	0.0054	79.8684	91.4	0.0	129.24
$L_{dir}(-1)(-15:25)^{Iter} >$	0.0054	10.0268	91.3	0.0	129.13
$L_{dir}(-15:25)^{Iter} >$	0.0054	20.3144	91.3	0.0	129.06
$L_{dir}(-15:25)^{Iter} * N_{dir}(-15:25)^{Iter} >$	0.0054	100.6550	91.1	0.0	128.86
$\lvert\theta_{Iter}-\theta_{dipole}+2^\circ\rvert <$	0.0054	129.9380	91.1	0.0	128.83
$L_{dir}(-15:75)^{MPE} >$	0.0054	31.1137	91.0	0.0	128.72
$\lvert\theta_{Bayes}-\theta_{Iter}\rvert <$	0.0085	68.4410	90.2	0.0	127.61
$L_{dir}(-15:75)^{MPE} > 140\ or\ L_{wid}(-15:75)^{MPE} >$	0.0054	50.0023	89.8	0.0	127.06
$L_{dir}(-15:25)^{MPE} >$	0.0054	20.0927	89.8	0.0	126.94
$L_{dir}(-1)(-15:25)^{MPE} >$	0.0054	10.0250	89.3	0.0	126.25
$N_{dir}(-15:25)^{MPE} >$	0.0085	5.0490	89.2	0.0	126.09
$\lvert S^{phit}(Iter)\rvert/(\theta^{MPE}-85^\circ)$	0.0266	0.0045	88.7	0.0	125.41
$\lvert S^{phit}(Iter)\rvert/(\theta^{Iter}-85^\circ)$	0.0070	0.0043	88.2	0.0	124.76
$\lvert\theta_{MPE}-\theta_{Bayes}\rvert <$	0.0070	74.9942	87.0	0.0	123.08
$COG_\rho <$	0.0054	49.9910	86.0	0.0	121.56
$\theta^{Bayes} >$	0.0085	71.0870	83.4	0.0	117.98
$\Psi(MPE,Bayes) <$	0.0087	60.9300	83.4	0.0	117.88
$\Psi(Bayes,Iter) <$	0.0085	64.8900	83.1	0.0	117.52
$\lvert v\rvert_{LF}(\mathrm{m/ns})>$	0.0054	0.1100	82.7	0.0	116.9
$L_{up}-L_{down}(Iter) <$	0.0085	-12.8910	81.7	0.0	115.61
$\lvert\theta_{Bayes}-\theta_{LF}\rvert <$	0.0067	67.8946	81.0	0.0	114.61
$\lvert\theta_{Bayes}-\theta_{dipole}\rvert <$	0.0070	63.3960	80.6	0.0	114.06
$\Psi(Bayes,LF) <$	0.0070	79.9688	79.1	0.0	111.8
$L_{dir}(-15:25)^{MPE} * N_{dir}(-15:25)^{MPE} >$	0.0094	901.3530	73.0	0.0	103.2
$L_{dir}(-15:25)^{MPE} * (N_{dir}(-15:25)^{MPE}-2) >$	0.0293	707.7400	70.7	0.0	99.94
$L_{dir}(-15:25)^{Iter} * (N_{dir}(-15:25)^{Iter}-2) >$	0.0097	732.5160	67.5	0.0	95.48

tested cut	$\lvert S^{phit}(Iter)\rvert/$ $(\theta^{MPE}-90°)$	$L_{dir}(-15:75)^{MPE}\cdot$ $(N_{dir}(-15:75)^{MPE}-2)$	tested cut (value)	$atm\ \nu\ MC$ $(ice\ layers)$	$BG\ MC$ $(bulk\ ice)$	F^{max}
$\lvert S^{phit}(MPE)\rvert/(\theta^{MPE}-85°)$	0.0296	756.8020	0.0076	113.3	0.0	160.21
$N_{dir}(-15:75)^{MPE}>$	0.0088	520.5510	6.0232	112.5	0.0	159.08
$N_{dir}(-15:75)^{Iter}>$	0.0088	564.0290	6.6068	112.4	0.0	158.98
$(\lvert S^{phit}(MPE)\rvert\cdot\lvert S^{van}(MPE)\rvert)^{(1/2)}<$	0.0186	878.3550	0.3193	112.4	0.0	158.94
$(\lvert S^{phit}(Iter)\rvert\cdot\lvert S^{van}(Iter)\rvert)^{(1/2)}<$	0.0186	878.6230	0.3278	111.4	0.0	157.52
$L^{phit}(Iter)<$	0.0088	627.7870	5.9680	111.2	0.0	157.29
$L_{up}-L_{down}(Iter)<$	0.0088	627.7600	-3.0869	110.9	0.0	156.9
$\lvert S^{phit}(MPE)\rvert/(\theta^{MPE}-90°)$	0.0289	756.8370	0.0085	109.0	0.0	154.13
$\lvert S^{MPE}(van)\rvert<$	0.0090	721.3920	0.4863	108.8	0.0	153.82
$\lvert S^{Iter}(van)\rvert<$	0.0090	721.0700	0.4858	108.7	0.0	153.75
$log(energy^{Iter})<$	0.0088	721.0700	1.1128	108.3	0.0	153.1
$\lvert S^{phit}(Iter)\rvert/(\theta^{MPE}-90°)$	0.0159	721.2940	0.0088	108.3	0.0	153.1
$3\cdot I_1/(I_1+I_2+I_3)<$	0.0088	721.1850	0.7997	108.3	0.0	153.1
$L^{MPE}<$	0.0088	721.3350	33.1866	108.3	0.0	153.1
$L^{shower}/L^{Iter}>$	0.0088	721.3740	0.9502	108.3	0.0	153.1
$\theta^{Iter}>$	0.0088	721.0750	95.3836	108.3	0.0	153.1
$log(energy^{MPE})<$	0.0088	721.1720	1.1263	108.3	0.0	153.1
$L^{shower}-L^{MPE}>$	0.0186	953.0320	-8.5816	107.3	0.0	151.75
$L^{shower}/L^{MPE}>$	0.0180	953.7360	0.5118	106.5	0.0	150.55
$L^{Iter}<$	0.0250	968.8390	8.3775	105.2	0.0	148.71
$L^{phit}(MPE)<$	0.0186	953.0010	5.3232	103.3	0.0	146.02
$\lvert S^{phit}(Iter)\rvert/(\theta^{MPE}-85°)$	0.0250	1210.2800	0.0149	88.0	0.0	124.51
$L_{dir}(-15:75)^{Iter}*N_{dir}(-15:75)^{Iter}>$	0.0202	1210.2300	601.2300	87.8	0.0	124.16
$L_{dir}(-15:75)^{MPE}*(N_{dir}(-15:75)^{MPE}-2)>$	0.0202	1210.2500	365.4570	87.8	0.0	124.16
$\lvert\theta_{MPE}-\theta_{Iter}+1°\rvert<$	0.0202	1210.0500	41.8892	87.8	0.0	124.16
$\theta^{MPE}>$	0.0202	1210.0600	95.0663	87.8	0.0	124.16
$N_{dir}(-15:75)^{Iter}-N_{dir}(-15:75)^{shower}>$	0.0202	1210.2400	0.1756	87.8	0.0	124.16
$L_{dir}(-15:75)^{MPE}*N_{dir}(-15:75)^{MPE}>$	0.0202	1210.1500	766.3450	87.8	0.0	124.16
$L^{shower}-L^{Iter}>$	0.0202	1209.9900	-0.4958	87.8	0.0	124.16
$N_{dir}(-15:75)^{Iter}-N_{dir}(-15:75)^{shower}>$	0.0202	1210.0100	-2.4859	87.8	0.0	124.16
$I_1/I_3<$	0.0202	1210.0700	0.7596	87.8	0.0	124.16
$L_{up}/L_{down}(MPE)<$	0.0202	1210.0800	1.2542	87.8	0.0	124.15
$N_{dir}(-15:75)^{MPE}/N_{ch}>$	0.0202	1210.0000	0.1007	87.8	0.0	124.15
$\lvert\theta_{MPE}-\theta_{Iter}+3°\rvert<$	0.0202	1210.1400	168.4120	87.8	0.0	124.15
$\lvert\theta_{MPE}-\theta_{Iter}\rvert<$	0.0202	1210.0100	44.3770	87.8	0.0	124.15
$\lvert\theta_{MPE}-\theta_{LF}+6°\rvert<$	0.0202	1210.0000	79.5192	87.8	0.0	124.15
$\lvert\theta_{Bayes}-\theta_{dipole}\rvert<$	0.0202	1210.0000	159.8070	87.8	0.0	124.13
$\Psi(dipole,LF)<$	0.0202	1209.9900	168.7270	87.8	0.0	124.12
$\Psi(MPE,LF)<$	0.0202	1210.2500	77.8585	87.8	0.0	124.11
$\Psi(MPE,dipole)<$	0.0202	1210.2100	169.0260	87.8	0.0	124.11

tested cut	$\lvert S^{phit}(Iter)\rvert /$ $(\theta^{MPE} - 90^\circ)$	$L_{dir}(-15:75)^{MPE}.$ $(N_{dir}(-15:75)^{MPE} - 2)$	tested cut (value)	$atm\ \nu\ MC$ $(ice\ layers)$	$BG\ MC$ $(bulk\ ice)$	F^{max}
$L_{up} - L_{down}(MPE) <$	0.0202	1210.2300	-5.0354	87.7	0.0	124.1
$\Psi(MPE, Iter) <$	0.0201	1210.0000	64.5540	87.7	0.0	124.07
$\Psi(Iter, LF) <$	0.0201	1210.0400	75.6107	87.7	0.0	124.03
$\lvert\theta_{Iter} - \theta_{dipole} + 2^\circ\rvert <$	0.0201	1210.0800	129.7270	87.5	0.0	123.74
$N_{dir}(-15:25)^{Iter} >$	0.0202	1210.2500	3.9712	87.2	0.0	123.3
$\lvert\theta_{dipole} - \theta_{Bayes} + 3^\circ\rvert <$	0.0202	1197.7900	129.8320	87.1	0.0	123.21
$L_{up}/L_{down}(Iter) <$	0.0202	1210.0000	0.9699	86.8	0.0	122.72
$I_1/I_2 <$	0.0179	1210.2100	0.7283	86.6	0.0	122.51
$\lvert\theta_{MPE} - \theta_{Bayes} + 1^\circ\rvert <$	0.0202	1197.7900	89.9285	82.5	0.0	116.64
$\lvert\theta_{Bayes} - \theta_{Iter}\rvert <$	0.0202	1197.8100	89.9941	82.2	0.0	116.28
$\theta^{Bayes} >$	0.0250	1197.8400	55.0139	77.5	0.0	109.66
$\Psi(MPE, Bayes) <$	0.0250	1197.8200	89.8995	75.2	0.0	106.31
$\Psi(Bayes, Iter) <$	0.0249	1197.7900	89.9802	75.1	0.0	106.22
$\Psi(Bayes, LF) <$	0.0250	1197.8000	82.2002	74.9	0.0	105.98

tested cut	$\lvert S^{phit}(Iter)\rvert /$ $(\theta^{MPE} - 90°)$	$L_{dir}(-15:75)^{MPE}\cdot$ $(N_{dir}(-15:75)^{MPE} - 2)$	$\lvert S^{phit}(MPE)\rvert /$ $(\theta^{MPE} - 85°)$	tested cut (value)	$atm\ \nu\ MC$ $(ice\ layers)$	$BG\ MC$ $(bulk\ ice)$	F^{max}
$\lvert S^{phit}(MPE)\rvert/(\theta^{MPE} - 85°)$	0.0249	756.8280	0.0188	0.0076	113.2	0.0	160.15
$L^{phit}(Iter) <$	0.0090	564.0140	0.0074	5.9678	113.1	0.0	159.95
$N_{dir}(-15:75)^{MPE} >$	0.0088	520.5470	0.0259	6.3830	112.5	0.0	159.08
$N_{dir}(-15:75)^{Iter} >$	0.0088	564.0800	0.0242	6.0115	112.4	0.0	158.98
$(\lvert S^{phit}(Iter)\rvert \cdot \lvert S^{van}(Iter)\rvert)^{(1/2)} <$	0.0095	396.9440	0.0288	0.2633	111.5	0.0	157.74
$(\lvert S^{phit}(MPE)\rvert \cdot \lvert S^{van}(MPE)\rvert)^{(1/2)} <$	0.0106	756.8240	0.0271	0.3186	111.2	0.0	157.23
$\lvert S^{MPE}(van)\rvert <$	0.0090	721.3730	0.0283	0.4864	108.8	0.0	153.82
$\lvert S^{Iter}(van)\rvert <$	0.0090	721.2460	0.0348	0.4855	108.7	0.0	153.75
$\lvert S^{phit}(MPE)\rvert/(\theta^{MPE} - 90°)$	0.0088	721.0880	0.0207	0.0339	108.3	0.0	153.1
$\lvert S^{phit}(Iter)\rvert/(\theta^{MPE} - 90°)$	0.0105	721.4510	0.0339	0.0088	108.3	0.0	153.1
$L_{dir}(-15:75)^{MPE} * (N_{dir}(-15:75)^{MPE} - 2) >$	0.0088	721.4640	0.0211	392.4390	108.3	0.0	153.1
$L_{up} - L_{down}(Iter) <$	0.0202	1210.2100	0.0294	-3.0032	87.5	0.0	123.74

H.3 The Optimization Mode $atm\ \nu\ \%experiment$

The entries in the column $atm\ \nu\ MC$ and F^{max} have to multiplied by a factor of 1.43 to give the correct normalization corresponding to 65 days of detector life time as proposed by the simulation. Entries in the column experiment corrrespond to about 65 days life time of experimental data. A signal normalization correction of 0.7 had been chosen.

tested cut	$L_{dir}(-15:75)^{MPE}$. ($N_{dir}(-15:75)^{MPE}-2$)	tested cut (value)	*atm. ν MC* (*ice layers*)	*experiment*	F^{max}
$\|S^{phit}(Iter)\|/(\theta_{MPE}-90°)$	1150.7500	0.0058	77.2	78.0	109.12
$\|S^{phit}(Iter)\|/(\theta_{Iter}-85°)$	1150.8000	0.0043	71.8	72.0	101.5
$\|S^{phit}(Iter)\|/(\theta_{Iter}-90°)$	1120.3600	0.0047	71.1	72.0	100.58
$\|S^{phit}(MPE)\|/(\theta_{MPE}-90°)$	1129.9300	0.0040	67.7	68.0	95.81
$\|S^{phit}(Iter)\|/(\theta_{Iter}-95°)<$	973.0140	0.0047	67.4	68.0	95.3
$\Psi(MPE,Bayes)<$	1340.7900	16.4024	67.3	68.0	95.19
$\|S^{phit}(MPE)\|/(\theta_{MPE}-85°)$	1240.3500	0.0037	66.4	67.0	93.96
$\|\theta_{MPE}-\theta_{Bayes}+1°\|<$	1391.8000	6.0951	64.8	65.0	91.6
$\|S^{phit}(Iter)\|/(\theta_{MPE}-85°)$	1581.3200	0.0074	63.1	64.0	89.23
$L_{dir}(-15:25)^{Iter}*N_{dir}(-15:25)^{Iter}>$	1596.0400	427.2100	62.3	63.0	88.17
$L_{dir}(-15:25)^{Iter}>$	1580.6800	83.2976	62.3	63.0	88.13
$\|S^{phit}(Iter)\|<$	1582.5000	0.2976	61.7	62.0	87.33
$(\|S^{phit}(Iter)\|\cdot\|S^{van}(Iter)\|)^{(1/2)}<$	1342.0400	0.2002	61.5	62.0	86.96
$\|S^{phit}(MPE)\|/(\theta_{MPE}-95°)<$	1580.6300	0.0077	61.4	62.0	86.88
$L_{dir}(-15:25)^{Iter}*(N_{dir}(-15:25)^{Iter}-2)>$	1531.1400	520.6200	60.5	61.0	85.6
$\theta^{Bayes}>$	1552.3800	82.3060	60.5	61.0	85.56
$L_{dir}(-15:75)^{Iter}>$	1667.1300	116.4710	60.4	61.0	85.48
$\Psi(Bayes,LF)<$	1531.6100	37.9924	60.4	61.0	85.43
$\Psi(Bayes,Iter)<$	1567.9000	26.7698	59.9	60.0	84.77
$\|\theta_{Bayes}-\theta_{Iter}\|<$	1567.9100	22.3667	59.9	60.0	84.76
$L_{dir}(1)(-15:25)^{Iter}>$	1445.5700	117.6760	59.8	60.0	84.54
$L_{dir}(-15:25)^{MPE}*(N_{dir}(-15:25)^{MPE}-2)>$	1194.7400	797.8200	59.6	60.0	84.24
$L^{shower}-L^{Iter}>$	1678.5200	-0.0120	59.5	60.0	84.16
$L_{dir}(-15:75)^{MPE}>$	1678.1000	123.4730	59.4	60.0	84.04
$\|S^{van}(Iter)\|<$	1678.4900	0.3728	59.3	60.0	83.85
$\|S^{phit}(MPE)\|<$	1652.0800	0.2696	59.2	60.0	83.76
$L_{dir}(-15:75)^{Iter}>140$ *or* $L_{wid}(-15:75)^{Iter}>$	1680.5300	102.1520	59.1	60.0	83.64
$L_{up}/L_{down}(Iter)<$	1646.8200	0.9480	59.1	60.0	83.59
$log(energy^{Iter})<$	1532.9100	1.7858	59.1	60.0	83.55
$\|\theta_{Bayes}-\theta_{LF}+2°\|<$	1572.3200	30.1650	59.1	60.0	83.55
$L_{dir}(-15:75)^{Iter}*N_{dir}(-15:75)^{Iter}>$	1682.1700	1788.4600	59.0	60.0	83.45
$log(energy^{Iter})<$	1532.1500	1.7898	58.9	59.0	83.29
$L_{dir}(-15:75)^{Iter}*(N_{dir}(-15:75)^{Iter}-2)>$	1680.4600	1565.1700	58.6	59.0	82.9
$L_{up}-L_{down}(Iter)<$	1627.8900	-12.2122	58.5	59.0	82.73
$N_{ch}>$	1646.5000	19.1940	58.5	59.0	82.68
$L^{phit}(MPE)<$	1709.5000	5.7076	58.4	59.0	82.63
$\|S^{van}(MPE)\|<$	1691.8800	0.3686	58.4	59.0	82.62
$L_{dir}(-15:25)^{MPE}>$	1656.2300	97.5280	58.3	59.0	82.51
$L_{dir}(-15:75)^{MPE}>140$ *or* $L_{wid}(-15:75)^{MPE}>$	1705.7300	105.5060	58.3	59.0	82.44
$\|\theta_{MPE}-\theta_{Iter}\|<$	1691.8900	8.4800	58.2	59.0	82.35

tested cut	$L_{dir}(-15:75)^{MPE}$. $(N_{dir}(-15:75)^{MPE}-2)$	tested cut (value)	*atm. νMC* (*ice layers*)	*experiment*	F^{max}
$L_{up}-L_{down}(MPE)<$	1705.7300	-21.6443	58.1	59.0	82.17
$N_{ch}>$	1678.5000	18.6345	58.1	59.0	82.14
$L^{MPE}<$	1709.4200	15.4456	57.6	58.0	81.44
$\Psi(MPE,LF)<$	1723.8500	44.3352	57.5	58.0	81.38
$\Psi(Iter,LF)<$	1723.8600	42.3400	57.5	58.0	81.25
$3\cdot I_1/(I_1+I_2+I_3)<$	1723.8900	0.7233	57.4	58.0	81.14
$N_{dir}(-15:75)^{Iter}-N_{dir}(-15:75)^{shower}>$	1295.2400	9.8729	57.4	58.0	81.11
$I_1/I_3<$	1718.4900	0.5712	57.3	58.0	81.08
$L_{dir}(-15:25)^{MPE}*N_{dir}(-15:25)^{MPE}>$	1723.8700	329.5700	57.2	58.0	80.86
$\theta^{dipole}>60$ *or* $M^{dipole}<$	1724.1700	0.0816	57.1	58.0	80.71
$\lvert\theta_{dipole}-\theta_{LF}+5^\circ\rvert<$	1714.0800	90.1724	56.8	57.0	80.37
$N_{dir}(-15:25)^{MPE}>$	1723.8500	4.9585	56.5	57.0	79.84
$(\lvert S^{phit}(MPE)\rvert\cdot\lvert S^{van}(MPE)\rvert)^{(1/2)}<$	1340.8100	0.1721	56.4	57.0	79.8
$N_{dir}(-15:25)^{Iter}>$	1678.4800	5.9979	56.4	57.0	79.7
$\lvert\theta_{Iter}-\theta^{\circ}_{Like}\rvert<$	1758.4600	33.6039	56.3	57.0	79.64
$L_{dir}(-15:75)^{Iter}>140$ *or* $L_{vis}(-15:75)^{Iter}>$	1754.5100	24.8352	56.3	57.0	79.59
$L^{shower}-L^{MPE}>$	1758.5200	-8.4127	56.2	57.0	79.53
$\lvert\theta_{MPE}-\theta_{LF}+3^\circ\rvert<$	1758.4000	39.8098	56.2	57.0	79.46
$L_{dir}(1)(-15:25)^{MPE}>$	1758.4000	18.3285	56.2	57.0	79.44
$(I_1/I_2)/cos(\theta^{MPE})<$	1766.0000	-0.5122	56.1	57.0	79.36
$(I_1/I_2)/cos(\theta^{Iter})<$	1765.8300	-0.6138	56.1	57.0	79.36
$M^{dipole}>$	1765.5200	0.0014	56.1	57.0	79.36
$L_{up}/L_{down}(MPE)<$	1765.5400	1.1670	56.1	57.0	79.36
$L_{dir}(-15:75)^{MPE}*N_{dir}(-15:75)^{MPE}>$	1765.5900	1693.6000	56.1	57.0	79.36
$COG_z<$	1765.6300	169.9250	56.1	57.0	79.36
$L_{dir}(-15:75)^{MPE}*(N_{dir}(-15:75)^{MPE}-2)>$	879.3100	1765.7200	56.1	57.0	79.36
$\lvert\theta_{Iter}-\theta_{LF}\rvert<$	1765.6700	69.5932	56.1	57.0	79.36
$(3\cdot I_1/(I_1+I_2+I_3))/cos(\theta^{MPE})<$	1765.5300	-1.6061	56.1	57.0	79.34
$\Psi(MPE,Iter)<$	1765.6500	54.2322	56.1	57.0	79.34
$L_{dir}(-15:75)^{MPE}>140$ *or* $L_{vis}(-15:75)^{MPE}>$	1765.6900	10.0073	56.1	57.0	79.29
$\Psi(MPE,Iter)<$	1766.8500	49.0443	56.0	57.0	79.21
$L_{dir}(-15:75)^{MPE}*N_{dir}(-15:75)^{MPE}>$	1767.4000	1516.8700	56.0	57.0	79.2
$L_{dir}(-15:75)^{MPE}*(N_{dir}(-15:75)^{MPE}-2)>$	453.6380	1767.4000	56.0	57.0	79.2
$(I_1/I_2)/cos(\theta^{MPE})<$	1767.3700	-0.5428	56.0	57.0	79.2
$(I_1/I_3)/cos(\theta^{MPE})<$	1767.4000	-0.5062	56.0	57.0	79.2
$L_{dir}(-15:75)^{Iter}>140$ *or* $L_{vis}(-15:75)^{Iter}>$	1767.4000	10.0357	56.0	57.0	79.2
$\lvert\theta_{dipole}-\theta_{Bayes}+3^\circ\rvert<$	1678.4800	89.2028	55.8	56.0	78.9
$COG_\rho<$	1582.5400	43.9195	55.4	56.0	78.33
$log(energy^{MPE})<$	1409.1100	1.9175	55.3	56.0	78.25

tested cut	$L_{dir}(-15:75)^{MPE}$. ($N_{dir}(-15:75)^{MPE}-2$)	tested cut (value)	*atm. νMC* (*ice layers*)	*experiment*	F^{max}
$L^{Iter}<$	1516.8200	7.4971	52.8	53.0	74.62
$L^{shower}/L^{MPE}>$	1443.7200	0.6555	36.8	37.0	52.07
$N_{dir}(-15:75)^{MPE}>$	1553.0900	14.2453	36.3	37.0	51.27
$L^{Phit}(Iter)<$	1590.0600	3.8158	33.5	34.0	47.31
$L^{shower}/L^{Iter}>$	1572.8300	1.0518	54.6	56.0	46.81
$N_{dir}(-15:75)^{Iter}>$	1475.4500	16.5385	26.0	26.0	36.74
$\theta^{MPE}>$	1590.1600	115.6650	60.5	68.0	22.07
$I_1/I_2<$	1582.6900	0.5728	60.3	68.0	21.78
θ^{LF}	1582.5300	121.6390	59.4	69.0	19.22
$COG_z>$	1596.1100	-70.3390	61.2	73.0	17.79
θ^{Iter}	1595.9400	116.3500	60.4	72.0	17.73
$N_{dir}(-15:75)^{Iter}-N_{dir}(-15:75)^{shower}>$	1582.5800	5.4282	62.6	77.0	16.51
θ^{dipole}	1596.1200	118.8470	54.6	66.0	16.19
$M^{dipole}/\theta^{dipole}<$	1595.9900	-0.0327	58.3	72.0	15.75
$(3\cdot I_1/(I_1+I_2+I_3))/cos(\theta^{Iter})<$	1596.0100	-1.7373	62.3	78.0	15.69
$N_{dir}(-15:75)^{Iter}/N_{ch}>$	1596.0000	0.2931	63.0	80.0	15.29
$\Psi(dipole,LF)<$	1595.9500	67.1010	58.2	73.0	15.09
$N_{dir}(-15:75)^{MPE}/N_{ch}>$	1596.3000	0.2669	63.4	83.0	14.34
$\Psi(MPE,dipole)<$	1595.9900	141.8200	63.7	84.0	14.16
$\lvert v\rvert_{LF}$(m/ns)>	1595.9400	0.1004	63.9	85.0	13.89

tested cut	$L_{dir}(-15:75)^{MPE}$. $(N_{dir}(-15:75)^{MPE}-2)$	$\lvert S^{phit}(Iter)\rvert/(\theta_{MPE}-90^\circ)$	tested cut (value)	*atm. ν MC (ice layers)*	*experiment*	F^{max}
$\lvert S^{van}(MPE)\rvert <$	820.2680	0.0056	0.3204	84.3	85.0	119.28
$(\lvert S^{phit}(Iter)\rvert \cdot \lvert S^{van}(Iter)\rvert)^{(1/2)} <$	1067.1700	0.0080	0.2459	82.6	83.0	116.77
$L_{dir}(-15:25)^{Iter} >$	1020.2500	0.0060	58.1762	81.3	82.0	114.99
$L_{dir}(-15:25)^{Iter} * N_{dir}(-15:25)^{Iter} >$	988.7180	0.0058	333.1890	80.7	81.0	114.16
$N_{dir}(-15:75)^{Iter} - N_{dir}(-15:75)^{shower} >$	872.3350	0.0057	4.2163	80.6	81.0	113.92
$\theta^{dipole} >$	988.7100	0.0058	43.5907	80.5	81.0	113.89
$log(energy^{Iter}) <$	1076.7300	0.0105	1.7949	80.5	81.0	113.77
$L^{phit}(MPE) <$	1124.2000	0.0061	6.0227	79.3	80.0	112.18
$L_{dir}(-15:25)^{MPE} * N_{dir}(-15:25)^{MPE} >$	1020.2300	0.0059	419.7260	78.7	79.0	111.36
$L^{MPE} <$	931.9630	0.0080	14.1063	78.7	79.0	111.36
$\lvert\theta_{dipole} - \theta_{LF} + 5^\circ\rvert <$	1124.2500	0.0060	114.1860	78.4	79.0	110.9
$L_{dir}(-15:25)^{MPE} >$	1124.3300	0.0060	37.8048	78.4	79.0	110.89
$L_{up}/L_{down}(Iter) <$	782.8000	0.0049	0.9645	78.4	79.0	110.89
$N_{dir}(-15:75)^{Iter} - N_{dir}(-15:75)^{shower} >$	798.9830	0.0051	4.4691	78.3	79.0	110.79
$\lvert S^{van}(Iter)\rvert <$	820.2540	0.0050	0.3253	78.3	78.0	110.72
$\lvert S^{phit}(Iter)\rvert <$	909.4010	0.0061	0.2270	78.3	79.0	110.68
$L_{dir}(-15:25)^{MPE} * N_{dir}(-15:25)^{MPE} >$	1019.9000	0.0058	434.1670	78.2	79.0	110.63
$\lvert\theta_{Bayes} - \theta_{Iter}\rvert <$	864.9550	0.0071	62.9422	78.1	79.0	110.5
$\Psi(Iter, LF) <$	1018.2600	0.0054	44.1065	78.1	79.0	110.45
$\Psi(MPE, LF) <$	798.4630	0.0048	46.9244	77.8	78.0	110.05
$\lvert\theta_{MPE} - \theta_{LF} + 3^\circ\rvert <$	1130.2600	0.0058	67.5744	77.7	78.0	109.94
$L_{dir}(-15:75)^{Iter} >$	1129.9000	0.0058	95.2161	77.7	78.0	109.93
$\theta^{dipole} > 60$ *or* $M^{dipole} <$	1102.2200	0.0060	0.0675	77.7	78.0	109.93
$L_{dir}^{-1}(-15:25)^{Iter} >$	820.2880	0.0049	42.9546	77.5	78.0	109.62
$\lvert S^{phit}(Iter)\rvert/(\theta_{MPE} - 85^\circ)$	926.5420	0.0125	0.0043	77.5	78.0	109.61
$L_{up} - L_{down}(Iter) <$	782.8010	0.0048	-5.5664	77.3	78.0	109.25
$L_{dir}(-15:75)^{Iter} > 140$ *or* $L_{vis}(-15:75)^{Iter} >$	1150.8600	0.0059	10.0340	77.2	78.0	109.12
$\theta^{LF} >$	834.1070	0.0048	77.8868	77.1	78.0	109.11
$I_1/I_3 <$	1143.7300	0.0058	0.7107	77.1	78.0	109.06
$L^{shower} - L^{Iter} >$	1143.6900	0.0058	-0.4502	77.0	78.0	108.94
$3 \cdot I_1/(I_1 + I_2 + I_3) <$	814.8520	0.0048	0.7295	77.0	78.0	108.92
$\lvert\theta_{MPE} - \theta_{Iter}\rvert <$	1150.7300	0.0058	45.0658	76.8	77.0	108.68
$L_{dir}^{-1}(-15:25)^{MPE} >$	1035.7100	0.0058	71.1253	76.8	76.0	108.56
$\lvert S^{phit}(Iter)\rvert/(\theta_{MPE} - 90^\circ)$	1151.9500	0.0058	0.0117	76.7	77.0	108.48
$COG_z >$	1129.8700	0.0056	-99.9455	76.7	77.00	108.46
$\lvert S^{phit}(MPE)\rvert <$	1060.3700	0.0054	0.2708	76.5	77.0	108.25
$\lvert S^{phit}(MPE)\rvert/(\theta_{MPE} - 85^\circ)$	926.6280	0.0049	0.0043	76.5	77.0	108.24

tested cut	$L_{dir}(-15:75)^{MPE}\cdot$ $(N_{dir}(-15:75)^{MPE}-2)$	$\lvert S^{phit}(Iter)\rvert/$ $(\theta_{MPE}-90^{\circ})$	tested cut (value)	*atm. ν MC* (*ice layers*)	*experiment*	F^{max}
$\theta^{Bayes}>$	864.9620	0.0070	70.4541	76.4	77.0	108.03
$\Psi(Iter,LF)<$	986.1750	0.0050	50.1471	76.2	77.0	107.8
$\lvert S^{phit}(MPE)\rvert<$	1003.5100	0.0057	0.2110	76.0	75.0	107.48
$\Psi(Bayes,LF)<$	773.3630	0.0071	45.6036	75.8	76.0	107.22
$\theta^{Iter}>$	1129.9000	0.0055	95.9690	75.8	76.0	107.13
$L_{up}/L_{down}(MPE)<$	926.5180	0.0048	0.9684	75.6	76.0	106.9
$\Psi(Bayes,Iter)<$	945.3390	0.0073	44.7255	75.4	76.0	106.62
$L_{dir}(-15:75)^{MPE}*(N_{dir}(-15:75)^{MPE}-2)>$	181.5130	0.0054	1124.1000	75.2	76.0	106.32
$\lvert S^{phit}(MPE)\rvert/(\theta_{MPE}-90^{\circ})$	986.2350	0.0049	0.0059	75.1	76.0	106.25
$\Psi(MPE,Bayes)<$	945.0170	0.0073	32.8674	75.0	76.0	106.11
$\lvert\theta_{Bayes}-\theta_{LF}+2^{\circ}\rvert<$	1020.2200	0.0075	46.3930	74.6	75.0	105.45
$\lvert\theta_{MPE}-\theta_{Bayes}+1^{\circ}\rvert<$	208.2090	0.0060	33.0648	74.4	75.0	105.22
$L_{dir}(-15:75)^{Iter}>140$ *or* $L_{wid}(-15:75)^{Iter}>$	1062.2900	0.0051	79.5595	74.3	75.0	105.12
$\lvert S^{phit}(Iter)\rvert/(\theta_{Iter}-95^{\circ})<$	1019.9100	0.0049	0.0282	74.3	75.0	105.05
$\lvert S^{phit}(MPE)\rvert/(\theta_{MPE}-95^{\circ})<$	1020.0200	0.0049	0.0327	74.3	75.0	105.05
$L_{dir}(-15:75)^{MPE}>140$ *or* $L_{wid}(-15:75)^{MPE}>$	986.1550	0.0048	50.0479	73.8	74.0	104.42
$L_{dir}(-15:75)^{Iter}*N_{dir}(-15:75)^{Iter}>$	1150.8000	0.0058	736.1850	76.8	77.0	108.64
$N_{dir}(-15:25)^{Iter}>$	979.9950	0.0082	6.9600	73.4	74.0	103.85
$N_{ch}>$	1224.2700	0.0065	17.8449	73.0	74.0	103.28
$(\lvert S^{phit}(MPE)\rvert\cdot\lvert S^{van}(MPE)\rvert)^{(1/2)}<$	975.0490	0.0106	0.1720	71.7	72.0	101.35
$L_{dir}(-15:75)^{Iter}*(N_{dir}(-15:75)^{Iter}-2)>$	335.8510	0.0058	1376.3600	71.7	72.0	101.34
$\lvert S^{phit}(Iter)\rvert/(\theta_{Iter}-85^{\circ})<$	1268.6800	0.0057	0.0259	71.2	72.0	100.74
$\lvert S^{phit}(Iter)\rvert/(\theta_{Iter}-90^{\circ})<$	1295.7700	0.0060	0.0062	71.2	72.0	100.66
$\theta^{MPE}>$	1295.1500	0.0060	107.5040	71.1	72.0	100.59
$L_{dir}(-15:25)^{Iter}*(N_{dir}(-15:25)^{Iter}-2)>$	862.4120	0.0049	365.6880	70.8	71.0	100.13
$L_{up}-L_{down}(MPE)<$	602.5600	0.0042	-18.7495	70.7	71.0	100.05
$L_{dir}(-15:75)^{MPE}>$	779.1420	0.0042	76.4174	69.9	70.0	98.87
$L_{dir}(-15:25)^{MPE}*(N_{dir}(-15:25)^{MPE}-2)>$	850.0050	0.0081	711.1590	64.4	65.0	91.08
$N_{dir}(-15:25)^{MPE}>$	1363.0600	0.0109	6.8472	62.7	63.0	88.73

tested cut	$L_{dir}(-15:75)^{MPE.}$ $(N_{dir}(-15:75)^{MPE}-2)$	$\lvert S^{phit}(Iter)\rvert /$ $(\theta_{MPE}-90^{\circ})$	$\lvert S^{van}(MPE)\rvert$	tested cut tested cut	$atm.\ \nu\ MC$ $(ice\ layers)$	$experiment$	F^{max}
$\Psi(Iter,LF)<$	820.3160	0.0059	0.3425	43.1770	86.5	87.0	122.32
$L_{up}/L_{down}(Iter)<$	799.1730	0.0060	0.3229	0.9589	86.2	87.0	121.89
$L^{shower}-L^{MPE}>$	872.9440	0.0059	0.4150	-7.5044	85.1	86.0	120.35
$L_{up}-L_{down}(Iter)<$	864.4810	0.0061	0.3229	-7.1003	84.6	85.0	119.67
$log(energy^{Iter})<$	820.2590	0.0056	0.3203	1.3916	84.3	85.0	119.28
$L_{dir}(-15:25)^{Iter}>$	1150.7300	0.0117	0.3206	58.1440	83.6	84.0	118.19
$\lvert S^{phit}(Iter)\rvert<$	1144.3700	0.0106	0.2961	0.3866	82.7	83.0	116.94
$L^{MPE}<$	1169.2400	0.0117	0.3079	16.6577	82.4	83.0	116.58
$N_{dir}(-15:75)^{Iter}-N_{dir}(-15:75)^{shower}>$	1169.2100	0.0106	0.2962	1.3939	81.2	82.0	114.9
$(\lvert S^{phit}(Iter)\rvert\cdot\lvert S^{van}(Iter)\rvert)^{(1/2)}<$	1150.7900	0.0106	0.5363	0.2430	80.5	81.0	113.86
$\lvert S^{phit}(Iter)\rvert/(\theta_{MPE}-85^{\circ})$	974.6380	0.0059	0.2927	0.0221	80.2	81.0	113.47
$\Psi(MPE,LF)<$	1124.1900	0.0067	0.3204	52.1461	79.6	80.0	112.51
$\lvert\theta_{MPE}-\theta_{LF}+3^{\circ}\rvert<$	1129.8500	0.0067	0.3206	66.3721	79.5	80.0	112.48
$L_{dir}(-15:75)^{Iter}>$	1178.8100	0.0077	0.3079	110.8870	78.5	79.0	110.97
$\lvert S^{van}(Iter)\rvert<$	1224.2700	0.0091	0.5481	0.2972	77.4	78.0	109.48
$N_{dir}(-15:75)^{Iter}-N_{dir}(-15:75)^{shower}>$	1211.6000	0.0117	0.3397	5.6598	77.2	78.0	109.17
$L_{dir}(-15:25)^{Iter}*N_{dir}(-15:25)^{Iter}>$	1124.1900	0.0062	0.4059	452.0130	75.9	76.00	107.35
$L_{dir}(-15:25)^{MPE}>$	1224.7300	0.0074	0.3208	47.1225	75.6	76.0	106.88
$\lvert\theta_{dipole}-\theta_{LF}+5^{\circ}\rvert<$	1347.7400	0.0157	0.2971	176.1570	72.6	73.0	102.72
$\theta^{dipole}>60\ or\ M^{dipole}<$	1378.3200	0.0069	0.3971	0.2325	70.1	71.0	99.16
$L_{dir}(-15:25)^{MPE}*N_{dir}(-15:25)^{MPE}>$	1219.4600	0.0070	0.4059	772.6400	67.8	68.0	95.83
$N_{dir}(-15:25)^{Iter}>$	617.6630	0.0121	0.4148	7.6908	66.8	67.0	94.46
$L_{dir}^{-1}(-15:25)^{Iter}>$	1275.7300	0.0183	0.3841	118.2660	64.9	65.0	91.75

tested cut	$L_{dir}(-15:75\text{ns})^{MPE}$. $(N_{dir}(-15:75\text{ns})^{MPE}-2)$	$\lvert S^{phit}(Iter)\rvert/$ $(\theta_{MPE}-90°)$	$\lvert S^{van}(MPE)\rvert$	$\Psi(Iter,LF)$	tested cut (value)	*atm. ν MC* (*ice layers*)	*experiment*	F^{max}
$L_{up}-L_{down}(MPE)<$	937.0200	0.0115	0.3187	43.0633	-22.8041	96.9	97.0	137.01
$L_{up}-L_{down}(Iter)<$	983.6730	0.0162	0.3566	34.8709	-8.2982	93.7	94.0	132.58
$L_{up}/L_{down}(Iter)<$	960.8450	0.0114	0.2965	53.3620	0.9625	93.7	94.0	132.47
$L^{shower}-L^{MPE}>$	987.9500	0.0102	0.3488	58.2247	-6.7248	89.6	90.0	126.66
$(\lvert S^{phit}(Iter)\rvert\cdot\lvert S^{van}(Iter)\rvert)^{(1/2)}<$	1170.5200	0.0117	0.3650	53.4856	0.3105	85.1	86.0	120.41
$\Psi(MPE,LF)<$	1170.5100	0.0132	0.3204	44.5583	40.9622	83.6	84.0	118.29
$\lvert\theta_{dipole}-\theta_{LF}+5°\rvert<$	1144.3400	0.0111	0.3235	53.3113	94.0810	83.6	84.0	118.2
$N_{dir}(-15:75)^{Iter}-N_{dir}(-15:75)^{shower}>$	1177.5900	0.0117	0.3235	53.3094	1.1014	83.4	84.0	118.01
$L_{dir}(-15:25\text{ns})^{Iter}>$	1087.5100	0.0117	0.3078	46.2173	95.0557	81.9	82.0	115.86

tested cut	$L_{dir}(-15:75)^{MPE}\cdot$ $(N_{dir}(-15:75)^{MPE}-2)$	$\lvert S^{phit}(Iter)\rvert/$ $(\theta^{MPE}-90^{\circ})$	$\lvert S^{MPE}(van)\rvert$	$\Psi(Iter,LF)$	$L_{up}-$ $L_{down}(MPE)$	tested cut (value)	$atm\ \nu\ MC$ $(ice\ layers)$	$experiment$	F^{max}
$L_{up}-L_{down}(Iter)<$	983.1070	0.0142	0.3678	42.3405	-8.3151	-8.2192	95.9	96.0	135.55
$L^{shower}-L^{MPE}>$	1018.1700	0.0112	0.4141	61.2858	-16.2141	-7.2510	93.6	94.0	132.43
$L_{up}/L_{down}(Iter)<$	1156.5400	0.0118	0.3384	60.4077	-16.4621	0.9429	80.1	80.0	113.27

H.4 The Optimization Mode $exp\ (inv.cuts)\%experiment$

tested cut	$\lvert S^{phit}(Iter)\rvert/(\theta^{MPE}-90°)$	tested cut (value)	$experiment$ $(inv.cuts)$	$experiment$ $(cuts)$	F^{max}
$L_{dir}(-15:75)^{Iter} * N_{dir}(-15:75)^{Iter} >$	0.0040	1170.5100	65.5	66.0	92.7
$L_{dir}(-15:75)^{MPE} * (N_{dir}(-15:75)^{MPE}-2) >$	0.0041	779.5540	65.3	66.0	92.28
$\Psi(Iter, LF) <$	0.0038	46.5660	63.8	64.0	90.18
$N_{dir}(-15:75)^{Iter} - N_{dir}(-15:75)^{shower} >$	0.0040	4.9962	63.8	64.0	90.18
$N_{dir}(-15:75)^{Iter} - N_{dir}(-15:75)^{shower} >$	0.0045	6.9514	63.7	64.0	90.1
$L_{dir}(-15:75)^{MPE} * N_{dir}(-15:75)^{MPE} >$	0.0047	1412.2600	63.6	64.0	89.92
$\Psi(MPE, LF) <$	0.0038	45.8996	63.6	64.0	89.89
$\lvert\theta_{Iter} - \theta_{LF} + 6°\rvert <$	0.0038	29.9368	63.4	64.0	89.69
$\lvert\theta_{Iter} - \theta_{LF} + 7°\rvert <$	0.0038	30.9233	63.3	64.0	89.59
$\lvert\theta_{Iter} - \theta_{LF}\rvert <$	0.0038	30.3929	63.3	64.0	89.53
$log(energy^{Iter}) <$	0.0038	1.6764	63.3	64.0	89.48
$L_{dir}(-15:25)^{MPE} >$	0.0039	48.7260	63.2	64.0	89.35
$L_{up}/L_{down}(Iter) <$	0.0039	0.9508	63.1	64.0	89.23
$L_{dir}(-15:75)^{MPE} >$	0.0038	105.8940	63.1	64.0	89.2
$L_{dir}(-15:75)^{Iter} > 140$ *or* $L_{wid}(-15:75)^{Iter} >$	0.0038	95.1802	62.5	63.0	88.45
$L^{shower} - L^{Iter} >$	0.0038	0.0844	62.4	63.0	88.3
$L_{dir}(-1)(-15:25)^{MPE} >$	0.0038	13.0103	62.2	63.0	87.97
$I_1/I_2 <$	0.0037	0.5433	61.8	62.0	87.43
$I_1/I_3 <$	0.0037	0.4631	61.8	62.0	87.4
$L_{dir}(-15:75)^{Iter} >$	0.0038	143.2040	61.4	61.0	86.86
$L_{up} - L_{down}(Iter) <$	0.0039	-8.2917	61.4	62.0	86.81
$L_{dir}(-15:25)^{Iter} * (N_{dir}(-15:25)^{Iter}-2) >$	0.0038	171.0490	61.3	62.0	86.68
$\lvert S^{MPE}(van)\rvert <$	0.0036	0.3205	60.5	61.0	85.52
$\lvert\theta_{MPE} - \theta_{LF} + 3°\rvert <$	0.0036	33.8710	60.4	61.0	85.47
$\lvert S^{phit}(Iter)\rvert/(\theta^{Iter}-85°)$	0.0036	0.0033	60.4	61.0	85.42
$L_{dir}(-15:75)^{Iter} * (N_{dir}(-15:75)^{Iter}-2) >$	0.0036	639.5950	60.1	61.0	85.03
θ^{LF}	0.0035	106.7080	60.1	61.0	85.01
$L_{up} - L_{down}(MPE) <$	0.0035	-20.7942	60.0	61.0	84.88
$\theta^{Iter} >$	0.0036	122.1410	59.7	60.0	84.49
$N_{dir}(-15:75)^{MPE}/N_{ch} >$	0.0035	0.2077	59.6	60.0	84.31
$L_{dir}(-15:25)^{MPE} * N_{dir}(-15:25)^{MPE} >$	0.0039	389.8960	59.5	60.0	84.16
$3 \cdot I_1/(I_1+I_2+I_3) <$	0.0035	0.6266	59.4	60.0	84.01
$COG_z <$	0.0035	134.6790	59.1	59.0	83.62
$COG_z >$	0.0035	-68.7730	58.8	59.0	83.16
$L_{dir}(-1)(-15:25)^{Iter} >$	0.0035	49.8140	58.2	59.0	82.33
$\theta^{MPE} >$	0.0036	126.3600	58.1	58.0	82.1
$L^{shower}/L^{Iter} >$	0.0034	0.9839	57.3	58.0	81.07
$L^{phit}(MPE) <$	0.0036	5.3271	57.2	58.0	80.95
$\lvert v\rvert_{LF}$(m/ns)>	0.0035	0.1143	57.1	58.0	80.79
$\lvert S^{Iter}(van)\rvert <$	0.0034	0.3240	57.0	58.0	80.64

tested cut	$\lvert S^{phit}(Iter)\rvert/(\theta^{MPE}-90°)$	tested cut (value)	*experiment* (*inv.cuts*)	*experiment* (*cuts*)	F^{max}
$\lvert S^{phit}(Iter)\rvert/(\theta^{Iter}-95°) <$	0.0033	0.0048	56.8	57.0	80.28
$\Psi(MPE, Iter) <$	0.0033	59.1410	56.7	57.0	80.23
$(I_1/I_2)/cos(\theta^{MPE}) <$	0.0034	-1.1078	56.4	56.0	79.76
$\lvert\theta_{MPE}-\theta_{Iter}\rvert <$	0.0033	28.4011	56.4	57.0	79.71
$log(energy^{MPE}) <$	0.0033	1.5675	56.3	57.0	79.69
$(\lvert S^{phit}(Iter)\rvert \cdot \lvert S^{van}(Iter)\rvert)^{(1/2)} <$	0.0033	0.2562	56.3	57.0	79.69
$(3 \cdot I_1/(I_1+I_2+I_3))/cos(\theta^{MPE}) <$	0.0033	-1.6025	56.3	57.0	79.66
$N_{dir}(-15:75)^{Iter}/N_{ch} >$	0.0033	0.1437	56.3	57.0	79.66
$\lvert S^{phit}(Iter)\rvert/(\theta^{Iter}-90°)$	0.0033	0.0063	56.3	57.0	79.66
$(\lvert S^{phit}(MPE)\rvert \cdot \lvert S^{van}(MPE)\rvert)^{(1/2)} <$	0.0033	0.2931	56.3	57.0	79.66
$L_{dir}(-15:25)^{Iter} >$	0.0033	23.9737	56.3	57.0	79.56
$(I_1/I_2)/cos(\theta^{Iter}) <$	0.0033	-0.9313	56.2	57.0	79.53
$\theta^{dipole} > 60$ *or* $M^{dipole} <$	0.0033	0.1382	56.2	57.0	79.43
$(I_1/I_3)/cos(\theta^{MPE}) <$	0.0033	-0.7516	55.7	56.0	78.81
$(3 \cdot I_1/(I_1+I_2+I_3))/cos(\theta^{Iter}) <$	0.0033	-1.6855	55.6	56.0	78.66
$\Psi(dipole, LF) <$	0.0033	127.1480	55.4	56.0	78.35
$L^{MPE} <$	0.0033	17.4230	55.3	56.0	78.27
$\lvert S^{phit}(Iter)\rvert <$	0.0033	0.2656	55.2	56.0	78.01
$L^{phit}(Iter) <$	0.0037	4.9445	54.7	55.0	77.29
$\lvert S^{phit}(MPE)\rvert <$	0.0032	0.2566	54.1	55.0	76.5
$\lvert S^{phit}(MPE)\rvert/(\theta^{MPE}-85°)$	0.0032	0.0081	54.0	55.0	76.37
$\theta^{dipole} >$	0.0033	64.9070	53.9	54.0	76.21
$(I_1/I_3)/cos(\theta^{Iter}) <$	0.0033	-0.8225	53.7	54.0	75.88
$N_{dir}(-15:25)^{Iter} >$	0.0035	4.9629	53.6	54.0	75.78
$\lvert\theta_{dipole}-\theta_{LF}+5°\rvert <$	0.0032	167.0240	53.2	54.0	75.19
$\lvert S^{phit}(MPE)\rvert/(\theta^{MPE}-95°) <$	0.0032	0.0127	53.2	54.0	75.19
$\lvert S^{phit}(MPE)\rvert <$	0.0032	0.4170	53.2	54.0	75.19
$\lvert S^{phit}(Iter)\rvert/(\theta^{MPE}-85°)$	0.0032	0.0047	53.2	54.0	75.19
$L_{dir}(-15:75)^{MPE} > 140$ *or* $L_{wid}(-15:75)^{MPE} >$	0.0032	73.6380	53.0	52.0	74.93
$L_{dir}(-15:25)^{Iter} * N_{dir}(-15:25)^{Iter} >$	0.0035	550.3000	53.0	52.0	74.93
$L^{shower}-L^{MPE} >$	0.0032	-7.5462	51.4	51.0	72.64
$L_{up}/L_{down}(MPE) <$	0.0031	1.4670	51.0	52.0	72.18
$\lvert S^{phit}(Iter)\rvert/(\theta^{MPE}-90°)$	0.0072	0.0031	51.0	52.0	72.18
$\lvert S^{phit}(MPE)\rvert/(\theta^{MPE}-90°)$	0.0050	0.0026	50.9	51.0	72.02
$L^{Iter} <$	0.0045	7.9045	50.8	51.0	71.84
$\Psi(MPE, dipole) <$	0.0030	167.1720	50.5	51.0	71.48
$COG_{\phi} <$	0.0033	49.9980	49.4	50.0	69.81
$N_{ch} >$	0.0036	19.9041	48.1	49.0	67.96
$L^{shower}/L^{MPE} >$	0.0040	0.5826	46.8	47.0	66.13
$L_{dir}(-15:25)^{MPE} * (N_{dir}(-15:25)^{MPE}-2) >$	0.0049	638.9340	45.8	46.0	64.77
$N_{dir}(-15:75)^{MPE} >$	0.0046	10.8509	44.0	43.0	62.2
$M^{dipole} >$	0.0035	0.1365	38.2	39.0	54.05
$N_{dir}(-15:75)^{Iter} >$	0.0056	12.9904	33.8	34.0	47.85
$N_{dir}(-15:25)^{MPE} >$	0.0048	7.5610	30.5	30.0	43.09
$L_{max}(-15:75)(MPE) >$	0.0019	172.7830	9.0	10.0	12.78

tested cut	$\lvert S^{phit}(Iter)\rvert/(\theta^{MPE}-90°)$	$L_{dir}(-15:75)^{Iter}\cdot N_{dir}(-15:75)^{Iter}$	tested cut (value)	*experiment* (*cuts*)	*experiment* (*inv.cuts*)	F^{max}
$\lvert S^{MPE}(van)\rvert <$	0.0048	1336.1800	0.3202	67.9	68.0	95.96
$\lvert\theta_{Iter}-\theta_{LF}+6°\rvert <$	0.0041	1196.1400	44.3254	66.5	67.0	94.09
$\lvert\theta_{MPE}-\theta_{LF}+3°\rvert <$	0.0041	1196.1200	35.6519	66.5	67.0	94.01
$L_{up}/L_{down}(MPE) <$	0.0041	1196.1300	0.9674	66.5	67.0	93.98
$\lvert S^{phit}(Iter)\rvert/(\theta^{Iter}-95°) <$	0.0041	1196.1000	0.0049	66.3	67.0	93.8
$L^{phit}(Iter) <$	0.0041	1146.3300	5.7866	66.3	67.0	93.72
$\lvert S^{phit}(MPE)\rvert/(\theta^{MPE}-95°) <$	0.0041	1146.3900	0.0050	66.3	67.0	93.7
$\lvert S^{Iter}(van)\rvert <$	0.0048	1436.7400	0.3262	66.0	67.0	93.39
$\lvert S^{phit}(MPE)\rvert/(\theta^{MPE}-85°)$	0.0041	1158.7400	0.0042	65.9	66.0	93.19
$L_{dir}(-15:75)^{MPE}*(N_{dir}(-15:75)^{MPE}-2) >$	0.0041	1196.1000	398.7040	65.7	66.0	92.98
$L_{dir}(-15:25)^{Iter}*N_{dir}(-15:25)^{Iter} >$	0.0041	1196.1000	114.4500	65.7	66.0	92.85
$\Psi(MPE,dipole) <$	0.0041	1170.3300	125.1880	65.6	66.0	92.77
$COG_z >$	0.0042	1169.7300	-68.7710	65.6	66.0	92.77
$COG_z <$	0.0041	1196.1000	168.5530	65.6	66.0	92.72
$I_1/I_3 <$	0.0041	1196.0900	0.7919	65.6	66.0	92.72
$L_{dir}(-15:75)^{Iter}>140$ *or* $L_{vis}(-15:75)^{Iter} >$	0.0041	1196.1000	10.1021	65.6	66.0	92.72
$\lvert S^{phit}(Iter)\rvert <$	0.0041	1196.1200	0.4525	65.6	66.0	92.72
$\lvert S^{phit}(Iter)\rvert/(\theta^{Iter}-90°)$	0.0041	1196.1100	0.0112	65.6	66.0	92.72
$L^{shower}-L^{Iter} >$	0.0041	1196.1100	-0.3916	65.6	66.0	92.72
$L^{shower}/L^{Iter} >$	0.0041	1196.1000	0.9529	65.6	66.0	92.72
$\lvert S^{phit}(Iter)\rvert/(\theta^{MPE}-85°)$	0.0041	1196.1200	0.0061	65.6	66.0	92.72
$\theta^{MPE} >$	0.0040	1170.0200	100.3570	65.5	66.0	92.7
$\theta^{Iter} >$	0.0040	1170.1700	102.2210	65.5	66.0	92.7
$\lvert S^{phit}(Iter)\rvert/(\theta^{Iter}-85°)$	0.0040	1170.1300	0.0091	65.5	66.0	92.7
$I_1/I_2 <$	0.0040	1169.4000	0.8840	65.5	66.0	92.7
$\lvert S^{phit}(MPE)\rvert/(\theta^{MPE}-90°)$	0.0041	1196.5100	0.0070	65.5	66.0	92.7
$(I_1/I_3)/cos(\theta^{MPE}) <$	0.0040	1169.2900	-0.5387	65.5	66.0	92.7
$log(energy^{MPE}) <$	0.0041	1197.7000	1.2023	65.5	66.0	92.67
$L_{dir}(-15:75)^{MPE} >$	0.0040	1170.3100	35.6017	65.4	66.0	92.44
$\theta^{dipole} >$	0.0040	1170.5000	0.0138	65.3	66.0	92.28
$L_{dir}(-1)(-15:25)^{Iter} >$	0.0042	1194.1900	40.7708	65.2	66.0	92.26
$\lvert S^{phit}(Iter)\rvert/(\theta^{MPE}-90°)$	0.0041	1260.7600	0.0097	65.1	66.0	92.11
$L^{phit}(MPE) <$	0.0044	1386.5900	5.6855	64.9	65.0	91.85
$N_{dir}(-15:75)^{Iter}-N_{dir}(-15:75)^{shower} >$	0.0041	1196.1300	4.9883	64.9	65.0	91.8
$L_{dir}(-15:25)^{Iter} >$	0.0042	1169.0900	59.0549	64.7	65.0	91.49
$N_{dir}(-15:75)^{MPE}/N_{ch} >$	0.0044	1408.7900	0.2183	64.6	65.0	91.39
$(I_1/I_2)/cos(\theta^{Iter}) <$	0.0042	1325.5200	-1.0129	64.6	65.0	91.31
$L_{dir}(-15:75)^{Iter} >$	0.0039	1159.5800	95.6101	64.3	65.0	91
$(3\cdot I_1/(I_1+I_2+I_3))/cos(\theta^{Iter}) <$	0.0041	1323.2200	-1.5203	64.2	65.0	90.77
$L_{dir}(-15:75)^{MPE}*N_{dir}(-15:75)^{MPE} >$	0.0044	1234.2500	1312.0100	64.2	65.0	90.77
$L_{dir}(-15:75)^{Iter}*(N_{dir}(-15:75)^{Iter}-2) >$	0.0041	1323.5700	444.2010	64.2	65.0	90.77
$\lvert v\rvert_{LF} >$	0.0041	1323.2500	0.1000	64.2	65.0	90.77
$N_{dir}(-15:75)^{Iter}-N_{dir}(-15:75)^{shower} >$	0.0041	1326.0000	1.0707	64.1	65.0	90.72
$L^{shower}-L^{MPE} >$	0.0042	1236.5300	-7.9816	64.1	65.0	90.72

tested cut	$\lvert S^{phit}(Iter)\rvert / (\theta^{MPE} - 90°)$	$L_{dir}(-15:75)^{Iter} \cdot N_{dir}(-15:75)^{Iter}$	tested cut (value)	*experiment* (*cuts*)	*experiment* (*inv.cuts*)	F^{max}
$L_{up}/L_{down}(Iter) <$	0.0048	1436.4800	0.9502	64.0	65.0	90.56
$(\lvert S^{phit}(MPE)\rvert \cdot \lvert S^{van}(MPE)\rvert)^{(1/2)} <$	0.0048	1437.9400	0.2356	63.9	64.0	90.36
$\Psi(MPE, LF) <$	0.0044	1479.7100	53.8844	63.8	64.0	90.28
$L_{up} - L_{down}(MPE) <$	0.0041	1358.0100	-15.5394	63.8	64.0	90.25
$\Psi(Iter, LF) <$	0.0044	1484.8100	64.8375	63.8	64.0	90.2
$L_{dir}(-15:25)^{MPE} >$	0.0048	1479.7300	47.2223	63.4	64.0	89.71
$L_{up} - L_{down}(Iter) <$	0.0045	1485.0600	-6.4374	63.1	64.0	89.25
$(3 \cdot I_1/(I_1 + I_2 + I_3))/cos(\theta^{MPE}) <$	0.0044	1484.8900	-1.7317	62.7	63.0	88.63
$\lvert\theta_{Iter} - \theta_{LF} + 7°\rvert <$	0.0043	1485.2300	45.4134	62.5	63.0	88.45
$\lvert\theta_{Iter} - \theta_{LF}\rvert <$	0.0043	1479.5700	38.1714	62.5	63.0	88.4
$\theta^{dipole} > 60$ *or* $M^{dipole} <$	0.0048	1584.5200	0.0587	62.2	63.0	88.02
$L_{dir}(-15:75)^{MPE} > 140$ *or* $L_{wid}(-15:75)^{MPE} >$	0.0041	1436.0500	50.0255	61.3	62.0	86.71
$\lvert\theta_{dipole} - \theta_{LF} + 5°\rvert <$	0.0048	1651.8600	127.9100	61.3	62.0	86.63
$N_{dir}(-15:25)^{MPE} >$	0.0046	1477.1700	3.5288	61.1	62.0	86.45
$\Psi(dipole, LF) <$	0.0047	1660.9200	169.8680	60.7	61.0	85.88
$L^{MPE} <$	0.0044	1619.8800	18.6333	60.7	61.0	85.83
$L^{shower}/L^{MPE} >$	0.0048	1698.9900	0.4914	60.6	61.0	85.68
$L_{dir}(-15:75)^{Iter} * N_{dir}(-15:75)^{Iter} >$	0.0047	1673.6900	822.9910	60.6	61.0	85.65
$(I_1/I_2)/cos(\theta^{MPE}) <$	0.0047	1699.2700	-0.6102	60.2	61.0	85.09
$L_{dir}(-1)(-15:25)^{MPE} >$	0.0048	1619.5900	37.6374	60.2	61.0	85.09
$(I_1/I_3)/cos(\theta^{Iter}) <$	0.0044	1651.8400	-0.5967	59.9	60.0	84.67
$L_{dir}(-15:75)^{MPE} > 140$ *or* $L_{vis}(-15:75)^{MPE} >$	0.0046	1651.8200	11.6611	59.7	60.0	84.47
$L_{dir}(-15:25)^{MPE} * N_{dir}(-15:25)^{MPE} >$	0.0048	1638.0000	300.0120	58.4	59.0	82.59
$(\lvert S^{phit}(Iter)\rvert \cdot \lvert S^{van}(Iter)\rvert)^{(1/2)} <$	0.0068	1985.6000	0.2842	53.6	54.0	75.8
$L_{dir}(-15:25)^{Iter} * (N_{dir}(-15:25)^{Iter} - 2) >$	0.0044	1408.8300	426.5430	53.4	54.0	75.57
$3 \cdot I_1/(I_1 + I_2 + I_3) <$	0.0044	1673.7300	0.4714	53.4	54.0	75.55
$L_{dir}(-15:25)^{MPE} * (N_{dir}(-15:25)^{MPE} - 2) >$	0.0048	1208.2900	576.9970	48.1	49.0	68.04
$N_{dir}(-15:75)^{MPE} >$	0.0057	1351.5800	12.1998	30.2	31.0	42.73
$L_{dir}(-15:75)^{Iter} > 140$ *or* $L_{wid}(-15:75)^{Iter} >$	0.0000	-84.6739	0.0000	0.0	0.0	0

tested cut	$\lvert S^{phit}(Iter)\rvert/(\theta^{MPE}-90^\circ)$	$L_{dir}(-15:75)^{Iter}\cdot N_{dir}(-15:75)^{Iter}$	$\lvert S^{MPE}(van)\rvert$	tested cut (value)	*experiment* (*cuts*)	*experiment* (*inv.cuts*)	F^{max}
$COG_z >$	0.0048	1196.1400	0.3023	-71.3024	68.6	69.0	97.04
$\lvert S^{phit}(Iter)\rvert/(\theta^{Iter}-90^\circ)$	0.0047	1261.8100	0.3204	0.0147	68.6	69.0	97.02
$\lvert\theta_{Iter}-\theta_{LF}+6^\circ\rvert <$	0.0046	1261.7800	0.3354	35.9582	68.4	69.0	96.68
$\lvert S^{Iter}(van)\rvert <$	0.0048	1452.2500	0.3356	0.4755	66.1	67.0	93.52
$\lvert S^{MPE}(van)\rvert <$	0.0048	1443.6300	0.3475	0.3247	66.1	67.0	93.44
$\lvert S^{phit}(Iter)\rvert/(\theta^{MPE}-85^\circ)$	0.0048	1452.2500	0.3250	0.0073	65.9	66.0	93.19
$I_1/I_3 <$	0.0049	1451.9600	0.3205	0.6643	65.9	66.0	93.19
$\lvert\theta_{MPE}-\theta_{LF}+3^\circ\rvert <$	0.0049	1479.5500	0.3399	59.9157	65.7	66.0	92.98
$\lvert S^{phit}(Iter)\rvert/(\theta^{Iter}-95^\circ) <$	0.0045	1362.8300	0.3240	0.0052	65.6	66.0	92.72
$\lvert S^{phit}(MPE)\rvert/(\theta^{MPE}-95^\circ) <$	0.0048	1479.4600	0.3689	0.0050	64.8	65.0	91.64
$L^{shower}-L^{Iter} >$	0.0048	1629.9700	0.3453	-0.0184	61.8	62.0	87.43
$\Psi(MPE, dipole) <$	0.0056	1699.0000	0.3200	141.8210	61.3	62.0	86.65
$L_{up}/L_{down}(MPE) <$	0.0051	1699.1300	0.3235	1.8947	60.7	61.0	85.86
$\lvert S^{phit}(MPE)\rvert/(\theta^{MPE}-85^\circ)$	0.0050	1729.4700	0.3398	0.0165	59.9	60.0	84.67
$\lvert S^{phit}(Iter)\rvert/(\theta^{Iter}-85^\circ)$	0.0050	1729.4700	0.3398	0.0151	59.9	60.0	84.67
$L^{shower}/L^{Iter} >$	0.0053	1661.7100	0.3680	1.0363	58.3	59.0	82.44
$L_{dir}(-15:25)^{Iter} * N_{dir}(-15:25)^{Iter} >$	0.0047	1569.5400	0.3465	482.6660	58.2	58.0	82.31
$L_{dir}(-15:75)^{MPE} * (N_{dir}(-15:75)^{MPE}-2) >$	0.0057	1651.8500	0.3683	1300.5700	57.8	58.0	81.74
$L^{phit}(Iter) <$	0.0056	1651.8500	0.5111	4.9443	56.6	57.0	80.05
$\lvert S^{MRL}(MPE)\rvert <$	0.0057	1885.3400	0.3397	0.3360	56.6	57.0	80.02
$\lvert S^{phit}(Iter)\rvert <$	0.0076	1818.8200	0.3150	0.2906	56.4	57.0	79.71
$COG_z <$	0.0046	1348.4200	0.2071	160.8780	51.5	51.0	72.87

tested cut	$\lvert S^{phit}(Iter)\rvert/$ $(\theta^{MPE}-90^{\circ})$	$L_{dir}(-15:75)^{Iter}\cdot$ $N_{dir}(-15:75)^{Iter}$	$\lvert S^{MPE}(van)\rvert$	$COG_z >$	tested cut (value)	*experiment* (*cuts*)	*experiment* (*inv.cuts*)	F^{max}
$\lvert S^{phit}(Iter)\rvert/(\theta^{Iter}-90^{\circ})$	0.0048	1196.1300	0.3204	-68.7726	0.0275	69.2	70.0	97.86
$\lvert\theta_{Iter}-\theta_{LF}+6^{\circ}\rvert <$	0.0048	1482.1400	0.3507	-46.8707	35.8788	61.8	62.0	87.35